NORTHWESTERN UNIVERSITY

Search and Characterization of New Materials For Renewable Energy Applications Through First Principles Calculations and Machine Learning

A Dissertation

Submitted to the Graduate School

In Partial Fulfillment of the Requirements

For the degree

DOCTOR OF PHILOSOPHY

In Applied Physics

Bianca Baldassarri

September 2023

Abstract

Large scale adoption of sustainable technologies for energy production and storage can be greatly facilitated by scientific advances impacting efficiency, cost and availability. The study of materials is instrumental in both upgrading the performance of existing technologies and enabling the development of new ones, and ab-initio methods and machine learning represent powerful tools in accelerating the process of materials discovery and characterization. This thesis presents multiple works leveraging computational methods to enable increased understanding and predictions of different properties across various classes of materials for renewable energy applications. A large portion of the discussion is dedicated to the thermodynamics of oxygen loss, with particular focus on solar-thermochemical water splitting applications for the production of green hydrogen. After successfully confirming the predictive accuracy of DFT computations of oxygen vacancy formation energy through comparison with experimental data, multiple high-throughput DFT studies are conducted surveying different classes of materials and identifying hundreds of new candidates compounds for solar-thermochemical hydrogen (STCH) applications. The data generated and insight gained through the high-throughput studies are then leveraged to construct machine learning models predicting the oxygen vacancy formation energy, and uncover additional hundreds of new STCH candidate materials. The knowledge acquired from such works is subsequently applied in a different context by exploring the stability of oxygen in cathode materials for Li-ion batteries. Finally, the focus is shifted from bulk to surface phenomena by studying segregation and adsorption behaviours of interest for catalytic applications. A dataset of hundreds of DFT computed segregation energies is constructed and used to train a predictive model, and segregation and oxygen adsorption behaviours in mixed transition metal carbides are investigated to guide the search for new corrosion resistant supports for fuel cell applications.

Acknowledgements

I firstly want to express my gratitude towards my advisor, Prof. Chris Wolverton, for sharing his remarkable scientific insight and creative and compelling ideas, stimulating me to become an increasingly better communicator with his ability to express complex ideas and concepts with exceptional clarity, as well as for cultivating a wonderful working environment full of collaboration and understating. I also want to thank Prof. Sossina Haile, Dr Steven Torrisi, Prof. Brian Rosen, Dr Xin Qian and Dr Emanuela Mastronardo for the extremely stimulating and helpful collaboration, scientific insights, and sharing of ideas. I am indebted to many people in the Wolverton group who have graciously shared so much of their time and knowledge with me over the years. While the gratitude truly extends to everyone in the group, I particularly want to thank so much Prof. Jiangang He, Dr Vinay Hegde, Dr Abhijith Gopakumar and Dr Shane Patel for teaching me so many new skills and patiently sitting with me through endless discussions that at times went nowhere. I also want to express how insanely lucky I feel to be able to share life with all my friends and family, and thank them for the fun, love, support, openness and understanding, and for making life worth living.

Table of Contents

List of Figures

List of Tables

1. Introduction and Motivation

The dramatic increase in world energy demands,[1] the fast rate of consumption of the limited fossil fuel resources,[2] and the continuous rise of world temperatures[3] clearly indicate the need for sustainable energy sources. Although several sustainable technologies have been proposed and developed, widespread adoption can be facilitated by enhancing performance, reducing costs, and improving availability. In this context, computational investigations of materials can accelerate materials discovery and characterization.

An attractive alternative to fossil fuels is represented by hydrogen fuel, which offers a widespread presence of possible sources, lack of harmful combustion products, and possibility for an entirely carbon free production process involving only water and energy from the Sun.[4] While hydrogen production through solar power-driven splitting of water can be achieved with a variety of methods,[5,6] thermochemical cycles reach the highest theoretical efficiency by harvesting energy from the entire solar spectrum.[7–9] Solar-thermochemical hydrogen (STCH) production through direct single-step thermolysis lacks a practical implementation given its need for prohibitively high temperatures[10,11] and gas separation system.[12] As a consequence, current efforts focus on multiple step reactions, two step cycles being favored in order to limit the loss in thermodynamic efficiency accompanying the increase in number of steps.[13] Such cycles consist of a reduction step, in which an oxide compound looses oxygen upon heating from concentrated solar power, and a water-splitting step, where steam is flown though the material at lower temperatures, re-oxidizing the material and leaving hydrogen as a product. The two-step STCH redox process can either involve two different phases (an oxidized and a reduced one), or occur through the release of a nonstochiometric amount of oxygen δ from

the metal oxide retaining its original phase throughout the cycling process, taking the form:

$$MO_x \rightarrow MO_{x-\delta} + \frac{\delta}{2} O_2 \tag{1.1}$$

$$MO_{x-\delta} + \delta H_2O \rightarrow MO_x + \delta H_2 \tag{1.2}$$

Meredig and Wolverton have analyzed the two step redox reaction from a material-independent point of view and determined a window of reduction enthalpy (ΔH_{red}) and entropy (ΔS_{red}) for both reactions steps to be favourable[14] at operating conditions of interest. Searching for materials exhibiting ΔH_{red} and ΔS_{red} within this window on a large scale in order to guide experimental investigation represents an interesting endeavor to be undertaken with the use of ab-initio methods and machine learning, and occupies a significant portion of the works here presented.

Understanding driving mechanisms of oxygen loss is of interest not just in order to generate it and control it when advantageous, but also to prevent it when it can be of detriment. An example of the latter case is represented by Li-ion battery cathodes, where O loss is part of the degradation of the material with consequent loss of function. As the use of renewable energy technologies, like solar and wind power, for electricity generation becomes more prevalent and the shift towards electric-powered transportation accelerates, the development of batteries that offer higher energy density and are less susceptible to resource limitations is crucial for advancing sustainability. Typical batteries consist of three essential components: anode, cathode, and electrolyte, and their operation relies on the reversible release and insertion of lithium at the cathode and anode. To achieve high-performance lithium batteries, cathodes with high energy density are desirable given their significant contribution to the cost, weight, and volume of the battery.[15] Presently, the prevailing cathode materials are lithium-transition metal oxides of layered rocksalt-type and spinel structures. The selection of transition metal cations for these materials is constrained due to, among other reasons, issues related to their migration upon delithiation, with some of the commonly used transition metals facing resource-related challenges.[16] An alternative gaining increasing attention lies in the employment of disordered rocksalt-type (DRX) lithium-transition metal materials. Such

compounds can offer several advantages such as small volume changes during charge and discharge limiting structural degradation upon cycling, and, in the presence of lithium excess, lithium diffusion through percolating low barrier channels, and increased capacity through anionic redox.[15,17–19] Furthermore, by exploring the broad compositional space of transition metal cations, the limitations of traditional ordered cathodes can be potentially circumvented, improving performance and a reducing reliance on resource-constrained elements. Studies evaluating various disordered rock salt-type lithium-transition metal compounds are therefore of interest to identify potential new cathode materials. In the process of selecting suitable candidates, oxygen stability can play a significant role among the various screening criteria, as oxygen loss can have adverse effect on safety, structural stability and capacity[20,21]. The study of factors influencing oxygen stability in DRX materials therefore represents another interesting problem to be tackled through the use of DFT and machine learning, and a selected portion of ongoing work in this context is presented in the latter part of this thesis.

Oxygen also plays a crucial role as an external reactant in a diverse range of contexts, including processes that allow to harness the aforementioned hydrogen fuel for electricity production. In polymer electrolyte membrane (PEM) fuel cells, for example, after hydrogen atoms are separated into protons and electrons at the anode generating current, oxygen is flown through the cathode and reacts with the protons permeating through the electrolyte and the electrons from the external circuit forming water. PEM fuel cells present several advantages, such as high power density, relatively low operating temperatures and low weight and volume compared with other fuel cells, all characteristics making them particularly suitable for use in vehicle applications. The extent of future fuel cell implementation is however contingent upon addressing durability-related issues, the targets of which have yet to be met. Degradation at the cathode is caused my multiple processes, including, importantly, the corrosion of the carbon supporting the catalytic nanoparticles.[22,23] To overcome this limitation, efforts are being directed to the search for alternative support materials, with group IV-VI transition metal carbides (TMCs) attracting significant attention.[24–29] While Mo- and W- based TMCs exhibit appealing properties, they are prone to oxidation and dissolution.

Earlier TMCs, on the other hand, appear to have higher corrosion resistance, but at the cost of lower catalytic performance. The use of alloy carbides therefore represents a potential avenue to achieve simultaneous activity and stability,[30] and is the subject of the work presented in the thesis' concluding chapter.

2. Methods and Formalisms

2.1 Density Functional Theory

The Hamiltonian of a solid with M atoms and m electrons can be expressed as (within the Born-Oppenheimer approximation and neglecting relativistic effects):

$$H = \sum_{i}^{m} T_i + \sum_{i}^{M} V_N(\mathbf{r}_i) + \sum_{i,j\neq i}^{m} V_e(\mathbf{r}_i, \mathbf{r}_j) \tag{2.3}$$

Where the first term indicates the electronic kinetic energy and following two the potential energy due to the interaction between electrons and nuclei and among the electrons themselves. Due to the electron-electron interaction, the resulting many-electron wavefunction is not separable, making the problem unfeasible to solve exactly in these terms.

The approach at the core of density functional theory (DFT) consists in making the electronic density ρ the variable of interest. Two seminal theorems by Hohenberg and Khon[31] prove, respectively, that there exists a one to one correspondence between the ground state electronic density and external potential acting on an ensemble of interacting particles, and that a universal energy functional can be defined for any external potential, and its minimum (the ground state energy) is found by minimizing the electronic density, thus determining the exact ground state of the system. The problem can then be reframed, as outlined by Khon and Sham,[32] by substituting the interacting system with a real potential with a non-interacting system acted upon by a Khon-Sham single particle potential V_{EFF}, obtaining the Khon-Sham equation (which can be solved self-consistently

as the potential is a function of the density itself):

$$(-\frac{1}{2}\nabla^2 + V_{EFF})\psi_i = \varepsilon_i \psi_i \tag{2.4}$$

Where ψ_i and ε_i are the Khon-Sham wavefunction and the corresponding eigenvalues, and V_{EFF} is composed by three terms: the external potential of the nuclei, a Hartree potential describing the independent electronic Coulomb repulsion, and an exchange-correlation potential, which contains all remaining many-body effects of exchange and correlation.

Several approaches have been developed to determine the exchange-correlation potential, none of them exact. The most widely employed ones, the local density approximation (LDA)[33] and the generalized gradient approximation (GGA),[34] utilize the exchange-correlation energy of a uniform electron gas having the same density of the system at hand at the point of interest, in the second case also keeping into account the presence of gradients in the density. Further steps towards the "heaven of chemical accuracy"[35] can then be taken, for example, by including the second derivative of the electron density (meta-GGA) or incorporating a portion of Hartree-Fock exchange, the increase in accuracy however suffering from an increase in computational cost.

The residual self interaction present in the widely used exchange-correlation functionals leads to an over-delocalization of electrons of particular impact on more strongly localized systems such as 3d transition metal oxides.[36–40] Multiple strategies can be employed to address this issue. Hybrid schemes, for example, reduce part of the electron self repulsion, with successful results in representing several transition metal oxides[41].[40] A widely used method not suffering from particularly significant computational costs relies on the addition of a Hubbard-like potential to the energy functional (DFT+U) as introduced by Dudarev.[42]

DFT+U is of particular utility when dealing with high-throughput calculations, given its ease of implementation and very limited impact on simulation times, and is in fact implemented in computational materials databases such as the Open Quantum Materials Database (OQMD)[43,44] and the Materials Project.[45] The Hubbard U potential contains a U parameter, whose value for each

applicable element is often determined empirically, with "best fit" values often differing depending on the quantity under examination (eg. lattice parameter, band gap etc.), and the exchange correlation functional utilized in the computation.[38,46] As highlighted in the literature,[38,46–48] optimal U values are susceptible to changes in the local environment the transition metal atom of interest is immersed in, and are therefore influenced by variables such as the oxidation state of the transition metal and the surrounding ligands.

2.2 Zero Temperature Properties

Stability

The formation energy of a compound is defined as:

$$\Delta E_f(A_aB_b..) = E(A_aB_b..) - \sum_{i=A,B..} x_i E_i \tag{2.5}$$

Where $E(AB..)$ is the 0K DFT energy of the compound and x_i and E_i are the mole fractions and elemental energies of its constituents (which correspond to the DFT energies per atom, with an additional correction determined through fitting to experimental formation energies for a number of elements[44]).

In order to determine the thermodynamic stability of a compound utilizing DFT formation energies, a "convex hull" is constructed for the compounds in the relevant chemical space, as exemplified in Figure 2.1. Two useful quantities in this context are the convex hull distance (calculated as the difference between the hull energy at the composition of interest and the formation energy of the compound) and the decomposition energy (determined from the distance to the convex hull formed by all compositions aside from the one of interest). All compounds on the hull are considered stable, and have hull distance of zero, while all unstable phases have a positive convex hull distance. In the context of high-throughput DFT studies, the stability ΔE_{stab} is defined as the distance to the convex hull (positive for unstable compounds and negative for stable ones) formed by all phases except the one of interest.

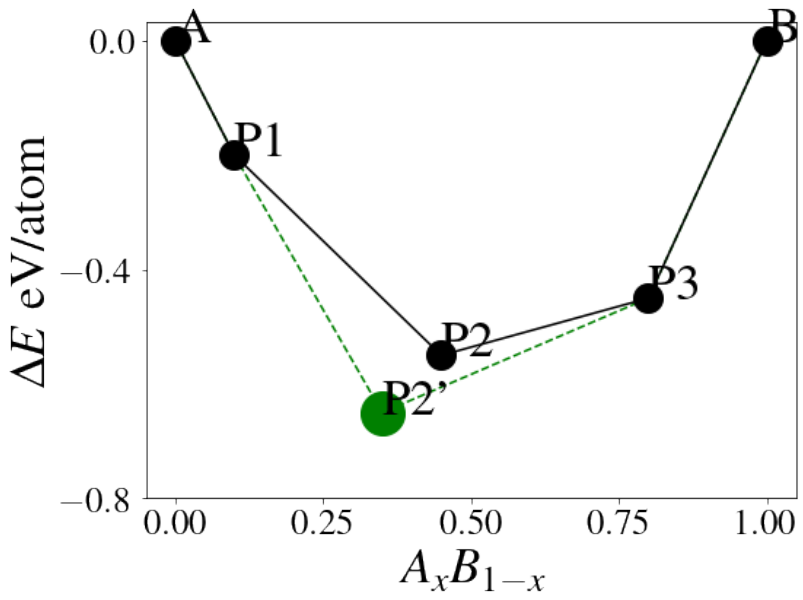

Figure 2.1: Example of the construction of the convex hull for a binary system, ΔE_{stab} for the stable phase P2 is defined with respect to the convex hull constructed using P2' (blue), while that for the unstable phase P2' is defined with respect to the hull constructed using P2 (magenta)

Oxygen Vacancy Formation Energy

While the change in enthalpy for a stochiometric reaction can be calculated by taking the DFT energy difference between the reduced and oxidized structures, the one involved in a non-stochiometric reduction reaction as the one in Eq. 1.1 is quantified through the oxygen-vacancy formation energy (E_{vf}):

$$E_{vf} = \frac{1}{\delta}E(MO_{x-\delta}) + E_O - \frac{1}{\delta}E(MO_x) \tag{2.6}$$

Where $E(MO_x)$ and $E(MO_{x-\delta})$ are the DFT 0k energies of, respectively, a bulk metal oxide cell, and a cell of the same structure containing an oxygen defect, and E_O is DFT reference energy of oxygen.

Surface Segregation Energy

In multielemental compounds, the composition in the bulk can differ from that at the surface. The preference of a solute element to be at the surface or in the bulk can be quantified by computing the

surface segregation energy, calculated as:

$$\Delta E_{segregation} = E_{surface}(host + solute) - E_{bulk}(host + solute) \tag{2.7}$$

where $E_{surface}(host + solute)$ and $E_{bulk}(host + solute)$ indicate the DFT energy of a host slab with a solute atom, respectively, in the surface layer and in one of the bulk layers.

Adsorbate Binding Energy

When an element is absorbed onto the surface of a host the binding energy of the adsorbate to the host can be calculated as:

$$E_{binding} = E_{slab}(host + adsorbate) - E_{slab}(host) - E(adsorbate) \tag{2.8}$$

where $E_{slab}(MC + O)$ and $E_{slab}(MC)$ indicate the DFT energy of a surface slab with and without the adsorbate, and E(O) indicates the DFT energy of the adsorbate specie.

2.3 Harmonic Lattice Dynamics

The motion of atoms in a crystal with L unit cells, each containing M atoms, can be described by the Hamiltonian (with the motion of the nuclei, where most of the mass resides, being considered):[49]

$$H = \sum_{l,m}^{L,M} \frac{\mathbf{p}_{l,m}^2}{m_{l,m}} + \Phi \tag{2.9}$$

Where the first term represents the kinetic energy of the nuclei (l and m indexing the unit cell and the atom respectively), and the second term the potential energy, which can be expanded as a Taylor series of the atomic displacements $u_{l,m,\alpha}$ (around $u_{l,m,\alpha} = 0$, l and m again indexing unit cell and atom, and α representing cartesian coordinates).

The core of the harmonic approximation to lattice dynamics consists in only retaining terms up

the second degree in the mentioned Taylor expansion, such that the Hamiltonian takes the form:[49]

$$H = \sum_{l,m} \frac{\mathbf{p}_{l,m}^2}{m_{l,m}} + \Phi_0 + \sum_{l,m,\alpha} \sum_{l',m',\alpha'} \Phi_{l,m,\alpha,l',m',\alpha'} u_{l,m,\alpha} u_{l',m',\alpha'} \tag{2.10}$$

Where $\Phi_{l,m,\alpha,l',m',\alpha'}$ represent the second order interatomic force constants, obtained by taking the second partial derivative of the potential with respect to the displacements $u_{l,m,\alpha}$ and $u_{l',m',\alpha'}$, evaluated in the equilibrium configuration.

The equations of motion (EOM) for the atoms in the crystal under the harmonic approximation then take the form:[49]

$$m\ddot{u}_{l,m,\alpha} = \sum_{l',m',\alpha'} \Phi_{l,m,\alpha,l',m',\alpha'} u_{l',m',\alpha'} \tag{2.11}$$

Seeking solutions having the form of plane waves (with wavevector **k**, branch index j, angular frequency $\omega_{\mathbf{k},j}$ and polarization $\mathbf{e}_{m,j,\mathbf{k}}$) and substituting them into the EOM, a "dynamical matrix" can be obtained. The diagonalization of such dynamical matrix then allows to determine the polarizations $\mathbf{e}_{m,j,\mathbf{k}}$ (which contain the information of the displacement of each atom m in the unit cell for the phonon mode k,j), and the vibrational frequencies $\omega_{\mathbf{k},j}$.

2.4 Finite Temperature Properties

Density of States

The diagonalization of the dynamical matrix at each **k** returns 3M frequency eigenvalues, from which a density of states can be constructed by grouping together frequencies in a given interval:[50]

$$g(\omega) = \frac{1}{L} \sum_{\mathbf{k},j} \delta(\omega_{\mathbf{k},j} - \omega) \tag{2.12}$$

To separately analyze the motion of each atom, the atom specific density of states projected along a unit vector $\hat{\mathbf{n}}$ can be obtained:[50]

$$g_m(\omega,\hat{\mathbf{n}}) = \frac{1}{L}\sum_{\mathbf{k},j}\delta(\omega_{\mathbf{k},j}-\omega)|\mathbf{e}_{m,j,\mathbf{k}}\cdot\hat{\mathbf{n}}|^2 \tag{2.13}$$

Vibrational Entropy

Thermodynamic properties can be derived by considering a solid with N atoms as a canonical ensemble of 3N independent quantum harmonic oscillators with frequencies $\omega_{\mathbf{k},j}$, having the partition function:[50]

$$Z = \prod_{\mathbf{k},j}\frac{e^{\omega_{k,j}/2k_BT}}{e^{\omega_{k,j}/k_BT}-1} \tag{2.14}$$

In particular, the vibrational entropy can be derived by taking the temperature derivative of the vibrational Helmholtz free energy (in turn obtained by mutiplying the natural logarithm of the partition function by a factor k_BT):[50]

$$S = \frac{1}{2T}\sum_{\mathbf{k},j}\omega_{\mathbf{k},j}\coth\frac{\omega_{\mathbf{k},j}}{2k_BT} - k_B\sum_{\mathbf{k},j}\ln(2\sinh\frac{\omega_{\mathbf{k},j}}{2k_BT}) \tag{2.15}$$

2.5 Machine Learning

Machine learning (ML) models are utilized predict properties of interest (the targets) through more easily available ones (the features) by recognizing underlying patterns in the available data. A training set is initially employed for the model to learn a representation of the target properties as a function of the features minimizing the discrepancy between predicted and computed target values. The performance of the trained model can then be tested on data that was not utilized for training, and utilized to predict target values for sets of data for which features are available and target properties are of interest.

3. Assessment of the Accuracy of DFT Computed Oxygen Vacancy Formation Energy

3.1 Background

The thermodynamics of oxygen release from metal oxide materials are fundamental to a number of energetic processes, and therefore drive materials selection for applications such as solid oxide fuel cells (SOFCs)[51,52] and solar thermochemical splitting of water and carbon dioxide.[7–9,53]

In this context, ab-initio methods and materials databases represent powerful tools to guide materials exploration on much larger scales than would be experimentally feasible by allowing for the screening of compounds based on specific properties of interest. In solar thermochemical hydrogen (STCH) production, for example, density functional theory (DFT) can be used to compute multiple quantities of interest for materials selection. Typical STCH cycles consist of a reduction step, in which a metal oxide compound loses oxygen upon heating, and a water-splitting step, where steam is supplied to the reduced material, which re-oxidizes producing hydrogen. Meredig and Wolverton have analyzed the thermodynamics of the two-step redox reaction and determined a window of values of the enthalpy change associated with the reduction reaction (ΔH_{red}) allowing for both reactions steps to be thermodynamically favourable.[14] Materials can thereby be screened for STCH applications with the use of DFT by evaluating their thermodynamic stability and computing

oxygen vacancy formation energy (ΔE_{vf}) to quantify ΔH_{red}.[54,55]

A class of materials that has attracted significant attention for use in STCH is that of perovskites oxides. The interest in such compounds, initially sparked from promising studies on strontium-doped lanthanum manganese perovskites,[56–59] is supported by a variety of attractive properties: structural stability up to high temperature, ability to withstand a large amount of oxygen loss, ease of oxygen diffusion, and a possibility for reduction at lower temperatures than Ceria, the benchmark material in the field.[56,57,60,61] Although the term "perovskite" is at times utilized somewhat broadly, the work by Breternitz and Schorr[62] provides a clear definition consisting of three specific characteristics: a ratio of 1:1:3 between the two cations and the anion (O in this case), an octahedral coordination of the B site cation, and a corner sharing octahedral network. This definition, which will be used throughout this and the next chapter, encompasses a number of different distortions of the ideal cubic perovskite structure. The lower symmetry distorted phases are commonly more energetically favourable at lower temperatures, with phase transitions to the higher symmetry phases, and ultimately the cubic phase, being observed in several materials when temperature is increased.[63–67]

Simulating finite temperature phenomena like oxygen release in STCH with a 0K methodology like DFT raises the possibility that the finite temperature structure differs from the stable one at 0K, introducing additional complexities. As such, examining the influence of crystal structure on the properties computed in an HT-DFT screening represents a fundamental part of evaluating its predictive power.

The phase change behavior of perovskites is an example of the conundrum arising when the high temperature and the 0K stable structure differ, and can significantly impact the computation of ΔE_{vf}. In the literature, studies computing the enthalpy change involved in oxygen release from perovskite structures differ in their approaches with regards to the choice of structures employed in the simulation. Ezbiri et al.[68] and Vieten et al.,[69] or example, employed structures derived from the cubic perovskite phase and examined their reduction to the corresponding brownmillerite phases. Gautam et al.[70] and Wexler[55] et al. examined several distorted perovskite prototype structures, and

introduced a vacancy in a supercell of the lowest DFT energy one. Deml et al.[41] and and Emery et.al[54] created vacancy-containing supercells of, respectively, structures reported in the Inorganic Crystal Structure Database (ICSD),[71,72] and perfect cubic perovskite structures. Indeed, a number of arguments in favor of the employment of a cubic cell, particularly within high-throughput studies, can be put forth: (i) its high degree of symmetry (and thus computational efficiency), (ii) some evidence supporting only a small difference in ΔE_{vf} between distortions that is comparable to experimental uncertainty,[54,73] and (iii) reports of phase transitions to cubic from more distorted phases at higher temperatures, like the ones at which STCH takes place.[63–67] As we will later detail, however, the cubic perovskite structure is often dynamically unstable at 0K, a factor that introduces difficulties in the computation of the oxygen vacancy formation energy.

Another factor that significantly influences the computation of ΔE_{vf} is the choice of Hubbard U parameter in DFT+U calculations. This is especially relevant for perovskites since a large portion of stable perovskites contain 3d transition metal elements.[54] The over-delocalization of electrons brought about by the residual self-interaction present in exchange-correlation functionals particularly effects systems like metal oxides containing 3d transition metals, and the introduction of a Hubbard-like potential to the energy functional[42] is a widely used option to address this delocalization.[36–40] DFT+U is especially useful within high-throughput applications given its ease of implementation and very limited impact on simulation times. The value of the U parameter contained in the Hubbard term is often determined empirically, and results are highly dependent not only on the element of interest, but also on its local environment, and on the quantity under consideration (eg. lattice constant, band gap...)[47] Studies in the literature on perovskites oxides and STCH materials differ in the U values employed, often opting for a constant value across elements and oxidation states. Deml et al.,[41] for example, applied U=3eV to all transition metals aside from U=5eV for Cu and Ag, while Ezbiri et al.[68] opted for the absence of a Hubbard U entirely. Gautam et al.[70] and Wexler et al., on the other hand,[55] performed SCAN+U calculations utilizing U values based on previous results from studies on the effect of U on SCAN calculations of transition metal oxides.[46,48] Reports of significant variations in reduction energies with U[38,73] motivate us to

examine the effects of U on ΔE_{vf} in more detail.

In chapter, we analyze both the influence of different crystal structures and that of different Hubbard U values on the oxygen vacancy formation energy. We identify issues in the computation of ΔE_{vf} in the presence of dynamically unstable structures, and develop a strategy to address them. We then perform a detailed, quantitative comparison of our DFT+U computational results with appositely generated experimental data of enthalpy of reduction, and find an accuracy between 0.2-0.6 eV/O. Several paragraphs in this chapter are quoted directly from our manuscript.[74]

3.2 Methodology

DFT Calculations All calculations have been conducted using the Vienna ab-initio simulation package (VASP),[75,76] with projector augmented wave (PAW) potentials[77] and the Perdew-Burke-Ernzehof (PBE)[78] generalized gradient approximation (GGA) for the exchange-correlation functional. A gamma centered *k*-point grid with a density of at least 8600 points per reciprocal atom was emploied, alongside and a plane wave cutoff energy of 520 eV. Self consistency was achieved when energies of subsequent iterations differed by less than 10^{-6} eV/cell, and, ionic relaxation was performed until forces were found to be below 0.01 eV/Å. For all ABO_3 compounds in Figure 3.5, additional calculations of the vacancy formation energy were performed with a plane wave cutoff of energy 800 eV, and relaxing until forces were below 0.001 eV/Å. In all cases, we observed a difference in the oxygen vacancy formation energies of less than 0.02 eV/O compared to the 520 eV plane wave cutoff and 0.01 eV/Åforce threshold (see Appendix).

The over-delocalization of electrons due to the residual self interaction present in exchange-correlation functionals[36–40] was treated through the addition of a Hubbard-like potential to the energy functional[42] (DFT+U). The influence of different U values on the vacancy formation energy of each compound was studied, and a "best fit" U was determined for Mn^{3+}, Mn^{4+}, Fe^{3+} Co^{3+} and Ni^{3+}. Comparison between DFT calculations of vacancy formation energies and experimental results of enthalpies of reduction are then provided for several sets of Hubbard U values: the "best fit U" vales,

OQMD U values, and a constant value of U=4eV for all transition metal elements. Spin polarization with a ferromagnetic configuration was applied to transition metal cations (initializing magnetic moments to $5\mu_B$) for the following reasons: (i) oxygen loss being measured at temperatures higher than spin ordering,[79,80] (ii) evidence of the limited influence of magnetic configuration on both bulk and defect DFT energies,[81] and (iii) in order to maintain consistency with the high-throughput studies discussed in the next chapter. For Co-containing compounds, a low-spin configuration (where magnetic moments are initialized to $0\mu_B$ for all Co atoms aside from the two neighboring the O vacancy in the vacancy-containing cell, which are initialized to $1\mu_B$) was utilized consistently for low-throughput calculations.

For all compounds, we calculated the oxygen vacancy formation energy for each unique oxygen site, and report the lowest one. We used the experimentally synthesized structure when dynamically stable, and a dynamically stable distortion otherwise, as described in Section 3.3. Defect containing cells with a minimum of 79 atoms were utilized to maximize accuracy (see Appendix for cell size convergence testing).

The lack of accuracy in the DFT energies of diatomic molecules requires the addition of an empirical correction to the DFT energy of the O_2 molecule, and hence to the reference energy (E_O) of equations 2.5 and 2.6. Such correction is generally determined by fitting formation energies of oxides to experimental data,[38,81–84] leading to a range of results depending on the data set utilized for the fit. Wang et al.,[38] Lee et al.[81] and Grindy et al.[83] have each selected a set of binary oxides of known structure, eliminating transition metal oxides due to further complexities associated with the use of DFT+U, and obtained similar values for E_O: -4.25 eV for Refs[38] and[81] (which utilized the same set of 7 binary oxides), and -4.33 eV for Ref[83] (where the pool was expanded to 15). Fig 3.2 illustrates the result of the fit of 13 of the 15 oxides in Grindy's work, performed with the same settings as the low-throughput calculations in this work, as well as with OQMD data, leading to a value of $E_O = -4.29$ eV in both cases. The value of the oxygen DFT reference energy of -4.52 eV employed in the OQMD framework was, however, determined by performing simultaneous fits of several elements (as detailed in Kirklin et al[44]), with a data set comprising all OQMD entries

for which experimental formation energy data was available. Arguments supporting either extreme of the range of values provided can be formulated, from the breadth of the data included in the OQMD approach, to the reliability gained by avoiding multiple concurrent fittings when restricting to non-transition metal binary oxides only. Fig 3.3 displays the result of a third fit, which aims to exploit the advantages of both the aforementioned strategies by limiting the data set to a few hundred oxides not containing any of the elements that have a correction applied to their DFT elemental energy, and leads to a yet different result of -4.43 eV. In light of the above discussion, we consider the choice of oxygen DFT reference energy value to introduce an additional complexity in the comparison between computation and experiment presented in the next section. For the present work, in the interest of consistency between high- and low-throughput data, we employ the OQMD value of $E_O = -4.52$ eV for all calculations, and emphasize the presence of an associated uncertainty of about 0.2 eV. We note that a change in the empirical correction factor for O_2 would result in a constant shift of all vacancy formation energies, i.e. the difference between two vacancy formation energies would be unaffected by this correction.

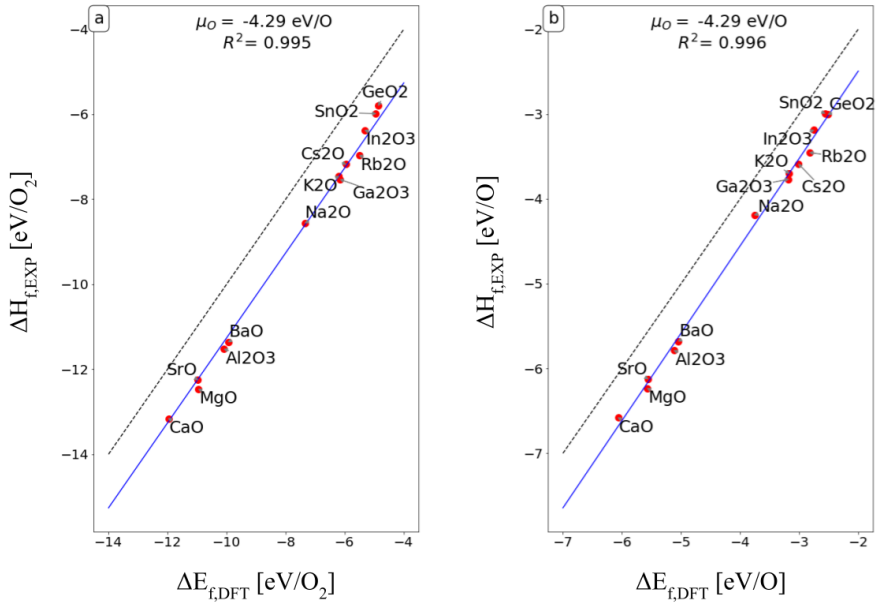

Figure 3.2: Fits of DFT formation energies (x axis) and experimental formation enthalpies (y axis) of 13 binary oxides of known structure, used to determine the empirical correction to the DFT energy of oxygen, (a) using the same settings as the low throughput calculations in this work (b) using OQMD data of the same compounds.

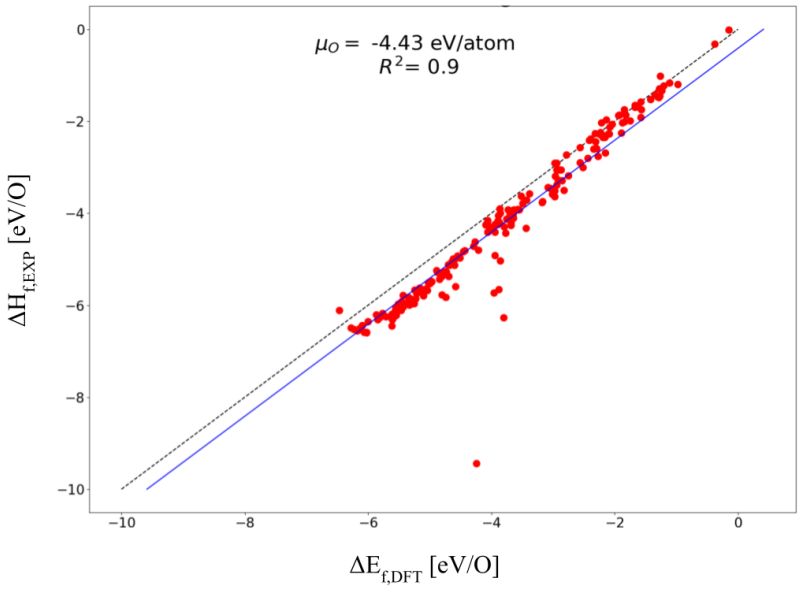

Figure 3.3: its of DFT formation energies (x axis) and experimental formation enthalpies (y axis) of any oxide not containing any other fit elements, using OQMD data

In order to determine the 0K dynamic stability of the compounds investigated in the next section, the phonon dispersion was calculated by means of the finite difference method as implemented in PHONOPY[50] utilizing 2x2x2 supercells (2x2x1 for cases in which the original cell contained 30 atoms). The presence of imaginary frequencies in the phonon band structure was considered as evidence of dynamic instability. The degree of instability was quantified with the energetic difference between the unstable phase and its lowest energy dynamically stable distortion on the OQMD, which we found to be positively correlated with the largest imaginary phonon frequency, as shown for a selected number of cubic perovskites in Fig 3.4.

3.3 Results

In order to assess the accuracy of DFT in guiding materials search based on reduction thermodynamics, we perform a detailed quantitative comparison between DFT ΔE_{vf} and experimental measurements of oxide reduction enthalpies. As mentioned in Section 3.1, this comparison is commonly complicated by several factors: the lack of appropriate experimental data, the choice of

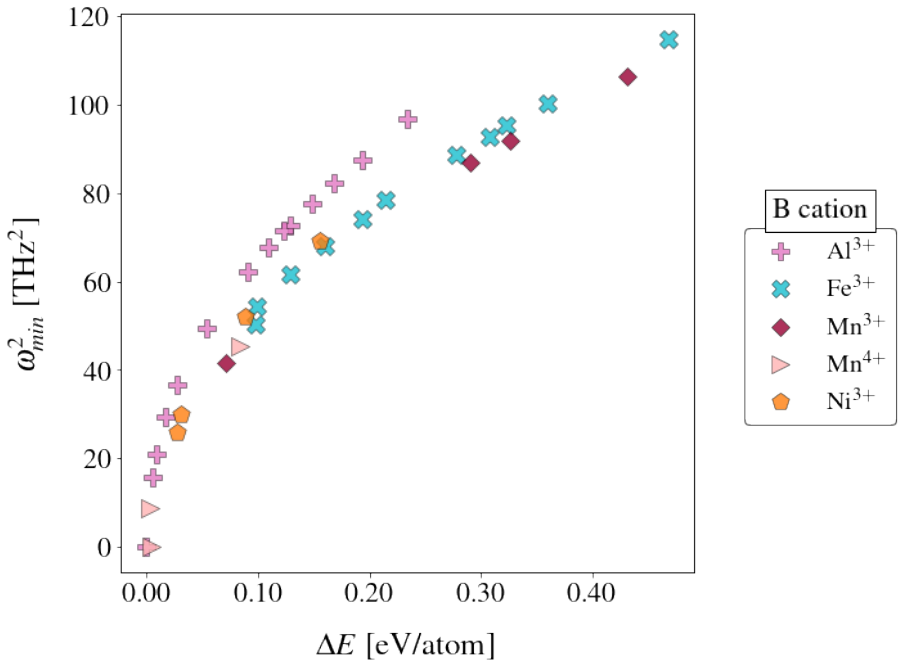

Figure 3.4: Relationship between two ways of quantifying the 'degree of dynamic instability' for a number of ABO_3 cubic perovskite oxides. On the x axis is the energy difference between the cubic phase and the lowest energy perovskite phase on the OQMD at the same composition, on the y axis the square of the largest imaginary frequency in the phonon band structure (in other words, the minimum frequency ω_{min}) of the cubic perovskite. A quadratic relationship is evident between the two, with slightly different trends depending on the B site cation, which is indicated by different markers.

Hubbard U in DFT+U calculations, and the choice of crystal structure to employ in the simulation for cases where 0K ground state structure differs from the finite-temperature-stabilized structure observed in experiment. In the following section, we first separately address each of these factors and then present the results of the comparison.

Experimental Data While a variety of experimental studies on examining metal oxide reduction have been conducted for STCH applications,[56–58,85–95] most of the available data focuses on hydrogen production cycles, reporting H_2 (or CO) yield and O_2 release rather than the thermodynamic quantities computed in DFT screenings.[14,41,54,68,96,97] We address this issue by selecting a number of ABO_3 compounds for synthesis and characterization. We perform thermogravimetric measurements on these compounds as a function of temperature and derive the standard state enthalpy and entropy of reduction, while also extracting structural information via in situ X-ray

Table 3.1: List of experimentally synthesized compounds on which TGA measurements were performed and the structures and energy differences of the structures of interest, from left to right: experimentally observed crystal structures (EXP) (if a phase transition was observed the high temperature structure is also reported, and the transition is indicated with an arrow),[79,80] dynamically stable distortions (DSD), ground state structures on the OQMD (DFT GS), energy difference between the cubic perovskite phase and the ground state structure on the OQMD (ΔE(CUB PEROV-DFT GS)), and energy difference between the experimentally observed structure and the dynamically stable distortion (ΔE(EXP-DSD)). Perovskite structures are indicated with "perov" and the crystal system of the distortion of interest (for example:for $YFeO_3$ the DFT GS structure is an orthorhombic perovskite with "$GdFeO_3$" prototype, which is indicated as "ortho perov"), while non-perovskite structures are indicated using the name of the prototype structure on ICSD (for example: $LuMnO_3$ $YMnO_3$ and $HoMnO_3$ have, in all three cases, a DSD structure with the same hexagonal structure as prototype: "$LuMnO_3$"). For all structures the spacegroup is reported in parenthesis. A visual representation of the structures can be found in Figures 11.65 and 11.66

Formula	EXP structure	DFT DSD structure	DFT GS structure	ΔE (CUB PER - DFT GS) $\frac{meV}{atom}$	ΔE (EXP-DSD) $\frac{meV}{atom}$
$PrCoO_3$	ortho perov (Pnma)	ortho perov (Pnma)	ortho perov (Pnma)	94	-
$SmCoO_3$	ortho perov (Pnma)	ortho perov (Pnma)	ortho perov (Pnma)	168	-
$LaCoO_3$	rhomb perov (R-3c)	rhomb perov (R-3c)	monocl perov ($P2_1/c$)	86	-
$CaMnO_3$	ortho perov (Pnma) $\rightarrow$ cub perov (Pm-3m)	ortho perov (Pnma)	ortho perov (Pnma)	101	-
$SrMnO_3$	"$BaMnO_3$" ($P6_3/mmc$)	"$CsCuBr_3$" ($C222_1$)	"$CsCuBr_3$" ($C222_1$)	44	29
$BaMnO_3$	"$BaNiO_3$" ($P6_3/mmc$)	"$KNiCl_3$" ($P6_3cm$)	"$KNiCl_3$" ($P6_3cm$)	115	1
$LaMnO_3$	rhomb perov (R-3c)	ortho perov (Pnma)	ortho perov (Pnma)	70	11
$YMnO_3$	"$LuMnO_3$" ($P6_3cm$) $\rightarrow$ "Be_3N_2" ($P6_3/mmc$)	"$LuMnO_3$" ($P6_3cm$)	"$LuMnO_3$" ($P6_3cm$)	313	-
$HoMnO_3$	"$LuMnO_3$" ($P6_3cm$) $\rightarrow$ "Be_3N_2" ($P6_3/mmc$)	"$LuMnO_3$" ($P6_3cm$)	"$LuMnO_3$" ($P6_3cm$)	364	-
$LuMnO_3$	"$LuMnO_3$" ($P6_3cm$)	"$LuMnO_3$" ($P6_3cm$)	"$LuMnO_3$" ($P6_3cm$)	483	-
$YFeO_3$	ortho perov (Pnma)	ortho perov (Pnma)	ortho perov (Pnma)	322	-
$HoFeO_3$	ortho perov (Pnma)	ortho perov (Pnma)	"$LuMnO_3$" ($P6_3cm$)	364	-
$LuFeO_3$	ortho perov (Pnma)	ortho perov (Pnma)	"$LuMnO_3$" ($P6_3cm$)	493	-
$LaNiO_3$	rhomb perov (R-3c)	rhomb perov (R-3c)	rhomb perov (R3c)	30	

measurements. The list of compounds and crystal structures is given in Table 3.1, and further details on the experimental measurements, techniques and results can be found in Ref.[79,98,99]

DFT Crystal Structure In our analysis we compare the effects of utilizing different choices of crystal structure on the DFT computed oxygen vacancy formation energy. To do so, we compute the oxygen vacancy formation energy utilizing four different structures (also referred to in Table 3.1) for each of the ABO_3 compositions selected for experimental investigation:

- the undistorted cubic perovskite structure in the Pm-3m spacegroup (labelled CUB PEROV)
- the lowest energy (or ground state) structure on the OQMD at that composition (labelled DFT

GS)

- the crystal structure observed during experimental measurements of oxygen loss (labelled EXP)

- a 'dynamically stable distortion' (labelled DSD)

The reason for the introduction of the DSD structure is to address the issues arising when the EXP structure is dynamically unstable at 0K (which will be detailed in the next paragraphs). In cases where the EXP structure is dynamically stable at 0K, the DSD and EXP structures coincide and the results for the calculation of the EXP structure are used directly. In the cases where the EXP structure is instead dynamically unstable, a suitable alternative structure is required for the calculations. Accordingly, we identify a dynamically stable structure amongst the phases present in the OQMD at that composition with the same oxygen framework as the respective experimentally observed structure. The DSD structure is lower in energy than the EXP structure and often corresponds to the ground state structure on the OQMD. The dynamical (in)stability of all structures is determined by performing phonon calculations as detailed in the Methods Section.

In order to distinguish the effects of differences in the crystal structure from the consequences of dynamic instability, we separate the contributions to the oxygen vacancy formation energy into two terms:

$$\Delta E_{vf} = \Delta E_{vf,UN} + \Delta E_{vf,R} \tag{3.16}$$

The first term indicates the effect of removing an O atom while keeping everything else in the structure fixed, and the second term indicates the effect of letting the atoms in the structure relax once the O vacancy is introduced.

More specifically, the first term, which we call the 'unrelaxed contribution' (UN), quantifies the DFT energy difference between a relaxed (with a relaxation of atomic positions and cell vectors performed while maintaining the symmetry of the initial structure) bulk metal oxide structure and that same structure containing the vacancy without any change in cell volume and shape or

coordinates of the remaining atoms:

$$\Delta E_{vf,UN} = E_{UN}(ABO_{3-\delta}) + E_O - E_R(ABO_3) \tag{3.17}$$

The second term, which we refer to as 'relaxation contribution' (R), corresponds to the energetic change of the vacancy-containing structure when allowing for relaxation of the cell and ionic positions:

$$\Delta E_{vf,R} = E_R(ABO_{3-\delta}) - E_{UN}(ABO_{3-\delta}) \tag{3.18}$$

Shown in Figure 3.5 are these two contributions to the oxygen vacancy formation energy and their correlations to the structural choices in the calculations (with U values set, for convenience, to those in the OQMD). In particular, we compare the results of calculating ΔE_{vf} utilizing a cubic perovskite structure, and utilizing the DSD structure. We do so to investigate the accuracy of calculating ΔE_{vf} utilizing a cubic perovskite structure even for compounds for which such structure is not the lowest energy perovskite distortion, which, as mentioned in the introduction, is a strategy previously adopted in the literature.

We start by examining the relaxation contribution (Figure 3.5 b), as we have found this term to be significantly affected by the consequences of dynamic instability. Dynamically unstable phases do not sit in an energetic minimum, but rather at a symmetry-dictated local maximum or saddle point. When a vacancy is introduced, the symmetry of the cell is lowered and the atomic displacements which occur to accommodate the defect can change the entire structure (even far away from the defect) into a more distorted lower energy state. Hence, the energetic difference between the bulk and the defective cell is smaller than if the bulk cell had been dynamically stable. In other words, the initial bulk state being higher in energy can be seen as artificially lowering the defect formation energy. This being an effect of symmetry and atomic displacements, it arises when the defective cell is allowed to relax. Shown in Figure 3.5 b is a comparison of the relaxation contribution to the oxygen vacancy formation energy computed for the dynamically stable distortions (y axis) and for the dynamically unstable cubic perovskite artistotypes (x axis). For all DSDs, relaxation

results in an energy decrease of about 1 eV/O. In contrast, the effect for cubic perovskite structures can be of several eV/O. The effect increases with the degree of dynamic instability of the cubic perovskite structure, here defined as the energetic difference between the energy of the dynamically unstable cubic perovskite phase and the lowest energy dynamically stable perovskite distortion. Furthermore, the magnitude of the energetic decrease upon relaxation of the defect-containing structure increases not only with the degree of instability, but also with the number of atoms that move during relaxation: the larger the vacancy-containing cell, the larger the energetic gain upon relaxation of the defective structure, and therefore the larger the lowering of ΔE_{vf}. This supercell size dependence present in dynamically unstable compounds can be understood by considering that the introduction of a vacancy results in a distortion of the entire cell, not merely locally around the vacancy. Therefore, the more atoms are present in the cell, the more atoms distort upon introducing the vacancy and letting the structure relax, and the more the energy of the vacancy containing cell decreases compared to an undistorted structure with the same number of atoms. This then means that the relaxation energy $\Delta E_{vf,R}$ per O vacancy increases with the size of the vacancy containing cell. Note that this effect occurs even if constraints on the cell volume and shape are applied upon relaxation. This means that an additional and non-trivial issue involved in the use of dynamically unstable structures for defect calculations is the lack of convergence of the defect formation energy with respect to cell size, as shown in Figure 3.6.

We now examine the 'unrelaxed contribution', $\Delta E_{vf,UN}$, which encapsulates effects apart from dynamic instability on ΔE_{vf}. In Figure 3.5 a, we compare the $\Delta E_{vf,UN}$ between the DSD structures and cubic perovskite structures. The orthorhombic and rhombohedral perovskites have very small deviations in $\Delta E_{vf,UN}$ between the DSD and cubic perovskite. This is an indication that, in the cases where we observe a large difference in ΔE_{vf} between calculations that use a dynamically unstable cubic perovskite structure and calculations that use a dynamically stable perovskite distortion, such difference is likely attributable to the dynamic instability of the cubic perovskite phase. For the cases where the DSD structure is a non-perovskite rather than perovskite, we observe a more significant difference in $\Delta E_{vf,UN}$ between DSD and CUBIC PEROV. The largest difference observed

is for $BaMnO_3$ where the oxygen octahedra in the DSD structure are face-sharing, rather than corner-sharing like in perovskites. The discrepancy is also present, in smaller scale, in $SrMnO_3$ for which the DSD structure contains both corner- and face-sharing octahedra. These structural differences are accompanied by differences in the DFT band gap(E_g), which (from OQMD) is E_g=0 for both $BaMnO_3$ and $SrMnO_3$ in the cubic perovskite phase, but non-zero in both cases for both the DSD and EXP structure, with values of 1.2 eV for "$CsCuBr_3$"-type $SrMnO_3$ and 1.1 eV for "$BaMnO_3$"-type $SrMnO_3$, and 1.9 eV for both "$BaNiO_3$"-type and "$KNiCl_3$"-type $BaMnO_3$. $YMnO_3$, $HoMnO_3$ and $LuMnO_3$, for which the difference between the unrelaxed ΔE_{vf}^{DSD} and $\Delta E_{vf}^{CUB\ PEROV}$ is much less pronounced, present a non-perovskite DSD structure in which the Mn cations are surrounded by polyhedra with 5 oxygen atoms as vertices, connected in a corner-sharing fashion, and have the same OQMD band gap in both the DSD and the cubic perovskite phase.

We also compare the relaxed and unrelaxed contributions of the DSD and EXP structures and show that the DSD surrogate structures can capture the energetics of O vacancy formation of the EXP structures without suffering from the issues of dynamic instability. In Fig 3.7 we plot $\Delta E_{vf,UN}$ and $\Delta E_{vf,R}$ comparing DSD and EXP structures. In all cases the difference in the $\Delta E_{vf,UN}$ is negligible, indicating that the DSD structures achieve the goal of capturing the ΔE_{vf} of the EXP structures when relaxation effects are not considered. As for the relaxation component, a small difference is visible for compounds for which the EXP structure is dynamically unstable. The difference $\Delta E_{vf,R}$ being more contained for EXP structures than for cubic perovskites can be traced back to the degree of dynamic instability being much smaller, and therefore leading to less evident lowering of ΔE_{vf} . While on a practical level a small degree of dynamic instability does not excessively appear to impact accuracy, the previous observations about the origin of atomic relaxations away from the vacancy and the lack of convergence with cell size still caution against the use of dynamically unstable structures.

Hubbard U Parameter Since the selected ABO_3 compounds all contain 3d transition metal atoms, we can assess the influence of the choice of Hubbard U parameter on the oxygen vacancy

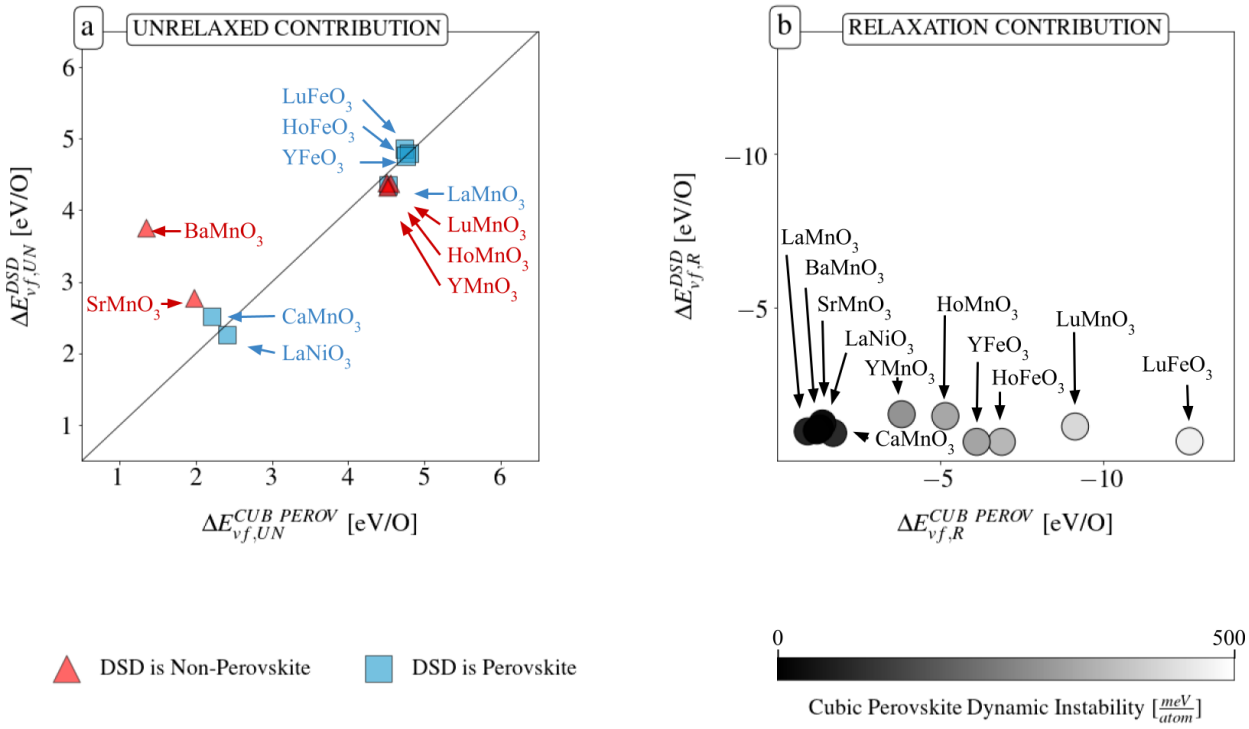

Figure 3.5: Contributions to the DFT-calculated oxygen vacancy formation energy utilizing the cubic and DSD structures: (a) energy of removing an O atom without allowing for ionic relaxation upon vacancy formation (Eq. 4), and (b) energy difference between the relaxed and unrelaxed vacancy-containing structures (Eq. 5). Increasing lightness in the data points color in (b) indicates increase in the degree of dynamic instability of the cubic structure, quantified by taking the DFT energy difference between the cubic and the lowest energy perovskite distortion for each compound. In (a), different colors/shapes indicate whether the structures belong to the perovskite family. U values are those employed in the OQMD and vacancy-containing supercells are of 119 atoms for $BaMnO_3$,, $YMnO_3$, $HoMnO_3$ and $LuMnO_3$ and 79 atoms for all others.

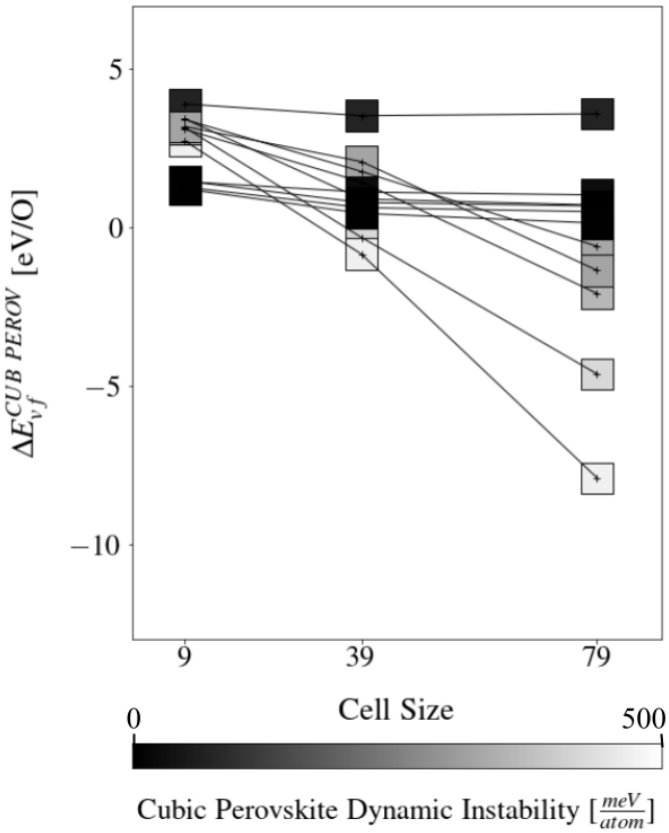

Figure 3.6: Change in oxygen vacancy formation energy with cell size for dynamically unstable cubic perovskite structures, displaying a lack of convergence with cell size, an effect more dramatic the larger the instability of the cubic structure, here quantified by taking the difference in formation energy between cubic and the lower energy perovskite distortion on the OQMD.

formation energy, and identify the "best fit" value (Table 3.2) by comparing with experiment. In general, with the exception of Fe^{3+} which shows a very weak dependence on the U parameter, a clear negative linear trend between U and ΔE_{vf} is visible for all compounds in Fig 3.8. Furthermore, compounds containing the same element in the same oxidation state show a similar rate of decrease of ΔE_{vf} with U and the same "best fit" value of U. Shown in Fig. 3.8 are also the 'best fit' U values determined by comparison with experimental data (represented with horizontal banners of thickness corresponding to the value ranges given by the error bars), and the values employed in the OQMD (marked with vertical lines). While the two are in general agreement for Co^{3+}, Mn^{3+} and Fe^{3+}, in the case of Mn^{4+} and, even more visibly, Ni^{3+}, OQMD U values appear to lead to a significant underestimation of the vacancy formation energy. In other words, the "best fit" U

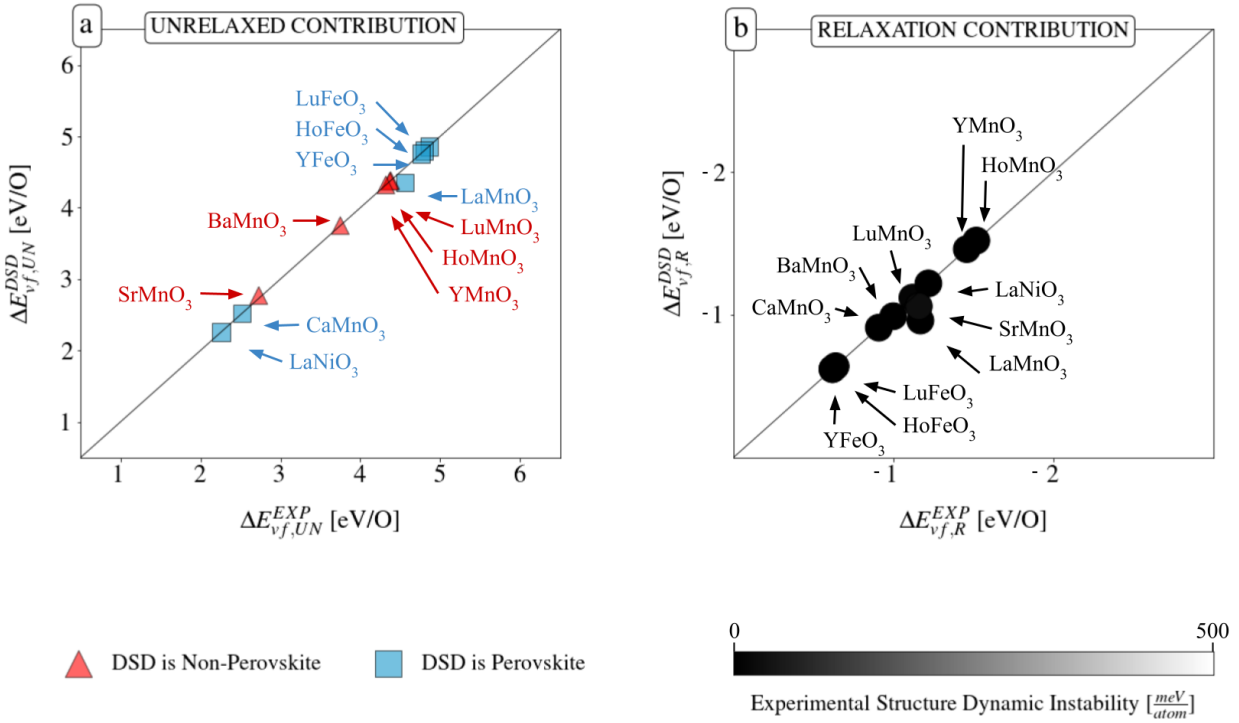

Figure 3.7: Comparison and DFT calculations of the oxygen vacancy formation energy utilizing the experimentally measured and DSD structure. On the left only electronic relaxation is performed upon vacancy formation, on the right the energy difference before and after ionic relaxation is considered. U values are those implemented in the OQMD and vacancy cell sizes are of 79 atoms (119 for $BaMnO_3$, $YMnO_3$, $HoMnO_3$ and $LuMnO_3$)

values are in multiple cases smaller than the U values employed in the OQMD. Given the limited extent of the data set and the influence of other variables (such as the correction of the oxygen DFT reference energy) on the oxygen vacancy formation energy, we consider this evidence to provide helpful insight to apply to our high-throughput results, but not yet sufficient to be interpreted as conclusive evidence of the optimal U values to apply to ΔE_{vf} calculations of perovskite oxides across the board. Therefore, we conduct the high-throughput study detailed in the next section utilizing OQMD U values (changing such values would involve very substantial changes to the database), but, in recognition of the indication of the underestimation that such U values induce in the vacancy formation energy, we favor compounds with ΔE_{vf} in the lower part of the window of interest for STCH.

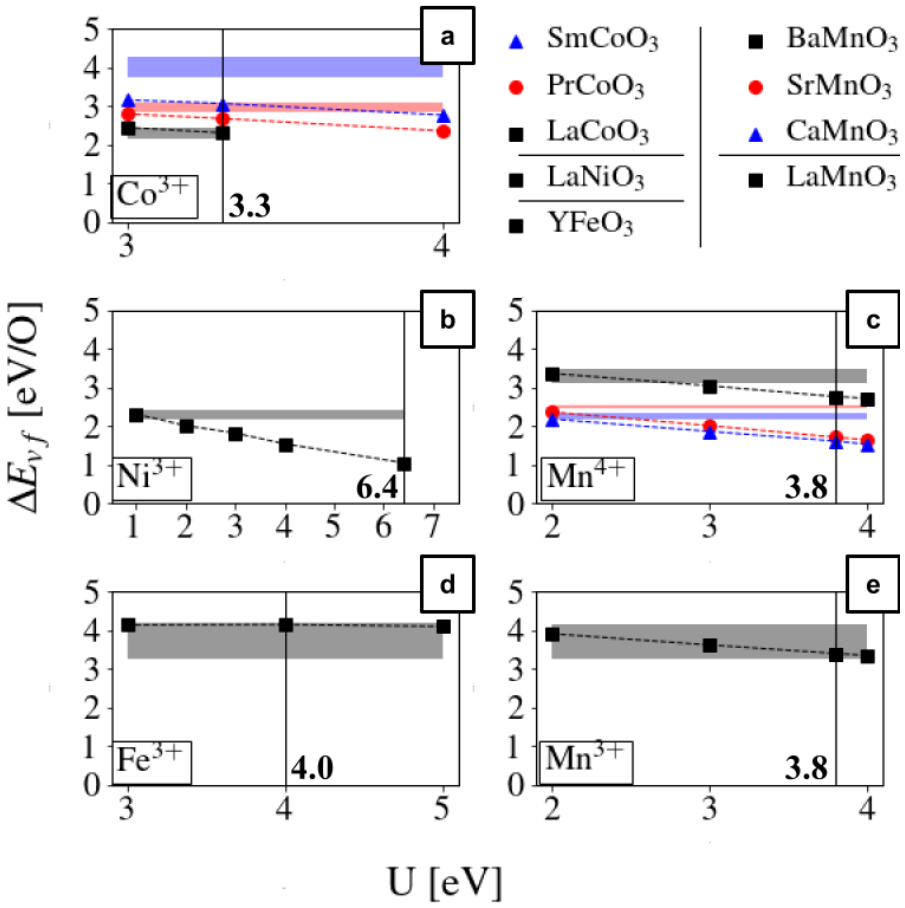

Figure 3.8: Variation of the computed oxygen vacancy formation energy with the U parameter for the ABO_3 compounds investigated for experimental comparison, for (a) $LnCo^{3+}O_3$ compounds; (b) $LaNi^{3+}O_3$; (c) $AMn^{4+}O_3$ compounds; (d) $YFe^{3+}O_3$; and (e) $LaMn^{3+}O_3$. Vertical lines indicate the value employed in the OQMD framework and horizontal banners represent experimental data, the thickness indicating the value ranges given by the error bars. DFT values are computed using the DSD structure with vacancy-containing cells of 79 atoms (119 for $BaMnO_3$)

Comparison Between DFT and Experiment Leveraging the insights gained in the above discussion, in Fig 3.9 we test the accuracy of DFT calculations of oxygen vacancy formation energy performed using the DSD structure and the "best fit" U (Table 3.2) by comparing them with the available experimentally derived enthalpies of reduction. DFT+U calculations exhibit an accuracy comparable to experimental uncertainty and also capture the relative magnitude of the oxygen-vacancy formation energy across materials, a crucial point in material prediction. In Figure 3.10 and 3.11 we preform the same comparison as Fig 3.9 utilizing, respectively, the same Hubbard U values as the ones utilized in the OQMD, and a constant Hubbard U value of 4 eV for all compounds. In

Table 3.2: List of cations and "best fit" U values determined by comparing the DFT computed oxygen vacancy formation energy and the experimentally measured enthalpy of reduction. The U values employed in the OQMD framework are also listed for reference

Cation	Co^{3+}	Ni^{3+}	Mn^{4+}	Fe^{3+}	Mn^{3+}
"Best Fit" U [eV]	3	1	2	4	3
OQMD U [eV]	3.3	6.4	3.8	4	3.8

both cases, Pearson and Spearman correlation coefficients remain greater than, respectively, 0.8 and 0.9, confirming the predictive ability of the DFT ΔE_{vf} calculations in differentiating and ranking reduction enthalpies across compounds, albeit with an expected increase in the mean absolute error by approximately 0.3 eV/O.

For practical reasons such as computational expense, different settings (such as defect cell size and Hubbard U values) than the ones in the low-throughput study in the present chapter are employed to perform the high-throughput studies in the next chapter. These 'high-throughput settings' are as follows: (i) U values from OQMD rather than 'best-fit' values from the previous section; (ii) lowest-energy structures at each composition, which we have argued are likely to coincide with DSD structure (this choice is further discussed in the next chapter); (iii) and vacancy-containing supercells of smaller sizes than the ones used in low-throughput. In order to validate the predictive power not only of the computational approach but of its high-throughput implementation as well, we separately test the agreement of the calculations performed with high-throughput settings with experiment. The relevant comparison is shown in Figure 3.12, where results are contrasted between the choice of a cubic perovskite structure employed by Emery at al.[54] (a) and the currently proposed one of the ground state structure (b). The underestimation of ΔE_{vf} due to dynamic instability is less dramatic when utilizing the very small 9 atom vacancy-containing cubic cell employed by Emery et al.[54] as compared to what is seen in Fig. 3.12 where 79 atom cells were used. However, the effect is nevertheless still present, as can also be inferred from the trends in Figure 4.14 and 4.19 presented further below. The agreement with experimental data is considerably improved when using the ground state structure, as can be seen by a decrease in average difference between DFT

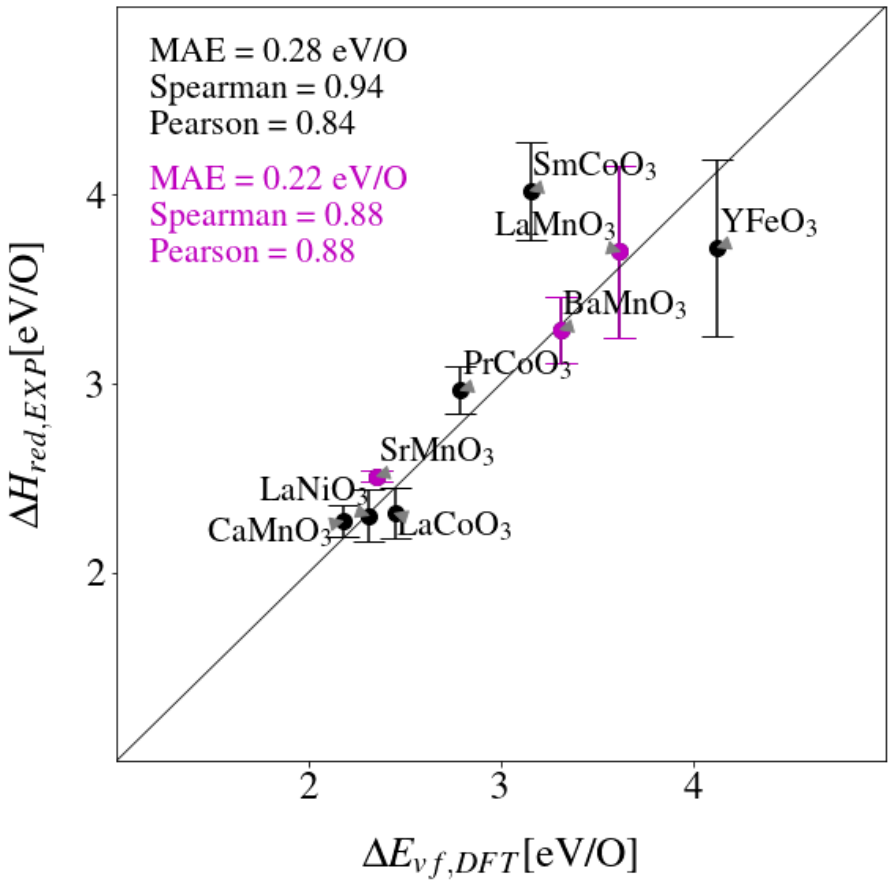

Figure 3.9: Comparison of the experimental and DFT values of the oxygen vacancy formation energy derived with best fit U values shown in Table 3.2. In black compounds simulated with the same structure as the experimentally measured one, in magenta compounds simulated using a dynamically stable distortion (DSD) maintaining the same type of O environment surrounding the redox-active cation as the experimentally stable structure. Vacancy-containing cell sizes are of 79 atoms (119 for $BaMnO_3$)

computations and experimental data, despite the error not being systematically lower for every single compound. The use of the ground state structure results in an even more significant increase in the Pearson and Spearman correlation (measuring respectively linear and monotonic character) of the data, indicating that the high-throughput computational settings likely provide a fundamentally appropriate description of the vacancy formation energy, even though smaller nuances (such as a non-optimal U value) still lead to a underestimation for some compounds. In addition to the calculations presented in this work, we have also examined the impact of utilizing the PBE-sol and SCAN functionals when computing the oxygen vacancy formation energy, again for a range of

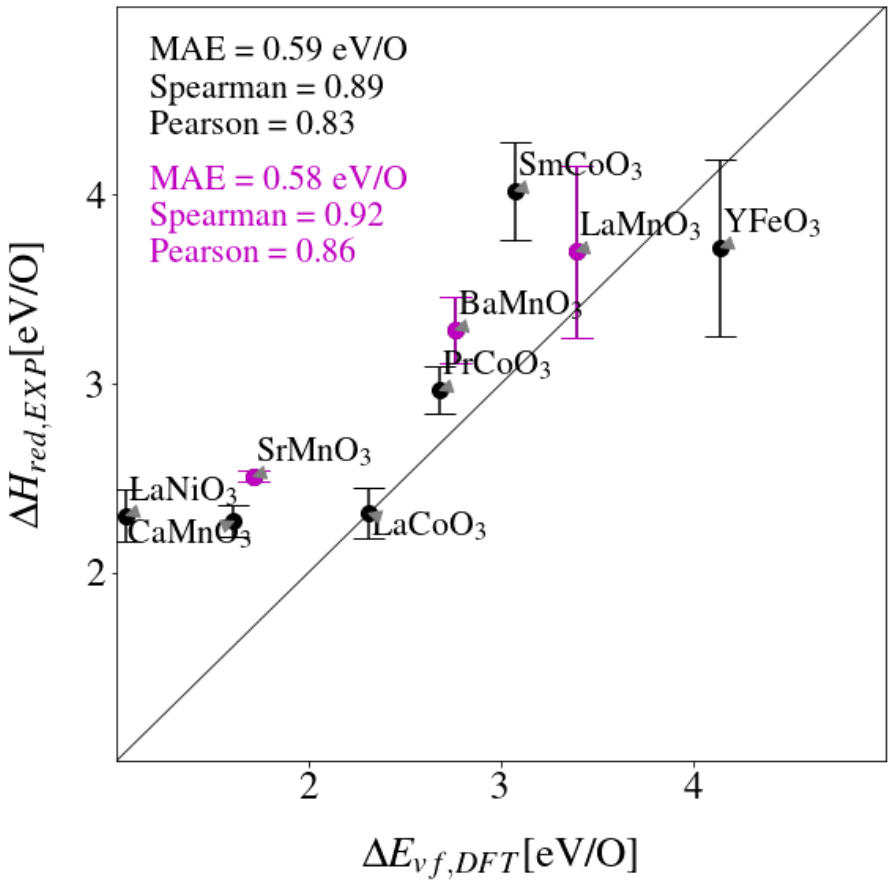

Figure 3.10: Comparison of the experimental and DFT values of the oxygen vacancy formation energy derived with U values from the OQMD and DSD structures. In black compounds simulated with the same structure as the experimentally measured one, in magenta compounds simulated using a dynamically stable distortion (DSD) maintaining the same type of O environment surrounding the redox active cation as the experimentally stable structure. Vacancy-containing cell sizes are of 79 atoms (119 for $BaMnO_3$)

Hubbard U values.[100]

As evident from Table 3.1, in addition to the 9 compounds illustrated in Fig 3.12 and 3.9, thermogravimetric measurements were also performed on two orthorhombic perovskite Fe-containing compounds ($LuFeO_3$ and $HoFeO_3$) and three Mn-containing hexagonal compounds ($LuMnO_3$, $HoMnO_3$ and $YMnO_3$).[79] The two ferrite compounds failed to display any significant oxygen loss uponheating; our computations agreed with this only when using the DSD structure and not the cubic (dynamically unstable) structure. As for $HoMnO_3$ and $YMnO_3$, evidence of a phase transformation from a "$LuMnO_3$"-type structure (with $P6_3cm$ space group) to a "Be_3N_2"-type

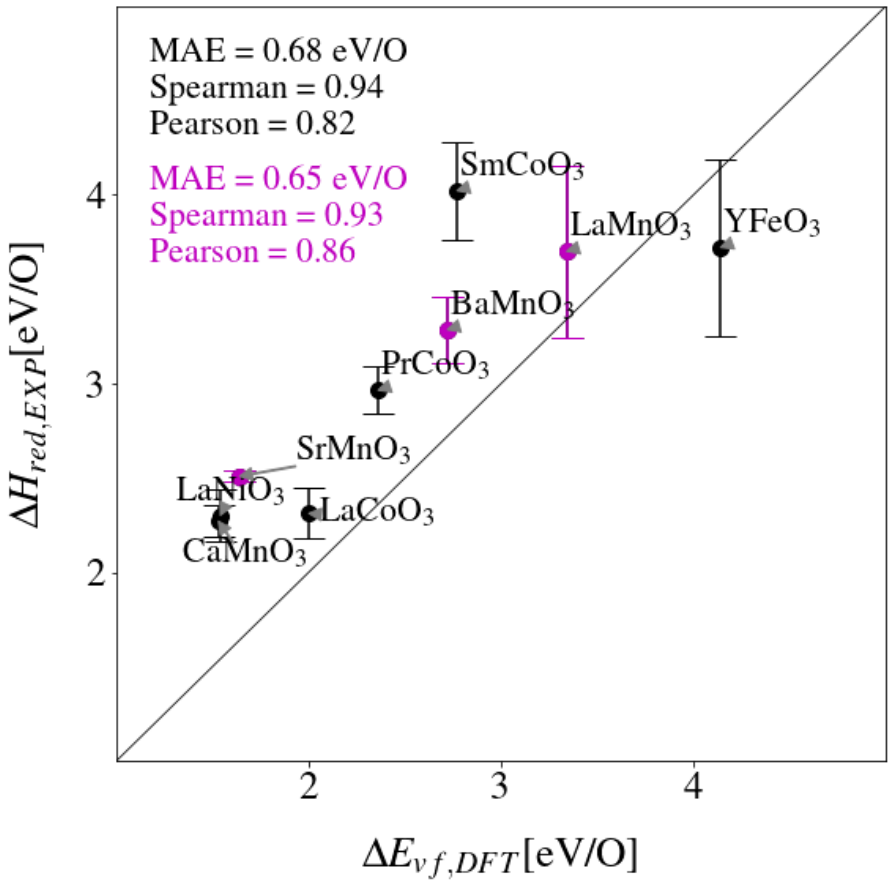

Figure 3.11: Comparison of the experimental and DFT values of the oxygen vacancy formation energy derived with U=4eV for all compounds and and DSD structures. In black compounds simulated with the same structure as the experimentally measured one, in magenta compounds simulated using a dynamically stable distortion (DSD) maintaining the same type of O environment surrounding the redox active cation as the experimentally stable structure. Vacancy-containing cell sizes are of 79 atoms (119 for $BaMnO_3$)

structure (with space group $P6_3/mmc$) was observed at higher temperatures, along with a sharp jump in the measured enthalpy (from 1.5 to 3 eV/O) and entropy (from 70 J/mol O/K to 170 J/mol O/K) of reduction.[99] The mechanism behind the jump in the thermodynamic quantities remains ambiguous. Results from DFT stability calculations show the "$LuMnO_3$"-type structure phase to be lower in energy for all three Mn-containing hexagonal compounds, and the calculations of oxygen vacancy formation energy performed with DSD structures ("$LuMnO_3$"-type) are in the range 3-3.5 eV/O for the three compounds.

The experimental methodology for determining the thermodynamics of oxygen vacancy forma-

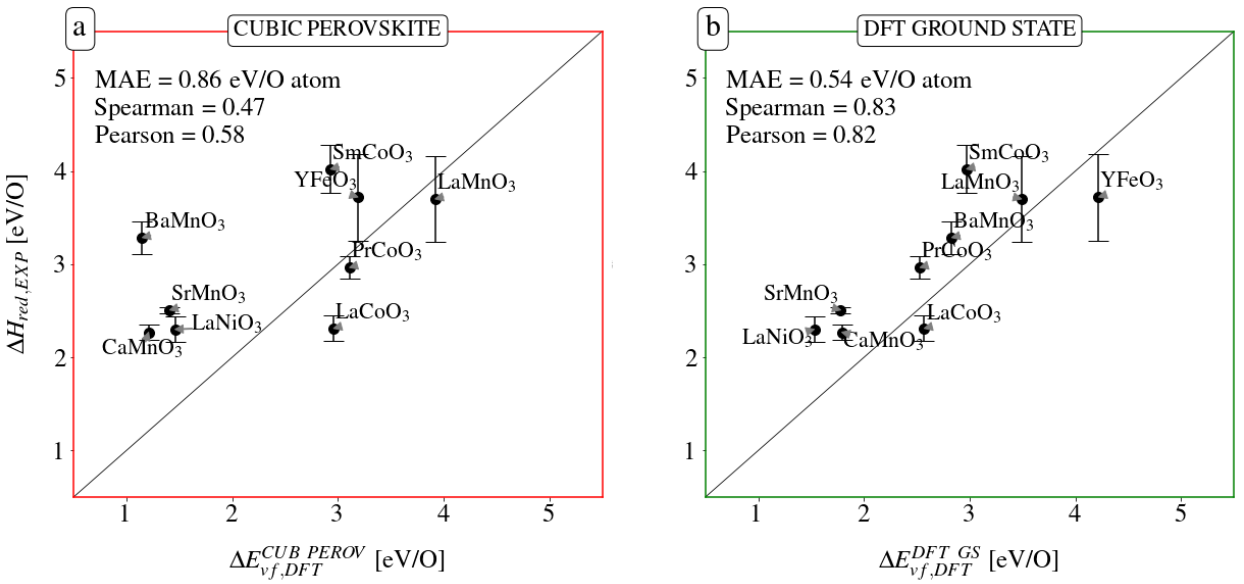

Figure 3.12: Comparison experimentally derived standard enthalpies of reduction and DFT computed of the oxygen vacancy formation energies, derived using (a) the cubic perovskite and (b) the DFT ground state structure, both with OQMD settings, highlighting the significantly higher agreement achieved with the latter approach. U values are those implemented in the OQMD, and vacancy-containing cells are of 9 atoms for cubic structures, and 19 (29 for $BaMnO_3$) for ground state structures.

tion yields the enthalpy as a function of non-stoichiometry.[101–105] For the purposes of comparison to the computed results, the experimental value is defined as the average enthalpy over the range from 0 to the δ_C , the non-stoichiometry implied by the removal of one oxygen from the supercell, assuming linearity extends to δ_C. We have compared this approach with different strategies for ensuring comparison between the same physical property, such as extrapolation of the experimental value to $\delta \to 0$. Because the dependence of the experimental enthalpy on δ is relatively weak for most compounds studied here,[79] the general aforementioned conclusions about the structure choice in computation and DFT prediction power remain consistent.

Overall, the evidence indicates that both the low-throughput and high-throughput approaches outlined in this work reliably predict materials reduction enthalpies accurately enough to differentiate promising candidates for STCH applications and guide experimental investigation.

4. High-Throughput DFT Surveys of Metal Oxides for Water-Splitting Applications

4.1 Background

As motioned in the previous chapter, the oxygen vacancy formation energy is one of the main quantities of interest to guide materials selection for STCH applications. New candidate metal oxides can be vetted by screening for materials with ΔE_{vf} large enough to split water but not so large as to require unreasonable temperatures to create vacancies.[14] Operation temperatures as well as the materials entropy of reduction influence the values of reduction enthalpy for which the both steps in a STCH cycle are thermodynamically favorable. Considering typical operating conditions, and keeping into account the evidence for an underestimation of the experimental ΔH_{red} in some computations of ΔE_{vf} mentioned in Section 3.3, we consider a ΔE_{vf} window between 2 and 5 eV/O, recognizing that even within this range, materials with $\Delta E_{vf} \geq 4$ eV/O may not undergo detectable reduction unless the entropy is extremely high (as is the case for ceria).

Having validated the efficacy of our computational approach in predicting ΔE_{vf} in the previous chapter, we now apply it on a large scale to perform high throughput DFT studies of multiple classes of metal oxides. In selecting the structure types to be targeted in the studies we consider multiple properties of interest for STCH applications: evidence of structural stability up to high temperature, ability to withstand a large amount of oxygen non-stoichiometry, ease of oxygen diffusion, and a wide compositional space to explore when decorating the structure. As already touched upon,

perovskites are a class of materials satisfying numerous of the above criteria, and are therefore the main class of materials included in the study. In addition to perovskite-type structures we also include other structural types presenting evidence of attractive properties like ease of oxygen diffusion, namely pyrochlore and spinel structures. Lastly, we also include other stable transition metal oxide structures in the OQMD which might not necessarily represent ideal STCH candidates but can be of interest for other applications, as well as contributing to creating a large and diverse dataset to be leveraged to develop predictive models of the oxygen vacancy formation energy.

As well as identifying hundreds of new STCH candidates, we generate a new pool of around 2500 vacancy formation energy calculations of over 1000 different materials with a variety of structures and compositions, all (in their pristine form) within 25 meV/atom of the convex hull. This constitutes the largest dataset of directly computed vacancy formation energy to date, to our knowledge. Several paragraphs in this chapter are quoted directly from our manuscripts[74].[106]

4.2 Methodology

All DFT calculations have been conducted using the Vienna ab-initio simulation package (VASP),[75,76] with projector augmented wave (PAW) potentials[77] and the Perdew-Burke-Ernzehof (PBE)[78] generalized gradient approximation (GGA) for the exchange-correlation functional. The calculations were conducted within the framework of OQMD, details on the settings employed can be found in Refs.[43,44] For compounds containing 3d transition metals or actinides, the over-delocalization of electrons due to the residual self interaction present in exchange-correlation functionals[36–40] was treated through the addition of a Hubbard-like potential to the energy functional,[42] and a spin polarization was applied with a ferromagnetic configuration, initializing magnetic moments to $5\mu_B$ (transition metals) and 7 μ_B (actinides). The oxidation state of each cation was determined using bond valence parameters as implemented in pymatgen,[107] and a small number of compounds were excluded from the dataset if they contained a rare earth element whose oxidation state differed from that of the pseudopotential used in the OQMD framework.

In the interest of selecting structures more likely to be synthesized and avoiding structures with a significant degree of dynamic instability, for each composition, ΔE_{vf} calculations were conducted with the lowest-energy structure at that composition. We created vacancy-containing supercells with a minimum of 15 atoms (see Appendix for cell size convergence), and considered each unique oxygen site.

The charge localized on each atom in each pristine structure of interest was determined through Bader charge analysis as implemented in pymatgen.[107] After the introduction of a neutral oxygen vacancy, the charge localization on each atom in the defect-containing structure was determined in the same fashion. The charge localization upon vacancy formation was then calculated by taking the difference in the charge localized on each atom in the defect-containing cell and in the perfect bulk cell. The charge localized upon vacancy formation was then summed over all atomic sites for each of the two cation species in each ABO_3 and $A_2B_2O_7$ compound, thus obtaining a total Δq_A and Δq_B. For ABO_3 compounds, the reducing (or redox-active) cation was then labeled based on the larger of the two Δq. We note that the nature of this labeling is approximate and not univocal; for example, for perovskite oxides, while the reducing cation coincides with the B site cation in the vast majority of cases, evidence of possible reduction of both A and B sites is present in a few cases.

4.3 Results

Before delving in each high-throughput study in detail, in Figure 4.13 we provide a visual representation of all the compounds for which the formation energies of oxygen vacancies were computed as individual datapoints (the lowest value of ΔE_{vf} for each compound is shown). Different markers indicate the compounds calculated within the high throughput study of perovskites (red triangles), pyrochlores (blue triangles) and double perovskites (cyan squares), as well as compounds on the OQMD convex hull with octahedrally coordinated transition metal cations, both from the ICSD (pink circles) and from other studies (black crosses). As will be further detailed in the next subsections, these high throughput studies have also led to the identification of hundreds of new STCH

candidates, highlighted in the figure through a green banner. Lists of the new perovskite, pyrochlore and double perovskite candidates are provided in the Appendix. The rest of the dataset will be publicly available following the publication of our other recent works[108,109].

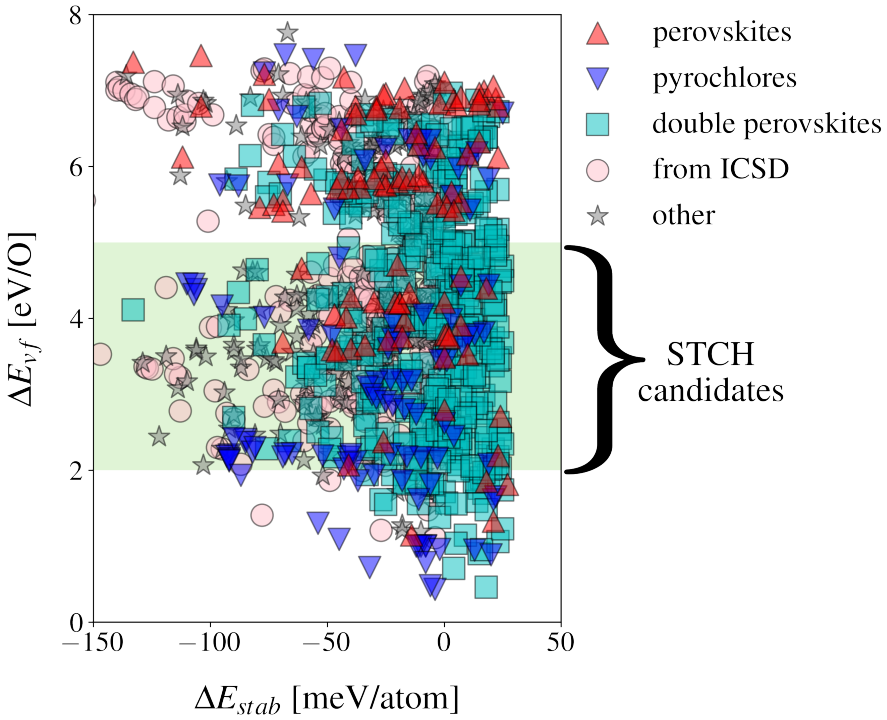

Figure 4.13: Oxygen vacancy formation energy of the compounds calculated within the high throughput study of perovskites (red triangles), pyrochlores (blue triangles) and double perovskites (cyan squares), as well as compounds on the OQMD convex hull with octahedrally coordinated transition metal cations, both from the ICSD (pink circles) and from other studies (black crosses). The window of interest of oxygen vacancy formation energy for STCH applications is highlighted in green

4.3.1 Perovskites

In a 2016 study of perovskite oxides, Emery et al[54] computed the DFT stability of all decorations of the ABO_3 perovskite structure (with A and B being metal cations), considering the four most common perovskite distortions. The authors identified over 250 stable compounds, with the rare earths and alkaline earth metals predominantly occupying the A site, and transition metals the B site. They also computed oxygen vacancy formation energies of the stable perovskites utilizing the cubic structure. We here extend their survey to include many additional competing non-perovskite

ABO_3 structures, and, most importantly, revise the computation of the oxygen vacancy formation energy by utilizing the ground state structure in place of the cubic perovskite structure, following the considerations about the issues brought about by dynamic instability discussed in Section 3.3. To identify new promising STCH candidates we first screen for thermodynamic stability by selecting the lowest energy structure of compounds with at least one structure lying within 25 meV/atom of the convex hull. We then apply a second filter based on ΔE_{vf} values for STCH applications.

For all compositions having a structure within 25 meV/atom from the convex hull in one of the perovskite distortions, we also computed the three other most common prototypes from the ICSD for ABO_3 compounds (see Figure 11.65 for a visual representation of the structures), and then selected the lowest energy 0K structure considering all available phases on the OQMD at each composition. Since the Emery study,[54] the OQMD has more than doubled in size to over 1 million calculations today.[110,111] This significant expansion of the database not only increases the reliability of any stability result by introducing other competing phases, but also resulted in the identification of several new stable ABO_3 metal oxide structures which are also included in the present study. In total, we screen $\sim$ 2200 compositions and $\sim$ 19400 structures, selecting stable ABO_3 metal oxides and computing ΔE_{vf} of $\sim$400 compounds. Of these, $\sim$150 have a perovskite structure as their lowest-energy structure.

In Figs 4.14 and 4.15, we show that using the ground state perovskite structure as opposed to the cubic perovskite structure significantly changes the ΔE_{vf} results. Fig 4.14 highlights how the underestimation in ΔE_{vf} increases with the size of the instability of the cubic structure, as can be seen in the evidently descending trends in $\Delta E_{vf}^{CUB\ PER}$ with increasing ΔE_{stab}. Although ΔE_{stab} quantifies thermodynamic stability, in this case it serves as a quantification of dynamic (in)stability as well since it reports the energetic difference between the cubic phase and the phase on the convex hull, which in the majority of the cases is a distorted orthorhombic perovskite. Fig 4.15 demonstrates that using the ground state structure as opposed to the cubic perovskite structure results in new promising candidates for water-splitting otherwise left out ("False Negatives") and excludes candidates erroneously determined to be promising ("False Positives"). To be clear, "False

Negatives" and "False Positives", are defined under the assumption that utilizing the ground state structure provides a more appropriate description of the vacancy formation energy than utilizing the dynamically unstable cubic perovskite structure, as discussed in Chapter2.5. Fig 4.17 and 4.18 display the same results, extended by including all non-perovskite structures present in the study as well, and highlight the same conclusions. A complete list of all ∼180 stable compounds with ΔE_{stab} in the 2-5eV/O window is available in the Appendix.

In both Fig 4.14 and Fig 4.15 we highlight the influence of cation identity on oxygen vacancy formation energy. In agreement with the previous observations by Wexler et al.[55] and Curnan et al.[73] on perovskites with 3d transition metal cations on the B site, we find that the B cation plays a primary role in determining ΔE_{vf}. We also find that, in the vast majority of cases, the B cation is the one on which the majority of the charge localizes upon vacancy formation, as determined by Bader charge analysis (see Fig 4.16 and discussion in the next paragraph). Furthermore, we observe the strong correlation between cation identity and ΔE_{stab} to persist when reproducing Fig 4.14 and Fig 4.15 including all non-perovskite structures and highlighting the identity of the cation on which the majority of the charge localizes (which we refer to as 'reducing cation', see Fig 4.17 and 4.18). This correlation can be connected to the energetic cost associated with the reduction of the cation: cations which are harder to reduce, such as Sc^{3+} lead to larger ΔE_{stab} and vice versa for easier-to-reduce cations such as Mn^{4+}. The relative trends in this energetic cost can be inferred from experimental data, for example, by looking at commonly reported oxidation states[71,72] (less common oxidation states reducing to more common ones implying a greater ease of reduction, and vice-versa), or at experimental measurements of reduction potentials.[112] Wexler et al.[55] recently introduced a quantification of the energy of reduction for each cation (and oxidation state) incorporating crystal field effects by leveraging differences in formation energies between structures containing the cation of interest in the initial and reduced oxidation state.

The charge localization on A and B site cations (Δq) upon oxygen vacancy formation in perovskites is illustrated in Fig 4.16. In the majority of the cases rare earth and alkaline earth metals are on the A site, both groups having significantly larger reduction energies than the transition

metals, which largely occupy the B sites. Unsurprisingly, in the vast majority of cases most of the charge localizes on the B site cations upon oxygen vacancy formation (i.e. we identify the B site cation as the reducing cation). In cases where a cation which is easier to reduce, such as Bi^{3+}, occupies the A site, a significant lowering of ΔE_{vf} compared to other compounds with the same B site cation can be observed, accompanied by a larger charge localization on the A site cation. In such cases (eg. $BiVO_3$, $BiCrO_3$, $BiMnO_3$, $TeFeO_3$) evidence for reduction on both sites can be observed, with $BiVO_3$ going as far as having most charge localizing on the A site cation. A suggestion of reduction of both A and B cations with Bi^{3+} on the A site was also put forth by Wexler et al.,[55] and can represent a desirable property as it would lead to an increase in the entropy change involved in the reduction reaction, and thus to a more favorable STCH cycle.[14,70]

When considering ΔE_{vf} in the lower end of the STCH window, availability and lack of prohibitive cost or toxicity, Mn^{4+}, Mn^{3+} and Co^{3+} emerge as the most promising redox-active cations for STCH applications (see Table 3), although we do note that our investigations of REMnO3 (YMnO3, LuMnO3 and HoMnO3) suggest higher temperatures to be needed to reduce "LuMnO3" type compounds.[79] Co^{3+} and Mn^{3+} have also been highlighted as promising B site cations in perovskites in the recent work by Wexler et al.,[55] despite differences in the specific predicted values probably due to the differences in exchange correlation functional and Hubbard U, and in the structures included in the study. While Mn^{4+} displays a rather low reduction enthalpy in perovskites, making it less attractive as the sole B-site element,[98] the oxygen vacancy formation energy can be increased by introduction of substitutional elements on the B site. We synthesized two Mn^{4+}-based mixed perovskites and, encouragingly, found these to display favourable redox thermodynamics and high fuel production upon cycling.[113,114] Attractive redox values for Mn^{3+} and Mn^{4+} were also previously reported in the work by Vieten et al. analyzing several mixed perovskites.[69] Among the other common B cation metal oxide elements identified in the study not suffering from particular cost and toxicity concerns, V^{3+}, Ti^{3+} and Cr^{3+} all appear to be too hard to reduce for STCH applications and Ni^{3+} potentially too easy. Lastly, while several Fe^{3+}-containing compounds display ΔE_{vf} values in the 2-5eV STHC window, such values all lie above 4eV/O,

and Fe^{3+}, previously suggested as an attractive cation by Wexler at al.,[55] is considered less likely to be promising candidate, as supported by the experimental observation of very limited if not entirely absent oxygen loss previously mentioned in the experimentally synthesized perovskite ferrite compounds.

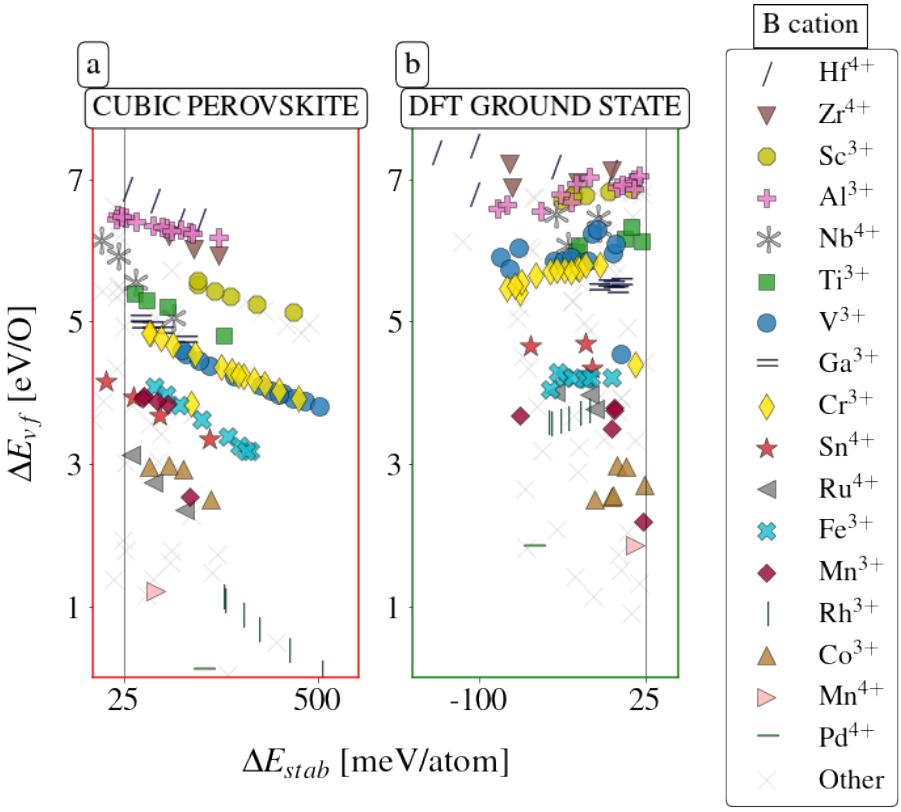

Figure 4.14: Oxygen vacancy formation energy derived using (a) the cubic perovskite structure, and (b) the ground state perovskite structure in the DFT simulations, displayed as a function of stability of the relevant structure. The left hand side clearly highlights a sharp decrease in ΔE_{vf} with increasing dynamic instability of the cubic phase. Different markers indicate different B-site cations.

For the vast majority of the stable perovskites identified in this study the ground state structure is a distortion of lower symmetry than the perfect cubic phase. An especially convenient metric to estimate the degree of structural distortion, given its simplicity and ease of computation, is the Goldschmidt tolerance factor[115] :

$$tolerance = \frac{r_A + r_O}{\sqrt{2}(r_B + r_O)} \tag{4.19}$$

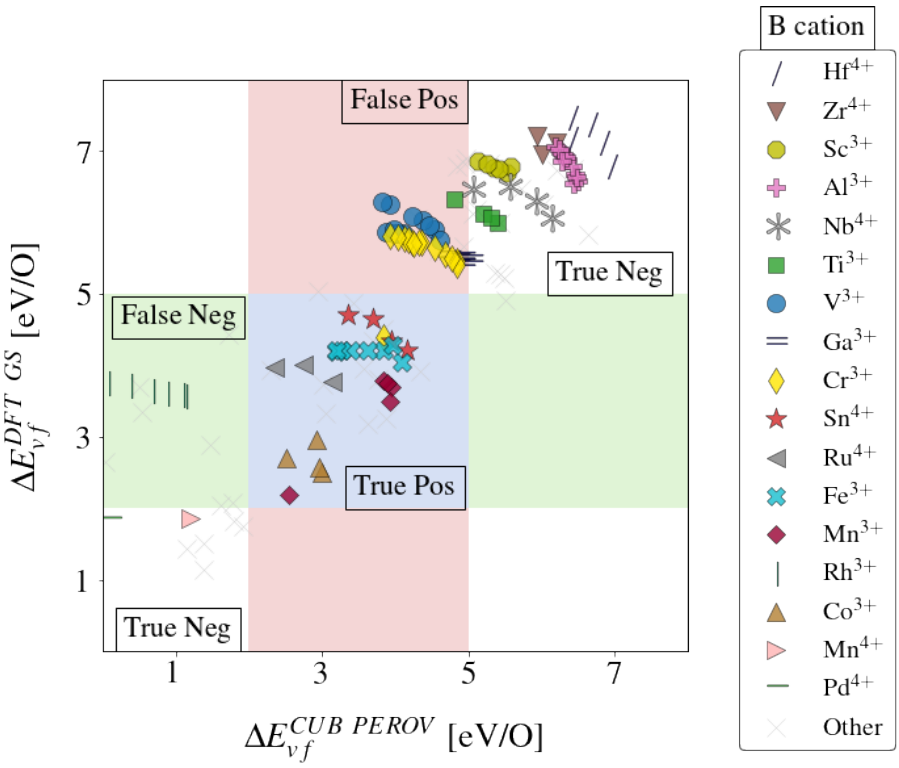

Figure 4.15: Comparison of oxygen vacancy formation energy calculated using the DFT ground state perovskite structure on the OQMD and the cubic perovskite structure. Areas in red indicate false positives (compounds which are in the window of interest for STCH when using the cubic perovskite structure but not the ground state structure), in green false negative (the opposite of the previous instance), and in blue true positives (compounds that would be deemed promising in both cases). Different markers indicate different B-site cations. Larger deviations from the diagonal largely correspond to compounds with a higher degree of dynamic instability of the cubic phase, as further highlighted in Fig 4.14

In Figure 4.19 we show how this metric, which is often used to predict the structure and synthesizability of a perovskite composition, can also capture two contrasting behaviours in the oxygen vacancy formation energy of perovskites when using the ground state versus the cubic structure. On the one hand, an inverse correlation with tolerance can be observed when utilizing ground state structure, in agreement with observations of compressive strain increasing the oxygen vacancy formation energy.[116] As rare earth cations occupy the A site in the majority of the ABO3 perovskites here analyzed, for the same B cation, higher values of the tolerance factor are associated with earlier rare-earth A cations, and lower values with later rare-earth A cations. The more distorted structures of perovskites that contain later rare-earth A cations are characterized by higher values of

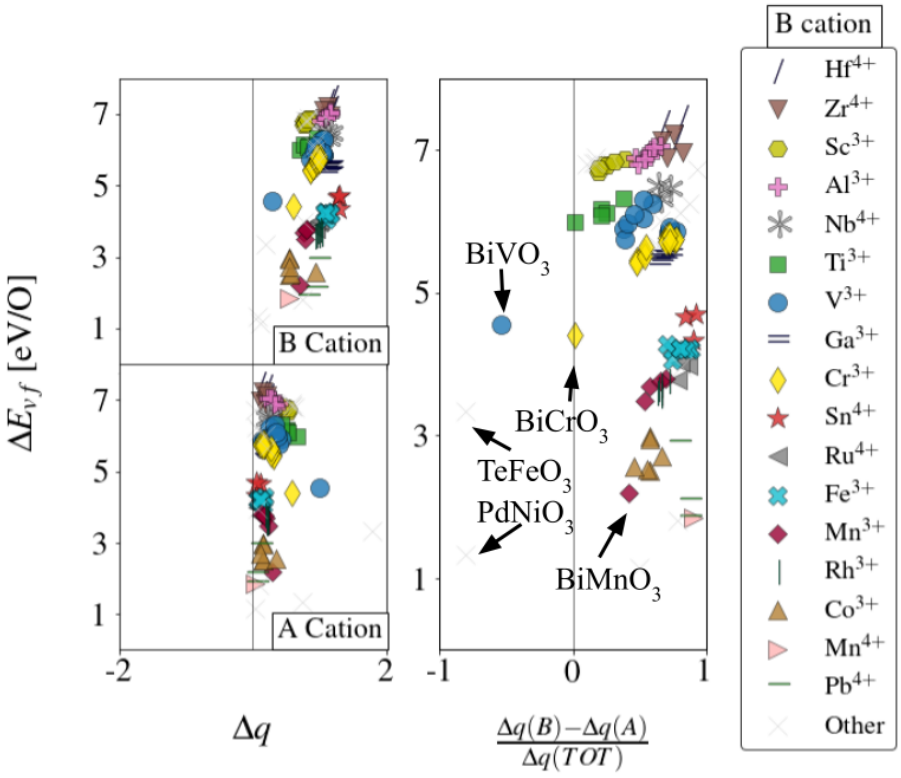

Figure 4.16: Correlation between the oxygen vacancy formation energy and the charge localized upon vacancy formation on the B cations and on the A cations in ABO_3 perovskites. In the near entirety of the cases the majority of the charge localizes on the B cation, unless the A cation is significantly easier to reduce, as is the case for $BiVO_3$.

the vacancy formation energy compared to other perovskites with the same B cation. They are also characterized by higher values of the magnetic moment of the B cation, indicating a decrease in the covalent character of the B-O bond, a behaviour similar to what observed by Varignon et al.[117] in Ni-based perovskites. In contrast, when the cubic structure is utilized, the observed trend is reversed, i.e. higher values of the tolerance factor are associated with higher values of the vacancy formation energy for compounds containing the same B cation, a behaviour that can be attributed once again to its dynamic instability. The more distorted the ground state structure, the larger the distance of the cubic structure from the energetic landscape minimum, and thus the larger the underestimation of ΔE_{vf} when using the cubic structure.

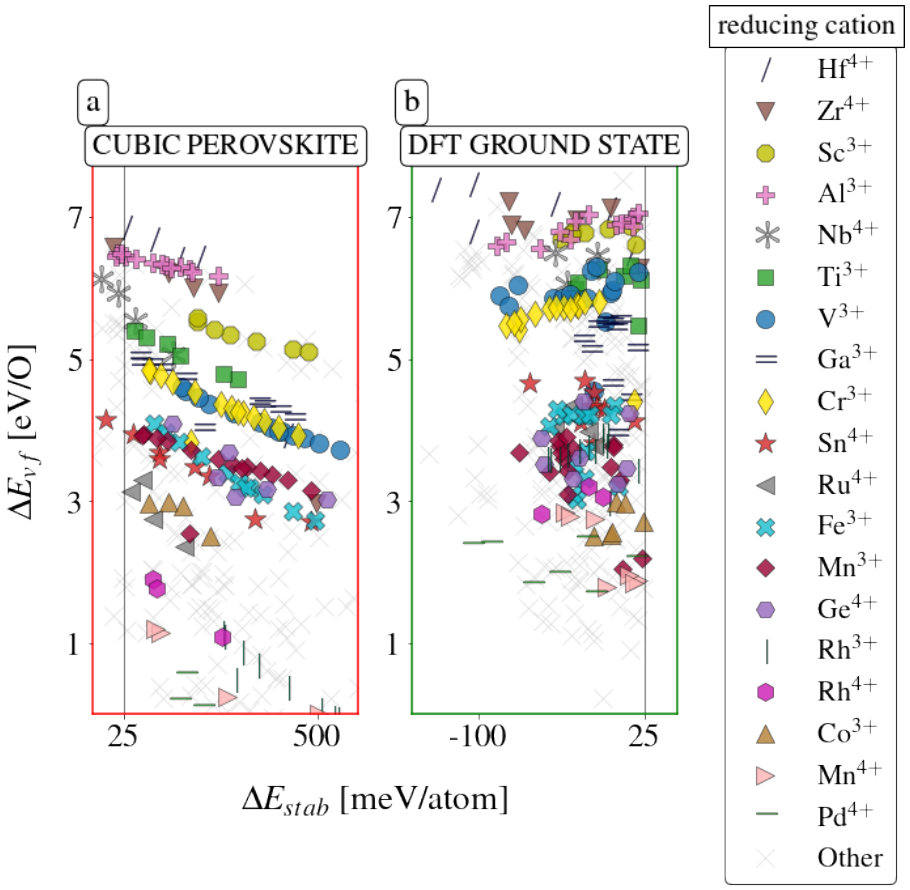

Figure 4.17: Oxygen vacancy formation energy derived using (a) the cubic perovskite structure, and (b) the ground state structure on the OQMD in the DFT simulations, displayed as a function of stability of the relevant structure. The left hand side clearly highlights a sharp decrease in ΔE_{vf} with increasing dynamic instability of the cubic phase. Different markers indicate different reducing cations.

4.3.2 Pyrochlores

In a recent study, He et al[109] computed DFT the stability of all possible $A_2B_2O_7$ compositions (with A and B being metal cations) in the pyrochlore structure, as well as the 2 competing structures most commonly found in the Inorganic Crystal Structure Database (ICSD).[71,72] More than 300 stable compounds were identified, with the A site being predominantly occupied by rare earth elements and the B site by transition metals. We performed oxygen vacancy formation energy calculations of the stable compounds and identified around 50 of them to lie within the widow of interest for STCH, a complete list is reported in the Appendix.

In Figure 4.20 b and c we present the results of oxygen vacancy formation energy calculations

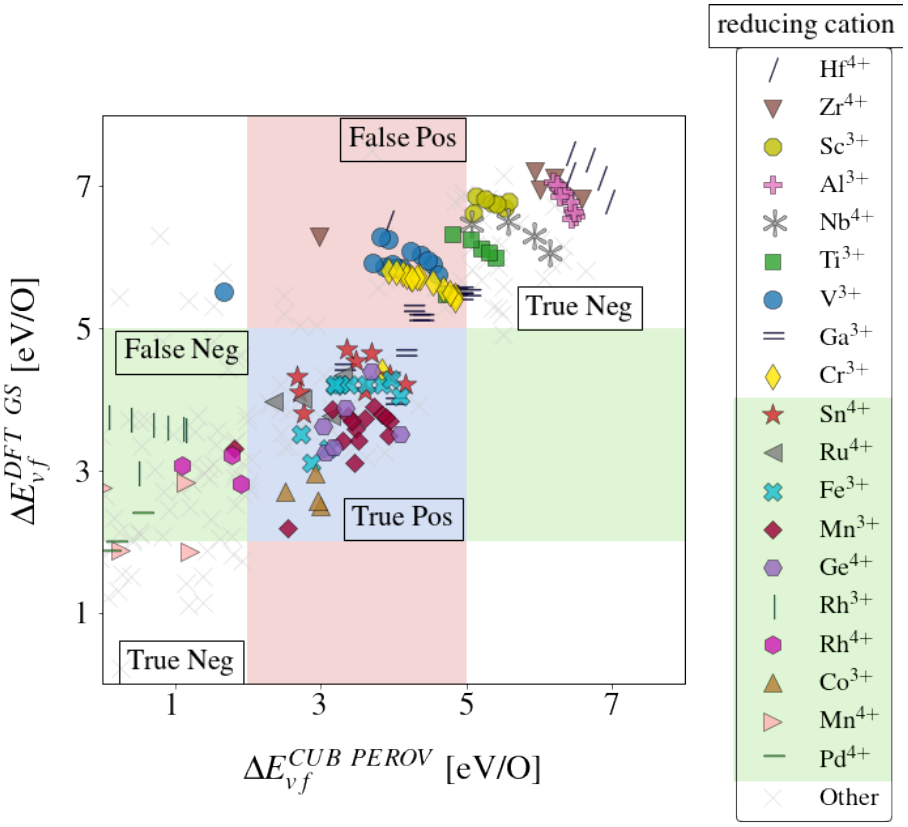

Figure 4.18: Comparison of oxygen vacancy formation energy calculated using the DFT ground state structure on the OQMD and the cubic perovskite structure. Areas in red indicate false positives (compounds which are in the window of interest for STCH when using the cubic perovskite structure but not the ground state structure), in green false negative (the opposite of the previous instance), and in blue true positives (compounds that would be deemed promising in both cases). Different markers indicate different reducing cations.

of stable pyrochlore compounds, and also display perovskite compounds in Figure 4.20 a for comparison. Like the perovskites examined above, pyrochlore oxides have multiple non-equivalent vacancy sites. The difference between the sites, however, is not just in the lengths and angles of the bonds between the oxygen and its nearest neighbor cations, but also in the species of the neighboring cations. For one of the sites the nearest neighbors (NN) to the O atom are B cations, while for the other the nearest neighbors are A cations (see Fig 11.67 for a visual representation of the structure). Both vacancy sites are represented in Figure4.20: the site with B cations as NN (also referred to as "V1") in Figure4.20 b, and the site with A cations as NN (also referred to as "V2") in NN Figure4.20 c, with different markers indicating the B site cations in both cases. A significant difference can be

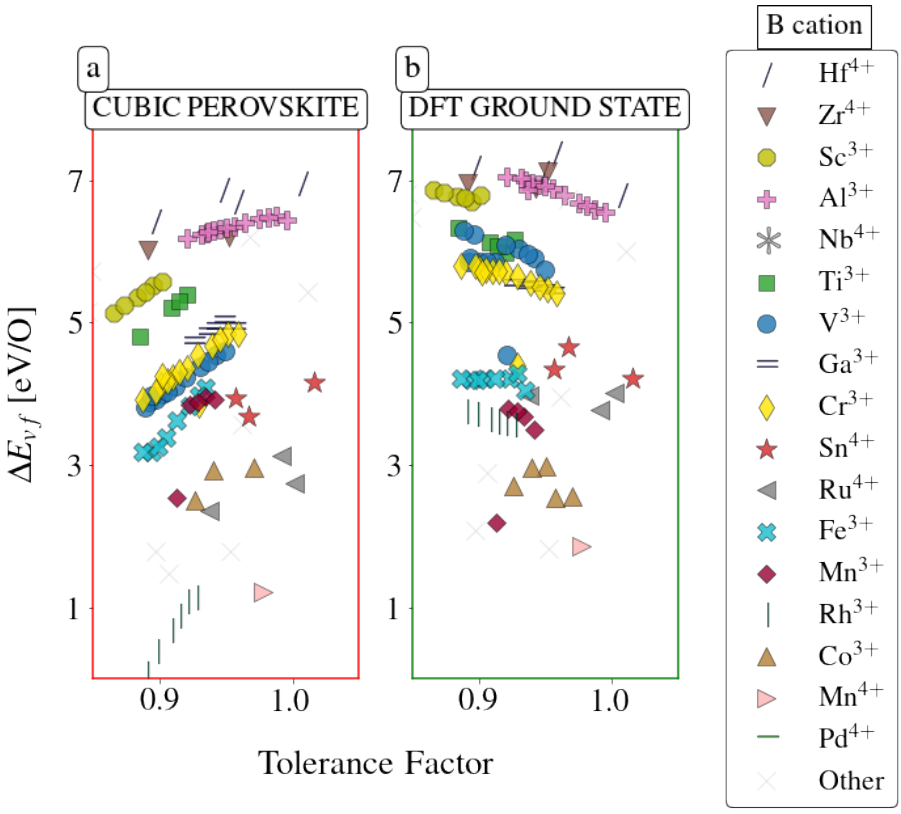

Figure 4.19: Oxygen vacancy formation energy derived using (a) the cubic structure, and (b) the ground state structure in the DFT simulations, displayed as a function of the tolerance factor computed using a bond valence method.[118] Different markers and colors symbolize different B site cations and oxidation states.

observed between the two sites, with the vacancy formation energy of sites surrounded only by rare earth cations being significantly higher than that of the sites with transition metal neighbors, which in turn has similar values to perovskites with the same B transition metal cation neighbors.

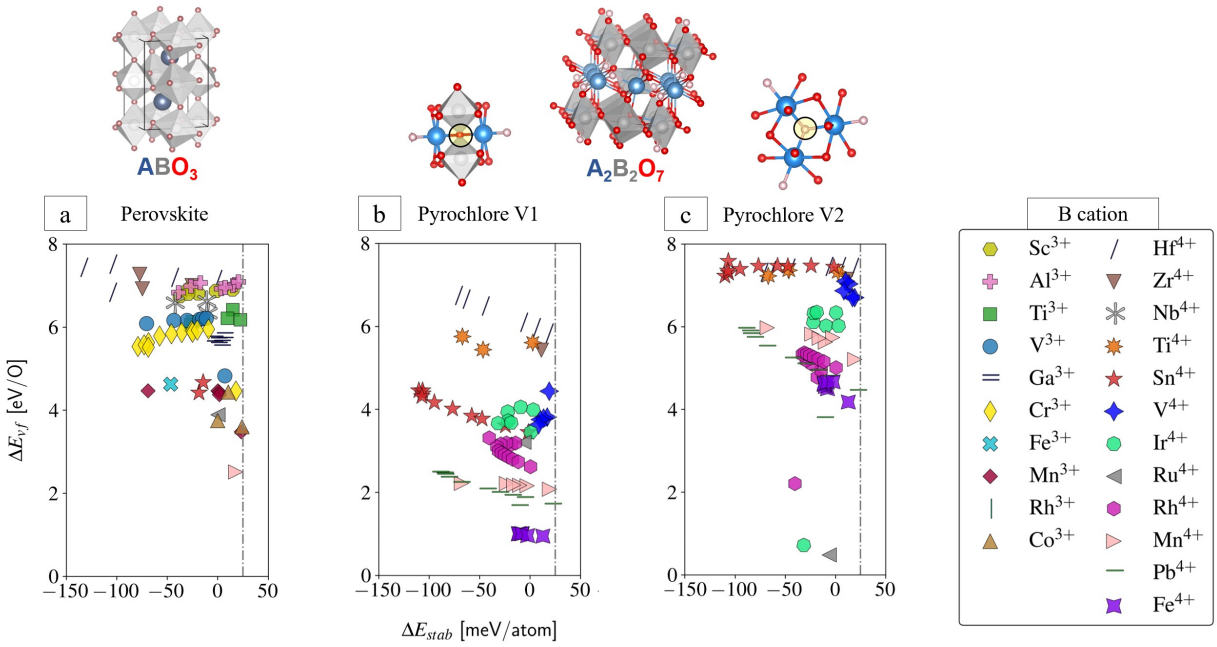

Figure 4.20: Oxygen vacancy formation energy of (a) ABO_3 perovskite oxides, and (b) and (c) $A_2B_2O_7$ pyrochlore oxides. In (a) ΔE_{vf} of the lowest energy vacancy is reported, as all vacancy sites have the same A and B cation nearest neighbors. In (b) ΔE_{vf} of sites with A and B cations (where B cations are the closest) as nearest neighbors is reported, and in (c) ΔE_{vf} of sites with only A cation nearest neighbors is reported. In all cases different markers and colors indicate the species and oxidation state of the B cation of each given compound. The vertical line indicates the 25meV stability cutoff applied for compound selection.

4.3.3 Double Perovskites

A natural extension of the work on simple perovskites presented in Section consists in applying a similar methodology, to double perovksites, a class of materials obtained by A and B site substitution of the perovskite structure,[119–122] in the presence of ordering. Similarly to perovskites, double perovskites exist in a variety of distortions of the ideal structure, but with the additional complexity introduced by the A or B site ordering,[120,121] therefore opening a much larger compositional and structural space.

A first high-throughput DFT stability study of 10^4 $A_2BB'O_6$ compounds has been completed by J.He et al,[108] comprising over 35,000 calculations surveying multiple distortions[120] of the idea rock salt B ordered structure. Such structure is the most commonly observed one for $A_2BB'O_6$ double perovskites and is characterized by an alternation between the B and B' cation on both rows and

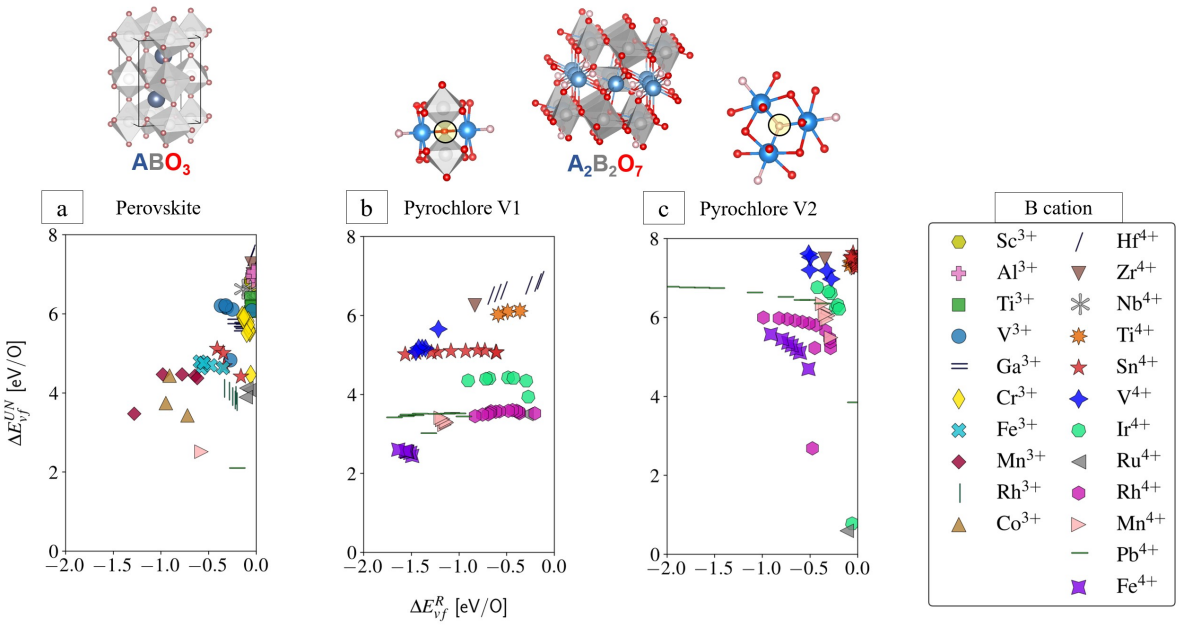

Figure 4.21: Unrelaxed ($\Delta E_{vf,UN}$) vs relaxation ($\Delta E_{vf,R}$) contributions to the oxygen vacancy formation energy of (a) ABO_3 perovskite oxides, and (b) and (c) $A_2B_2O_7$ pyrochlore oxides. In (a) ΔE_{vf} of the lowest energy vacancy is reported, as all vacancy sites have the same A and B cation nearest neighbors. In (b) ΔE_{vf} of sites with A and B cations (where B cations are the closets) as nearest neighbors is reporeted, and in (c) ΔE_{vf} of sites with only A cation nearest neighbors is reported. In all cases different markers and colors indicate the species and oxidation state of the B cation of each given compound.

columns[119–121] (see Fig 11.67 for a visual representation of the structure). To determine the lowest energy phase, 10 different distortions of $A_2BB'O_6$ perovskites were considered (P21/c, C2/m, P1, P-1, I4/m, I4/mmm, R3, R-3, R-3m, Fm-3m), with A=Ca, Sr, Ba and La (and, for the most common P21/c structure, A=Zn, Cd, Hg and Pb), and 50 metal elements on the B sites, totaling around 10,000 compositions. The 3 most common $A_2BB'O_6$ competing phases on the ICSD were also calculated. Using this strategy, more than 500 stable (within 25 meV/atom of the OQMD convex hull) double perovskites were identified. For each of those compounds, we computed the vacancy formation energy of all non-unique oxygen sites.

Once again, a strong influence of the identity of the cations neighboring the vacancy on ΔE_{vf} can be observed. Due to the nature of the rocksalt-type B site ordering of the double perovskite structure, each unique O is bonded to both B site cation species (B and B'). Examining cases in which both B and B' are among the species highlighted in Figure 4.20, similar trends to those identified in simple

perovskites and pyrochlores can be observed. For example, among $La_2AlB'O_6$ double perovskites, having B'=V^{3+}, Cr^{3+}, and Fe^{3+} leads to a progressively lower vacancy formation energy (with values of, respectively, 6.2 eV/O, 5.8 eV/O and 4.4 eV/O). Similarly, Mn^{4+} is associated with a lower ΔE_{vf} than Sn^{4+} when occupying the B' site in $Ca_2ZrB'O_6$ (2.8 eV/O vs 4.7 eV/O). While the above examples highlight the dominant role in determining ΔE_{vf} to be played by the easiest to reduce cation, significant differences in ΔE_{vf} can also be identified when the identity of the other cations is changed. Once again, the trends identified in simple perovskites and pyrochlores appear to hold, with, for example, B=Hf^{4+}, Zr^{4+}, and Ti^{4+} leading to a progressively lower ΔE_{vf} in Ca_2BMnO_6 (with values of, respectively 3.0 eV/O, 2.8 eV/O and 2.3 eV/O)

4.3.4 Other Metal Oxides

In addition to the data produced through the high-throughput studies presented above, we also screened the OQMD for metal oxide compounds satisfying the following criteria: (i) the compound lies on the convex hull, (ii) the compound contains transition metal cations, (iii) oxygen is the only anion species, and (iv) the transition metal cations have octahedral coordination to oxygen anions. Of these compounds, about half were reported on the ICSD, and the other half consists of hypothetical compounds calculated to be DFT stable. The hypothetical compounds were discovered exploiting several different strategies: solution of experimental diffraction data using database searching,[123] machine learning prediction leveraging an improved version of CGCNN,[124] substitution of chemically similar elements into already-known compounds,[125,126] and inclusion of compounds discovered in the work of Wang et al.[127] For all compounds, we computed the oxygen vacancy formation energy of different unique vacancy sites.

5. Machine Learning Predictions of Oxygen Vacancy Formation Energy

5.1 Background

As seen in the previous chapters, one of the most useful thermodynamic properties to compute through the use of DFT for materials screening is the energy of formation of neutral oxygen vacancies (ΔE_{vf}). In order to effectively utilize ΔE_{vf}-based screening strategies to search for new materials, large datasets of defect energies will be required. Compared to defect-free bulk DFT calculations, which are relatively inexpensive and publicly available for 10^5-10^6 compounds in databases such as the OQMD[43,44] and the Materials Project,[45] ΔE_{vf} calculations can be significantly more expensive due to the creation of supercells and the consideration of multiple possible vacancy sites, as well the lower symmetry of the defect-containing structure.

Hence, in order to screen large pools of candidate materials, researchers have sought more computationally efficient ways to generate ΔE_{vf} predictions. A number of previous studies attempted to identify predictors of ΔE_{vf} which would allow bypassing DFT defect calculations entirely, relying on properties available from DFT calculations of the defect-free structure, and in some cases even proposing structural and compositional descriptors that do not require any DFT calculation at all. Deml et al. developed two different models of ΔE_{vf} based on a linear combination of descriptors.[41,96] The first work[96] leveraged a training set of 10 perovskite oxides and utilized the bulk material's formation enthalpy and bandgap as descriptors. The subsequent work[41] expanded the

training set to 45 binary and ternary oxides with a variety of crystal structure types, and expressed ΔE_{vf} as a function of the formation enthalpy, the average difference in Pauling electronegativity between the oxygen and its nearest neighbor cations and, replaced the bandgap with the energy difference between the oxygen p band center and the middle of the band gap. Wan et al[128] then utilized the model predictions on 1750 oxides from the second work to identify simple descriptors of ΔE_{vf} solely based on compositional features. They tested several regression methods and identified the best descriptors to be the difference in Pauling electronegativity between the oxygen and its nearest neighbor cation and the fraction of valence electrons in the material belonging to oxygen. Leveraging instead the dataset of around 300 ΔE_{vf} calculations of perovskite oxides by Emery et al.,[54] Liu et al.[129] also aimed to identify simple features not requiring any DFT calculation, considering elemental properties and proposing a descriptor composed of cation valence, electronegativity and atomic radii. Recently, Wexler et al.[55] introduced a description of ΔE_{vf} as a linear combination of DFT defect-free stability, band gap, reduction energy of the metal cations neighboring the vacancy and bond strength between the oxygen and its neighboring metal cations. With such features, they presented two linear models, one trained on a set of 142 oxygen vacancies of perovskite oxides lying within 25 meV/atom of the convex hull, and another one trained on perovskites in any of 6 considered distortions without any stability restriction. Approaching the problem from a more general point of view, Witman et al[130] selected $\sim$200 different oxides spanning 63 space groups and 14 elements and computed the formation energy of all unique defects in each structure, thereby generating a dataset of over 1000 defect energies. The authors then employed a significantly more complex type of learning than any of the previously mentioned studies, adapting the CGCNN model originally introduced by Xie et al.[131] to predict any type of defect formation energy by including oxidation state and site-specific information.

The examples of models of ΔE_{vf} present in the literature contain significant differences with regards to the training set, the features, and the type of models employed to describe the vacancy formation energy. All three of these factors can significantly affect ΔE_{vf} predictions in terms of accuracy, generality, interpretability and training time.

Features: one can broadly divide feature types in two categories: (i) global, i.e. quantities that are single-valued for each defect-free compound, such as the formation energy and the bandgap, and (ii) site-specific, i.e. that depend on the specific O vacancy site under consideration, and are multi-valued for each each defect-free compound, such as any feature that depends on the nearest neighbors of the vacancy site. Models only containing global features are limited in that, since such features don't allow for the differentiation of single vacancy sites, the model will give the same prediction for all O vacancy sites in the same material. Furthermore, features related to the metal cations can be further divided into either (i) element-specific, such as the Pauling electronegativity, or (ii) element- and valence-specific such as the ionic radius. Models that heavily rely on non-valence specific cation features are limited in their ability to differentiate the behaviour of compounds containing the same elements but in different oxidation states.

Training Set: models with smaller training sets containing less structural and compositional variety will be less likely to give accurate predictions when extrapolating to new structures and compositions that are less represented in the training data. Furthermore, training sets containing structures that are significantly off the convex hull or are not the lowest-energy structure at each composition are more likely to contain dynamically unstable structures, which present significant complications when computing the DFT oxygen vacancy formation energy (see Section 3.3).

ML Model: linear models, while being fast and intuitive, do not capture more complex relationships between descriptors and target properties, are sensitive to outliers and can be prone to overfitting. On the other side, non-linear models are capable of identifying useful feature representation by leveraging complex relationships between variables and can perform better upon extrapolation, but, particularly in the case of neural networks, come at a greater cost in terms of training time and interpretability, and typically require a larger amount of training data to perform well.

In this chapter, we leverage the dataset of oxygen vacancy formation energy calculations introduced in the previous chapter to investigate the above aspects of ΔE_{vf} prediction and develop new models. We introduce new descriptors of ΔE_{vf} and compare their performance with that of

the descriptors previously employed in the literature. We find the random forest models using the features introduced in this work to achieve the best performance, obtaining a mean absolute error on testing of ∼0.3 eV/O, comparable to the accuracy observed upon comparison of DFT computations of oxygen vacancy formation energy when compared to experimental result seen in Section 3.3. We then subsequently leverage the models predictions to aid in the search for materials for STCH applications, and successfully identify over 250 new candidates. Several paragraphs in this chapter are quoted directly from our manuscript.[106]

5.2 Methodology

The performance of models utilizing four different regression techniques was investigated: random forest regression(RFR), support vector regression (SVR), kernel ridge regression (KRR) and linear regression (LR). In all cases, the models were developed utilizing the Scikit-learn Python library, and optimizing the hyperparameters through a grid search.

5.3 Results

5.3.1 Data

Combining the data from all the high-throughput DFT studies describes in the previous chapter, our entire dataset contains 2677 different oxygen vacancy formation energy calculations of 1157 different metal oxides. Figure 5.22 shows the distribution of the entire dataset over spacegroups and elements. Structures belonging to 55 different spacegroup appear in the dataset, with the highest frequency spacegroups being P21/c (to which most of the $A_2BB'O_6$ double perovskites belong to), Pnma (to which most ABO_3 perovskites belong to), and Fd-3m (to which $A_2B_2O_7$ pyrochlores belong to). 66 different cation elements are considered, with 90% appearing at least 5 times in the dataset, and 75% appearing at least 20 times. Figure 5.23 shows the distribution of ΔE_{vf} values across the dataset, and differentiates the "unrelaxed" and "relaxation" contributions (see Section

3.3) to the vacancy formation energy.

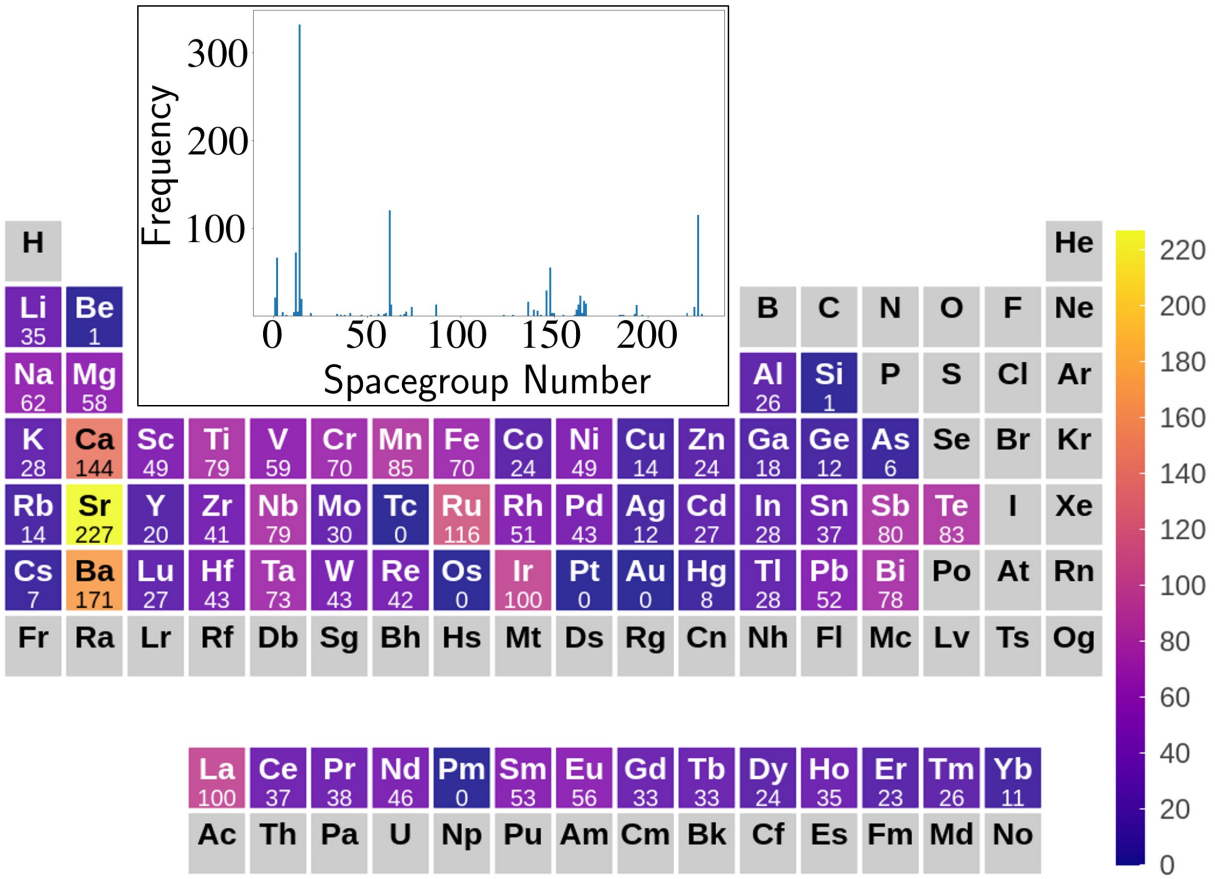

Figure 5.22: Distribution of the compounds in the entire dataset over elements (lighter shades indicating more compounds containing that element) and spacegroups (where each spacegroup is indicated by its number index).

5.3.2 Machine Learning Models

In developing a model for predicting the oxygen vacancy formation energy we have multiple goals. We firstly aim to identify simple-to-extract features that only rely on compositional and generic structural information and can be combined with the widely employed Magpie feature set introduced by Ward et al.[132] to specifically target oxygen vacancy formation energy prediction. We then also want to leverage the wealth of information generated through DFT calculations of the pristine structure of interest to compose a feature set containing only a small number of descriptors with

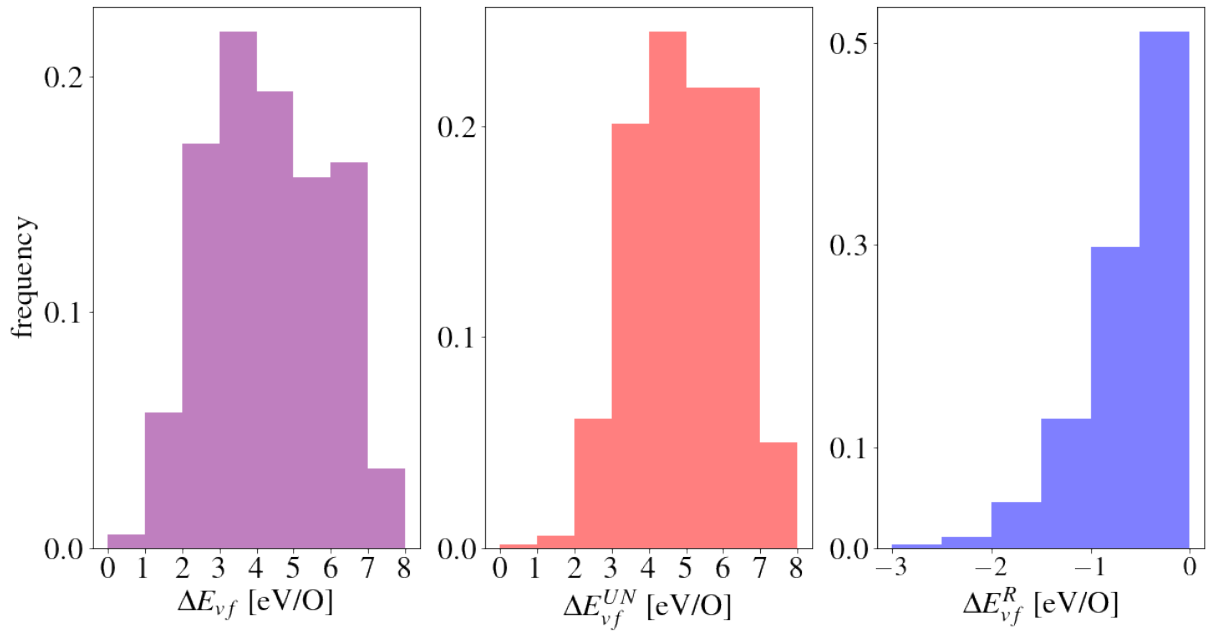

Figure 5.23: Distribution of values of the oxygen vacancy formation energy, and of its relaxation ($\Delta E_{vf,R}$) and unrelaxed ($\Delta E_{vf,UN}$) contributions for the compounds contained in the dataset.

intuitive relation to oxygen vacancy formation energy. In both cases, we then want to use the features in conjunction with prediction algorithms capable of identifying relationships between features and target property that go beyond linearity while still being fast and interpretable, and achieve reliable predictive accuracy starting with even just a few hundred training points. We introduce the selected features in Section 5.3.2.1, where we also describe other features previously employed in the literature which we will use for comparison. In Section 5.3.2.2 we then train random forest models on the data introduced in the previous chapter and compare the performance obtained using various combinations of features, including previous feature sets employed in the literature. We find the models using the feature sets introduced in this work to be the best performing ones out of the ones examined, achieving a mean absolute error as low as ∼0.3 eV/O. Finally, in Section 5.3.3 we employ such models to predict the oxygen vacancy formation energy of newly calculated, DFT stable (within 25 meV/atom of the convex hull), A and B site ordered AA'BB'O_6 double perovskites and select the most promising ones for STCH applications.

5.3.2.1 Features

The present section is dedicated to the description of various features used for ΔE_{vf} predictions. First, the choices behind the two feature sets selected in this work (referred to as Feature set I and Feature set II) are detailed. Then, other features used in previous works are listed and briefly described, explicitly mentioning which ones can be classified as global features, and which as site-specific. The nomenclature introduced in this section to refer to each feature and feature set is utilized for the rest of the paper.

Our first step is to introduce features capable of accounting for the strong influence, which we have highlighted in the previous chapter, of the atomic species and oxidation state of the cations in each metal oxide on the oxygen vacancy formation energy. In order to differentiate each cation in our dataset while capturing the energetic change involved in the breaking of the bonds and the redistribution of charge involved in the creation of an oxygen vacancy, we compute the unrelaxed oxygen vacancy formation energy (see Methods and Section 3.3) of a binary oxide containing each such cation. We refer to this quantity as $\Delta E_{vf}^{MO_x}$, where M indicates the cation species, the oxidation state is $2x^+$, and the binary oxides are selected by looking for the lowest energy MO_x compounds in the OQMD. The values of $\Delta E_{vf}^{MO_x}$ for the cations included in this work are displayed in Figure 11.64. Trends in accordance with what we observed for perovskites and pyrochlore oxides can be identified: (i) rare-earth and alkali metal species having larger $\Delta E_{vf}^{MO_x}$ than most transition and post-transition metals, (ii) and $\Delta E_{vf}^{MO_x}$ decreasing with increasing period among the same transition metal series, and (iii) being larger for smaller oxidation states for the same metal.

We then construct two feature sets that leverage the information contained in the descriptor detailed above.

Feature set I contains two types of features:

- Magpie:

  The Magpie feature set introduced by Ward et al., which contains stoichiometric attributes (such as the number of elements in the compound), elemental properties statistics (such as the average atomic number of the elements in the compound), electronic structure attributes (such

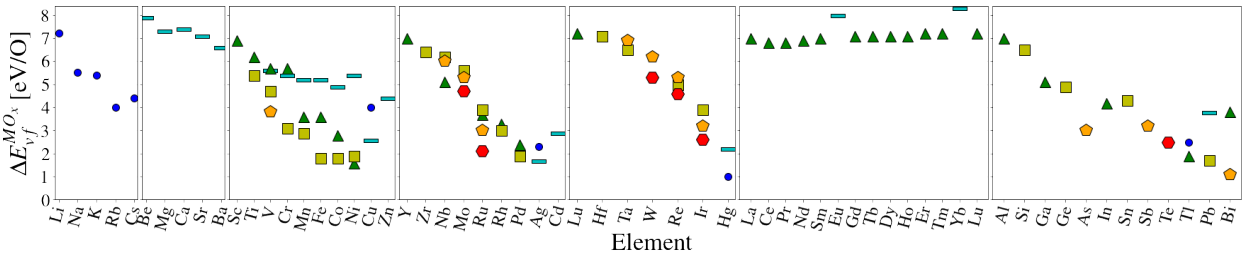

Figure 5.24: $\Delta E_{vf}^{MO_x}$ of all M^{2x+} cations included in the dataset. Different markers indicate different oxidation states: blue circles for 1+, cyan lines for 2+, green triangles for 3+, yellow squares for 4+, orange pentagons for 5+, and red hexagons for 6+. Trends across groups, periods and oxidation states can be observed: rare-earth and alkali metal species have larger $\Delta E_{vf}^{MO_x}$ than most transition and post-transtion metals, and $\Delta E_{vf}^{MO_x}$ decreases with increasing period among the same transition metal series, and is larger for smaller oxidation states for the same metal.

as the average number of d electrons across elements in the compound), and ionic compound attributes (such as the "ionic character" of the compound).[132] These are all global features.

- stats($\Delta E_{vf}^{MO_x}$):

  Statistics over features constructed from the unrelaxed vacancy formation energy of binary oxides. Two particular quantities are selected. (i) min($\Delta E_{vf}^{MO_x}$): the lowest value of $\Delta E_{vf}^{MO_x}$ among all M^{2x+} cations in the structure, which is a global feature. Considering, for example, the pyrochlore Lu_2Mn_2O7, where Mn^{4+} is the easiest to reduce cation, min($\Delta E_{vf}^{MO_x}$) would correspond to $\Delta E_{vf}^{MnO_2}$. (ii) $< \Delta E_{vf}^{MOx,NN} >$: the weighted average of $\Delta E_{vf}^{MO_x}$ over all M^{2x+} cations neighboring the vacancy, which is a site-specific feature. The weights are defined to sum to 1, and to be larger for cations with smaller $\Delta E_{vf}^{MO_x}$, so as to reflect the dominant role in determining ΔE_{vf} that cations with smaller $\Delta E_{vf}^{MO_x}$ have, as observed in the previous chapter. Specifically, for each cation i neighbouring the vacancy having $\Delta E_{vf}^{MO_{x,i}}$, its weight is defined as $w_i = \frac{1}{1+(E_{vf}^{MO_{x,i}} - min(E_{vf}^{MO_{x,NN}}))} \frac{1}{\sum_i w_i}$, where $min(E_{vf}^{MO_{x,NN}})$ is the lowest $\Delta E_{vf}^{MO_x}$ among the cations neighboring the vacancy. Considering again the example of pyrochlore Lu_2Mn_2O7, which has two types of vacancy sites (V1 where neighbors are 2 B and 2 A cations, and V2 where neighbors are 4 A cations), for V1 $< \Delta E_{vf}^{MOx,NN} >$ would correspond to $2w_{MnO_2}\Delta E_{vf}^{MnO_2} + 2w_{Lu_2O_3}\Delta E_{vf}^{Lu_2O_3}$ with $w_{Lu_2O_3} = \frac{1}{1+(E_{vf}^{Lu_2O_3} - \Delta E_{vf}^{MnO_2})} \frac{1}{2w_{MnO_2}+2w_{Lu_2O_3}} \sim 0.1$

and $w_{MnO_2} = 1\frac{1}{2w_{MnO_2}+2w_{Lu_2O_3}} \sim 0.4$, and for V2 $< \Delta E_{vf}^{MOx,NN} >$ would correspond to $\Delta E_{vf}^{Lu_2O_3}$. The selection of these quantities is aimed at capturing the influence that the nature of the cations neighboring the vacancy has on the oxygen vacancy formation energy, and reflecting the dominant role of cations with smaller $\Delta E_{vf}^{MO_x}$.

A major advantage of only requiring compositional and generic structural information is that this feature set can in principle be utilized without the need for any previous DFT calculation of the bulk structure, and only necessitates a structural prototype decorated with all the elemental combinations of interest (which is often the starting point of high-throughput studies). We note that a significant caveat of the above consideration is that, upon relaxation, atomic positions can at times change enough for the oxidation state of the cations determined from the relaxed and unrelaxed structure to differ. Given that cation oxidation states play a major role in ΔE_{vf}^{MOx}-related features, this can significantly affect predictions. To assess the extent of the impact of this effect, we determine the oxidation states of all cations in all compounds in our dataset before and after relaxation, finding that in 90% of the cases they remain the same. We therefore conclude that, while not an infallible strategy, Feature set I can be used to coarsely screen ΔE_{vf} of compounds prior to running DFT calculations. For example, within a search for new compounds with a specific structural prototype(s) and ΔE_{vf} in a target range, we can use an ML model with Feature set I to produce ΔE_{vf} predictions on the unrelaxed structures, and then reduce the number of DFT calculations of the pristine structures by only computing structures with a predicted ΔE_{vf} within a range of interest (ideally larger than the final target range so as to reduce possible false negatives).

Feature set II, which excludes Magpie features and is thus much smaller, is composed of the following features:

- stats($\Delta E_{vf}^{MO_x}$):

  The same two quantities described in the previous paragraph, with the only difference that the weights used to calculate are now also inversely proportional to the bond length between O and the relevant neighboring cation in order to capture more information on the local environment surrounding the vacancy.

- ΔE_f:

  The formation energy of the compound, aiming to capture energy change related to breaking bonds across the whole compound. This is a global feature.

- $(E_{Op}^{site} + E_g)$:

  The energy difference between the center of mass of the p band of the oxygen atom which becomes vacant and the first unoccupied state in the band structure (as computed using the pristine structure before introducing the vacancy), aiming to capture the energetic change associated with the change of state of the electrons previously involved in the bond with the O atom becoming vacant. This is a site-specific feature.

Having a feature set containing only a small number of features presents the advantage of being versatile, less prone to overfitting risk, and interpretable.

In order to compare the predictive value of our features against features used in other studies, we compute the following features from other studies:

- V_r^{NN}:

  The maximum reduction potential of the cations neighboring the vacancy. For each cation M with oxidation state x, the reduction potential is calculated by taking the energetic difference between the energy of the ground state polymorph of the binary oxide $MO_{x/2}$ and the energy of the ground state polymorph of the binary oxide $MO_{(x-1)/2}$, and accounting for the O energy. This is a site-specific feature. This feature was introduced in the work by Wexler et al.,[55] where more details can be found. We note that in Wexler et al.[55] the ground state polymorphs are taken from the Materials Project while in the present work they are taken from the OQMD.

- E_g:

  The band gap of the bulk compound of interest. This is a global feature. This feature was utilized in the work by Wexler et al.,[55] where more details can be found.

- ΣE_b^{NN}:

  The sum of the crystal bond dissociation energy of the cations neighboring the vacancy. For each M with oxidation state x, the crystal bond dissociation energy is calculated by taking the ratio between the cohesive energy of the ground state polymorph of the binary oxide $MO_{x/2}$ and the number of M-O bonds present in that binary oxide. In turn, the cohesive energy of a binary oxide $MO_{x/2}$ is calculated by subtracting the cohesive energy of the metal and the bond dissociation energy of O_2 from the formation energy of the binary oxide. This is a site-specific feature. This feature was introduced in the work by Wexler et al.,[55] where more details can be found. Once again, we note that in Wexler et al.[55] the ground state polymorphs are taken from the Materials Project while in the present work they are taken from the OQMD.

- ΔE_{stab}:

  The stability of the bulk compound of interest. This is a global feature. This feature was utilized in the work by Wexler et al.,[55] where more details can be found.

- $(E_{Op} + 0.75E_g)$:

  The sum of the bandgap and the difference in energy between the Fermi energy and the center of mass of the oxygen p band of a compound. This is a global feature. This feature was introduced in the work by Deml et al.,[41] where more details can be found.

- $< \Delta\chi^{NN} >$:

  The average difference in Pauling electronegativity between oxygen and its first nearest neighbors. This is a global feature. This feature was introduced in the work by Deml et al.,[41] where more details can be found, and was also employed in the work by Wan et al.[128]

- $\Delta\chi^{1stNN}$:

  The site specific difference in Pauling electronegativity between oxygen and its closest cation. This is a site-specific feature. When evaluating the performance of the features utilized in the works by Deml et al.[41] and Wan et al.[128] in the next section, this feature, rather than the previous one is utilized. The reason behind this choice is that, while the original works

only predict one ΔE_{vf} value for each compound, in this work we separately predict the values of different vacancy sites, and we therefore consider the substitution of the average electronegativity difference with the site specific one to provide a fairer evaluation in this case. We also note that this substitution improves the performance of the two feature sets.

- $\#e^-_O/\#e^-_{tot}$

  The product of the number of electrons in a single O atom and the number of O atoms in the compound of interest, divided by the total number of electrons in the compound of interest. This is a global feature. This feature was introduced in the work by Wan et al.,[128] where more details can be found.

5.3.2.2 Models Performance

Having introduced numerous descriptors of the oxygen vacancy formation energy in the previous section, we now test and compare the performance achieved by machine learning algorithms using different combinations of such descriptors. The machine learning algorithm of choice for most of the analysis is a random forest regressor,[133] both due to its reportedly solid performance across a variety of tasks, robustness against overfitting, speed and interpretability, and since, as we will show, it yields lower error than other tested regressors (kernel ridge, support vector machine, and linear regression). To give a more complete insight, we also examine correlation coefficients between the different descriptors.

We first test the predictive accuracy of the feature sets introduced in this work with different amounts of training data. Figure 5.25 displays the mean absolute error achieved by a random forest model utilizing the two feature sets against training set size, with a fixed test set size of 500 datapoints. In all cases, training and testing set are selected such that, even in the presence of multiple different vacancy sites for the same compound, the sites are separated so that each compound only appears in one of the two sets, i.e. performance testing is only on entirely unseen compounds. For all ranges of training data, the two feature sets display a very similar performance, achieving a mean absolute error as low as 0.3 eV/O when the full training set size is utilized.

We also compare the two feature sets with the Magpie feature set (black square) and highlight the doubling in accuracy (halving in MAE) that occurs when introducing the binary ΔE_{vf}-related features (blue triangle). In addition to the performance tests just described, we also investigate the accuracy achieved when predicting the unrelaxed and relaxation contributions to the vacancy formation energy (respectively, ΔE_{vf}^{UN} and ΔE_{vf}^{R}, see Section 3.3) independently from each other. We find that, when utilizing a training set of 2000 datapoints and Feature set I, the MAE upon prediction of ΔE_{vf}^{UN} is of $\sim$0.2 eV/O and that of ΔE_{vf}^{R} is of $\sim$0.1 eV/O. To put the above results in context, we note that, for the compounds included in our dataset, ΔE_{vf}^{UN} spans a range of $\sim$8eV, while ΔE_{vf}^{R} lies between 0 and -2eV for the vast majority of the cases, with a magnitude smaller than 1eV in over half of the cases (see Fig 5.23). This highlights the opportunity for achieving a more accurate ΔE_{vf} prediction by identifying features capable of capturing the mechanisms involved ionic relaxation upon vacancy formation (i.e. targeting the relaxation component), which is of interest for future improvements.

We then compare the performance of the feature sets introduced in this work with those present in the literature. The differences in the training sets, both in terms of size and content, and in the regressors used in previous studies can lead to significant differences in performance upon extrapolation. Therefore, in order to achieve a transparent comparison, we opt for utilizing the same training set (the one presented in this work) and regressor (a random forest regressor) for different models that utilize the feature sets introduced in each work we consider. The results are displayed in Figure 5.26, where "Ref A" indicates the work by Wan et al.[128] (marked with green stars), "Ref B" the work by Deml et al[41] (marked with yellow crosses), "Ref C" the work by Wexler et al.[55] (marked with cyan plus signs), and "This Work" refers to the feature set introduced in this work that leverages DFT bulk calculation information (i.e. the one previously referred to as Feature Set II, marked with red triangles in both 5.25 and Fig 5.26). Through the comparison we see that, for all training set sizes, the random forest model using the feature set introduced in this work systematically outperforms the other models. Among the other models, the one utilizing the feature set developed by Wexler et al.[55] also shows remarkable performance, reaching a mean absolute error

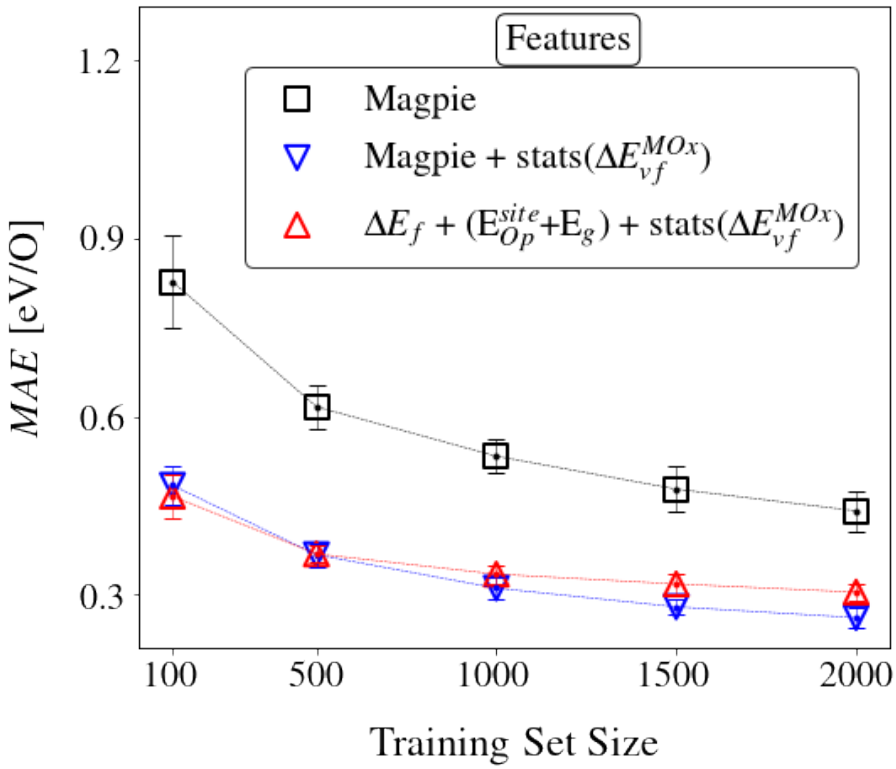

Figure 5.25: Performance of random forest models utilizing different feature sets as a function of training set size. The datapoints are centered on averages over 10 random choices of training data, with error bars representing standard deviations. The marker indicate different feature sets. The black square indicates the Magpie feature set. The blue triangle indicates the feature set composed of Magpie features and information on the oxygen vacancy formation energy of binary oxides with the same cations as the ones neighboring the vacancy, i.e. Feature set I described in Section 5.3.2.1. The red triangle indicates the feature set which uses information from DFT bulk calculations, i.e. Feature set II described in Section 5.3.2.1. The test set size is always 500. Train and test set are randomly selected with the enforcement of the condition that each composition can only appear in one of the two sets. Without this condition, as many compounds have multiple non-equivalent vacancy sites, it is likely that a purely random train-test separation would lead to different sites of the same compound appearing in the two sets.

below 0.4 eV/O. We attribute a significant role in such achievement to the presence of features which clearly capture the difference both in specie and in oxidation state of the metal cations neighboring the vacancy, which we have seen to have a primary impact on ΔE_{vf} in the previous chapter. We deem the absence of such type of feature to be the main reason limiting the accuracy reached by the model utilizing the feature set introduced by Deml et al.[41] Lastly, the feature set chosen by Wan et al[128] appears to produce significantly less accurate predictions, although we note that the aim of the authors was to identify a particularly simple set of features and avoid overfitting. Since previous

works have focused on compounds with a non-zero DFT bandgap, and $\sim 25\%$ of the compounds in our dataset have a zero OQMD-computed DFT bandgap, we also reproduce Figure 5.26 limiting the training and testing set to the compounds with $E_g > 0$. The results of this additional performance test, displayed in Fig 5.27, are largely similar to those presented in Figure 5.26, with evidence of a modest performance improvement for the models utilizing the feature sets introduced by Wexler et al and Wan et al, but the overall predictive hierarchy between feature sets is left unchanged. In addition to the above comparison of the predictive power of random forest models utilizing different feature sets in the literature, we also consider performance of the convolutional neural network introduced by Witman et al.[130] The lowest mean absolute error upon prediction of oxygen vacancy formation energy with a compound-wise train/test split (i.e. with the same logic applied in this study as described in the previous paragraph) is reported to be 0.45 ± 0.12 eV/O, and to have been achieved with 10-fold cross validation and a training set of over 10^3 datapoints. We however note that the training set utilized by the authors is composed of a variety of vacancy types, and that cation vacancy formation energies are likely to be less informative for oxygen vacancy prediction. We therefore point out that out of the 1481 defect energies present in the entire dataset, only 795 are from oxygen vacancies.

To gain further insight on the predictive utility of each of the individual features composing the feature sets just discussed, we now examine both their statistical correlation to ΔE_{vf}, and the informational gain they carry in comparison with the Magpie feature set. Throughout this discussion we refer to the different features using the nomenclature introduced in Section 5.3.2.1, where we explain in detail the significance and computation of each feature. In Figure 5.28 a we first report the Pearson and Spearman coefficients of each single feature in correlation with the vacancy formation energy. Features are ordered based on the magnitude of their correlation with the vacancy formation energy, and it can be clearly seen that features related to cation reduction ($\Delta E_{vf}^{MO_x}$, $\Delta E_{vf}^{MO_x,NN}$, and V_r^{NN}) exhibit the highest magnitude of correlation to the vacancy formation energy. The formation energy (ΔE_f) and band structure-related properties containing information about the oxygen p band ($E_{Op}^{site} + E_g$ and $E_{Op} + 0.75E_g$) also show a strong correlation with ΔE_{vf}, all having Pearson and

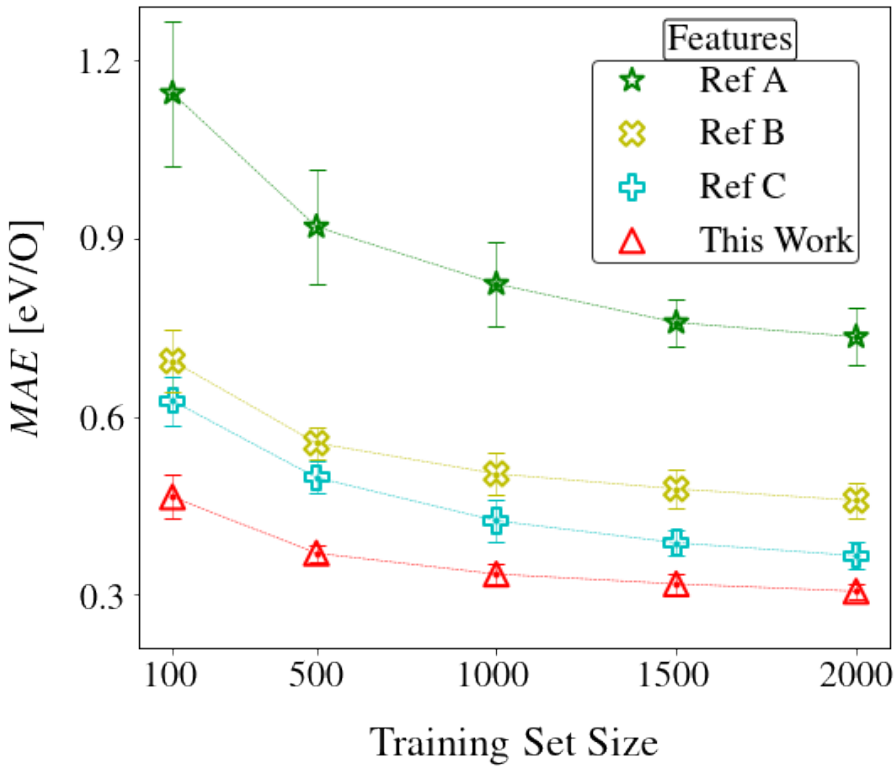

Figure 5.26: Mean absolute error of prediction of oxygen vacancy formation energy by random forest models utilizing different feature sets as a function of training set size. "Ref A" indicates the work by Wan et al.[128] (where the set of features is: $\Delta\chi^{1stNN}$, $\#e^-_O/\#e^-_{tot}$, the total number of atoms, O atoms and electrons per formula unit, and the fraction of O atoms), "Ref B" the work by Deml et al[41] (where the set of feature is: ΔE_f, $(E_{Op} + 0.75E_g)$ and $\Delta\chi^{1stNN}$), "Ref C" the work by Wexler et al.[55] (where the set of features is: V_r^{NN}, E_g, ΣE_b^{NN} and ΔE_{stab}), and "This Work" indicates Feature set II described in the previous section. The test set size is always 500 and train and test set are randomly selected with the enforcement of the condition that each composition can only appear in one of the two sets.

Spearman coefficients above 0.67. In Figure 5.28 b we then examine the predictive accuracy of each feature when employed in a random forest model along with the Magpie feature set. The aim of this analysis is twofold. Firstly, to broaden the range of correlation types considered, as, while informational, the Pearson and Spearman coefficients don't recognize all types of dependence between variables that can be leveraged by, eg. a random forest model. Secondly, to benchmark the utility of each additional feature compared to what could already be captured with an easily available, readily implementable, and widely used feature set. To perform the comparison, we compute the mean absolute error achieved by a random forest model with different training set sizes and a fixed test set size of 500 datapoints, starting with the Magpie feature set (black square),

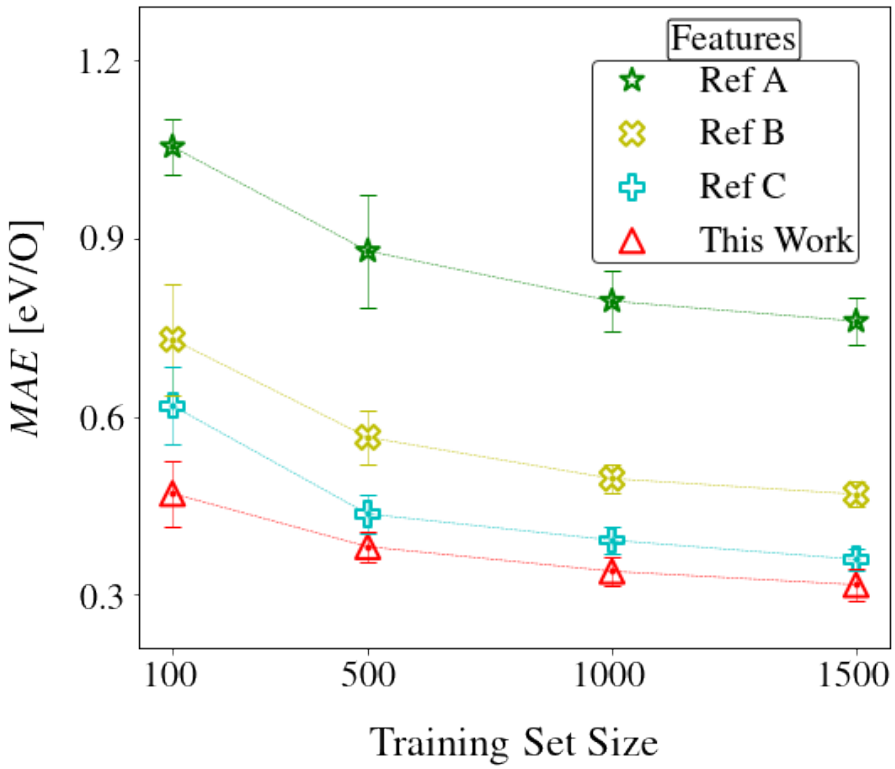

Figure 5.27: Mean absolute error of prediction of oxygen vacancy formation energy by random forest models utilizing different feature sets as a function of training set size. "Ref A" indicates the work by Wan et al.[128] (where the set of features is: $\Delta\chi^{1stNN}$, $\#e^-_O/\#e^-_{tot}$, the total number of atoms, O atoms and electrons per formula unit, and the fraction of O atoms), "Ref B" the work by Deml et al[41] (where the set of feature is: ΔE_f, $(E_{Op}+0.75E_g)$ and $\Delta\chi^{1stNN}$), "Ref C" the work by Wexler et al.[55] (where the set of features is: V_r^{NN}, E_g, ΣE_b^{NN} and ΔE_{stab}), and "This Work" indicates Feature Set B described in the previous section. The test set size is always 400 and train and test set are randomly selected from compounds in the dataset that have a non-zero OQMD computed DFT band gap, with the enforcement of the condition that each composition can only appear in one of the two sets.

and then including one additional feature individually. We firstly notice that site-specific features, which are marked with circles, generally outperform global ones, marked with squares. A major exception to the above observation are the $\Delta E_{vf}^{MO_x}$-related features. In fact, especially for lower training sizes, but in general throughout any training set size, the features related to cation reduction are very apparently the best performing ones. Such features are the two introduced in this work: $\Delta E_{vf}^{MO_x}$ and $\Delta E_{vf}^{MO_x,NN}$, and the one introduced by Wexler et al,[55] V_r^{NN}. This evidence corroborates our earlier observation that the presence of element- and oxidation state- specific information in the feature set introduced by Wexler et al in plays a significant role in its competitive performance.

We also remark that, while features such as the formation energy of the pristine structure ΔE_f do not exhibit any significant improvement in prediction accuracy of ΔE_{vf} when added to the Magpie feature set, this does not indicate a lack of utility in ΔE_{vf} prediction per se (as we can see by the correlation coefficients in Fig 5.28 a) but rather a redundancy with the information already captured by Magpie (Magpie is in fact utilized for predictions of ΔE_f itself[132,134,135]).

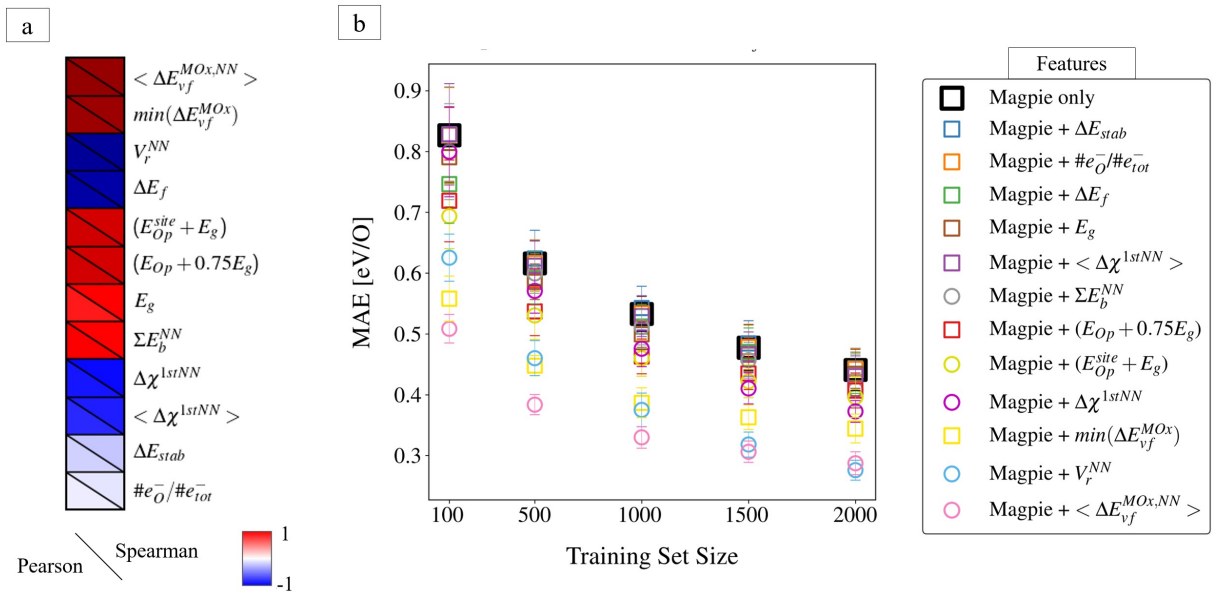

Figure 5.28: (a) Pearson (lower left triangle) and Spearman (upper right triangle) correlation coefficients of each feature with the oxygen vacancy formation energy. Red indicates positive correlation and blue indicates negative correlation, with darker shades indicating a stronger correlation. Feature names utilize the nomenclature introduced in Section 5.3.2.1 and are ordered top to bottom by magnitude (absolute value) of the correlation coefficients. (b) Mean absolute error of prediction of oxygen vacancy formation energy by random forest models utilizing different feature sets as a function of training set size. The black square indicates the case where only the Magpie feature set is utilized, while all other markers indicate the Magpie feature set plus one additional feature. When the additional feature is site-specific (i.e. contains information that depends on the site of the oxygen vacancy, such as nearest neighbors), the marker is circular, otherwise the marker is squared. The test set size is always 250 and train and test set are randomly selected with the enforcement of the condition that each composition can only appear in one of the two sets.

Finally, we test the effect that different regressors have on ΔE_{vf} predictions, when using the same training and feature set (see Fig 5.29). We test random forest (RF), support vector (SVR), kernel ridge (KRR) and linear regressors (LR), with the different sets of features examined in Figure 5.26. Random forest emerges as the best performing algorithm in all cases, with support vector

and kernel ridge following, and linear regression achieving a significantly more limited accuracy. Furthermore, the feature set introduced in this work achieves the lowest mean absolute error across all regressors, its predictive power being by far the least affected by regressor choice among the feature sets considered.

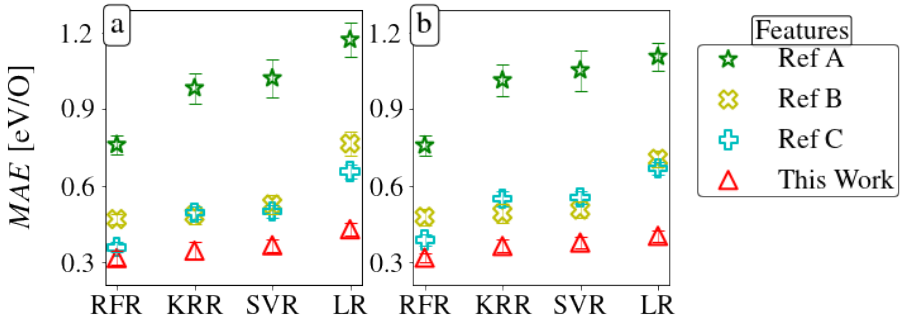

Figure 5.29: Mean absolute error of prediction of oxygen vacancy formation energy of different combinations of features and regressors. In (a) results are obtained by considering on the full dataset (2000 training data, 500 test), and (b) only compounds with a non-zero OQMD computed DFT band gap (1500 training data, 400 test). RFR indicates random forest regression, SVR, support vector regression, KRR kernel ridge regression, and LR linear regression. "Ref A" indicates the work by Wan et al.[128] (where the set of features is: $\Delta\chi^{1stNN}$, $\#e_O^-/\#e_{tot}^-$, the total number of atoms, O atoms and electrons per formula unit, and the fraction of O atoms), "Ref B" the work by Deml et al[41] (where the set of feature is: ΔE_f, $(E_{Op}+0.75E_g)$ and $\Delta\chi^{1stNN}$), "Ref C" the work by Wexler et al.[55] (where the set of features is: V_r^{NN}, E_g, ΣE_b^{NN} and ΔE_{stab}), and "This Work" indicates Feature Set B described in the previous section.

5.3.3 New Predictions

Having demonstrated the predictive power of random forest models utilizing the feature sets we introduced, we now exemplify their use in the search for new materials. Specifically, we choose to focus on new compounds for STCH applications. In this context, the perovskite family possesses a number of attractive properties, such as ability to withstand high temperature, and accomodate oxygen defects, and ease of oxygen diffusion. Having already studied both simple ABO_3 perovskites and B site ordered $A_2BB'O_6$ double perovskites in the previous chapter, we now take the next step in combinatorial complexity by considering two different cation species on both the A and the B site. In order to avoid the creation of large supercells to simulate disordered atomic configurations, we focus on ordered compounds. While numerous examples of B site ordered double perovskites are

present in the literature, ordering on the A site appears more infrequent, often being stabilized by anion or cation vacancies.[121] A number of examples of concurrent A and B site ordering in double perovskites have however been reported in compounds such as $NaNdMnWO_6$, where the A cations assume a layered-type of ordering, and the B cations assume a rocksalt configuration analogous to that of the double perovskites presented in Section 4.3.[136,137] We therefore choose to focus on this structure type, and in particular the $NaNdMnWO_6$ structural prototype, which crystallizes in a monoclinic cell presenting both out-of-phase rotations of the oxygen octahedra about the [110] direction of the cubic structure and in-phase rotation of the octahedra about the [001] direction[136] (see Fig 11.67 for a visual representation of the structure).

To search for new STCH compounds with $NaNdMnWO_6$ structure type, we apply two screening criteria: thermodynamic stability and oxygen vacancy formation energy. In particular, we look for compounds within 25meV/atom of the OQMD convex hull and with a ΔE_{vf} between 2 and 4.5 eV/O. In the past, this type of screening has been conducted by first computing the stability of all decorations of the structural prototype of interest, and subsequently computing the vacancy formation energy of the stable compounds identified in the previous step. In the present case, considering all distinct metal cations decorations of $AA'_2BB'O_6$ double perovskite cation sites leads to millions of possible combinations. In order to render the problem computationally tractable, we employ multiple strategies to decrease the number of candidates.

As a first step, we reduce the number of compositions to be evaluated for thermodynamic stability. To do so, we first limit the possible cations occupying each site to specific groups that are more likely to lead to stable and ordered compounds.[137] In particular, we circumscribe the A site cations to alkali and alkali earth metals (K,Na,Rb,Ca,Sr,Ba), the A' ones to rare earth elements, the B cation to transition metals (any 3d, 4d, 5d transition metal), and the B' cation to early, high-valent transition metals (Ti, Zr, Hf, V, Nb, Ta, Cr, Mo, W). We then leverage the Feature set I introduced in Section 5.3.2.1 (the one containing only compositional and generic structural information) to predict the compounds' vacancy formation energies and apply a first, coarser, filter eliminating compounds having all predicted ΔE_{vf} values above 4.5 eV/O. Through this combined strategy, we

reduce the number of compounds to ∼8600. We then perform stability calculations on the remaining compounds, and find over 600 of them to lie within 25meV of the OQMD convex hull. While the possibility of such compounds presenting cation disorder upon synthesis is conceivable, previous calculations on two recently experimentally reported mixed perovskites have shown that oxygen vacancy formation calculations performed on the ordered double perovskite equivalent of the mixed perovskite produced results accurate enough to guide candidate selection for STCH.[113,114]

Having identified several hundred new stable (within 25 meV of the hull) $AA'_2BB'O_6$ candidates, we employ the random forest model using Feature set II introduced in Section 5.3.2.1 (the one containing information from the DFT calculation of the defect-free structure) to predict their oxygen vacancy formation energies. For each compound, six unique oxygen sites can be identified (one in each A layer, and four between the two A layers), making the prediction goal not only to differentiate ΔE_{vf} among different compounds, but also among different sites in the same compound, in order to predict the smallest value of ΔE_{vf} for each compound. In the majority of cases, the model predicts ΔE_{vf} of all the O sites in the same compound to be within 0.3 eV/O of each other. We perform preliminary calculations on a subset of 5 compounds, and confirm the models predictions of lack of large difference between vacancies before relaxation, but however observe more significant differences upon relaxation in some cases, with the vacancies between the two A layers having a more negative ΔE^R_{vf} (and therefore a smaller ΔE_{vf}). Based on these observations, we restrict our candidate search by considering only the O vacancy sites between the two A layers. We then select the compounds with the smallest predicted ΔE_{vf} lying in the target STCH range and directly compute their vacancy formation energy within the OQMD framework. Through such calculations, we both confirm the predictive power of the model, finding ΔE_{vf} values to lie in the exact range in over 75% of the cases, and within 0.5 eV/O of the range in 99% of the cases, and identify over 250 new STCH candidates, a complete list of which is reported in the Appendix. Within such candidates, we highlight the presence of cations previously identified as promising for STCH applications: Mn^{3+} (in compounds like (Ca,Sr)(Y,La,Ce,Pr,Sm,Tb,Gd,Dy)Mn(Ti,V)O_6), Mn^{4+} (in compounds like Na(Y,Ce,Pr,Sm,Nd,Gd,Tb,Tm,Ho,Dy)Mn(Ti,Zr,Hf)O_6) and Co^{3+} (in compounds

like (Ca,Sr)(La,Nd,Pr,Dy)$CoTiO_6$).

6. Computational Study of the Entropy of Oxygen Vacancy Formation in Metal Oxides

6.1 Background

The formation of oxygen vacancies can have favourable effects for various technologies. As highlighted in the previous chapters, the presence oxygen loss plays a fundamental role in STCH, with typical two step cycles relying on oxygen release at higher temperature to then harvest H_2 upon flowing water vapour in the oxygen deficient material at lower temperatures.[7–9,56–58] Analogous processes utilizing on oxygen loss for a two step reduction-oxidation reaction also find application for air separation[69] and splitting of CO_2 into CO and O_2.[56–58,68,138] In solid oxide fuel cells (SOFCs) the vacancy sites are instrumental for bulk oxide ion diffusion, providing pathways for the transport of the ions.[51,52] Oxygen off-stoichiometry can also be advantageous in a variety of other applications, for example photocatalysis[139] and piezocatalysis.[140]

As seen in previous chapters, significant efforts have been dedicated to the computation of oxygen vacancy formation energies (ΔE_{vf}), covering a range of different structure types and a vast array of compositions.[41,54,96,130] The availability of sizeable datasets of ΔE_{vf} calculations has then offered the possibility of uncovering trends across materials and developing predictive models,[41,54,96,128–130] presenting an even larger potential for materials investigation.

Finite temperature properties such as the entropy of defect formation, however, remain less studied on a computational level. Naghavi et al.[141] examined the entropic contribution originating

from the coupling between orbital and spin angular momenta in lanthanide ions, finding the reduction of Ce^{4+} ions to result in an exceptionally large value compared to all other lanthanide atoms, and uncovering a particularly significant contribution the large entropy of reduction of Ceria, the benchmark material in STCH.[53,105] The solid state entropy of reduction of Ceria was also at the center of a study by Gopal and van de Walle,[142] who computed configurational and vibrational entropic contributions through cluster expansion Hamiltonian-based Monte Carlo simulations. While still investigating defect formation in Ceria, Grieshammer et. al[143] targeted the vibrational component alone, examining multiple types of defects including O vacancies. Similar small-scale studies examining the vibrational entropy of O vacancy formation in a specific material of interest have been conducted for a limited number of metal oxide compounds.[144,145] Wider-ranging studies than the ones present in the literature are of interest to deepen the understating of the role of the solid state vibrational entropy of O vacancy formation in processes like the ones involved in STCH, and investigate common features and differences between materials.

In this study, we examine the the change in solid state vibrational entropy involved in the formation of oxygen vacancies (ΔS_{vib}) in 10 different metal oxide compounds, crystallizing in different structure types: perovskite, double perovskite, hexagonal "LuMnO_3"-type, and pyrochlore. We consider the process of formation of neutral oxygen vacancies, where, rather than the lattice itself acting as a reservoir for the oxygen becoming vacant, the final state of oxygen is accounted for with a gaseous entropy term discussed in the last section of the text. We both highlight common features in ΔS_{vib} between the compounds examined, such as the trend with temperature, and identify significant differences, such as the contributions from the cations neighboring the vacancy. Examining the mechanisms leading to positive or negative contributions to ΔS_{vib}, we find the lengthening of the bonds between the cations where charge localizes upon vacancy formation and the neighboring oxygen atoms to lead to an increase in vibrational entropy, and the loss of the O atom itself to be the main contribution responsible for the steady decrease in ΔS_{vib} at higher temperatures. We also compare the change in solid state vibrational entropy to other significant contributions to the total entropy of vacancy formation, namely the gas entropy of O_2 and the configurational entropy, finding

ΔS_{vib} to play a smaller but non-negligible role. Several paragraphs in this chapter are quoted directly from our manuscript.[146]

6.2 Methods

All DFT calculations have been conducted using the Vienna ab-initio simulation package (VASP),[75,76] with projector augmented wave (PAW) potentials[77] and the Perdew-Burke-Ernzehof (PBE)[78] generalized gradient approximation (GGA) for the exchange-correlation functional. A plane wave cutoff energy of 520 eV was employed, with a gamma centered k-point grid with a density of at least 8600 points per reciprocal atom, and spin polarization was applied with a ferromagnetic configuration, initializing magnetic moments to $5\mu_B$. The over-delocalization of electrons in compounds containing 3d transition metals due to the residual self interaction present in exchange-correlation functionals[36–40] was treated through the addition of a Hubbard-like potential to the energy functional.[42] Results in Sections 6.3.1 and 6.3.2 are presented for a constant value of U=4eV for all compounds (U=3.8eV for the "$LuMnO_3$"-type compounds), but the effect of utilizing different U values is explored in Section 6.3.3.

Phonon dispersions were calculated by means of the finite difference method as implemented in PHONOPY.[50] The solid state vibrational entropy of vacancy formation ΔS_{vib} (per O vacancy) was calculated by computing the difference in vibrational entropy between the pristine and vacancy-containing cell, which for an $A_xB_yO_z$ compound can be expressed as:

$$\Delta S_{vib} = S_{vib}(A_xB_yO_{z-\delta}) - S_{vib}(A_xB_yO_z) \tag{6.20}$$

Where $S_{vib}(A_xB_yO_{z-\delta})$ is the vibrational entropy of the defect containing cell (containing one O vacancy), and $S_{vib}(A_xB_yO_z)$ is the vibrational entropy of the defect-free cell, both of which are calculated from structures where both volumes and atomic positions are allowed to relax (i.e. at p=0). Note that, while the vibrational entropy of vacancy formation is a function of temperature, we refer to it as ΔS_{vib} instead of $\Delta S_{vib}(T)$ for shorthand in many instances in the text.

ΔS_{vib} was computed for 10 different compounds: the orthorhombic perovskites $LaMnO_3$, $CaMnO_3$, $YFeO_3$ and $LaFeO_3$, the B site ordered double perovskites Sr_2MnTiO_6 and Ca_2MnTiO_6, the "$LuMnO_3$"-type compounds $YMnO_3$, $HoMnO_3$ and $LuMnO_3$, and the pyrochlore $Lu_2Mn_2O_7$. For each compound, vacancy containing structures were obtained by introducing an oxygen vacancy (V_O) in supercells of, respectively, 80 atoms for perovskite oxides, 90 atoms for "$LuMnO_3$"-type compounds, and 88 atoms for pyrochlore oxides. 1x2x1 supercells of the 80 atom cells (where the b axis is shorter than the a and c axis before doubling) were constructed for phonon calculations of perovskite oxides, such that phonon calculations were conducted with cell dimensions $\gtrsim$ 10Åalong all directions for all compounds. The above are the largest cell dimensions that could be considered at a reasonable computational cost.

In Section 6.3.1, in order to investigate the effect of temperature on the contribution from different frequencies to the total the vibrational entropy of V_O formation, the quantity $\Delta S_{vib}(\omega, T)$ is computed by only integrating the entropy up to a frequency ω (with $\Delta g(\omega)$ indicating the density of states difference between the defective and pristine structures):

$$\Delta S_{vib}(\omega, T) = \int_0^{\omega} (\frac{1}{2T} coth(\frac{\omega}{2k_B T}) - k_B ln(2sinh(\frac{\omega}{2k_B T}))) g(\omega) d\omega \tag{6.21}$$

In Section 6.3.4, other contributions to the total entropy of V_O formation are examined. ΔS_{vib} only accounts for the change in the solid state vibrational entropy (at the harmonic level) of the metal oxide upon introducing an O vacancy, and is calculated as the difference in vibrational entropy between two cells with a different number of atoms (specifically, one less O atom in the defect-containing cell). The vibrational entropy of O in its final gas state is accounted for (along side the translational and rotational contributions) in the gas entropy term (discussed in Section 6.3.4). The total entropy of O vacancy formation can then be calculated as:

$$\Delta S_{tot} = \Delta S_{vib} + 1/2 S(O_2) + \Delta S_{other} \tag{6.22}$$

Where $1/2 S(O_2)$ represents the gas entropy contribution and ΔS_{other} accounts for contributions to

the total entropy of V_O formation other than the change in solid state vibrational entropy and the gas entropy. For the compounds examined in this text, we consider the main contribution to ΔS_{other} to be from the configurational entropy, as further discussed in Section 6.3.4, but other sources of entropy, such as electornic configurational[141] and magnetic can also contribute to the total entropy of V_O formation.

6.3 Results

In Figure 6.30 we compare the solid state vibrational entropy of Vo formation of all the compounds we selected as a function of temperature, subdividing by structure type: (a) perovskite, (b) "$LuMnO_3$"-type and (c) pyrochlore. It can be observed that, in all cases, an initial increase in ΔS_{vib} is followed by a peak around room temperature, and then a steady decrease. Despite the general similarities in the overall temperature behaviour, differences can be observed between materials, mainly in terms of the height and location of the peak, and of the rate of descent. We analyse these behaviours over the next sections. Firstly, in Section 6.3.1, we rationalize the general shape of the temperature dependence of ΔS_{vib}, identifying the main contributions to each feature of the curve. In Section 6.3.2 we then analyze single atomic contributions to the vibrational entropy, highlighting similarities and differences between compounds. Finally, in Section 6.3.4, we examine the configurational and gas phase contributions to the entropy of vacancy formation.

6.3.1 Temperature Behaviour of the Vibrational Entropy

As visible in Figure 6.30, two basic components of the trend of ΔS_{vib} with T can be identified: an initial increase and a subsequent decrease. In order to investigate the origin of these features, we first visualize the differences in the phonon density of states of the pristine and of the vacancy containing structure and the contributions to the entropy of different vibrational frequency regions at various temperatures. To connect the ΔS_{vib} vs T curve to the contribution from different atoms in the structure, we then also examine their individual contributions to the phonon density of states.

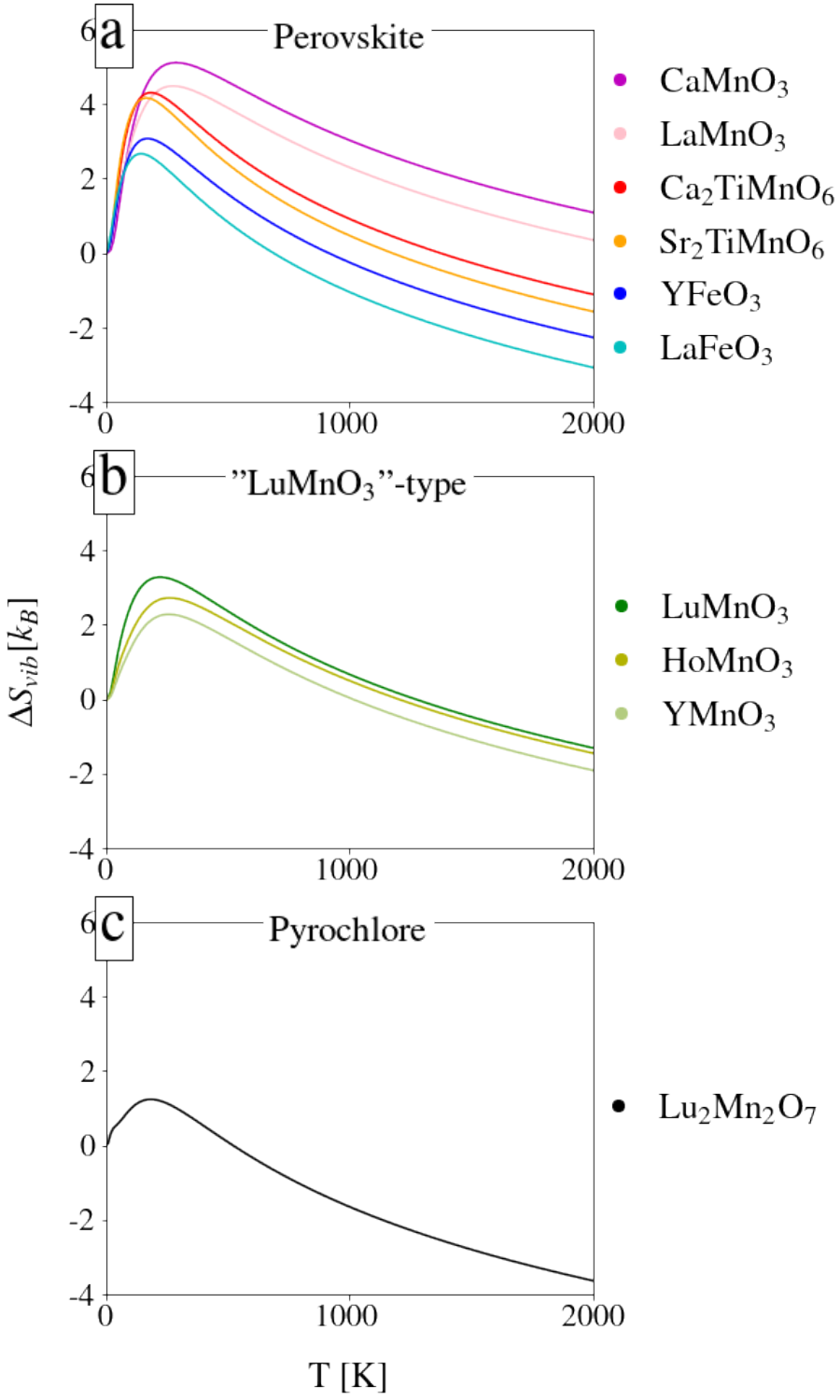

Figure 6.30: Solid state vibrational entropy of O vacancy formation as a function of temperature for compounds with (a) a perovskite structure, (b) a "$LuMnO_3$"-type structure, and (c) a pyrochlore structure.

As the general features of the ΔS_{vib} vs T curve are common to all compounds we studied, we select one specific compound, $HoMnO_3$ to illustrate and density of states-related properties in the main text, reporting the remaining compounds in the supplementary text.

We start the investigation of the origin of temperature dependence ΔS_{vib} on T of by examining general features of the phonon density of states (DOS) of $HoMnO_3$. In Fig 6.31 (a) we first compare the DOS of the pristine and defect-containing structure. Several differences can be noticed in the phonon DOS of the defective structure when compared to the pristine one, most notably an additional lower frequency ($\sim$ 2 THz) peak and a red-shift in the frequencies of states at higher frequencies ($\sim$ 17 THz). Having compared the two DOS curves (defect-containing and pristine) separately, we then compute their difference, and integrate it over vibrational frequency, as shown through the black dotted line In Fig 6.31 (b). The integrated Δ DOS has positive values for all lower frequencies, with then a peak at around 17 THz followed by a decrease to negative values for higher frequencies. To examine how the contribution of different frequencies to the vibrational entropy changes with temperature we also display in Figure 6.31 (b) the running integral of the vibrational entropy of vacancy formation, $\Delta S_{vib}(\omega, T)$ (defined in Eqn. 6.21), for 5 different temperature values (identified through different colors). At lower temperatures, the dominant contribution to the vibrational entropy comes from smaller frequencies, where the integrated Δ DOS is positive, which is consistent with the initial growth of ΔS_{vib} with temperature observed in Figure 6.30. As temperature increases, however, larger frequencies start to have a larger weight, and, due to the now no longer negligible contribution from the frequencies at which the integrated Δ DOS is negative, ΔS_{vib} starts decreasing.

Having identified the main features in the phonon density of states which determine the dependence of ΔS_{vib} on T, we now investigate the source of these features. To do so, we separate the contributions to the phonon band structure from the different atoms in the structure. In Figure 6.32 we display the atom projected phonon density of states (PDOS) of (a) the pristine structure, and (b) the vacancy-containing structure of $HoMnO_3$. In the low frequency region the contributions from the heaviest (in this case Ho) atoms dominate, while O, being the lightest species, is mainly

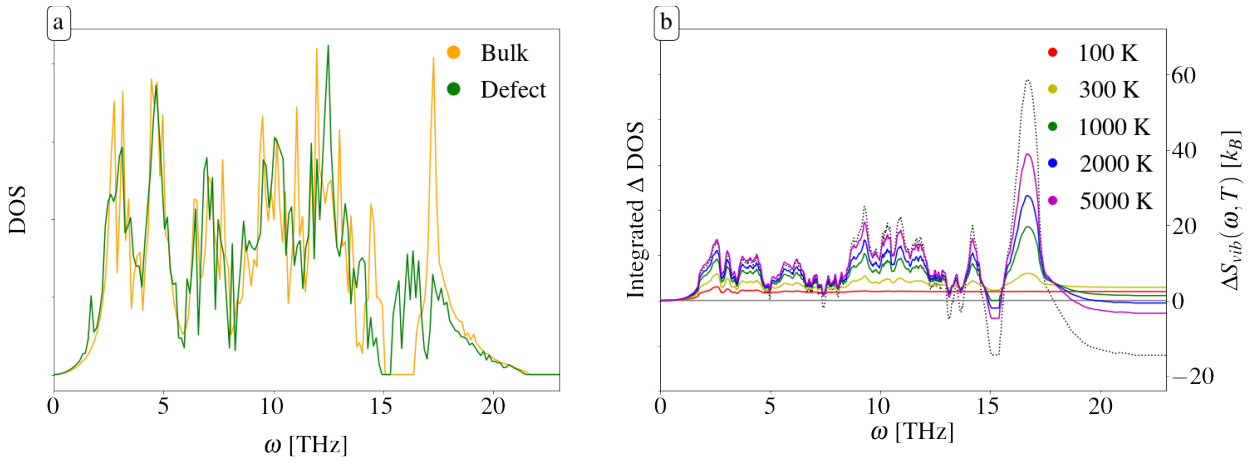

Figure 6.31: (a) phonon density of states of the pristine ("bulk", orange) and vacancy-containing ("defect", green) structures of $HoMnO_3$. (b) lefthand y axis: Difference in the density of states between vacancy-containing and bulk structures, integrated over vibrational frequencies (black dotted line). Righthand y axis: $\Delta S_{vib}(\omega, T)$ (see eqn. 6.21), the vibrational entropy difference between the bulk and vacancy-containing structure of $HoMnO_3$, containing only contributions up to the vibrational frequency value indicated in the x axis (solid lines of different colors indicating different temperatures)

associated with the higher frequency region. The low frequency peak observed in the defect DOS in Figure 6.31(a) is associated with a redshift of the vibrational frequency of the Ho atom neighboring the vacancy, which is consistent with bond-breaking. A similar redshift is also associated with the vibrational frequencies of the Mn atoms neighboring the vacancy. We consider both such redshifts to determine the initial positive value of the integrated Δ DOS and of ΔS_{vib}. As for the oxygen atoms, a redshift upon vacancy formation can also be observed in the region ∼15-17 THz, which is responsible for the peak in the integrated DOS. However, the higher density of states in the pristine structure at larger frequencies (∼ 18 THz), which we also associate with the presence of one additional oxygen atom (the one becoming vacant) in the pristine structure, eventually dominates leading to a decrease in ΔS_{vib}. We note that, even if the vibrational contribution from the oxygen in its final gaseous state as part of the O_2 molecule was added to the computation of ΔS_{vib}, the results would be very similar to what displayed in Figure 6.30, due to the vibrational frequency of molecular oxygen being significantly higher than that of oxygen in the metal oxide lattice. An estimate of the vibrational entropy of vacancy formation entirely excluding the contribution from the oxygen atom becoming vacant can be obtained by first computing the atomic projections of

the vibrational entropy of the pristine cell, then calculating their sum excluding the contribution from the O becoming vacant, and finally subtracting the result from the vibrational entropy of the vacancy containing cell. Such a computation, resulting in the pristine cell having the same number of atoms as the defective cell, results in the entropy difference plateauing to positive values after the initial growth, leaving the ranking between compounds unchanged (see Fig 6.33).

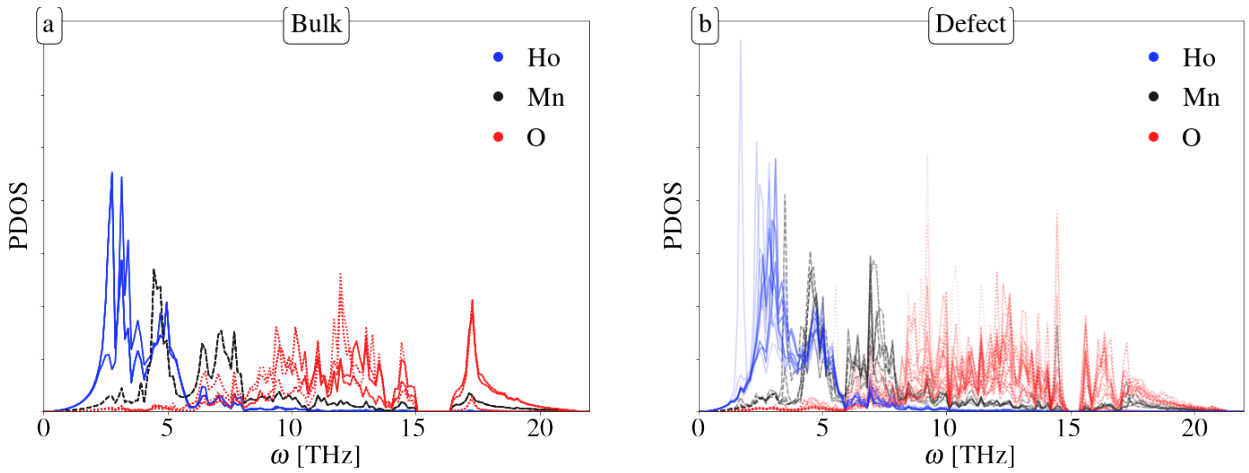

Figure 6.32: Atom projected phonon density of states of (a) the bulk structure and (b) the vacancy-containing structure of $HoMnO_3$. Red dotted lines represent contributions from O atoms, grey dashed lines from Mn atoms, and blue solid lines from Ho atoms.

6.3.2 Atomic Contributions to the Vibrational Entropy

After an brief look at general characteristics of the contribution of different atoms in the structure to the phonon density of states presented in the previous section for an exemplary material ($HoMnO_3$), the present section provides in depth look at the atomic contributions to the vibrational entropy of all compounds included in the study. The analysis is carried out by first grouping the atoms based on their distance to the vacancy, and then examining them singularly. A and B cations are differentiated from O anions, and changes in charge localization and bond length are included in the discussion.

Figure 6.34 displays the per atom contribution to ΔS_{vib} (ΔS_{vib}^{atom}) for the different atoms in each compound, with the atoms being clustered in 6 different groups (8 groups for double perovskites):

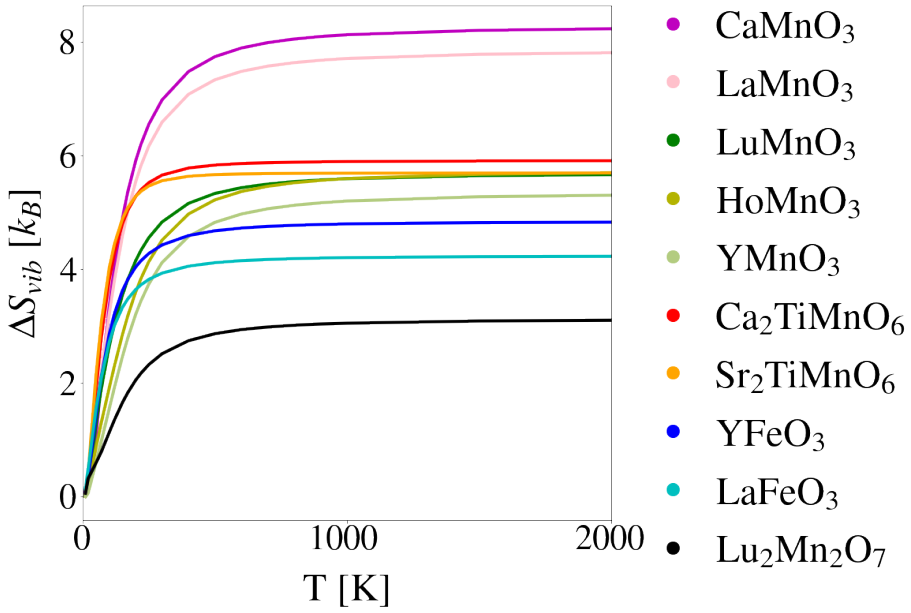

Figure 6.33: Change in solid state vibrational entropy upon formation of an oxygen vacancy computed excluding the contribution from the oxygen atom becoming vacant, and displayed as a function of temperature

(i) the A cations neighboring the O vacancy site, referred to as "A NN" (ii) the B cations neighboring the O vacancy site, referred to as "B NN" (and, for double perovskites, (ii.i) the B' cations for neighboring the O vacancy site, referred to as "B' NN", where "B" indicates Mn and "B'" indicates Ti) (iii) the O anions bonded to the A and B cations neighboring the vacancy, referred to as "O 2NN" (iv) all other A cations, referred to as "A other", (v) all other B cations, referred to as "B other" (and, for double perovskites, (v.i) all other B' cations, referred to as "B' other"), and (vi) all other O cations, referred to as "O other". The histograms are color-coded to indicate the number of atoms in each group (darker colors indicating more atoms), and, once again, the figure is divided in sub-figures grouping the compounds by structure type: (a) "$LuMnO_3$"-type, (b) pyrochlore, and (c) perovskite.

Comparing different compounds, multiple commonalities and differences in the contributions to the vibrational entropy from each group of atoms can be highlighted. Firstly, in all cases, the largest per atom contribution to ΔS_{vib} is associated with the cations neighboring the vacancy, with a second sizeable contribution coming from the O atoms bonded to those cations. Significant variations can however be observed in both the magnitude and the sign of the contributions from the

cations nearest neighbors to the O vacancy. Fe based perovskites, for example, show a fairly larger "B NN" contribution compared to Mn based perovskites. The ultimately larger value of ΔS_{vib} in $LaMnO_3$ and $CaMnO_3$ compared to $YFeO_3$ and $LaFeO_3$ can attributed to the largest contributions from "O 2NN" atoms and non-nearest neighbor cations, which despite their smaller per-atom contribution compared to NN cations, are larger in number. Mn based double perovskites, on the other hand, show a large positive contribution from the Mn nearest neighbor, but, concurrently, a large negative contribution from the Ti nearest neighbor. A consistently larger "A NN" contribution can be identified in Mn based "$LuMnO_3$"-type compounds compared to perovskites, with the "B NN" contribution being significantly larger in $LuMnO_3$ than in $YMnO_3$ and $HoMnO_3$. Finally, the pyrochlore $Lu_2Mn_2O_7$ displays a large positive "B NN" contribution and an equally large, but, negative "A NN" contribution.

To gain deeper insight on the origin of the different features highlighted in Figure 6.34, we plot in Figure 6.37 all the ΔS_{vib}^{atom} contributions from individual atoms separately (i.e. to each atom corresponds a single data-point). We correlate ΔS_{vib}^{atom} to the change in average vibrational frequency of each atom upon vacancy formation ($\Delta < \omega^{atom} >$), and we also discuss changes in charge localization and bond lengths. In this instance, the datapoints are color-coded based on the average vibrational frequency of the atom of interest in the pristine structure ("$< \omega_{BULK}^{atom} >$"). The marker shapes are then chosen to distinguish A cations (squares), B cations (diamonds), and O anions (circles), with a superimposed star to mark the A and B cations neighboring the vacancy (those referred to as "A NN", "B NN" and "B' NN" in Figure 6.34), and a superimposed asterisk to mark the O anions bonded to the cations neighboring the vacancy (those referred to as "O 2NN" in Figure 6.34). We recognize once again some of the features previously identified in Figure 6.34, but also observe additional details.

In general, a strong correlation between the change in the average vibrational frequency associated with each atom ($\Delta < \omega^{atom} >$) and its contribution to the solid state vibrational entropy of vacancy formation (ΔS_{vib}^{atom}) can be observed: atoms experiencing stronger redshifts in frequency give a stronger positive contribution to ΔS_{vib}, and the opposite for blueshifts. A second correlation

between ΔS_{vib} and the average vibrational frequency associated with each atom prior to defect formation ("$< \omega_{BULK}^{atom} >$") can also be observed. Specifically, for the same change in frequency, atoms with contributions dominating the lower frequency range (A cations) have a larger impact on the vibrational entropy than atoms with contributions dominating the higher frequency range (O anions). In other words, if a line were to be fitted to the datapoints belonging to each group of atoms in Figure 6.37, the line associated with A atoms would be steeper that associated with O atoms. The presence of color-coding based on "$< \omega_{BULK}^{atom} >$" also allows to observe differences in vibrational frequencies among each group (i.e. among A cations, B cations and O anions). In addition to more evident observations, such as heavier A cations like Lu vibrating at lower frequencies than much lighter cations like Ca, more subtle differences can also be observed. Among the "$LuMnO_3$"-type compounds, for example, Y cations are associated with visibly higher vibrational frequencies compared to Ho and Lu, in accordance with the lower ΔS_{vib} of $YMnO_3$ compared to $LuMnO_3$ $HoMnO_3$. This feature can also be noticed when comparing the integrated Δ DOS of the 3 compounds (see Fig S3) in the 0-3 THz range, where $LuMnO_3$ and $HoMnO_3$ have an almost identical trend, with an initial growth starting at lower frequencies than $YMnO_3$.

Having discussed general aspects of the correlation between ΔS_{vib}^{atom} and $\Delta < \omega^{atom} >$), we now concentrate on the individual contributions from different atom types in each structure. On the whole, we again recognize the cations neighboring the vacancy, and the O atoms bonded to them, as the ones associated with the most sizeable per-atom contributions to ΔS_{vib}. However, differences between B and A cations within the same compound, and between compounds, are evident.

Focusing first the B-site cations, we observe a lengthening of the majority of B-O bonds of the B cations neighboring the O vacancy, consistent with the localization of charge on such cations upon vacancy formation. The significant frequency redshift (and consequent positive contribution to ΔS_{vib}) observed for the B atoms neighboring V_O is therefore not only related to the breaking of their bond to the oxygen atom that becomes vacant, but also to the softening of many of their bonds to the other neighboring O atoms. Larger ΔS_{vib}^{atom} and $\Delta < \omega^{atom} >$ are associated with a larger change in the cation's magnetic moment, consistent with a larger change in the charge localized on the atom

upon vacancy formation. $LaFeO_3$, $YFeO_3$, Ca_2TiMnO_6, Sr_2TiMnO_6 and $Lu_2Mn_2O_7$, which exhibit the largest contribution from B cations neighboring the vacancy, all display changes in the magnetic moment by $\sim$0.6-0.7μ_B on each "B NN" Fe or Mn cation, while the magnetic moment of two Mn atoms neighboring the vacancy in $LaMnO_3$ and $CaMnO_3$ changes by an average $\sim 0.3\mu_B$. Similarly, while the Mn atoms neighboring the vacancy in $YMnO_3$ and $HoMnO_3$ display a change in magnetic moment of around $\sim 0.1\mu_B$, in $LuMnO_3$, two of the three Mn atomic neighboring the vacancy (the ones with the largest visible frequency redshift) change by about $\sim 0.4\ \mu_B$. Furthermore, the only large per-atom contribution to ΔS_{vib} associated with a cation not neighboring the O vacancy can be observed in double perovskite oxides, and corresponds to the second Mn cation where the majority of the charge localizes upon vacancy formation (the first Mn cation where charge localizes being the one neighboring the vacancy). The large decrease in the average vibrational frequency of this second Mn cation can once again be traced back to the lengthening of the bonds to its neighboring O anions resulting from the additional negative charge localized on it. On the opposite end to what just observed, the absence of significant charge localizing on the Ti cation neighboring the vacancy in the two double perovskite oxides can be related to its ΔS_{vib}^{atom} contribution opposing that of the Mn atom neighboring the vacancy. Despite the breaking of the bond between the Ti atom and the oxygen becoming vacant, the shortening of the remaining Ti-O bonds appears to result in a dominant negative contribution ΔS_{vib}, and blueshift of the average vibrational frequency associated with the Ti atom.

Differently from the B cations described above, no sizeable change in the charge localized on the A cations neighboring the vacancy is observed upon V_O formation. While still experiencing bond breaking, the change in length of the remaining A-O bonds varies in sign, resulting often in smaller "A NN" ΔS_{vib}^{atom} values compared to the ones associated with "B NN". The compounds for which the most sizeable "A NN" contributions can be observed are the 3 "$LuMnO_3$"-type oxides, and the pyrochlore oxide. In the first case, the breaking of the bond between the oxygen becoming vacant and its closest A cation results in a shift of such cation in the opposite direction to the previously occupied O site. Such shift is accompanied by a mixed shortening and lengthening of the remaining

A-O bonds, with the bonds becoming longer, however, coinciding with the ones associated with longitudinal force constants of greater magnitude, an observation in line with the overall positive contribution to ΔS_{vib}. In pyrochlore $Lu_2Mn_2O_7$, on the other hand, upon the breaking of the Lu-O bond of the two Lu atoms nearest to V_O, a shortening of the remaining Lu-O bonds be observed across the board, resulting in an overall negative contribution to ΔS_{vib}.

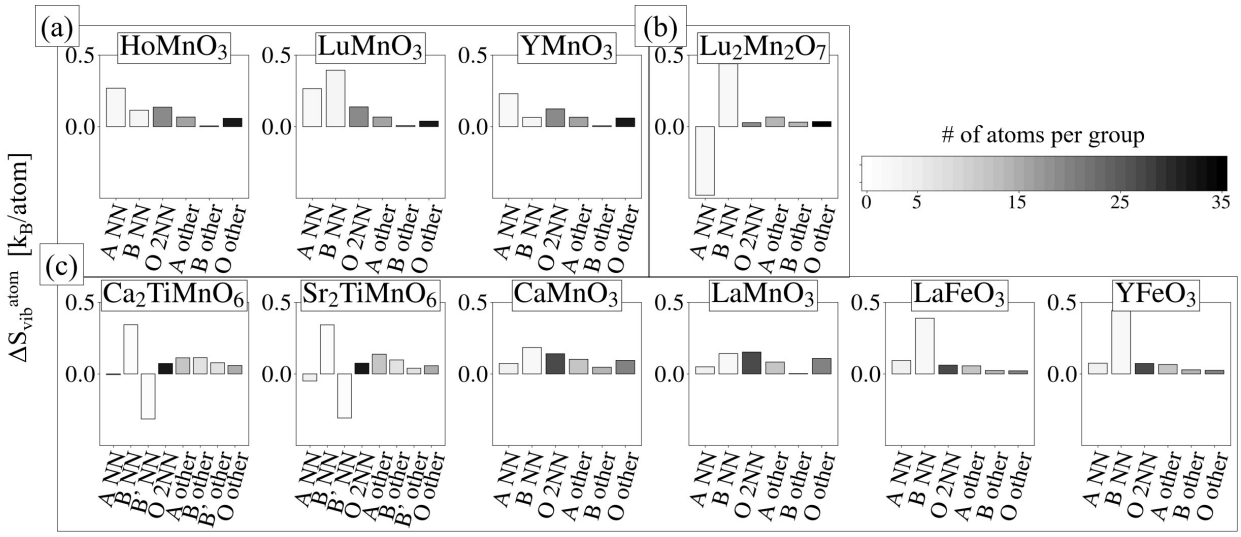

Figure 6.34: Per-atom contribution to the solid state vibrational entropy of O vacancy formation in: (a) "$LuMnO_3$"-type, (b) pyrochlore, and (c) perovskite structures. Atoms are divided in 6 groups (8 groups for double perovskites): (i) the A cations neighboring the O vacancy site, referred to as "A NN" (ii) the B cations neighboring the O vacancy site, referred to as "B NN" (and, for double perovskites, (ii.i) the B' cations for neighboring the O vacancy site, referred to as "B' NN", where "B" indicates Mn and "B'" indicates Ti) (iii) the O cations bonded to the A and B cations neighboring the vacancy, referred to as "O 2NN" (iv) all other A cations, referred to as "A other", (v) all other B cations, referred to as "B other" (and, for double perovskites, (v.i) all other B' cations, referred to as "B' other"), and (vi) all other O cations, referred to as "O other". Histograms colors indicate the number of atoms in each group (darker colors indicating more atoms)

6.3.3 Influence of Hubbard U on the Vibrational Entropy

DFT calculations of metal oxides containing 3d transition metals, like the ones studied in this work, suffer from an over-delocalization of electrons brought about by the residual self-interaction present in exchange-correlation functionals. The addition of a Hubbard-like term to the energy functional[42,36,37,38,39],[40] which carries a very limited additional computational cost, is a widely employed strategy to address this issue, and the one utilized in the present work. The value of

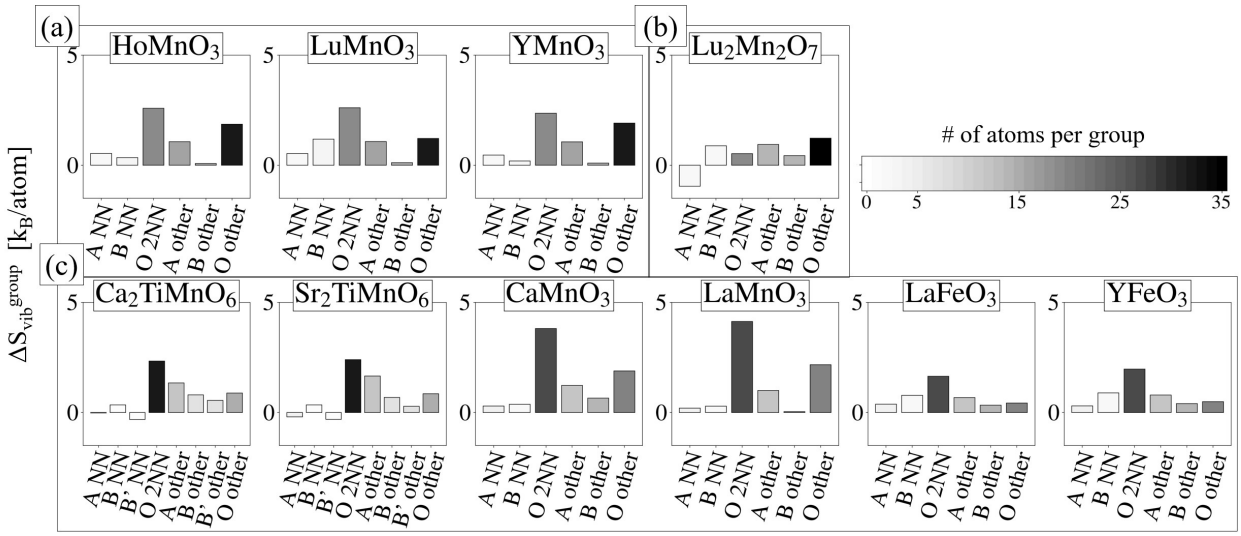

Figure 6.35: Contributions to the solid state vibrational entropy of O vacancy formation in: (a) "$LuMnO_3$"-type, (b) pyrochlore, and (c) perovskite structures. Atoms are divided in 6 groups (8 groups for double perovskites): (i) the A cations neighboring the O vacancy site, referred to as "A NN" (ii) the B cations neighboring the O vacancy site, referred to as "B NN" (and, for double perovskites, (ii.i) the B' cations for neighboring the O vacancy site, referred to as "B' NN", where "B" indicates Mn and "B'" indicates Ti) (iii) the O cations bonded to the A and B cations neighboring the vacancy, referred to as "O NN2" (iv) all other A cations, referred to as "A other", (v) all other B cations, referred to as "B other" (and, for double perovskites, (v.i) all other B' cations, referred to as "B' other"), and (vi) all other O cations, referred to as "O other". Histograms colors indicate the number of atoms in each group (darker colors indicating more atoms)

the U parameter contained in the Hubbard term can have sizeable effects on different properties, and optimal values vary with the transition metal of interest and with the local environment it is immersed in.[47]

We here investigate the influence of different U values on the vibrational entropy of vacancy formation of different compounds. Given the significant computational expense involved in each ΔS_{vib} calculation, we perform this investigation for a subset of the compounds, spanning different structures, and different identities and oxidation states of the 3d transition metal B cations. As shown in Figure 6.38, the largest change in vibrational entropy with U value can be observed for $YMnO_3$, with Ca_2TiMnO_6 and $LaFeO_3$ displaying small to negligible differences between U values. Examining the individual atomic contributions to the vibrational entropy of defect formation (see Fig S4), it appears that for $YMnO_3$, a decrease in U value leads to lower contributions across the board, while Ca_2TiMnO_6 and $LaFeO_3$ display very little response to changes in U on all atomic

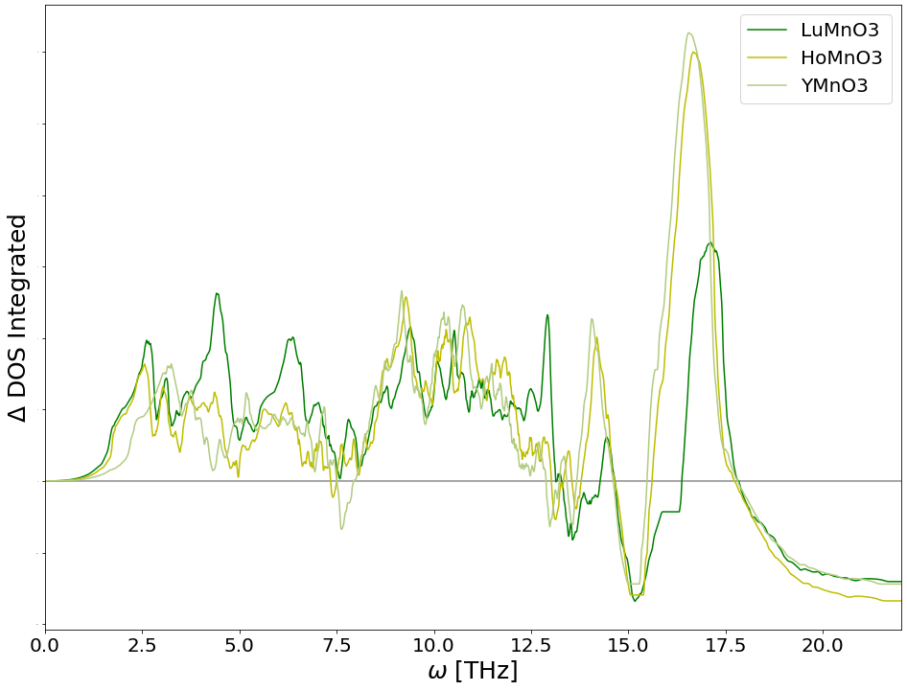

Figure 6.36: Integrated difference in the density of states between vacancy-containing and pristine cells of $LuMnO_3$, $HoMnO_3$ and $YMnO_3$

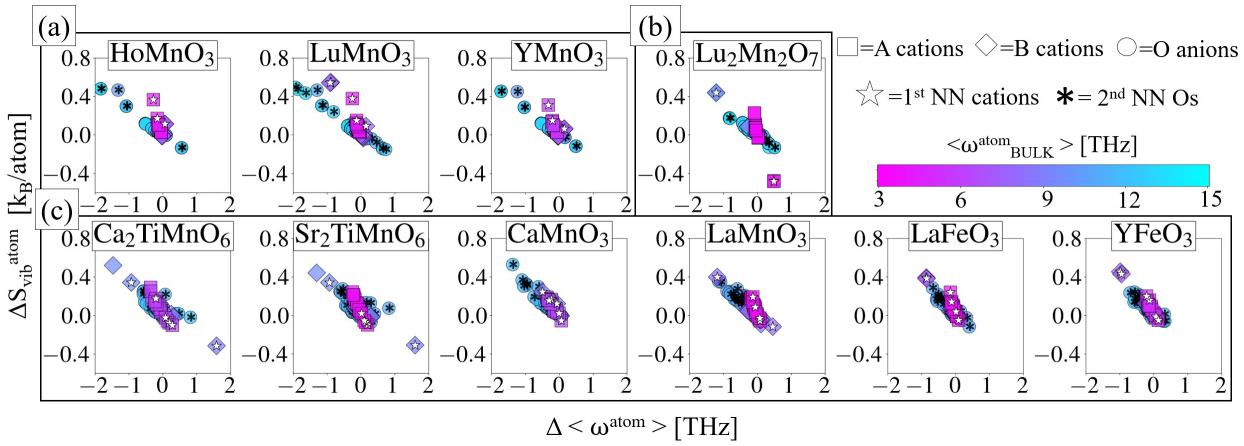

Figure 6.37: Per-atom contribution to the solid state vibrational entropy of O vacancy formation in: (a) "$LuMnO_3$"-type, (b) pyrochlore, and (c) perovskite structures, as a function of change in average vibrational frequency of each atom upon vacancy formation. Each datapoint represents a single atom in the compound, color-coded based on the average vibrational frequency of the atom of interest in the pristine structure ("$< \omega^{atom}_{BULK} >$"). The marker shapes distinguish A cations (squares), B cations (diamonds), and O anions (circles), with a superimposed star to mark the A and B cations neighboring the vacancy (those referred to as "A NN", "B NN" and "B' NN" in Figure 6.34), and a superimposed asterisk to mark the O anions bonded to the cations neighboring the vacancy (those referred to as "O 2NN" in Figure 6.34).

contributions.

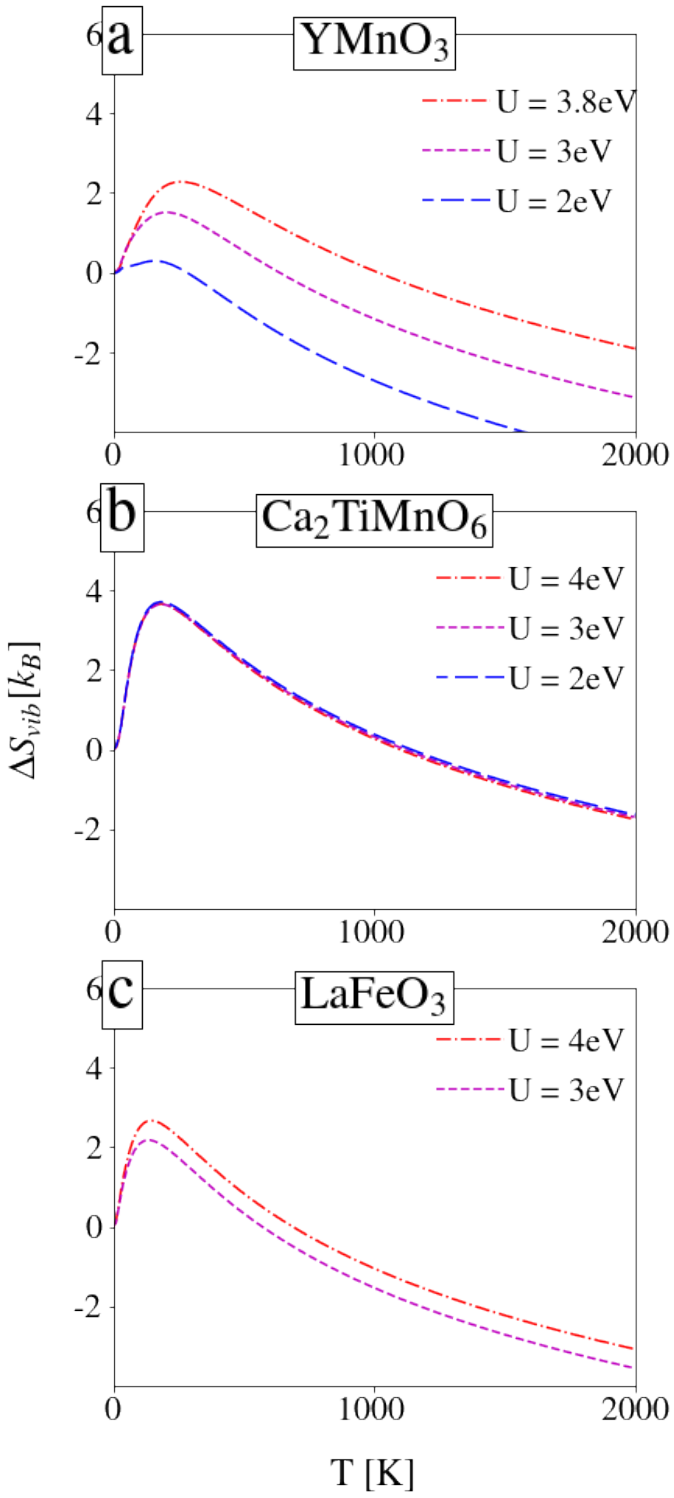

Figure 6.38: Change in solid state vibrational entropy with temperature for different Hubbard U values for (a) $YMnO_3$, (b) Ca_2TiMnO_3 and (c)$LaFeO_3$

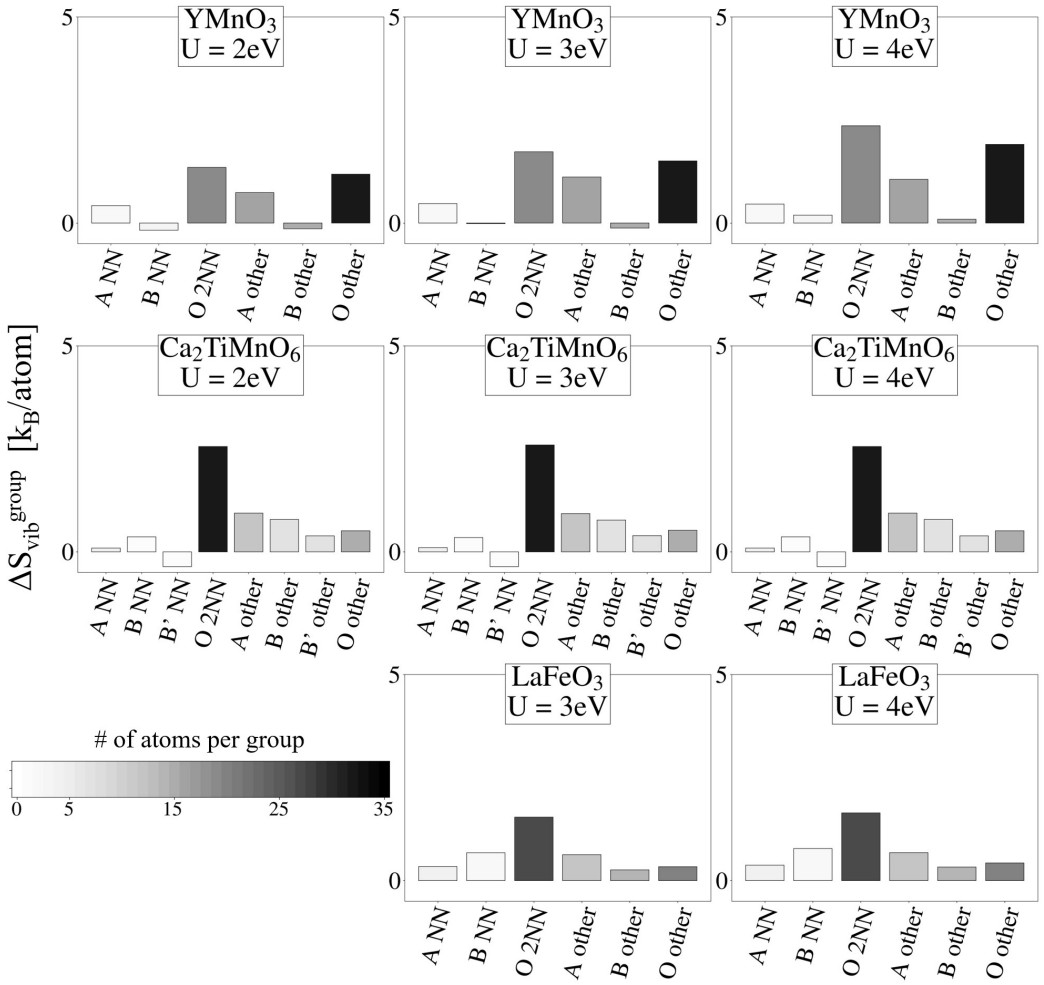

Figure 6.39: Contributions to the solid state vibrational entropy of O vacancy formation in $YMnO_3$, Ca_2TiMnO_6 and $LaFeO_3$ for different values of the Hubbard U parameter. Atoms are divided in 6 groups (8 groups for double perovskites): (i) the A cations neighboring the O vacancy site, referred to as "A NN" (ii) the B cations neighboring the O vacancy site, referred to as "B NN" (and, for Ca_2TiMnO_6 , (ii.i) the B' cations for neighboring the O vacancy site, referred to as "B' NN", where "B" indicates Mn and "B'" indicates Ti) (iii) the O cations bonded to the A and B cations neighboring the vacancy, referred to as "O NN2" (iv) all other A cations, referred to as "A other", (v) all other B cations, referred to as "B other" (and, for Ca_2TiMnO_6 , (v.i) all other B' cations, referred to as "B' other"), and (vi) all other O cations, referred to as "O other". Histograms colors indicate the number of atoms in each group (darker colors indicating more atoms)

6.3.4 Total Entropy of O Vacancy Formation

Having examined the change in solid state vibrational entropy upon vacancy formation in the previous sections, we now discuss other sources of entropy playing a significant role in the total entropy

of vacancy formation. As mentioned in Section , ΔS_{vib} only includes vibrational contributions from the metal oxide itself, and does not account for the final gaseous state of the oxygen being lost by the metal oxide. Therefore, the oxygen gas entropy is the first contribution we discuss in the present section. Furthermore, the multiplicity of sites upon which defects can be introduced results in an additional, defect concentration-dependent, contribution to the total entropy, in the form of configurational entropy.

The oxygen gas entropy can be accounted for as half of the gas entropy of the O_2 molecules, and can be extracted from tabulated standard values.[147] Figure 6.40 displays the derived non-configurational entropy of O vacancy formation, computed by combining the gas entropy and the solid state vibrational entropy contributions. In all cases, in addition to the visible dominance of the gas entropy contribution, the temperature dependences of ΔS_{vib} and $\Delta S(O_2)$ can also be observed to counterbalance each other, leading to an almost constant value of the non-configurational entropy above room temperature.

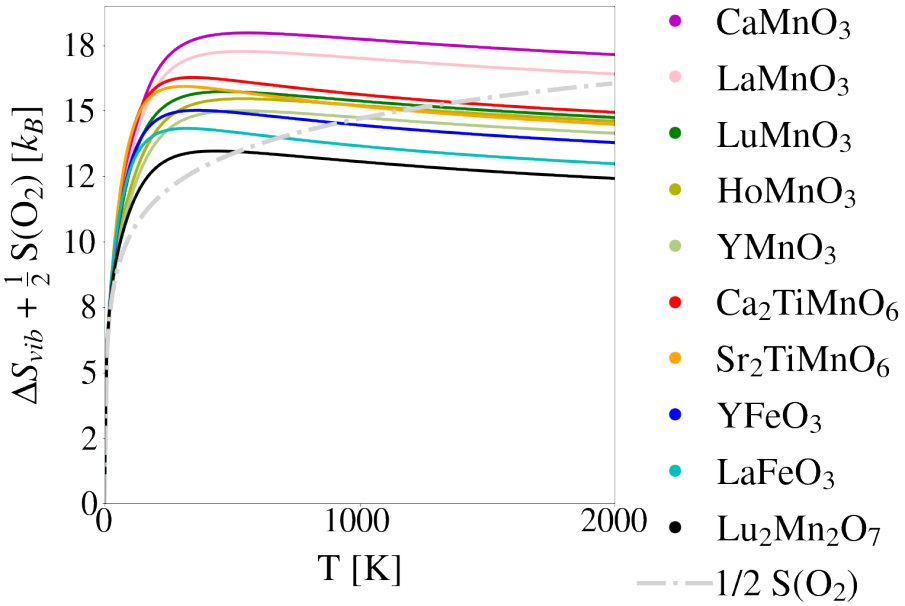

Figure 6.40: Sum of the solid state vibrational entropy of O vacancy formation (ΔS_{vib}), and the gas entropy of oxygen (1/2 $S(O_2)$) as a function of temperature for the compounds investigated in Sections 6.3.1 and 6.3.2

The configurational entropy associated with the formation of oxygen vacancies can be computed analytically assuming dilute solution behaviour. In this case, the per-vacancy contribution is a

function of the non-stoichiometry δ, which varies depending on the the available sites, and, if relevant, on the energy difference between them. For the compounds included in this study, and for nonstoichiometry values between $\delta = 0.01$ and $\delta = 0.1$, this results in values ranging between ~ 3 k_B and ~ 6 k_B. In addition to multiplicity of configurations associated with the oxygen vacancy, a similar reasoning can be applied to the cations undergoing reduction, with again configurational entropy values depending on possible sites (eg. for the compounds in this study, sites on the A sublattice are not included as they do not show evidence of reduction, but reduction on both the A and B sublattices can be observed in other cases[70]). Considering all B sites, aside from the ones occupied by Ti atoms in double perovskites, for nonstoichiometry values between $\delta = 0.01$ and $\delta = 0.1$, this additional entropy contribution varies between ~ 1 k_B and ~ 8 $k_B$for the compounds in this study. It should be however noted that that deviations from ideal values of the configurational entropy can often be observed as a results of phenomena like interactions between defects.[142]

Entropies of reduction for a number of the compounds investigated in this work were reported in recent experimental studies by Qian et al.[7911311499] and Mastronardo et al.[98] Comparison between computational results and experimental data is however complicated by multiple factors. Firstly, the three "$LuMnO_3$"-type compounds displayed evidence of a phase transition to a (dynamically unstable at 0K) "Be_3N_2"-type structure, with a jump in the extracted thermodynamic quantities of reduction the mechanisms behind which remain ambiguous[79] . $LaMnO_3$ was synthesizes in an rhombohedral perovskite structure (rather than the orhtorhombic DFT ground state), dynamically unstable at 0K. Both $CaMnO_3$ and Ca_2TiMnO_6 were also observed to undergo a phase transition, in this case to the cubic perovksite phase (again dynamically unstable at 0K), leaving only a small range of values for which oxygen loss was measured from the ground state distorted perovskite structure. Furthermore, cation disorder on the B lattice was experimentally observed in both Ca_2TiMnO_6 and Sr_2TiMnO_6. Finally, $YFeO_3$ displayed very limited oxygen loss, impacting the accuracy of the extracted entropy and enthalpy of reduction. In addition to the just mentioned complications, the experimental uncertainties of 0.5-2.5 k_B are comparable in magnitude to differences between compounds in our calculated vibrational entropies, and the impact of potential deviations from

the ideal configurational entropy represent an additional source of uncertainty in the total entropy calculation. Overall, we refrain from reporting a detailed comparison between calculations and experimental results as we believe it would not provide substantial evidence either supporting or refuting the predictive accuracy of the vibrational entropy calculations reported in this work.

7. Oxygen Stability in Disordered Rock Salt Lithium Transition Metal Oxides

7.1 Background

Disordered rock salt (DRX) lithium transition metal oxide materials are attracting growing interest as new cathode materials for Li-ion batteries due to multiple attractive properties. Cation disorder can result in small volume changes during charge and discharge limiting structural degradation upon cycling, and, in the presence of lithium excess, lithium diffusion through percolating low barrier channels can be activated, and anionic redox can be leveraged for increased capacity.[15,17–19] Without the limits of traditional ordered cathodes, the large compositional space of transition metal cations can be explored to both increase performance and to circumvent resource-related issues concerning commonly employed metals like cobalt.[16]

In an exceptionally wide ranging work, Liu et al.[148] recently surveyed thousands of candidate DRX compounds. The DFT stability of special quasi-random (SQS) representations of DRX structures, as well as the most common rock salt type $LiMO_2$ structures, was directly computed and utilized as a first filter for candidate materials. Short range order preferences were then estimated, and compounds were further ranked based on evaluations of their average voltage and capacity.

While capacity and voltage are primary aspects of cathode selection, oxygen stability can play an

important role. Oxygen loss can be a safety concern, promote phase transitions to spinel structures in layered materials with an adverse effect on voltage, and lead to transition metal reduction and rearrangement thereby impacting capacity and structural stability[20,21]. The ability to evaluate oxygen stability on a computational level is therefore an aspect of interest for material selection.

Despite their many advantages, lithium excess disordered rock salt structures present several complexities that directly affect oxygen bonding and complicate the understanding of the mechanisms governing oxygen stability. The presence of disorder favours for example the occurrence of a variety of different oxidation states for the transition metal cations in a way which can be non-trivial to determine, and, as noted in previous chapters, can have a large impact on oxygen vacancy formation energy. Disorder also leads to differing numbers and configurations of Li cations neighboring the oxygen sites, which can effect the energetics of the O bands and thereby the ease of oxygen removal.[18] Furthermore, the introduction of Li-excess and the onset of delithiation are accompanied by changes in the oxidation states of the transition metal cations, once again modifying the energetics of oxygen vacancy formation. In order to be able to utilize oxygen stability as screening criterion for candidate materials, a deeper understating of all the above behaviours is desired.

In this chapter, we discuss a selected portion of ongoing work in understanding and predicting oxygen stability across a variety of DRX candidate materials.

7.2 Methodology

All calculations have been conducted using the Vienna ab-initio simulation package (VASP),[75,76] with projector augmented wave (PAW) potentials[77] and the Perdew-Burke-Ernzehof (PBE)[78] generalized gradient approximation (GGA) for the exchange-correlation functional. A gamma centered *k*-point grid with a density of at least 8600 points per reciprocal atom was employed, alongside and a plane wave cutoff energy of 520 eV. Self consistency was achieved when energies of subsequent iterations differed by less than 10^{-6} eV/cell, and ionic relaxation was performed until

forces were found to be below 0.01 eV/Å. The over-delocalization of electrons due to the residual self interaction present in exchange-correlation functionals[36–40] was treated through the addition of a Hubbard-like potential to the energy functional[42] (DFT+U), with the same U values employed in the OQMD[43,44] and a spin polarization with a ferromagnetic configuration was applied to transition metal cations.

7.3 Results

Given the previously mentioned complexities of lithium rich DRX systems, in order to deconstruct the mechanisms involved in oxygen vacancy formation, we examine multiple different structural configurations, and investigate differences in cation valence and arrangement and their impact on oxygen loss. In this analysis we focus on one exemplary material composition, while also providing wider ranging observations and insights from the ongoing study of several other candidate materials throughout the discussion .

We start by examining the layered structure of the exemplary material, which presents multiple characteristics facilitating its analysis, such as the transition metal cation elements appearing to have the same oxidation state throughout the structure. Examining the oxygen vacancy formation energy of all oxygen sites in the compound, we obseve in all cases values consistent in both relative and absolute magnitude with the ease of reduction of the cations in the structure determined in Section 4.3, 3.3 and 5.3. Oxygen sites with a larger number of harder to reduce cation neighbors also display larger vacancy formation energy, and, upon analyzing the change in atomic magnetic moments upon vacancy formation, charge appears to localize on all three of the transition metal cations neighboring the vacancy. Similar behaviours have also been recognized in the layered structures of other candidate compounds, with in several cases additional complexities being present as a consequence of cations in different sites across the structures having different oxidation states, and resulting in greater variations in the oxygen vacancy formation energy.

In Figure 7.41 we then examine the oxygen vacancy formation energies of all oxygen sites in the

disordered rock salt structure. Differently from the layered structure, O sites differ in the number of Li nearest neighbors (NN), which appear to have a primary effect on the vacancy formation energy. The larger the number of lithium cations neighboring the oxygen atom, the closer the center of its p band is to the Fermi energy, consequently lowering the energetic cost involved in the formation of a vacancy. This trend is consistent with previous observations of lithium bonding arrangement leading to large changes p band energy, and thereby ease of oxygen removal.[18] Such a trend was also observed in all other DRX compounds under examination in the broader scope of this work, with an average Pearson correlation coefficient between ΔE_{vf} and $E_{Op}^{site} + E_g$ of ~ 0.85, and, in all cases, the easiest to remove oxygen always having 5 Li nearest neighbors. A very strong correlation can also be identified between ΔE_{vf} and the electrostatic energy difference between the pristine and vacancy containing structure calculated with nominal charges, therefore establishing two powerful descriptors of vacancy formation energy in DRX structures. Examining atomic magnetic moments, we observe once again charge localizing on the cations neighboring the vacancy. Differently from the layered structure, however, evidence of one of the cations having a larger oxidation state (which is for many transition metal cations associated with a greater ease of reduction) can be observed, with charge localizing on such cation upon vacancy formation even in cases in which it does not neighbor the vacant site. For the sites having 5 Li nearest neighbors, for example, the charge can be seen to localize on the only NN transition metal cation and on the aforementioned higher oxidation state cation upon vacancy formation in all cases.

Since the SQS structures employed in the high-throughput DFT screening lack the presence of oxygen sites having 6 neighboring Li cations, a type of environment very likely to be present in real DRX compounds, we study a modification of such structures where a pair of Li-TM cations are swapped so as to manufacture a local 6 Li NN environment while retaining charge balance with the same oxidation states of the cations. As can be seen in Figure 7.42, the p band of the site with 6 Li NNs lies closer to the Fermi energy compared to all other sites, requiring less energy to form a vacancy, in agreement with the general trends previously identified. Examination of atomic magnetic moments reveals the charge to localize on the easiest to reduce TM cations upon vacancy

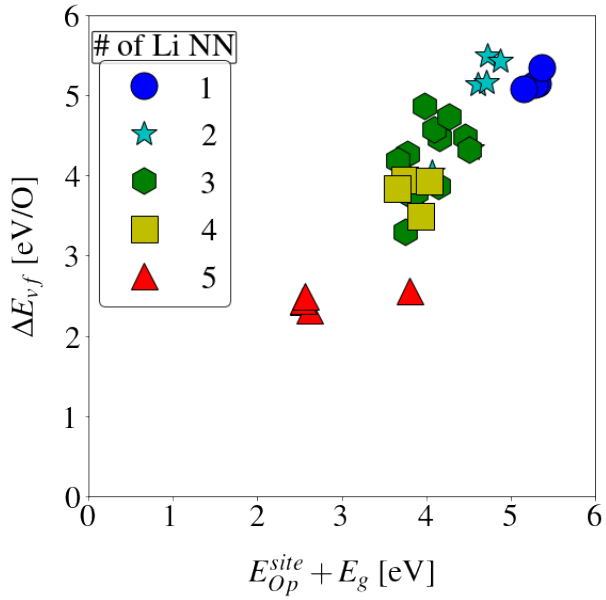

Figure 7.41: Oxygen vacancy formation energy of different sites in the exemplary DRX material's structure as a function of the energy difference between the average energy of the oxygen p band of the site becoming vacant. Different markers indicate different number of Li cations neighboring the vacancy

formation.

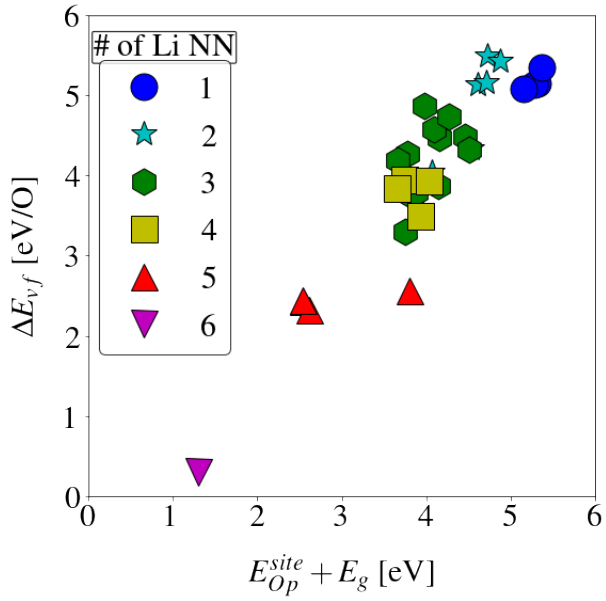

Figure 7.42: Oxygen vacancy formation energy of different sites in the exemplary DRX material's structure as a function of the energy difference between the average energy of the oxygen p band of the site becoming vacant. Different markers indicate different number of Li cations neighboring the vacancy

Finally, we examine the more complex cases brought about by lithium excess and delithiation. In Figure 7.43 we compare the oxygen vacancy formation energy of the exemplary DRX material's structure (a) in the absence of lithium excess or delithiation, (b) in the presence of 20 % Li-excess, (c) with Li-excess and a vacant Li site. In all cases the strong correlation between ΔE_{vf} and the number of Li NNs, as well as the energy of the oxygen p band, can be observed to hold. Furthermore, the formation of lithium vacancies appears to additionally weaken the binding of some of the oxygen atoms, primarily the ones neighboring the Li vacancy itself.

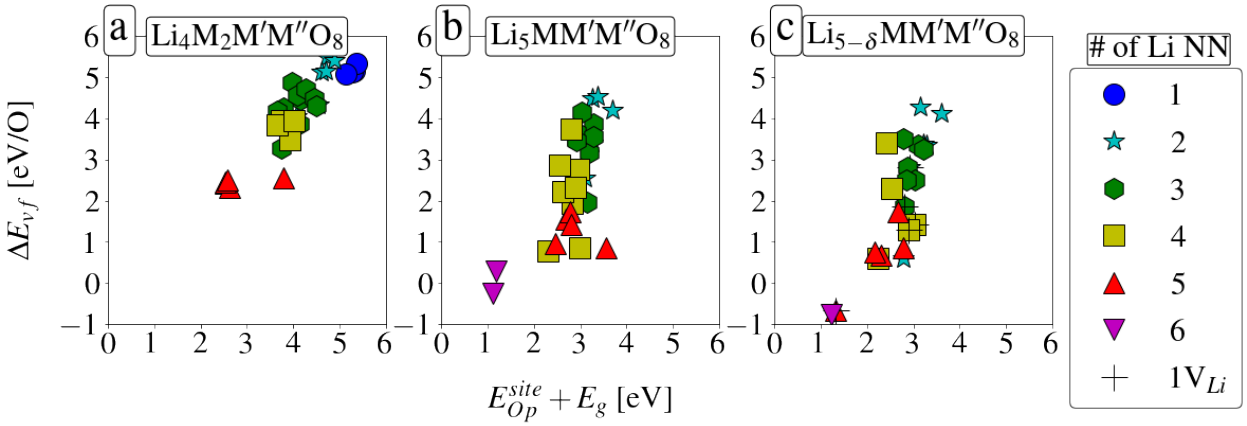

Figure 7.43: Oxygen vacancy formation energy of different sites in (a) the DRX structure (b) the Li-excess DRX structure, and (c) Li-excess DRX structure with a Li vacancy, as a function of the energy difference between the average energy of the oxygen p band of the site becoming vacant. Different markers indicate different number of Li cations neighboring the vacancy, the plus sign in (c) indicating the O atoms neighboring the Li vacancy

Overall strong predictors of relative trends in oxygen vacancy formation energy between different sites in the same DRX compounds have been identified, drastically reducing the number of calculations required to estimate the lower bound to ΔE_{vf} in each compound. Comparisons between different compounds, on the other hand, still present complexities, such as variations in oxidation states across transition metal cation sites. Machine learning models targeting the prediction of ΔE_{vf} across compounds are being developed, considering a variety of features aiming to capture the different bonding environment of O across the structures.

8. Surface Segregation Energies of Transition and Post-Transition Metals

8.1 Background

Surface composition plays a fundamental role in determining a system's reactivity. The introduction of a solute specie on the surface a host system can favourably modify catalytic activity and selectivity, as seen for example by Kyriakou et al.[149] upon doping of Pd on Cu 111. It can also help reduce adverse effects such as CO poisoning through the decrease of CO binding strength, as reported by Liu et al.[150] when introducing Pt on a Cu 111 surface. The presence of different species underneath the surface of a catalyst metal can also significantly affect reaction energies and mechanisms, as for instance observed by Duan et al.[151] upon examination of the addition of different transition metal sub-layers to Pt 111 surface slabs. For a specific bulk composition, the concentration of species at the surface can be tuned to enhance catalytic performance, as demonstrated by Suntivich et al.[152] with Pt-Au nanoparticles. Surface segregation, in which an alloy component migrates from the bulk to the surface layer, can therefore be crucial for promoting or suppressing chemical reactions.

In order to evaluate the segregation behavior of different solute-host combinations, surface segregation energies ($\Delta E_{segregation}$) can be examined on a computational level, and have been the subject of multiple works in the literature.[153–161] Particularly influential and large scale studies were conducted by Ruban et al[153] and Nilekar et al.,[154] wherein the dilute surface segregation energies of a 24 by 24 matrix of transition metal solute-host pairs were calculated. Such works utilized the

linear muffin tin orbital method, the atomic sphere approximation, the local density approximation for the exchange correlation energy, and lacked the inclusion of the effect of the relaxation of atomic positions. The investigation of the impact of such approximations on calculation results is then of interest to determine the accuracy of the reported $\Delta E_{segregation}$ values.

Transition metals have been at the center of numerous works studying catalytic behaviour and surface segregation[151,153–161] . Post transition metal and metalliod elements such as Sn, Te, Tl, Pb and Bi, have also attracted interest for a number of catalytic applications.[162,163] Their segregation behaviour, however, appears to remain less studied, motivating the interest towards the creation of a database similar to the one produced by Ruban et al[153] targeting group XII to XVI elements.

Large scale DFT calculations of surface segregation energies come at a significant computational cost, and the development of models capable of describing segregation behaviour without the need for direct DFT computation is therefore of interest. Multiple efforts in the literature have been directed towards this goal.[155,164–166] Ologunagba and Kattel explored several elemental features in conjunction to gradient boost regression trained on the data produced by Ruban et al.[153] Farsi et. al directly computed segregation energies[155] to different Pt, Ir, Pd, and Rh surfaces and developed a statistical model capable of distinguishing the behaviour of different surfaces. Salem et al.[166] leveraged Farsi's calculations to construct a machine learning model utilizing composition- and bonding-based features. Rao et al.[165] computed the energies of different solute configurations and developed a bound-counting-based model to describe them. Out of the descriptors proposed in the literature, surface energies and atomic radii of the constituting elements display a particularly strong correlation with segregation behaviour,[153] which can be in connected to their role as driving forces of segregation: species with larger radii and smaller surface energies are driven to migrate to the surface. While the computation of surface energies is costly itself, in a recent work, Tran et al.[158] published a database of DFT computed surface energies of over 100 polymorphs of 70 elements, rendering $E_{surface}$ an easily accessible feature to be leveraged in machine learning models.

In this chapter we tackle all of the three above mentioned aspects of surface segregation energy computation, that is: (i) assessment of the influence of various computational choices on the

$\Delta E_{segregation}$ calculations (ii) creation of a database of segregation energies of post-transition metals, and (iii) development of a predictive model.

8.2 Methodology

All DFT calculations have been conducted using the Vienna ab-initio simulation package (VASP),[75,76] with projector augmented wave (PAW) potentials[77] and the Perdew-Burke-Ernzehof (PBE)[78] generalized gradient approximation (GGA) for the exchange-correlation functional. A plane wave cutoff energy of 520 eV was employed, and spin polarization was applied with a ferromagnetic configuration, initializing magnetic moments to $5\mu_B$. Different atomic relaxation schemes were investigated, as detailed in the next section. Surface slabs with a minimum of 7 atomic layers and 10 Åof vacuum were utilized, with larger slab and vacuum thicknesses showing no significant difference in surface segregation energy (see Appendix).

8.3 Results

8.3.1 Accuracy of Surface Segregation Energy Calculations

Upon the introduction of a solute atom, the local environment surrounding it undergoes changes to accommodate it, and the relaxation of atomic positions can have a non-negligible effect on the properties of the system. We therefore start our analysis by examining the effect of such relaxation on the surface segregation energy, differentiating the optimization of multiple degrees of freedom. In Figure 8.44 we display the surface segregation energy of 4d transition metal solutes (25% in-layer concentration) to the 111 surface of a FCC Pt host, and compare the effects of : (i) allowing for partial relaxation by freezing the bottom 3 atomic layers to their bulk lattice position while optimizing the atomic positions in the other layers (green squares), and (ii) allowing for a full relaxation of the slab (cyan crosses: the optimization is stopped when the magnitude of the residual forces on each atom is smaller than 0.01 eV/Å, yellow plus sings: the optimization is stopped

when the total energy of the system changes by less than 10^{-5} eV between each ionic step, as implemented in the OQMD framework). In all cases we see that, as long as the positions of the atoms surrounding the solute are allowed to relax, only very minor changes in $\Delta E_{segregation}$ can be observed between different relaxation schemes. In order to gain further insight on the impact of atomic relaxation, in Figure 8.45 we separately examine the energetic change due to relaxation of the atomic positions upon introduction of the solute atom (i) in a bulk layer (blue triangles) and (ii) in the surface layer (red triangles), also reporting, for comparison, (iii) the difference between the two (magenta diamonds), which equates to the energetic change due to relaxation of the atomic positions upon segregation of the solute to the surface. It can be observed that, while the effect of relaxation is sizeable both at the surface and in the bulk, the two effects largely cancel out when examining surface segregation, resulting in a smaller, although non-negligible, effect on $\Delta E_{segregation}$.

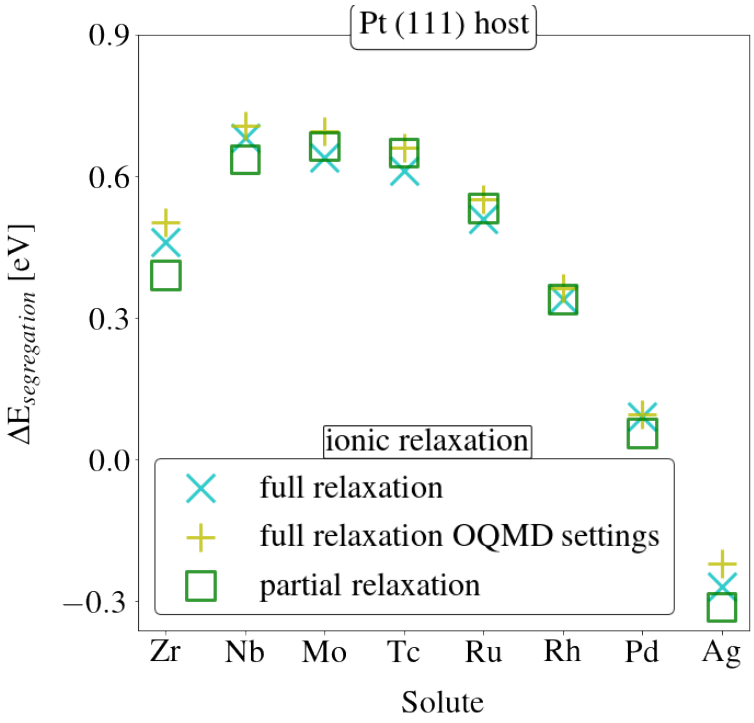

Figure 8.44: Surface segregation energy of transition metal solutes to the 111 surface of FCC Pt, with different markers indicating relaxation schemes for the slab.

Solute atoms can occupy a multiplicity of sites in sub-surface atomic layers, with significant differences in energy as well as on catalytic properties. In the present study, we focus on the

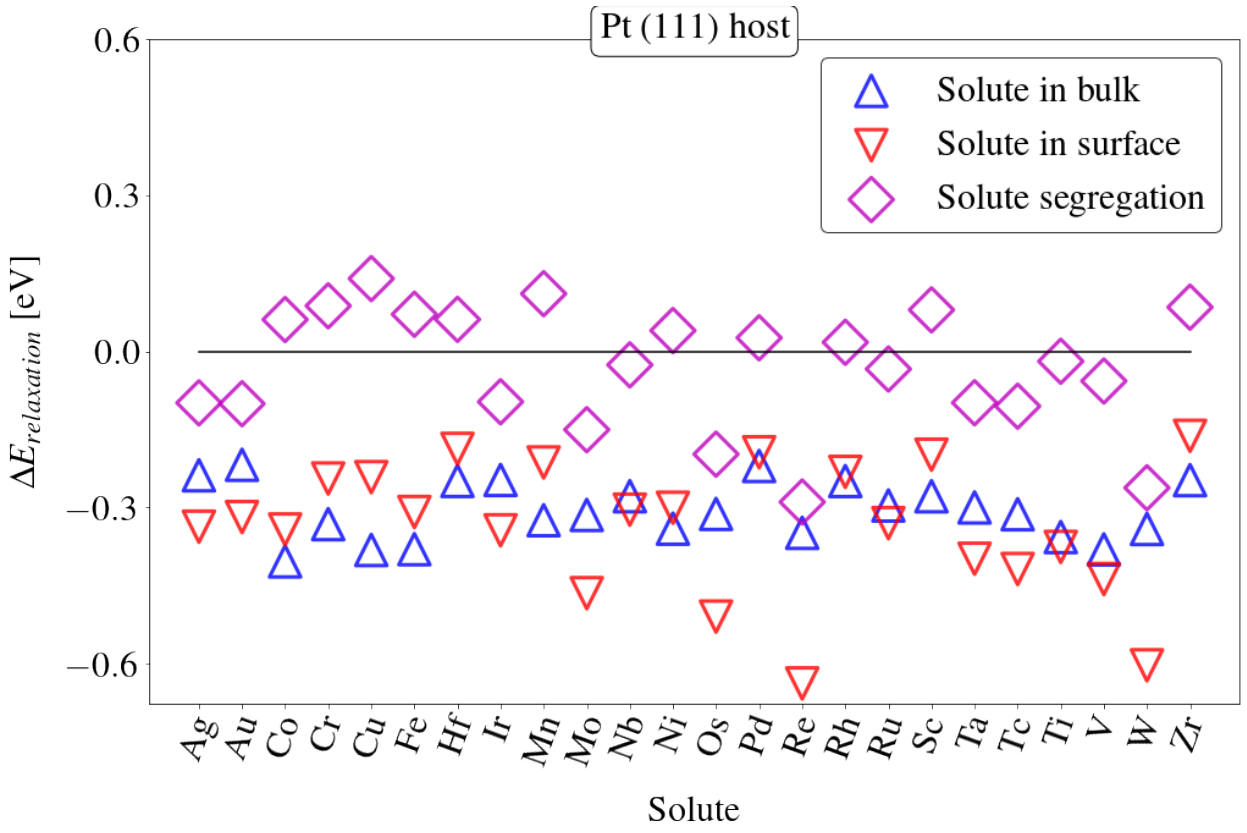

Figure 8.45: Change in energy after allowing the relaxation of atomic positions after the introduction of a solute atom in a Pt slab, red triangles indicate the relaxation energy when the solute is in a bulk layer, blue triangles indicate the relaxation energy when the solute is in the surface layer, and magenta diamonds indicate the difference between the previous two, which also equates to the difference surface segregation energy between a case where atoms are allowed to relax and a case in which they are not.

computation of energetic differences between a solute at the surface and in the bulk, and are therefore interested in the layer representing the bulk to be deep enough for the segregation energy not to change if a deeper layer is utilized instead. In Figure 8.46 we examine $\Delta E_{segregation}$ of transition metal solutes (25 % in-layer concentration) on (a) the 111 surface of FCC Pt, and (b) the 110 surface of BCC Fe, with different depths of the sub-surface layer containing the solute atom. We see that in all cases segregation to the surface from layers beyond the 4^{th} is constant in value.

In order to represent dilute behaviour, the in-layer concentration of solute specie should be small enough for the surface segregation energy to be converged with respect to it. Increase in slab width (needed to achieve more dilute concentrations), however, comes at a significant computational

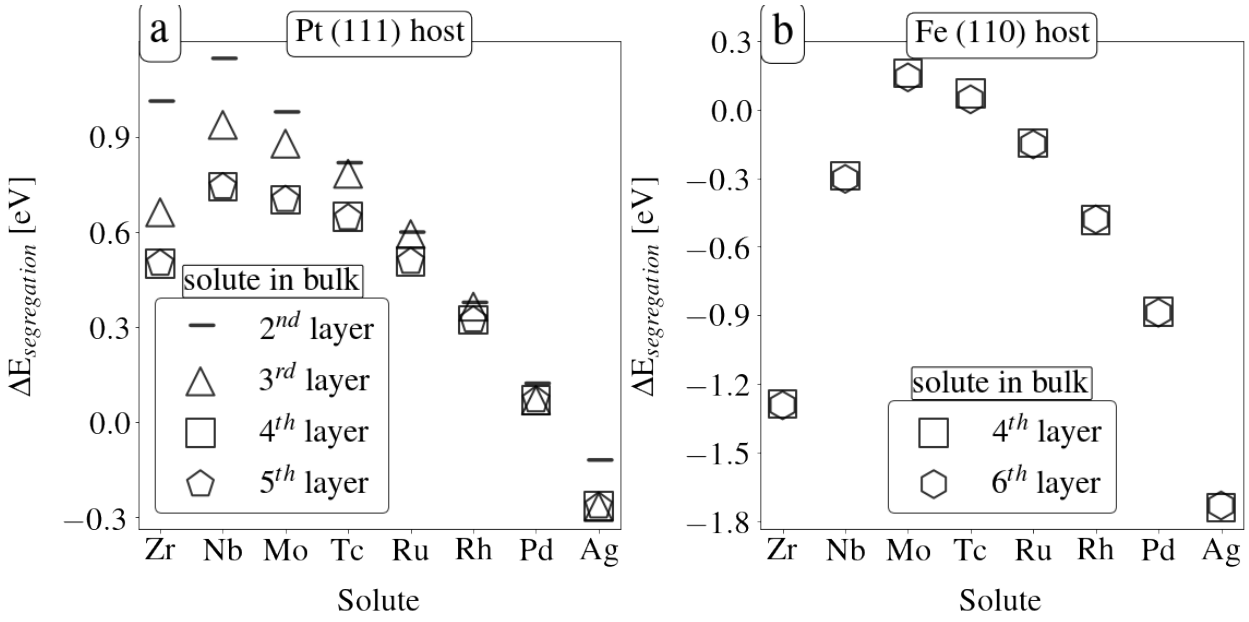

Figure 8.46: Surface segregation energy of transition metal solutes from a sub-surface layer indicated with different markers to the (a) 111 surface of FCC Pt and (b) the 100 surface of BCC Fe.

expense, such that in practice a compromise between dilution and computational efficiency has to be established. In Figure 8.47 and 8.48 we examine the surface segregation energy different concentrations of transition metals solutes in Pt and Fe hosts. In most cases, $\Delta E_{segregation}$ cab be observed to be converged to within ~ 0.1 eV a with a 11% solute concentration (achieved with a 3x3 surface slab).

Having established an adequate representation of dilute behaviour, we now compare our calculations with the ones reported by Ruban et al.[153] In Figure 8.49 and 8.50, it can be seen that the results presented in the work by Ruban et al. are accurate enough to successfully (i) identify trends across transition metal hosts and solutes, (ii) distinguish segregation and anti-segregation behaviour, and (iii) differentiate stronger and weaker (anti)segregation. Despite the existence of non-negligible differences between our DFT results and Ruban's calculations for a number of solute-host pairs, we consider the above evidence sufficient to deem Ruban's results accurate enough not to require to be re-computed.

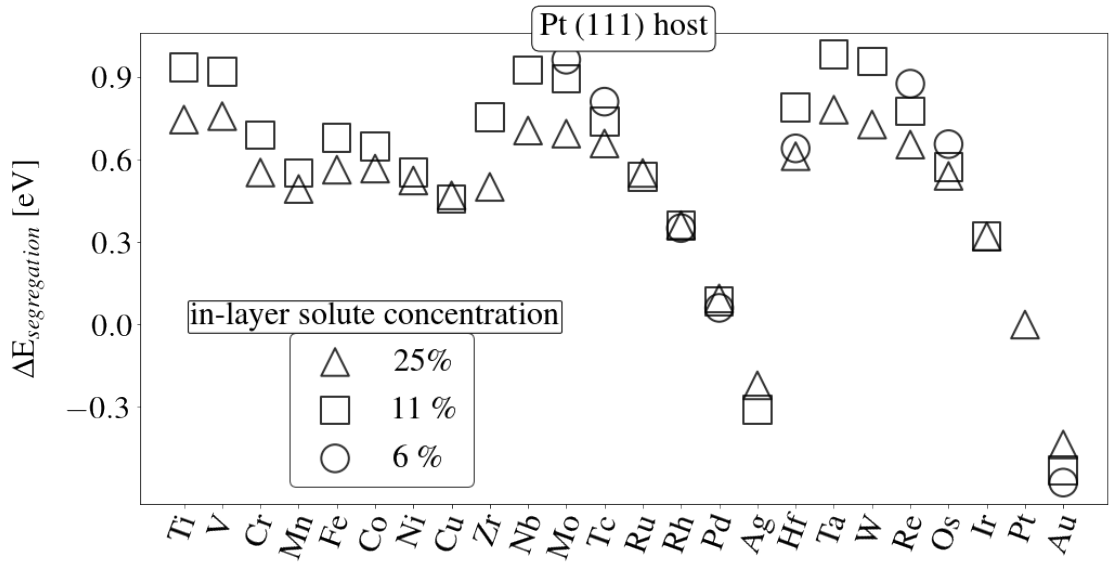

Figure 8.47: Surface segregation energy of transition metal solutes from a sub-surface layer to the 111 surface of FCC Pt, with different markers indicating different in-layer concentrations of the solute.

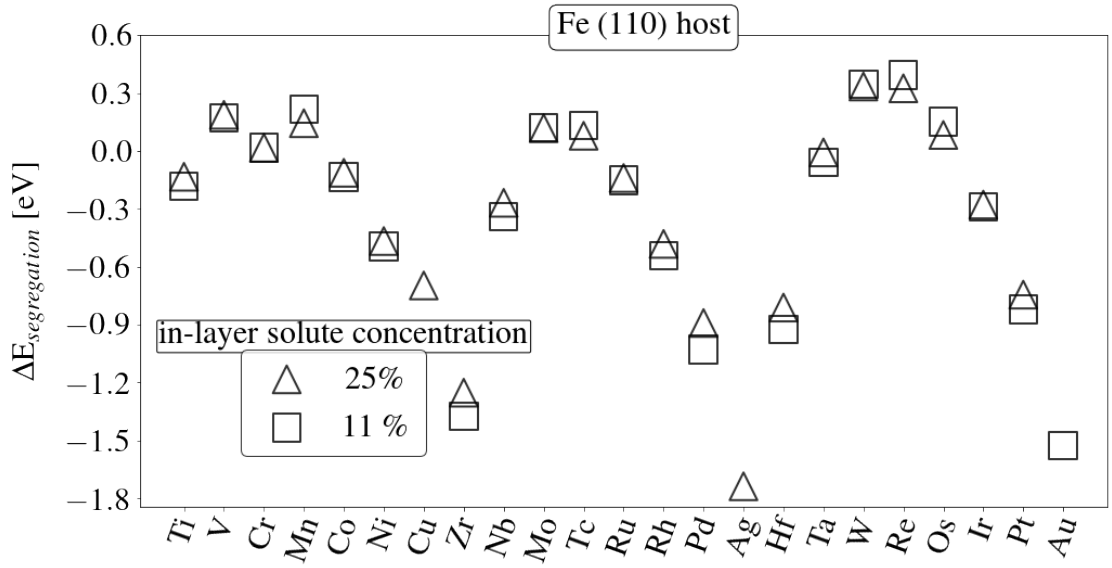

Figure 8.48: Surface segregation energy of transition metal solutes from a sub-surface layer to the 110 surface of BCC Fe, with different markers indicating different in-layer concentrations of the solute.

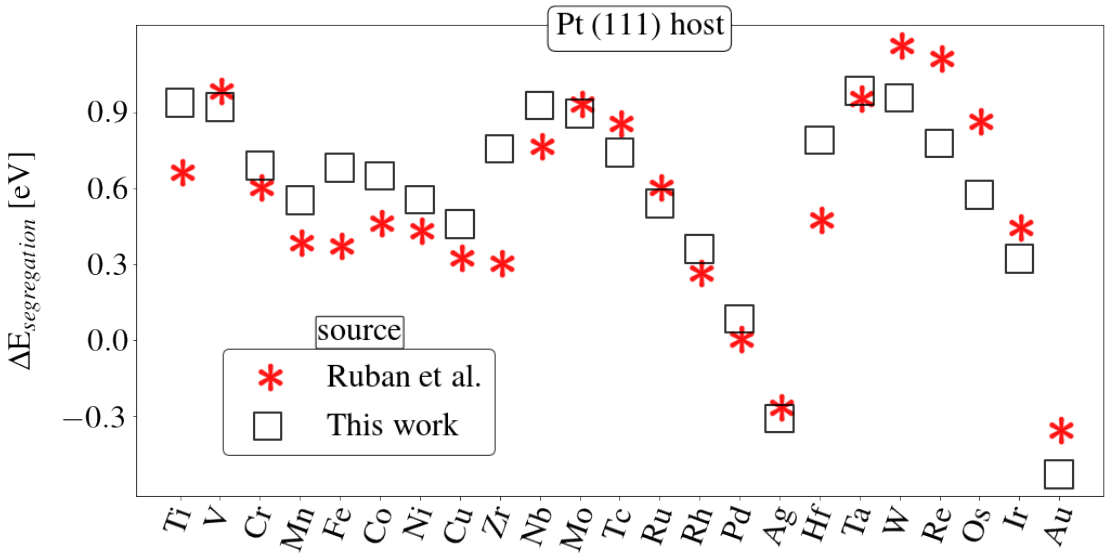

Figure 8.49: Comparison of the surface segregation energy of transition metal solutes from a sub-surface layer to the 111 surface of FCC Pt, as calculated in this work with a 3x3, 7 layer slab, indicated with black squares, and as reported in the work by Ruban et al.,[153] indicated with red stars

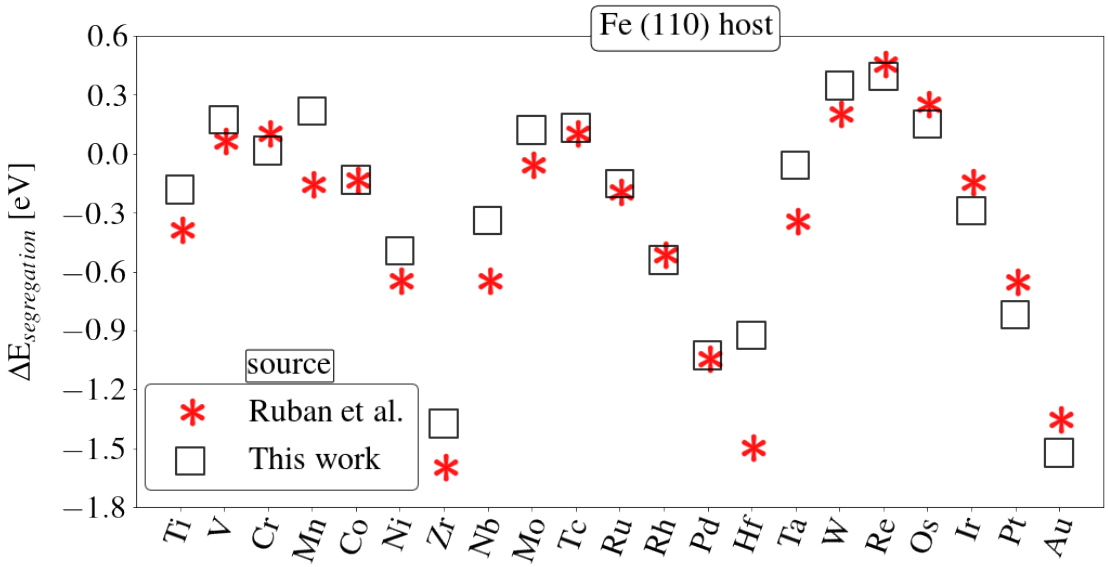

Figure 8.50: Comparison of the surface segregation energy of transition metal solutes from a sub-surface layer to the 110 surface of BCC Fe, as calculated in this work with a 3x3, 7 layer slab, indicated with black squares, and as reported in the work by Ruban et al.,[153] indicated with red stars

8.3.2 High Throughput DFT Calculations of Surface Segregation Energies of Transition Metal Solutes in Post-Transition Metal Hosts

Having positively assessed the reliability of the results presented by Ruban et al.,[153] we take those results a starting point, and expand the database of surface segregation energy to closed packed transition metal surfaces by including post-transition metal and metalloid solutes. We consider the 24 host transition metals investigated by Ruban et al., in combination with 10 group XIII to XVI solutes: Al,Ga,Ge,In,Sn,Sb,Te,Tl and Bi, and construct slabs of a minimum of 7 layers and 10 Åof vacuum, with an 11% in-layer solute concentration. The computed surface segregation energies are displayed in Figure 8.51, with rows being associated with hosts and columns with solutes, and different colors indicating different segregation behaviour (stronger blues for stronger antisegregation, stronger reds for stronger segregation, and lighter colors for more neutral behaviours). In the vast majority of the cases a strong segregating behaviour of the post-transition metal solutes can be observed, in line with their smaller surface energies[158] and larger atomic radii[167] compared to their transition metal hosts. Trends among host transition metals similar to those observed in Ruban's data can also be recognized, with earlier and later transition metal hosts being less prone to solute segregation than group VI to IX transition metals hosts.

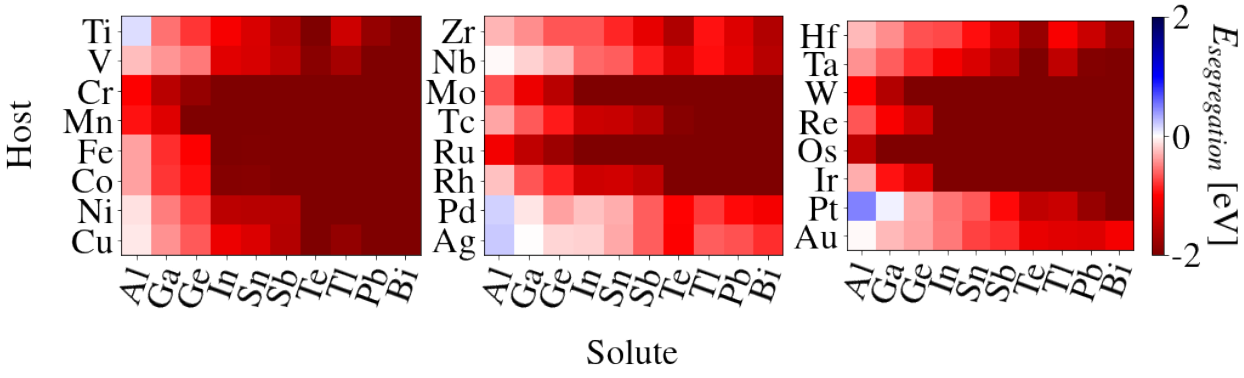

Figure 8.51: Surface segregation energies of post-transition metal solutes in transition metal hosts. The structure of the host is the DFT ground state, and the surface is the lowest energy surface for each structure type. Stronger red colors indicate stronger anti-segregation, and stronger blue colors indicate stronger segregation, white indicates neutral behaviour.

8.3.3 Machine Learning Model of Surface Segregation Energy

By combining the results presented in the previous section to those published by Ruban et al.,[153] a dataset of over 800 surface segregation energy calculations can be constructed. In addition to providing hundreds of new datapoints, the inclusion of post transition metal solutes introduces a diversity in properties which would otherwise be unlikely to be captured when only considering transition metals, therefore representing a beneficial development compared to previous studies in the literature. The combined dataset can serve as a sizeable and diverse training set to develop machine learning models and evaluate the predictive utility of different features, which is the focus of the present section.

In constructing a set of features, we leverage easily accessible properties of the host and the solute while also highlighting differences between the two specie as well as between the bulk and surface environment. A large number of descriptors previously employed in the literature are considered (which include compositional attributes such as the electronegativity, as well as structural attributes such as the coordination in the bulk and at the surface) in addition to other commonly available features (such as ground state volume per atom and valence state). Figure 8.52 provides a visualization of the typical performance upon testing achieved by a ransom forest model with a 20-80 split conditional on solute species only appearing on one of the two sets (we consider this to be a more realistic exemplification of its use). Data points collected from the work by Ruban et al.[153] are represented with blue squares, while ones associated with the calculations presented in the previous section are represented with black circles, both groups appearing to be well predicted by the model, which displays a mean absolute error on testing of ~ 0.2 eV.

Upon investigation of the feature importance we note that the difference in surface energy between host and solute drastically dominates, with the only other significant contributions being from the surface energy of the host and the size differences of the two specie (quantified via the ground state volume per atom and the atomic radii published by Vainshtein[167]). As previously mentioned, this strong correlation to differences in surface energies and atomic radii between hosts and solutes can be rationalized by considering their role in promoting or suppressing segregation

behaviour. We note that the inclusion of a single type of surface for each host is likely to underestimate the importance of features such as the coordination number at the surface, the examination of differences between multiple surfaces of the same transition metal host will therefore be the first step in future developments of the present work.

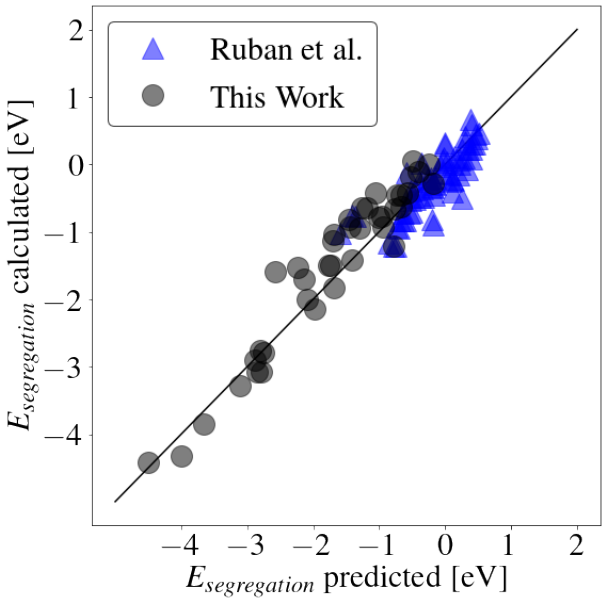

Figure 8.52: Performance upon testing (80-20 split where a solute specie can only appear in either training or testing) of a random forest model containing several compositional and structural attributes predicting the surface segregation energy of transition metal (Ruban et al.[153]) and post-transition metal (this work, see Section 8.3.2) solutes in transition metal hosts.

9. Oxygen Binding to Mixed Transition Metal Carbides

9.1 Background

One of the factors limiting the durability of fuel cells is the corrosion of the carbon supporting the Pt catalyst in the cathode through an oxidation reaction forming carbon dioxide.[23] To overcome this limitation, efforts are being directed to the search for alternative materials, with group IV-VI transition metal carbides (TMCs) attracting significant attention. Multiple works have examined Mo- and W- based TMCs in particular, finding evidence of mechanical stability, high conductivity and high catalytic activity, accompanied, however, by vulnerability to oxidation and dissolution.[24–29] Earlier TMCs, on the other hand, appear to have higher corrosion resistance, but at the cost of lower catalytic performance. Given these observations, a possible avenue to develop new TMC-based supports can be explored by considering new compounds alloying different transition metals and evaluating the effect that this has on their surface properties.

In the exploration of new materials, ab-initio methods can represent a powerful tool to guide and accelerate candidate selection, and surface properties and interactions have been at the center of a plethora of computational studies. Notably, in a recent effort to accelerate the discovery of new high performance catalysts, Chanussot et al[168] developed the Open Catalyst (OC20) database, containing over 1M DFT calculations of adsorption energies spanning a wide range of materials, surfaces, and adsorbates. The breadth and volume of the data contained in OC20 is significantly

larger than any previous catalyst DFT dataset effort, and has opened the door for numerous efforts in the advancement of machine learning predictions of adsorption-related properties.

In the context of the search for new corrosion resistant metal carbide supports for fuel cell applications, an easily accessible quantity on a computational level that can be used as a predictor of oxidation potential (which can in turn be related to corrosion resistance) of metal carbides is the oxygen binding energy (OBE). Kimmel et al[169] first found evidence of a correlation between the oxidation potential of metal carbides and the oxygen binding energy of the parent metal, and Hamo et al[30] and Tereshchuk et al[170] then identified such relationship to hold with the OBE of the metal carbide itself. In both cases, trends across chemical groups and periods were identified, with the binding being stronger the earlier the group and a the later the period of the transition metal.

While previous results of oxygen binding energy of simple transition metals and transition metal carbides can be a helpful starting point, they are not likely to hold in all conditions. Numerous works in the literature have examined the influence of structural and compositional changes on surface binding energies.[171–183] In general, differences in the surface electronic properties occur as a result of changes in the valence states of the surface metals due to changes in coordination, available binding sites, strain, and interactions with the the valence states of other metal or carbon atoms. Given the strong relationship between surface states and adsorption energies, all such changes can give rise to significant changes in adsorption behaviour, and the effects might be in contrast with each other. This motivates us to examine these effects in detail.

In this chapter we examine the evolution of the oxygen absorption behaviour on transition metal carbide surfaces upon the introduction of different transition metal solutes. We focus on three metal carbides of interest: MoC, WC and Mo_2C, and introduce group IV and V transition metal solute atoms on preferred surfaces. For each TMC, we consider four solute transition metal species that have previously shown evidence of increase corrosion resistance: Ta, Ti, Hf and Zr.

9.2 Methodology

All calculations have been conducted using the Vienna ab-initio simulation package (VASP),[75,76] with projector augmented wave (PAW) potentials[77] and the Perdew-Burke-Ernzehof (PBE)[78] generalized gradient approximation (GGA) for the exchange-correlation functional. A plane wave cutoff energy of 520 eV was employed, and electronic and ionic convergence were determined at, respectively, 10^{-6} eV and 10^{-2} eV/Å.

For Mo_2C, we considered the hexagonal α phase, where Mo atoms form a hexagonally close packed structure with carbon atoms randomly filling half of the octahedral interstitial sites.[184] While no unified model α-M_2oC for DFT calculations is available, Shi et al.[185] compared the possible configurations of occupation of C sites in a in a 12 atom cell and determined an eclipsed configuration with a Mo-C-Mo-C stacking mode to be the most stable, regardless of the functional employed in the calculation. Such structure has also been employed by Haines et al.[186] and Han et al.[187] Wang et al.[188] considered an equivalent variation of the eclipsed configuration and compared all low index surfaces, finding the 101 surface, and specifically the mixed metal and carbon termination (from hereon referred to as Mo/C termination), to be the most stable one for most values of the C chemical potential considered. We independently confirmed such observation and selected such surface for our calculations. For MoC and WC, we considered the stable phase on the OQMD convex hull, in both cases and experimentally well known, ordered, hexagonal crystal structure with P-6m2 space group (once again commonly referred to as α phase). We selected the metal termination of the 001 surface following evidence of its higher stability and stronger binding to adsorbates.[30,170]

We first computed the segregation energy of the the solute Ta,Ti,Zr and Hf atoms on the selected surfaces. For the Mo/C termination of the 101 surface of Mo_2C, we utilized a 1x1 surface slab of 56 atoms, 6 of which on each surface, and a 10Åvacuum layer, and we only allowed the top 12 to relax their ionic positions. We found a positive segregation energy (i.e. lack of segregation to the surface) for Ti and Ta, and a negative segregation energy for Zr and Hf. For the metal terminated 001 surfaces of WC and MoC, we utilized 2x2 surface slab of 5 metal and 4 carbon layers, with the

bottom 3 layers frozen, and a 10Åvacuum layer. For both metal carbides, we found all solutes to have a negative segregation energy. The observed trends in segregation energies are similar to those of the corresponding pure transition metals, as shown in Figure 9.53.

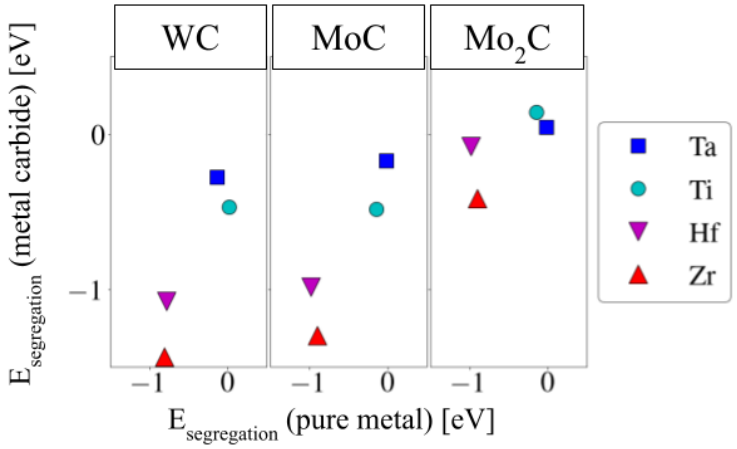

Figure 9.53: Surface segregation energies of Ta,Ti,Zr and Hf solutes in MoC, WC, Mo_2C hosts. The segregaiton energies in the metal carbides are compared to those in the pure metal, finding similar trends.

For the solutes showing surface segregation tendency (i.e. having a negative surface segregation energy), we then computed the oxygen binding energy (OBE) for 0%,25%,50%,75% and 100% concentration of solute at the surface. For the Mo/C termination of the 101 surface of Mo_2C we utilized a 1x1 slab of 32 atoms, 6 of which on each surface. We considered all bridge and top sites for O adsorption, and find the bridge site between the topmost two metal atoms to be the most favourable one. For the metal terminated 001 surfaces of MoC and WC we utilized slabs of 8 atomic layers, with the bottom 2 frozen in place. We considered all non-equivalent top bridge and hollow binding site for all types of surface solute concentration. In all cases the more highly coordinated sites resulted to have the strongest binding. However, among the hollow sites, HCP sites resulted more favourable in some cases (generally, the for lower concentrations of solutes at the surface), and FCC sites in others. We therefore report the binding energy for both types of hollow sites.

9.3 Results

In order to investigate the effect of different ranges of interactions of between oxygen and the surface solute metal atoms, we examine multiple solute and adsorbate configurations. In particular, we focus on differentiating 1^{st} and 2^{nd} nearest neighbor (NN) interactions considering oxygen binding to sites with the following configurations (in all cases the oxygen coverage was 25% and the notation corresponds to: [# of solute atoms that are 1^{st}NN to the O adsorbate atom, # of solute atoms that are 2^{nd}NN to the O adsorbate atom]):

- for the HCP hollow site of the 001 surface of WC and MoC:
  $[0,0],[1,0],[2,0],[3,0],[0,3],[1,3],[2,3],[3,3]$
- for the bridge site of the 101 surface of Mo_2C:
  $[0,0],[1,0],[2,0],[2,1],[2,2]$

The above configurations allow us to examine effect of having an increasing number of solute atoms occupying 1^{st} and 2^{nd} nearest neighbor sites to the oxygen in isolation from each other (i.e. we produced datapoints with a varying number of 1^{st} NN solute atoms and a fixed number of 2^{nd} NN ones, and viceversa). We can then construct a linear model of oxygen binding energy of a similar nature to the ones utilized by Anderson et al.[189] and Liu et al.,[190] and express OBE as a function of the number of solute atoms occupying the 1^{st} and 2^{nd} nearest neighbors to the adsorbate:

$$OBE = E_0 + E_{1NN}\#1NN + E_{2NN}\#2NN \tag{9.23}$$

Where E_0 is the oxygen binding energy to the pure metal carbide, #1NN and #2NN are the number of solute atoms among the 1^{st} and 2^{nd} nearest neighbors to the absorbate, and E_{1NN} and E_{2NN} are the changes in OBE due to the presence of solute atoms in the first and second nearest neighbor shell of the adsorbate.

In Figures 9.54, 9.55 and 9.58 we display the oxygen binding energy of, respectively, WC, MoC and Mo_2C surface with different solutes for the different NN configurations listed above,

with dashed and dotted line representing the linear fitting satisfying equation 9.23. In all cases the binding is to the most favourable sites: HCP hollow sites for MoC and WC and bridge sites between two Mo atoms in Mo_2C. Dotted lines connect datapoints with the same number of 1^{st} NN solute atoms (therefore indicating the effect of changes in the number of 2^{nd} NN solute atoms), and dashed lines connect datapoints with the same number of 2^{nd} NN solute atoms (therefore indicating the effect of changes in the number of 1^{st} NN solute atoms). Steeper lines indicate a stronger influence of the solute specie under consideration on the OBE of the metal carbide. It can be seen that, in all cases, both 1^{st} and 2^{nd} NN interactions with the solute atoms lead to a lowering of the oxygen binding energy, with the 1^{st} NN interactions having a stronger effect.

In Figure 9.59 we summarize the results of the linear fits by displaying E_{1NN} and E_{2NN} of all solutes and metal carbide combinations examined. This allows us to easily compare both the effect of different solute atoms on the oxygen binding energy of the same host metal carbide, and to contrast any observation with the OBE trends previously reported in the literature for the host and solute metals in their pure metal and metal carbide forms. For both metals and metal carbides, a strengthening of the oxygen binding was observed the earlier the group and a the later the period of the transition metal, with the OBE of Zr<Ti<Ta<Mo<W[169] and HfC<ZrC<TiC<TaC<MoC<WC.[170] Consistently with the weaker oxygen binding associated with Mo an W compared to Hf,Zr,Ti,Ta, we observe the addition of the latter metals as solutes to strengthen the binding of oxygen to WC, MoC and Mo_2C surfaces in all cases. However, multiple differences with respect to the OBE trends of the pure metals can be noticed. While the OBE of Ta is reported to be significantly weaker than Ti and Zr, 1^{st} NN interactions of O with Ta solute atoms on the 001 surfaces of both MoC and WC display bond strengthening effect greater than in the case of Zr. In turn, the strengthening effect of 1^{st} NN Zr atoms appears to be significantly smaller than that of 1^{st} NN Ti and Hf atoms. Furthermore, Ti also shows 2^{nd} NN interactions of a stronger nature than any of the other solute metals. In addition to considering the binding to the most favourable sites (HCP) in MoC and WC (reported in blue in Figure 9.59) , we here also report (in red) the effects that solute Hf,Zr,Ti,Ta atoms have on the strength of the binding of the FCC sites, which are the most favourable ones in pure TiC,ZrC

and HfC (the fits for FCC sites are displayed in 9.56 and 9.57). This allows us to observe two phenomena: the first is that the the trends in the strength of the 1^{st} and 2^{nd} NN contributions of different solute atoms remain the same between FCC and HCP sites (i.e. Ti has much stronger 2^{nd} NN contributions than Zr for example), the second is that the binding strengthening effect of the solute atoms is much more pronounced for FCC sites, which results in those sites becoming more favourable for higher (∼>50%) solute concentrations. The summary of NN contributions across hosts and solutes in Figure 9.59 also allows us to compare the effect of the same solute on different hosts. We notice that, for example, both Zr and Hf have significantly greater effects on the binding of oxygen to the bridge sites of the Mo/C terminated 101 surface of Mo_2C, than to the hollow HCP sites of the 001 metal surfaces of MoC and WC, which highlights the importance of considering differences in surface morphology and site preference.

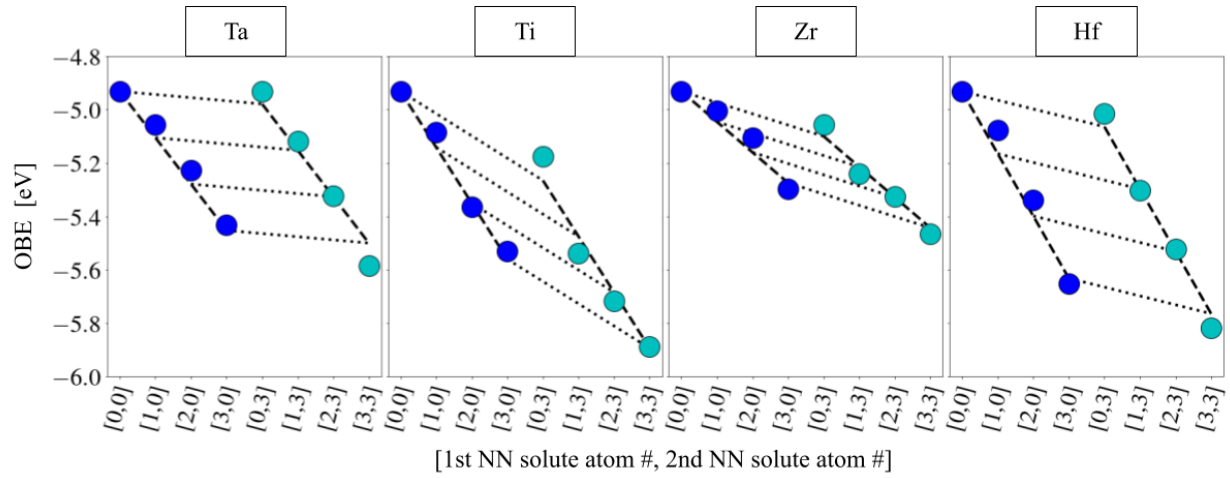

Figure 9.54: Oxygen binding energy to the metal termination of the 001 surface of WC with Ta,Ti,Zr and Hf solute atoms on the surface. Markers indicate the computed binding energy of O to HCP hollow sites with the number of 1^{st} and 2^{nd} nearest neighbor solute atoms specified on the x axis, blue markers indicate sites with no solute atoms in the 2^{nd} NNs and cyan markers indicate sites with at least one solute atom in the 2^{nd} NNs. Lines represent the linear fitting according to equation 9.23. Dotted lines connect datapoints with the same number of 1^{st} NN solute atoms and dashed lines connect datapoints with the same number of 2^{nd} NN solute atoms.

In order investigate the effects leading to the trends observed in Figure 9.59, we examine in further detail the case of 100% solute surface concentration, where the differences between solutes

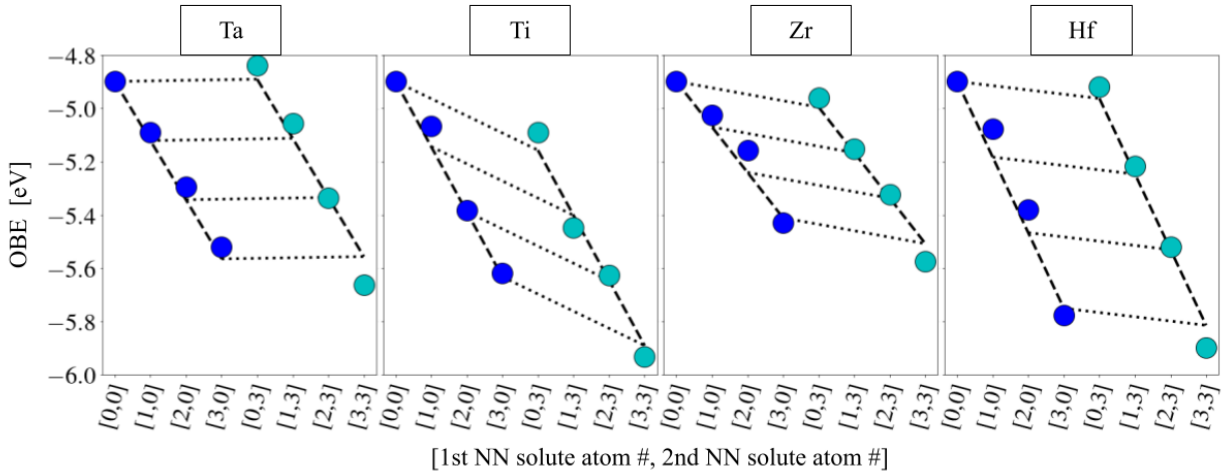

Figure 9.55: Oxygen binding energy to the metal termination of the 001 surface of MoC with Ta,Ti,Zr and Hf solute atoms on the surface. Markers indicate the computed binding energy of O to HCP hollow sites with the number of 1^{st} and 2^{nd} nearest neighbor solute atoms specified on the x axis, blue markers indicate sites with no solute atoms in the 2^{nd} NNs and cyan markers indicate sites with at least one solute atom in the 2^{nd} NNs. Lines represent the linear fitting according to equation 9.23. Dotted lines connect datapoints with the same number of 1^{st} NN solute atoms and dashed lines connect datapoints with the same number of 2^{nd} NN solute atoms.

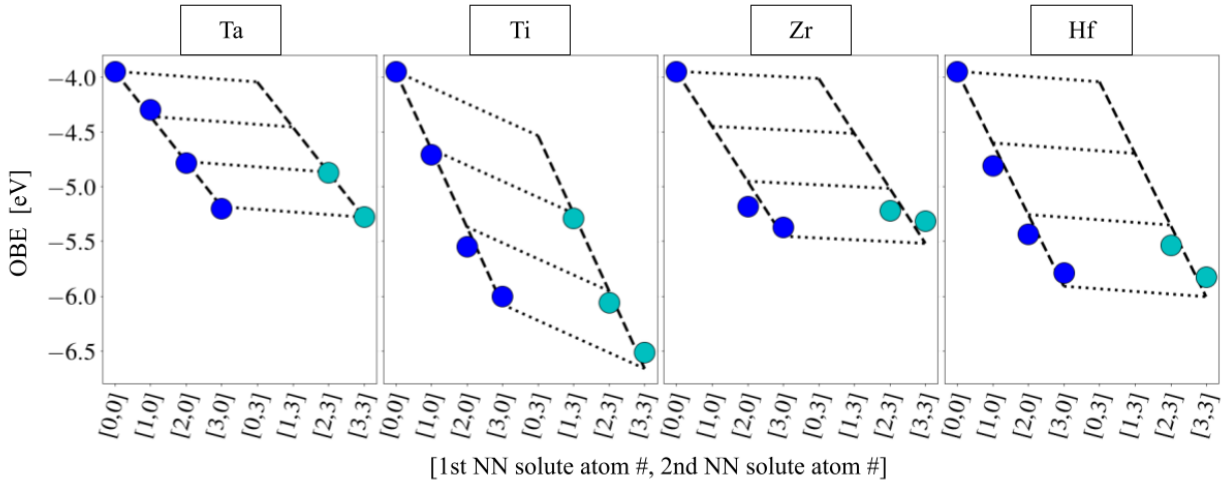

Figure 9.56: Oxygen binding energy to the metal termination of the 001 surface of WC with Ta,Ti,Zr and Hf solute atoms on the surface. Markers indicate the computed binding energy of O to FCC hollow sites with the number of 1^{st} and 2^{nd} nearest neighbor solute atoms specified on the x axis, blue markers indicate sites with no solute atoms in the 2^{nd} NNs and cyan markers indicate sites with at least one solute atom in the 2^{nd} NNs. Lines represent the linear fitting according to equation 9.23. Dotted lines connect datapoints with the same number of 1^{st} NN solute atoms and dashed lines connect datapoints with the same number of 2^{nd} NN solute atoms.

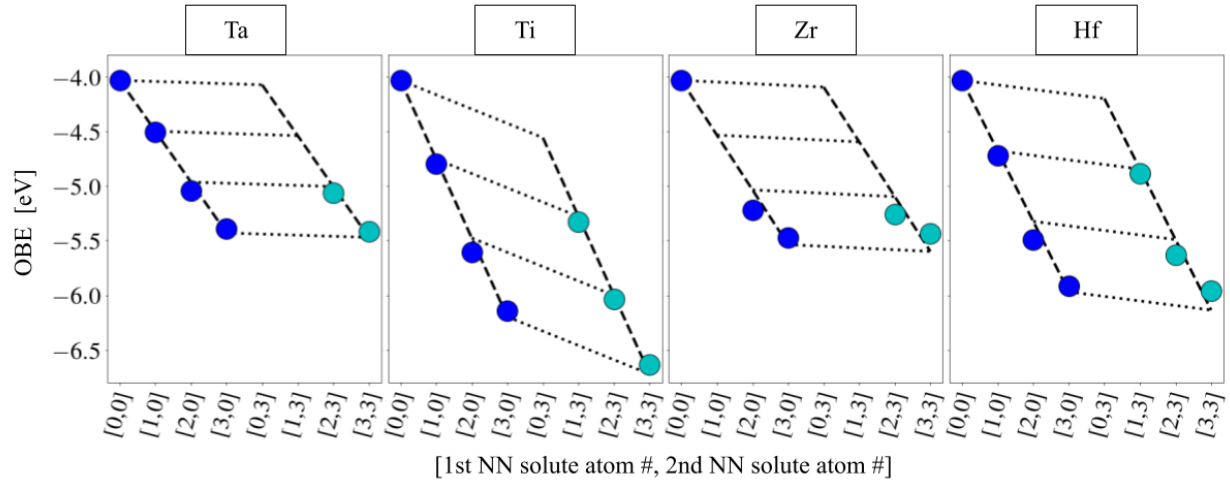

Figure 9.57: Oxygen binding energy to the metal termination of the 001 surface of MoC with Ta,Ti,Zr and Hf solute atoms on the surface. Markers indicate the computed binding energy of O to FCC hollow sites with the number of 1^{st} and 2^{nd} nearest neighbor solute atoms specified on the x axis, blue markers indicate sites with no solute atoms in the 2^{nd} NNs and cyan markers indicate sites with at least one solute atom in the 2^{nd} NNs. Lines represent the linear fitting according to equation 9.23. Dotted lines connect datapoints with the same number of 1^{st} NN solute atoms and dashed lines connect datapoints with the same number of 2^{nd} NN solute atoms.

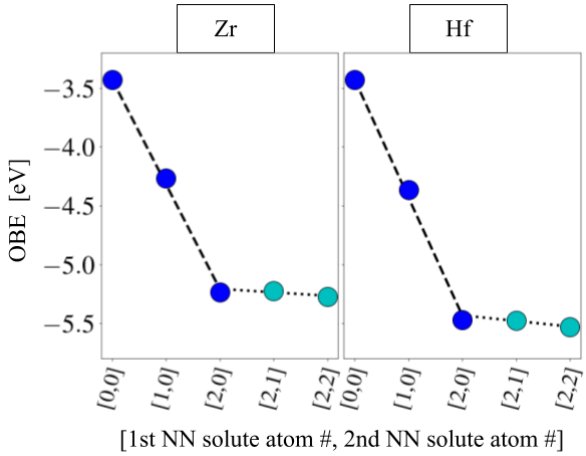

Figure 9.58: Oxygen binding energy to the mixed metal carbon termination of the 101 surface of Mo_2C with Zr and Hf solute atoms on the surface. Markers indicate the computed binding energy of O to bridge sites with the number of 1st and 2nd nearest neighbor solute atoms specified on the x axis, blue markers indicate sites with no solute atoms in the 2nd NNs and cyan markers indicate sites with at least one solute atom in the 2nd NNs. Lines represent the linear fitting according to equation 9.23. Dotted lines connect datapoints with the same number of 1st NN solute atoms and dashed lines connect datapoints with the same number of 2nd NN solute atoms.

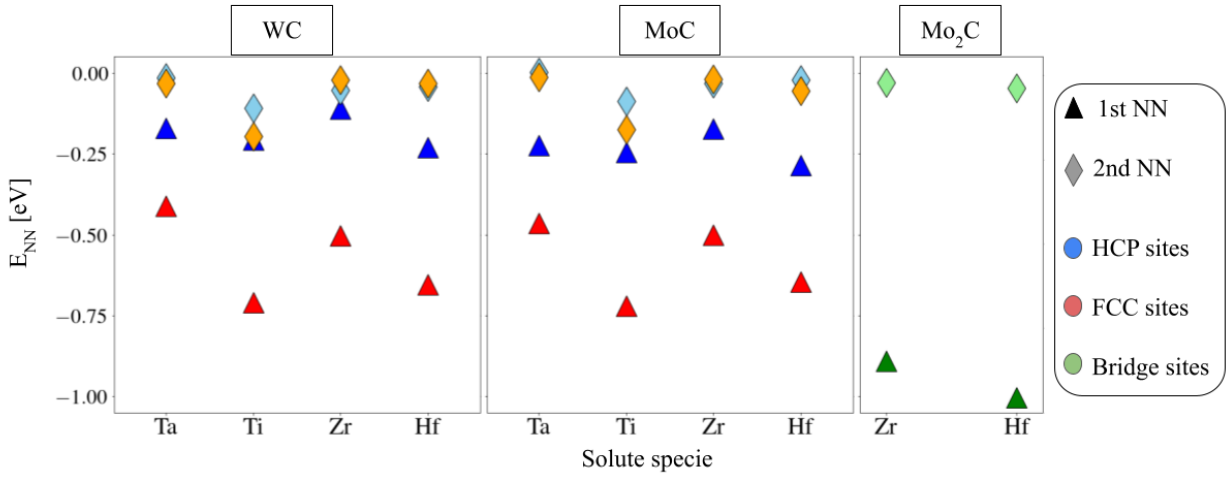

Figure 9.59: Effect of Ta,Ti,Zr and Hf solute atoms on oxygen binding energy to the surfaces of host WC, MoC, Mo_2C quantified with E_{1NN} and E_{2NN} according to equation 9.23.

are exacerbated. The surface layers of Ta,Ti,Zr and Hf on α-WC and α-MoC differ from their carbide phases in various aspects: the M-M distance on the surface is reduced, the atomic layers have different stacking, and the M-C distance also changes. Furthermore, the presence of different metals (Mo or W) in the bulk also leads to interactions between such metals and the surface metals, the carbon, and the adsorbate. We explore each of the above aspects.

Firstly, we consider the change in surface M-M distance. When on the surface of WC and MoC, Ta,Ti,Zr and Hf atoms all are under compressive strain, i.e. they have a lower M-M distance than in their pure metal carbide phases, as detailed in Table 9.3. To examine the effect of this lowering in the M-M distance in isolation from other effects, we compute the OBE of the metal carbides as a function of strain in the direction parallel to the surface. While applying strain to the slab also changes the M-C distance, the magnitude of such change is significantly smaller than that of the change in M-M distance. As shown in Figure 9.60, for strain values lower than 5%, compressive strain results in a stronger binding in all cases other than for the FCC sites in TaC. When the compressive strain increases even further though, we observe, especially on FCC sites, an inversion of the trend, with the binding starting to get weaker the larger the compression.

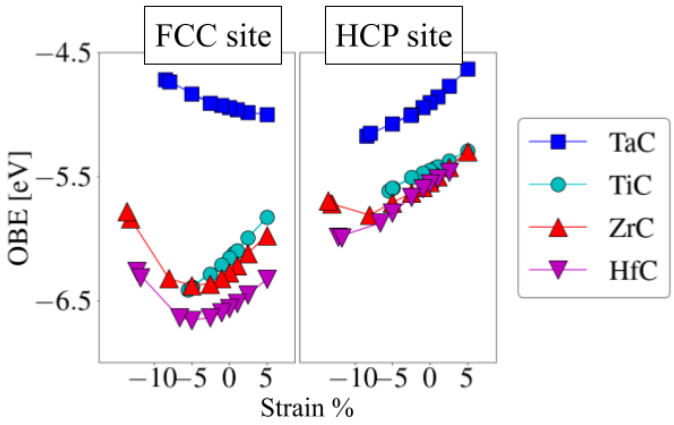

Figure 9.60: Oxygen binding energy of metal carbides as a function of strain. Each marker indicates a different metal carbide

Table 9.3: Strain of Ta,Ti,Zr and Hf at the surface of MoC and WC

Surface Metal	Strain on α-WC	Strain on α-MoC	Strain on β-MoC
Ta	-8.5%	-8%	-2.6%
Ti	-5.5%	-5%	+0.6%
Zr	-13.6%	-13.1%	-8%
Hf	-12.3%	-11.8%	-6.6%

We next examine the effect of having different metals in the bulk layers, and differentiate it from both surface strain effects and differences in the stacking of the atomic layers. In order to do so, we now consider Ta,Ti,Zr and Hf surface layers on the 111 surface of the cubic β phase of MoC, which has the same stacking as TaC,TiC,ZrC and HfC. In Figure 9.61 a, we compare β-MoC slabs with one surface layer Ta,Ti,Zr and Hf (marked with a black circle) with TaC,TiC,ZrC and HfC slabs with the same surface M-M distance as in β-MoC (marked with back cross). While not nearly as large of an effect as the one of strain analysed in the previous paragraph, we see a weakening of the binding of O to Zr and Hf surfaces when Mo occupies the sub-surface metal layer.

Finally, we incorporate the effect of the structural difference differences in the stacking of the metal layers. To do so, in Figure 9.61 b, we compare α-MoC slabs with one surface layer Ta,Ti,Zr and Hf (marked with a black circle) with two other conditions: (i) TaC,TiC,ZrC and HfC slabs with the same surface M-M distance as in α-MoC (marked with back cross), and (ii) α-MoC slabs,

where, in addition to the surface layer, the first metal layer under the surface one is of the same species (i.e. Ta,Ti,Zr or Hf) (marked with back plus sign). When comparing α-MoC with one and two Ta,Ti,Zr or Hf layers we see once again that the effect of having Mo in the sub-surface metal layer is a weakening of the binding of O to Zr and Hf surfaces. We also however observe that Ta,Ti,Zr and Hf on the surface of α-MoC with a sub-surface layer of the same specie have significantly lower OBE than on the surface of their parent metal carbide with the same M-M distance.

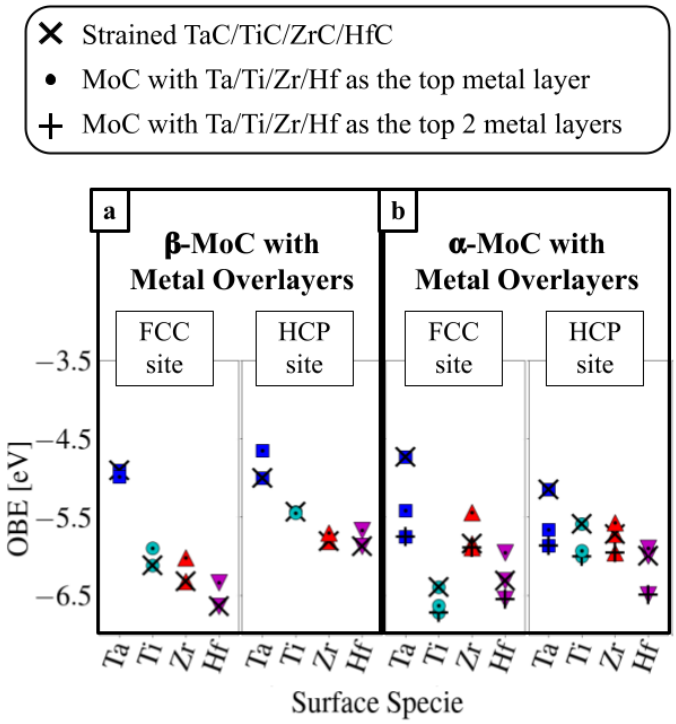

Figure 9.61: Oxygen binding energy of Ta,Ti,Zr,Hf layers on hexagonal MoC the plus sign indicates the case where the top two metal layers of the surface are Ta,Ti,Zr or Hf, while the circle indicates that only the surface layer is, while all other metal layers are Mo

In summary, through the exploration of different combinations of solute, hosts, and solute surface concentrations, we highlight the complexity brought about by the alloying of different transition metal carbides. We examine different factors, such changes in metal-metal and metal-carbon distance, as well as interaction between different metals, and highlight their role in determining changes in surface absorption behaviour. Most importantly, we show evidence for the disruption

of trends in surface adsorption properties of pure metal carbides upon alloying, highlighting the importance of performing direct examinations of the systems of interest rather than relying on the extrapolation of trends present in simple systems.

10. Summary and Outlook

In this thesis we presented multiple works targeting the understanding and prediction of different properties across various classes of materials, all under the common umbrella of renewable energy applications.

A large portion of the discussion is dedicated to the thermodynamics of oxygen loss, a phenomenon of relevance in several technologies, with a special focus on solar-thermochemical water splitting for green hydrogen production (STCH). After successfully assessing the accuracy of DFT-computed oxygen vacancy formation energies compared with experimental data, we presented the result of multiple high-throughput studies evaluating thermodynamic stability and O vacancy formation across several structure types, most notably perovskite-type oxides. Within such studies, we identified hundreds of new STCH candidate compounds, complete lists of which are reported in the appendix. We also identified trends related to metal oxide reduction and developed machine learning models capable of predicting the vacancy formation energy with an accuracy comparable to that of DFT calculations against experimental data. Natural extensions of this work would include the assessment of the predictive power of our descriptors across more diverse structure types, and the development of new features as needed, an undertaking which we have commenced by investigating oxygen loss behaviours in multiple rock salt-type lithium transition metal oxide compounds. Our initial results confirmed the utility of site-specific properties related to electronic-structure and cation reduction, but also indicated the presence of additional complexities related to binding and charge distribution compared to the ordered transition metal oxides examined in the previous high throughput studies. To address such complexities a variety of new bonding-, electronic structure-

and charge distribution- related features are being evaluated, and future avenues will involve the construction of more complex models leveraging different types of learning algorithms.

In conjunction with the energy, we have also examined the entropy of oxygen vacancy formation for a selected group of metal oxides with diverse structure types, including perovskite-type ones. Our analysis indicated the solid state vibrational contribution to be characterized by a temperature dependence counteracting that of oxygen gas, therefore lessening the variation of the total entropy of vacancy formation with temperature. While non-negligible differences in vibrational entropy were recognized between compounds, suggesting it to be a tunable quantity in the search for new STCH compounds, its magnitude was generally observed to be significantly smaller than the gas and dilute configurational entropy, indicating a more promising strategy to involve focusing on different sources of entropy. An interesting avenue in this sense is represented by the search of new Ce^{4+}-containing compounds so as to leverage the large contribution from the on site electronic entropy of reduction. As one of the main drawbacks of Ceria is its large enthalpy of reduction, a strategy for computational studies can be the search for new compounds capable of leveraging Ce reduction at a lower enthalpy cost, as exemplified on a small scale by the recent work by Naghavi et al.[191]

We have then moved our focus from bulk to surface phenomena, by studying segregation and adsorption behaviours of interest for catalytic applications. We have generated a new pool of data evaluating the segregation behaviour of post transition metals, and identified useful descriptors for large scale prediction of surface segregation energies. Natural extensions of this work would then include the examination of different surfaces and the inclusion of more complex chemistries, once again assessing the predictive power of current features at each degree of extrapolation and developing new features as needed. A small scale investigation of such type was conducted on transition metal carbides, were segregation trends analogous to the corresponding transition metal systems were observed. The examination of binding strength of oxygen to the surfaces of these mixed transition metal carbides revealed the existence of more complex behaviours than those predicted by simply extrapolating oxygen adsorption trends in transition metals or pure transition

metal carbides. These observations motivate the interest in conducting large scale studies examining different configurations to gain a deeper understating of the mechanisms governing oxygen binding in these systems, and predict new transition metal carbide materials with higher corrosion resistance.

List of Publications

- B. Baldassarri, J. He, X. Qian, E. Mastronardo, S. Griesemer, S. M. Haile, and C. Wolverton "Accuracy of DFT Computed Oxygen-Vacancy Formation Energies and High-Throughput Search of Solar Thermochemical Water-Splitting Compounds", Phys. Rev. Mat. (accepted, 2023)

- J. Shen, S. Griesemer, A. Gopakumar, B. Baldassarri, J.E. Saal, M. Aykol, V. Hegde, and C. Wolverton "Reflections on One Million Compounds in the Open Quantum Materials Database (OQMD)", Journal of Physics: Materials (2022)

- X. Qian, J. He, E. Mastronardo, B. Baldassarri, C. Wolverton and S. M. Haile "Outstanding Properties and Performance of $CaTi_{0.5}Mn_{0.5}O_{3\text{-}\delta}$ for Solar-Driven Thermochemical Hydrogen Production", Matter (2021)

- X. Qian, J. He, E. Mastronardo, B. Baldassarri, Y. Weizi, C. Wolverton and S. M. Haile "Favorable redox thermodynamics of $SrTi_{0.5}Mn_{0.5}O_{3\text{-}\delta}$ in solar thermochemical water splitting", Chem. Mater. (2020)

- J. He, B. Baldassarri, and C. Wolverton "Assessment of Exchange-Correlation Functionals on Oxygen Vacancy Formation Energies of Metal Oxides", (under review)

- B. Baldassarri, J. He, A. Gopakumar, S. Griesemer, S. Torrisi, A. Salgado Casanova, T. Liu, and C. Wolverton "Oxygen Vacancy Formation Energy in Metal Oxides: High Throughput DFT Studies and Machine Learning Predictions", (in prep.)

- B. Baldassarri, J. He, and C. Wolverton "DFT Study of Vibrational Entropies of Oxygen Vacancy Formation in Metal Oxides", (in prep.)

- J. He, B. Baldassarri, and C. Wolverton "Stability Map of Double Perovskite Oxides", (in prep.)

- J. He, B. Baldassarri, J. Hecter, and C. Wolverton "Stability Map of Pyrochlore Oxides", (in prep.)

Bibliography

[1] U. E. I. Administration, International energy outlook, 2021.

[2] U. E. I. Administration, International energy outlook 2021, 2021.

[3] J. Blunden, E. T. Boyer, Temperature [in state of the climate in 2021], Bulletin of the American Meteorological Society 103(8) (2022) S27–S28.

[4] A. Z. L. Shalpback, Hydrogen-storage materials for mobile applications, Nature 414 (2001) 353–358.

[5] M. Carmo, D. L. Fritz, J. Mergela, D. Stolten, A comprehensive review on pem water electrolysis, International Journal of Hydrogen Energy 38 (2013) 4901–4934.

[6] M. G. Walter, E. L. Warren, J. R. McKone, S. W. Boettcher, Q. Mi, E. A. Santori, N. S. Lewis, Solar water splitting cells, Chemical Reviews 110(11) (2010) 6446–6473.

[7] G. De Beni, C. Marchetti, A. Mark, A chemical process to decompose water using nuclear heat, 1972.

[8] T. Nakamura, Hydrogen production from water utilizing solar heat at high temperatures, Sol. Energy 19 (1977) 467–475.

[9] Z. Wang, R. Roberts, G. Naterer, K. Gabriel, Comparison of thermochemical, electrolytic, photoelectrolytic and photochemical solar-to-hydrogen production technologies, Int. J. Hydrogen Energy 37 (2012) 16287–16301.

[10] T. Kodama, N. Gokon, Thermochemical cycles for high-temperature solar hydrogen production, Chemical Reviews 107 (2007) 4048–4077.

[11] T. Kodama, High-temperature solar chemistry for converting solar heat to chemical fuels, Prog. Energy Combust. Sci. 29 (2003) 567.

[12] A. Kogan, Direct solar thermal splitting of water and on-site separation of the products. ii. experimental feasibility study, Int. J. Hydrogen Energy 23 (1998) 89–98.

[13] C. Perkins, A. Weimer, Likely near-term solar-thermal water splitting technologies, Int. J. Hydrogen Energy 29 (2004) 1587.

[14] B. Meredig, C. Wolverton, First-principles thermodynamic framework for the evaluation of thermochemical h2o- or co2-splitting materials, Physical Review B 89 (2009) 245119.

[15] R. J. Clement, Z. Lun, G. Ceder, Cation-disordered rocksalt transition metal oxides and oxyfluorides for high energy lithium-ion cathodes, Energy Environ. Sci. 13 (2020) 345–373. doi:10.1039/C9EE02803J.
URL http://dx.doi.org/10.1039/C9EE02803J

[16] B. E. Murdock, K. E. Toghill, N. Tapia-Ruiz, A perspective on the sustainability of cathode materials used in lithium-ion batteries, Advanced Energy Materials 11 (39) (2021) 2102028. doi:https://doi.org/10.1002/aenm.202102028.
URL https://onlinelibrary.wiley.com/doi/abs/10.1002/aenm.202102028

[17] J. Lee, A. Urban, X. Li, D. Su, G. Hautier, G. Ceder, Unlocking the potential of cation-disordered oxides for rechargeable lithium batteries, science 343 (6170) (2014) 519–522.

[18] D.-H. Seo, J. Lee, A. Urban, R. Malik, S. Kang, G. Ceder, The structural and chemical origin of the oxygen redox activity in layered and cation-disordered li-excess cathode materials, Nature chemistry 8 (7) (2016) 692–697.

[19] M. Okubo, A. Yamada, Molecular orbital principles of oxygen-redox battery electrodes, ACS Applied Materials & Interfaces 9 (42) (2017) 36463–36472, pMID: 29016101. doi:10.1021/acsami.7b09835.

[20] M. Gu, I. Belharouak, J. Zheng, H. Wu, J. Xiao, A. Genc, K. Amine, S. Thevuthasan, D. R. Baer, J.-G. Zhang, N. D. Browning, J. Liu, C. Wang, Formation of the spinel phase in the layered composite cathode used in li-ion batteries, ACS Nano 7 (1) (2013) 760–767, pMID: 23237664. doi:10.1021/nn305065u.

[21] E. Hu, X. Yu, R. Lin, X. Bi, J. Lu, S. Bak, K.-W. Nam, H. L. Xin, C. Jaye, D. A. Fischer, et al., Evolution of redox couples in li-and mn-rich cathode materials and mitigation of voltage fade by reducing oxygen release, Nature Energy 3 (8) (2018) 690–698.

[22] L. Du, Y. Shao, J. Sun, G. Yin, J. Liu, Y. Wang, Advanced catalyst supports for pem fuel cell cathodes, Nano Energy 29 (2016) 314–322, electrocatalysis. doi:https://doi.org/10.1016/j.nanoen.2016.03.016.
URL https://www.sciencedirect.com/science/article/pii/S2211285516300362

[23] J. C. Meier, C. Galeano, I. Katsounaros, J. Witte, H. J. Bongard, A. A. Topalov, C. Baldizzone, S. Mezzavilla, F. Schüth, K. J. J. Mayrhofer, Design criteria for stable pt/c fuel cell catalysts, Beilstein J. Nanotechnol. (5) (2014) 44–67. doi:doi:10.3762/bjnano.5.5.

[24] Y. N. Regmi, G. R. Waetzig, K. D. Duffee, S. M. Schmuecker, J. M. Thode, B. M. Leonard, Carbides of group iva, va and via transition metals as alternative her and orr catalysts and support materials, J. Mater. Chem. A 3 (2015) 10085–10091. doi:10.1039/C5TA01296A.
URL http://dx.doi.org/10.1039/C5TA01296A

[25] Y. Liu, T. G. Kelly, J. G. Chen, W. E. Mustain, Metal carbides as alternative electrocatalyst supports, ACS Catalysis 3 (6) (2013) 1184–1194. doi:10.1021/cs4001249.

[26] M. A. Abdelkareem, T. Wilberforce, K. Elsaid, E. T. Sayed, E. A. Abdelghani, A. Olabi, Transition metal carbides and nitrides as oxygen reduction reaction catalyst or catalyst support in proton exchange membrane fuel cells (pemfcs), International Journal of Hydrogen Energy (2020).

[27] L. Elbaz, J. Phillips, K. Artyushkova, K. More, E. L. Brosha, Evidence of high electrocatalytic activity of molybdenum carbide supported platinum nanorafts, Journal of The Electrochemical Society 162 (9) (2015) H681. doi:10.1149/2.0991509jes.
URL https://dx.doi.org/10.1149/2.0991509jes

[28] R. B. Levy, M. Boudart, Platinum-like behavior of tungsten carbide in surface catalysis, Science 181 (4099) (1973) 547–549. doi:10.1126/science.181.4099.547.
URL https://www.science.org/doi/abs/10.1126/science.181.4099.547

[29] W.-F. Chen, J. T. Muckerman, E. Fujita, Recent developments in transition metal carbides and nitrides as hydrogen evolution electrocatalysts, Chem. Commun. 49 (2013) 8896–8909. doi:10.1039/C3CC44076A.
URL http://dx.doi.org/10.1039/C3CC44076A

[30] E. R. Hamo, P. Tereshchuk, M. Zysler, D. Zitoun, A. Natan, B. A. Rosen, Corrosion Resistance and Acidic ORR Activity of Pt-based Catalysts Supported on Nanocrystalline Alloys of Molybdenum and Tantalum Carbide, Journal of The Electrochemical Society 166 (16) (2019) F1292–F1300. doi:10.1149/2.0251916jes.

[31] P. Hohenberg, W. Khon, Inhomogeneous electron gas, Physical Review 136 (1964) 864.

[32] W. Khon, L. J. Sham, Self-consistent equations including exchange and correlation effects, Physical Review 140 (1965) 1133.

[33] R. O. Jones, O. Gunnarsson, The density functional formalism, its applications and prospects, Reviews of Modern Physics 61 (1989) 689.

[34] J. P. Perdew, Y. Wang, Accurate and simple analytic representation of the electron-gas correlation energy, Physical Reviews B 45 (1992) 13 245.

[35] J. P. Perdew, A. Ruzsinszky, J. Tao, V. N. Staroverov, G. E. Scuseria, G. I. Csonka, Prescription for the design and selection of density functional approximations: More constraint satisfaction with fewer fits, The Journal of Chemical Physics 123 (6) (08 2005).

[36] B. Himmetoglu, A. Floris, S. de Gironcoli, M. Cococcioni, Hubbard-corrected dft energy functionals: The LDA+U description of correlated systems, Quantum Chemistry 114 (2013) 14–19.

[37] F. Zhou, M. Cococcioni, C. A. Marianetti, D. Morgan, G. Ceder, First-principles prediction of redox potentials in transition-metal compounds with LDA+U, Phys. Rev. B 70 (2004) 235121.

[38] L. Wang, T. Maxisch, G. Ceder, Oxidation energies of transition metal oxides within the GGA+U framework, Phys. Rev. B 73 (2006) 195107.

[39] S. Lutfalla, V. Shapovalov, A. T. Bell, Calibration of the DFT/GGA+U method for determination of reduction energies for transition and rare earth metal oxides of Ti, V, Mo, and Ce, J. Chem. Theory Comput. 7 (2011) 2218.

[40] V. L. Chevrier, S. P. Ong, R. Armiento, M. K. Y. Chan, G. Ceder, Hybrid density functional calculations of redox potentials and formation energies of transition metal compounds, Phys. Rev. B 82 (2010) 075122.

[41] A. M. Deml, A. M. Holder, R. P. O'Hayre, C. B. Musgrave, V. Stevanovic, Intrinsic material properties dictating oxygen vacancy formation energetics in metal oxides, J. Phys. Chem. Lett. 6 (2015) 1948–1953.

[42] S. L. Dudarev, G. A. Botton, S. Y. Savrasov, C. J. Humphreys, Sutton, Electron-energy-loss spectra and the structural stability of nickel oxide: An LSDA+U study, A. P. . Phys. Rev. B: Condens. Matter Mater. Phys. 57 (1998) 1505–1509.

[43] J. E. Saal, S. Kirklin, M. Aykol, B. Meredig, C. Wolverton, Materials design and discovery with high-throughput density functional theory: The open quantum materials database (OQMD), JOM 65 (2013) 1501–1509.

[44] S. Kirklin, J. E. Saal, B. Meredig, A. Thompson, J. W. Doak, S. Aykol, M. andRuhl, C. Wolverton, The open quantum materials database (OQMD): assessing the accuracy of dft formation energies, Comput. Mater. 1 (2015) 15010.

[45] A. Jain, S. P. Ong, G. Hautier, W. Chen, W. D. Richards, S. Dacek, S. Cholia, D. Gunter, D. Skinner, G. Ceder, K. A. Persson, Commentary: The materials project: A materials genome approach to accelerating materials innovation, APL Materials 1 (1) (2013).

[46] G. Sai Gautam, E. A. Carter, Evaluating transition metal oxides within dft-scan and SCAN$+u$ frameworks for solar thermochemical applications, Phys. Rev. Materials 2 (2018) 095401.

[47] M. Aykol, C. Wolverton, Local environment dependent GGA+U method for accurate thermochemistry of transition metal compounds, Phys. Rev. B 90 (2014) 115105.

[48] O. Y. Long, G. Sai Gautam, E. A. Carter, Evaluating optimal u for 3d transition-metal oxides within the scan+ u framework, Physical Review Materials 4 (4) (Apr. 2020).

[49] M. Dove, Introduction to Lattice Dynamics, Cambridge University Press, 1993.

[50] A. Togo, I. Tanaka, First principles phonon calculations in materials science, Scr. Mater. 108 (2015) 1–5.

[51] S. B. Adler, Factors governing oxygen reduction in solid oxide fuel cell cathodes, Chem. Rev 104 (2004) 47914843.

[52] J. A. Kilner, M. Burriel, Materials for intermediate-temperature solid-oxide fuel cells, Annu. Rev. Mater. Res 44 (2014) 365393.

[53] W. C. Chueh, C. Falter, M. Abbott, D. Scipio, P. Furler, S. M. Haile, A. Steinfeld, High-flux solar-driven thermochemical dissociation of co_2 and h_2o using nonstoichiometric ceria, Science 330 (6012) (2010) 1797–1801.

[54] A. A. Emery, J. E. Saal, S. Kirklin, V. I. Hegde, C. Wolverton, High-throughput computational screening of perovskites for thermochemical water splitting applications, Chem. Mater. 28 (2016) 5621–5634.

[55] R. B. Wexler, G. S. Gautam, E. B. Stechel, E. A. Carter, Factors Governing Oxygen Vacancy Formation in Oxide Perovskites, Journal of the American Chemical Society 143 (33) (2021) 13212–13227.

[56] A. H. McDaniel, E. C. Miller, D. Arifin, A. Ambrosini, E. N. Coker, R. O'Hayre, W. Chueh, J. Tong, Sr- and Mn-doped $LaAlO_{3-\delta}$ for solar thermochemical H_2 and CO production, Energy Environ. Sci. 6 (2013) 2424–2428.

[57] J. R. Scheffe, D. Weibel, A. Steinfeld, Lanthanum-strontium- manganese perovskites as redox materials for solar thermochemical splitting of H_2O and CO_2, Energy Fuels 27 (2013) 4250–4257.

[58] A. McDaniel, A. Ambrosini, E. Coker, J. Miller, W. Chueh, R. O'Hayre, J. Tong, Nonstoichiometric perovskite oxides for solar thermochemical H_2 and CO production, Energy Procedia 49 (2014) 2009–2018.

[59] C. K. Yang, Y. Yamazaki, A. Aydin, S. M. Haile, Thermodynamic and kinetic assessments of strontium-doped lanthanum manganite perovskites for two-step thermochemical water splitting, . Mater. Chem. A 2 (2014) 13612.

[60] J. R. Scheffe, A. Steinfeld, Oxygen exchange materials for solar thermochemical splitting of H_2O and CO_2: a review, Mater. Today 17 (2014) 341–348.

[61] A. Demont, S. Abanades, E. Beche, Investigation of perovskite structures as oxygen-exchange redox materials for hydrogen production from thermochemical two-step water-splitting cycles, J. Phys. Chem. C 118 (2014) 12682.

[62] J. Breternitz, S. Schorr, What defines a perovskite?, Adv. Energy Mater 8 (2018) 1802366.

[63] B. J. Kennedy, B. A. Hunter, High-temperature phases of $srruo_3$, Phys. Rev. B 58 (1998) 653–658.

[64] B. J. Kennedy, C. J. Howard, B. C. Chakoumakos, High-temperature phase transitions in $srzro_3$, Phys. Rev. B 59 (1999) 4023–4027.

[65] B. J. Kennedy, C. J. Howard, B. C. Chakoumakos, High-temperature phase transitions in $srhfo_3$, Phys. Rev. B 60 (1999) 2972–2975.

[66] C. J. Howard, K. S. Knight, B. J. Kennedy, E. H. Kisi, The structural phase transitions in strontium zirconate revisited, Journal of Physics: Condensed Matter 12 (45) (2000) L677.

[67] K. Knight, Structural phase transitions in baceo3, Solid State Ionics 74 (3) (1994) 109–117.

[68] M. Ezbiri, M. Takacs, B. Stolz, J. Lungthok, A. Steinfeld, R. Michalsky, Design principles of perovskites for solar-driven thermochemical splitting of CO_2, J. Mater. Chem. A, 15 (2017) 15105.

[69] J. Vieten, B. Bulfin, P. Huck, M. Horton, D. Guban, L. Zhu, Y. Lu, K. A. Persson, M. Roeb, C. Sattler, Materials design of perovskite solid solutions for thermochemical applications, Energy Environ. Sci. 12 (2019) 1369–1384.

[70] G. Sai Gautam, E. B. Stechel, E. A. Carter, Exploring Ca–Ce–M–O (M = 3d Transition Metal) oxide perovskites for solar thermochemical applications, Chemistry of Materials 32 (23) (2020) 9964–9982.

[71] The inorganic crystal structure data base, J. Chem. Inf. Model. 23 (1983) 66–69.

[72] A. Belsky, M. Hellenbrandt, V. L. Karen, P. Luksch, New developments in the inorganic crystal structure database (ICSD): accessibility in support of materials research and design., Acta Crystallogr.Sect. B: Struct. Sci. 58 (2002) 364–369.

[73] M. T. Curnan, J. R. Kitchin, Effects of concentration, crystal structure, magnetism, and electronic structure method on first-principles oxygen vacancy formation energy trends in perovskites, The Journal of Physical Chemistry C 118 (49) (2014) 28776–28790.

[74] B. Baldassarri, J. He, X. Qian, E. Mastronardo, S. S. Griesemer, S. Haile, C. Wolverton, Accuracy of DFT Computed Oxygen-Vacancy Formation Energies and High-Throughput Search of Solar Thermochemical Water-Splitting Compounds, Pyhsical Review of Materials (2023).

[75] G. Kresse, J. Furthmuller, Efficiency of ab-initio total energy calculations for metals and semiconductors using a plane-wave basis set, Comput. Mater. Sci 6 (1996) 15–50.

[76] G. Kresse, Furthmuller, Efficient iterative schemes for ab initio total-energy calculations using a plane-wave basis set, J. E. Phys. Rev. B: Condens. Matter Mater. Phys. 54 (1996) 11169–11186.

[77] G. Kresse, D. Joubert, From ultrasoft pseudopotentials to the projector augmented-wave method., Phys. Rev. B: Condens. Matter Mater. Phys. 59 (1999) 1758–1775.

[78] J. P. Perdew, K. Burke, M. Ernzerhof, Generalized gradient approximation made simple, Phys. Rev. Lett. 77 (1996) 3865–3868.

[79] X. Qian, Nonstoichiometric Perovskite Oxides for Solar-Driven Thermochemical Water Splitting, Ph.D. thesis, Northwestern University (2021).

[80] E. Mastronardo, X. Qian, J. M. Coronado, S. M. Haile, Impact of La doping on the thermochemical heat storage properties of $CaMnO_{3-\delta}$, Journal of Energy Storage 40 (2021) 102793.

[81] Y.-L. Lee, J. Kleis, J. Rossmeisl, D. Morgan, Ab initio energetics of $LaBO_3$ (001) (B = Mn, Fe, Co, and Ni) for solid oxide fuel cell cathodes, Phys. Rev. B: Condens. Matter Mater. Phys. 80 (2009) 224101.

[82] A. Jain, G. Hautier, S. P. Ong, C. J. Moore, C. C. Fischer, K. A. Persson, G. Ceder, Formation enthalpies by mixing GGA and GGA+U calculations, Phys. Rev. B 84 (2011) 045115.

[83] S. Grindy, B. Meredig, S. Kirklin, J. E. Saal, C. Wolverton, Approaching chemical accuracy with density functional calculations: Diatomic energy corrections, Phys. Rev. B 87 (2013) 075150.

[84] V. Stevanovic, S. Lany, X. Zhang, A. Zunger, Correcting density functional theory for accurate predictions of compound enthalpies of formation: Fitted elemental-phase reference energies, Phys. Rev. B 85 (2012) 115104.

[85] L. Nalbandian, A. Evdou, V. Zaspalis, $La_{1-x}Sr_xMO_3$ (M = Mn, Fe) perovskites as materials for thermochemical hydrogen production in conventional and membrane reactors, Int. J. Hydrogen Energy 34 (2009) 7162–7172.

[86] T. Kodama, Y. Nakamuro, T. Mizuno, A two-step thermochemical water splitting by iron-oxide on stabilized zirconia, Journal of Solar Energy Engineering, Transactions of the ASME 128 (2006) 3–7.

[87] S. Dey, B. S. Naidu, C. N. Rao, $Ln_{0.5}A_{0.5}MnO_3$ (Ln=Lanthanide, A= Ca, Sr) perovskites exhibiting remarkable performance in the thermochemical generation of CO and H_2 from CO_2 and H_2O, Chemistry - A European Journal 21 (19) (2015) 7077–7081.

[88] S. Dey, B. S. Naidu, A. Govindaraj, C. N. Rao, Noteworthy performance of $La_{1-x}Ca_xMnO_3$ perovskites in generating H_2 and CO by the thermochemical splitting of H_2O and CO_2, Physical Chemistry Chemical Physics 17 (1) (2015) 122–125.

[89] D. O'Keefe, C. Allen, G. Besenbruch, L. Brown, J. Norman, R. Sharp, K. McCorkle, Preliminary results from bench-scale testing of a sulfur-iodine thermochemical water-splitting cycle, International Journal of Hydrogen Energy 7 (5) (1982) 381–392.

[90] A. Le Gal, S. Abanades, Dopant incorporation in Ceria for enhanced water-splitting activity during solar thermochemical hydrogen generation 116 (25) (2012) 13516–13523.

[91] A. H. Bork, M. Kubicek, M. Struzik, J. L. Rupp, Perovskite $La_{0.6}Sr_{0.4}Cr_{1-x}Co_xO_{3-\delta}$ solid solutions for solar-thermochemical fuel production: Strategies to lower the operation temperature, Journal of Materials Chemistry A 3 (30) (2015) 15546–15557.

[92] L. Wang, M. Al-Mamun, P. Liu, Y. Wang, H. G. Yang, H. Zhao, $La_{1-x}Ca_xMn_{1-y}Al_yO_3$ perovskites as efficient catalysts for two-step thermochemical water splitting in conjunction with exceptional hydrogen yields, Cuihua Xuebao/Chinese Journal of Catalysis 38 (6) (2017) 1079–1086.

[93] L. Wang, M. Al-Mamun, P. Liu, Y. Wang, H. G. Yang, H. Zhao, Notable hydrogen production on $La_xCa_{1x}CoO_3$ perovskites via two-step thermochemical water splitting, Journal of Materials Science 53 (9) (2018) 6796–6806.

[94] F. He, F. Li, Perovskite promoted iron oxide for hybrid water-splitting and syngas generation with exceptional conversion, Energy and Environmental Science 8 (2) (2015) 535–539.

[95] M. Orfila, M. Linares, R. Molina, J. Á. Botas, R. Sanz, J. Marugán, Perovskite materials for hydrogen production by thermochemical water splitting, International Journal of Hydrogen Energy 41 (42) (2016) 19329–19338.

[96] A. M. Deml, V. Stevanovic, C. L. Muhich, C. B. Musgrave, R. O'Hayre, Oxide enthalpy of formation and band gap energy as accurate descriptors of oxygen vacancy formation energetics, Energy Environ. Sci. 7 (2014) 1996–2004.

[97] R. Michalsky, V. Botu, C. M. Hargus, A. A. Peterson, A. Steinfeld, Design principles for metal oxide redox materials for solar-driven isothermal fuel production, Adv. Energy Mater. 5 (2015) 1401082.

[98] E. Mastronardo, X. Qian, J. M. Coronado, S. M. Haile, The favourable thermodynamic properties of Fe-doped $CaMnO_3$ for thermochemical heat storage, J. Mater. Chem. A 8 (2020) 8503–8517.

[99] X. Qian, S. M. Haile, T. C. Davenport, E. Mastronardo, Experimental protocols for the assessment of redox thermodynamics of nonstoichiometric oxides: A case study of $YMnO_{3-\delta}$, Journal of the American Ceramic Society 105 (6) (2022) 4375–4386.

[100] J. He, B. Baldassarri, C. Wolverton, Assessment of exchange-correlation functionals on oxygen vacancy formation energies of metal oxides, under rewiew (2023).

[101] J. Kuo, H. Anderson, D. Sparlin, Oxidation-reduction behavior of undoped and Sr-doped $LaMnO_3$ nonstoichiometry and defect structure, J. Solid State Chem. 83 (1989) 52–60.

[102] J. Nowotny, M. Rekas, Defect chemistry of (La,Sr)MnO3, J. Am. Ceram. Soc. 81 (1998) 67–80.

[103] J. Mizusaki, M. Yoshihiro, S. Yamauchi, K. Fueki, Nonstoichiometry and defect structure of the perovskite-type oxides $La_{1-x}Sr_xFeO_{3-\delta}$, J. Solid State Chem. 58 (1985) 257–266.

[104] J. Mizusaki, Y. Mima, S. Yamauchi, K. Fueki, H. Tagawa, Nonstoichiometry of the perovskite-type oxides $La_{1-x}Sr_xCoO_{3-\delta}$, Solid State Chem. 80 (1989) 102–111.

[105] Y. Hao, C.-K. Yang, S. M. Haile, Ceria–zirconia solid solutions ($Ce_{1-x}Zr_xO_{2\delta}$, $x \leq 0.2$) for solar thermochemical water splitting: A thermodynamic study, Chemistry of Materials 26 (20) (2014) 6073–6082.

[106] B. Baldassarri, J. He, A. Gopakumar, S. Griesemer, S. Torrisi, A. Salgado Casanova, T. Liu, C. Wolverton, Oxygen Vacancy Formation Energy in Metal Oxides: High Throughput DFT Studies and Machine Learning Predictions, in prep.

[107] S. P. Ong, W. D. Richards, A. Jain, G. Hautier, M. Kocher, S. Cholia, D. Gunter, V. L. Chevrier, K. A. Persson, G. Ceder, Python materials genomics (pymatgen): A robust, open-source python library for materials analysis, Comput. Mater. Sci. 68 (2013) 314–319.

[108] J. He, B. Baldassarri, C. Wolverton, Stability Map of Double Perovskites, In Preparation (2022).

[109] J. He, B. Baldassarri, J. Hecter, C. Wolverton, Stability Map of Pyrochlore Oxides, In Preparation (2022).

[110] H.-C. Wang, S. Botti, M. A. L. Marques, Predicting stable crystalline compounds using chemical similarity, npj Computational Materials 7 (2021) 2057–3960.

[111] J. Shen, S. Griesemer, A. Gopakumar, B. Baldassarri, J. E. Saal, M. Aykol, V. Hegde, C. Wolverton, Reflections on one million compounds in the open quantum materials database (oqmd), Journal of Physics: Materials (2022).

[112] CRC Handbook of Chemistry and Physics, 87th ed Editor-in-Chief: David R. Lide (National Institute of Standards and Technology). CRC Press/Taylor and Francis Group: Boca Raton, FL. 2006.

[113] X. Qian, J. He, E. Mastronardo, B. Baldassarri, C. Wolverton, S. M. Haile, Favorable redox thermodynamics of $SrTi_{0.5}Mn_{0.5}O_{3\tilde{}\delta}$ in solar thermochemical water splitting, Chemistry of Materials 32 (21) (2020) 9335–9346.

[114] X. Qian, J. He, E. Mastronardo, B. Baldassarri, W. Yuan, C. Wolverton, S. M. Haile, Outstanding Properties and Performance of $CaTi_{0.5}Mn_{0.5}O_{3\tilde{}\delta}$ for Solar-Driven Thermochemical Hydrogen Production, Matter 4 (2) (2021) 688–708.

[115] V. M. Goldschmidt, Die gesetze der krystallochemie, Naturwissenschaften 14 (1926) 477–485.

[116] H. A. Tahini, X. Tan, U. Schwingenschlögl, S. C. Smith, Formation and migration of oxygen vacancies in $SrCoO_3$ and their effect on oxygen evolution reactions, ACS Catalysis 6 (8) (2016) 5565–5570.

[117] J. Varignon, M. Grisolia, J. Iniguez, Complete phase diagram of rare-earth nickelates from first-principles, npj Quant Mater 2 (21) (2017).

[118] M. W. Lufaso, P. M. Woodward, Prediction of the crystal structures of perovskites using the software program spuds, Acta Crystallographica Section B 57 (2001) 725–738.

[119] M. T. Anderson, K. B. Greenwood, G. A. Taylor, K. R. Poeppelmeier, B-cation arrangements in double perovskites, Progress in Solid State Chemistry 22 (3) (1993) 197–233.

[120] C. J. Howard, B. J. Kennedy, P. M. Woodward, Ordered double perovskites - A group-theoretical analysis, Acta Crystallographica Section B: Structural Science 59 (4) (2003) 463–471.

[121] G. King, P. M. Woodward, Cation ordering in perovskites, Journal of Materials Chemistry 20 (28) (2010) 5785–5796.

[122] S. Vasala, M. Karppinen, A2BBO6 perovskites: A review, Progress in Solid State Chemistry 43 (1-2) (2015) 1–36.

[123] S. D. Griesemer, L. Ward, C. Wolverton, High-throughput crystal structure solution using prototypes, Phys. Rev. Mater. 5 (10) (2021).

[124] C. Park, C. Wolverton, Developing an improved crystal graph convolutional neural network framework for accelerated materials discovery, Phys. Rev. Materials 4 (2020).

[125] H. Glawe, A. Sanna, E. K. U. Gross, M. A. L. Marques, The optimal one dimensional periodic table: A modified pettifor chemical scale from data mining, New Journal of Physics 18 (9) (2016).

[126] G. Hautier, C. Fischer, V. Ehrlacher, A. Jain, C. G., Data mined ionic substitutions for the discovery of new compounds, Inorganic Chemistry 50 (2) (2011) 656–663.

[127] H. Wang, S. Botti, M. A. L. Marques, Predicting stable crystalline compounds using chemical similarity, npj Computational Materials 7 (1) (2021) 12.

[128] Z. Wan, Q. Wang, D. Liu, J. Liang, Data-driven machine learning model for the prediction of oxygen vacancy formation energy of metal oxide materials, Physical Chemistry Chemical Physics 23 (29) (2021) 15675–15684.

[129] S. Liu, J. Wang, Z. Duan, K. Wang, W. Zhang, R. Guo, F. Xie, Simple Structural Descriptor Obtained from Symbolic Classification for Predicting the Oxygen Vacancy Defect Formation of Perovskites, ACS Applied Materials and Interfaces 14 (9) (2022) 11758–11767.

[130] M. Witman, A. Goya, T. Ogitsu, A. McDaniel, S. Lany, Materials discovery for high-temperature, clean-energy applications using graph neural network models of vacancy defects and free-energy calculations, ChemRxiv (2023). doi:10.26434/chemrxiv-2022-frcns.

[131] T. Xie, J. C. Grossman, Crystal Graph Convolutional Neural Networks for an Accurate and Interpretable Prediction of Material Properties, Physical Review Letters 120 (14) (2018) 145301. arXiv:1710.10324, doi:10.1103/PhysRevLett.120.145301.
URL https://doi.org/10.1103/PhysRevLett.120.145301

[132] L. Ward, A. Agrawal, A. Choudhary, C. Wolverton, A general-purpose machine learning framework for predicting properties of inorganic materials, npj Computational Materials 2 (July) (2016) 1–7.

[133] L. Breiman, Random forests, Machine Learning 45 (2001). doi:https://doi.org/10.1023/A:1010933404324.

[134] L. Ward, R. Liu, A. Krishna, V. I. Hegde, A. Agrawal, A. Choudhary, C. Wolverton, Including crystal structure attributes in machine learning models of formation energies via voronoi tessellations, Phys. Rev. B 96 (2017) 024104. doi:10.1103/PhysRevB.96.024104.
URL https://link.aps.org/doi/10.1103/PhysRevB.96.024104

[135] Y. Zhou, J. Gao, Y. Gui, J. Wen, Y. Wang, X. Huang, J. Cheng, Q. Liu, Q. Wang, C. Wei, Prediction of formation energies of ucr4c4-type compounds from magpie feature descriptor-based machine learning approaches, Optical Materials: X 16 (2022) 100196. doi:https://doi.org/10.1016/j.omx.2022.100196.
URL https://www.sciencedirect.com/science/article/pii/S2590147822000602

[136] G. King, S. Thimmaiah, A. Dwivedi, P. M. Woodward, Synthesis and characterization of new aabwo6 perovskites exhibiting simultaneous ordering of a-site and b-site cations, Chemistry of Materials 19 (26) (2007) 6451–6458. doi:10.1021/cm0716708.
URL https://doi.org/10.1021/cm0716708

[137] M. C. Knapp, Investigations into the Structure and Properties of Ordered Perovskites, Layered Perovskites, and Defect Pyrochlores, Ph.D. thesis, Ohio State University (2006).

[138] M. Roeb, M. Neises, N. Monnerie, F. Call, H. Simon, C. Sattler, M. Schmuker, R. Pitz-Paal, Materials-related aspects of thermochemical water and carbon dioxide splitting: A review, Materials 5 (2012) 2015–2054.

[139] H. Tan, Z. Zhao, W.-b. Zhu, E. N. Coker, B. Li, M. Zheng, W. Yu, H. Fan, Z. Sun, Oxygen Vacancy Enhanced Photocatalytic Activity of Pervoskite $SrTiO_3$, ACS Applied Materials & Interfaces 6 (21) (2014) 19184–19190. doi:10.1021/am5051907.

[140] M. Ji, J. H. Kim, C.-H. Ryu, Y.-I. Lee, Synthesis of self-modified black $BaTiO_{3x}$ nanoparticles and effect of oxygen vacancy for the expansion of piezocatalytic application, Nano Energy 95 (2022) 106993. doi:https://doi.org/10.1016/j.nanoen.2022.106993.

[141] S. A. Naghavi, A. A. Emery, H. A. Hansen, F. Zhou, V. Ozolins, C. Wolverton, Giant onsite electronic entropy enhances the performance of ceria for water splitting, Nature Communications 8 (2017).

[142] C. B. Gopal, A. van de Walle, Ab initio thermodynamics of intrinsic oxygen vacancies in ceria, Phys. Rev. B 86 (2012) 134117. doi:10.1103/PhysRevB.86.134117.

[143] S. Grieshammer, T. Zacherle, M. Martin, Entropies of defect formation in ceria from first principles, Phys. Chem. Chem. Phys. 15 (2013) 15935–15942. doi:10.1039/C3CP51913A.

[144] P. Agoston, K. Albe, Formation entropies of intrinsic point defects in cubic in2o3 from first-principles density functional theory calculations, Phys. Chem. Chem. Phys. 11 (2009) 3226–3232. doi:10.1039/B900280D.

[145] T. S. Bjorheim, M. Arrigoni, D. Gryaznov, E. Kotomin, J. Maier, Thermodynamic properties of neutral and charged oxygen vacancies in bazro3 based on first principles phonon calculations, Phys. Chem. Chem. Phys. 17 (2015) 20765–20774. doi:10.1039/C5CP02529J.

[146] B. Baldassarri, J. He, C. Wolverton, DFT Study of Vibrational Entropies of Oxygen Vacancy Formation in Metal Oxides, in prep.

[147] Thomas C. Allison, Nist-janaf thermochemical tables - srd 13 (2013). doi:10.18434/T42S31.
URL https://janaf.nist.gov/

[148] Liu, et al., High-throughput screening of short- and long-range order and electrochemical performance for rocksalt-type li-ion battery cathode materials design, in prep.

[149] G. Kyriakou, M. B. Boucher, A. D. Jewell, E. A. Lewis, T. J. Lawton, A. E. Baber, H. L. Tierney, M. Flytzani-Stephanopoulos, E. C. H. Sykes, Isolated metal atom geometries as a strategy for selective heterogeneous hydrogenations, Science 335 (6073) (2012) 1209–1212. doi:10.1126/science.1215864.
URL https://www.science.org/doi/abs/10.1126/science.1215864

[150] J. Liu, F. R. Lucci, M. Yang, S. Lee, M. D. Marcinkowski, A. J. Therrien, C. T. Williams, E. C. H. Sykes, M. Flytzani-Stephanopoulos, Tackling co poisoning with single-atom alloy catalysts, Journal of the American Chemical Society 138 (20) (2016) 6396–6399, pMID: 27167705. doi:10.1021/jacs.6b03339.
URL https://doi.org/10.1021/jacs.6b03339

[151] Z. Duan, G. Wang, A first principles study of oxygen reduction reaction on a pt(111) surface modified by a subsurface transition metal m (m = ni, co, or fe), Phys. Chem. Chem. Phys. 13 (2011) 20178–20187. doi:10.1039/C1CP21687B.
URL http://dx.doi.org/10.1039/C1CP21687B

[152] J. Suntivich, Z. Xu, C. E. Carlton, J. Kim, B. Han, S. W. Lee, N. Bonnet, N. Marzari, L. F. Allard, H. A. Gasteiger, K. Hamad-Schifferli, Y. Shao-Horn, Surface composition tuning of au–pt bimetallic nanoparticles for enhanced carbon monoxide and methanol electro-oxidation, Journal of the American Chemical Society 135 (21) (2013) 7985–7991, pMID: 23646922. doi:10.1021/ja402072r.

[153] Ruban, A. V. and Skriver, H. L. and Nørskov, J. K., Surface segregation energies in transition-metal alloys, Phys. Rev. B 59 (1999) 15990–16000. doi:10.1103/PhysRevB.59.15990.
URL https://link.aps.org/doi/10.1103/PhysRevB.59.15990

[154] A. U. Nilekar, A. V. Ruban, M. Mavrikakis, Surface segregation energies in low-index open surfaces of bimetallic transition metal alloys, Surface Science 603 (1) (2009) 91–96. doi:https://doi.org/10.1016/j.susc.2008.10.029.
URL https://www.sciencedirect.com/science/article/pii/S0039602808007279

[155] L. Farsi, N. A. Deskins, First principles analysis of surface dependent segregation in bimetallic alloys, Phys. Chem. Chem. Phys. 21 (2019) 23626–23637. doi:10.1039/C9CP03984H.
URL http://dx.doi.org/10.1039/C9CP03984H

[156] G. Wang, M. Van Hove, P. Ross, M. Baskes, Quantitative prediction of surface segregation in bimetallic pt–m alloy nanoparticles (m=ni,re,mo), Progress in Surface Science 79 (1) (2005) 28–45, x-th Symposium on Surface Physics, Prague, Czech Republic, 2005. doi:https://doi.org/10.1016/j.progsurf.2005.09.003.
URL https://www.sciencedirect.com/science/article/pii/S0079681605000511

[157] J. Creuze, I. Braems, F. Berthier, C. Mottet, G. Tréglia, B. Legrand, Model of surface segregation driving forces and their coupling, Phys. Rev. B 78 (2008) 075413. doi:10.1103/PhysRevB.78.075413.
URL https://link.aps.org/doi/10.1103/PhysRevB.78.075413

[158] R. Tran, Z. Xu, B. Radhakrishnan, D. Winston, W. Sun, K. A. Persson, S. P. Ong, Surface energies of elemental crystals, Sci Data 3 (2016) 160080.

[159] W. Chen, W. F. Schneider, C. Wolverton, Trends in atomic adsorption on pt3m(111) transition metal bimetallic surface overlayers, The Journal of Physical Chemistry C 118 (16) (2014) 8342–8349. doi:10.1021/jp410607k.

[160] Y. Ma, P. B. Balbuena, Pt surface segregation in bimetallic pt3m alloys: A density functional theory study, Surface Science 602 (1) (2008) 107–113. doi:https://doi.org/10.1016/j.susc.2007.09.052.
URL https://www.sciencedirect.com/science/article/pii/S0039602807009806

[161] Y. Zhang, Z. Duan, C. Xiao, G. Wang, Density functional theory calculation of platinum surface segregation energy in pt3ni (111) surface doped with a third transition metal, Surface Science 605 (15) (2011) 1577–1582. doi:https://doi.org/10.1016/j.susc.2011.05.032.
URL https://www.sciencedirect.com/science/article/pii/S0039602811002226

[162] J. Gao, H. Tao, B. Liu, Progress of nonprecious-metal-based electrocatalysts for oxygen evolution in acidic media, Advanced Materials 33 (31) (2021) 2003786. doi:https://doi.org/10.1002/adma.202003786.

[163] A. Hailu, A. A. Tamijani, S. E. Mason, S. K. Shaw, Efficient conversion of co2 to formate using inexpensive and easily prepared post-transition metal alloy catalysts, Energy & Fuels 34 (3) (2020) 3467–3476. doi:10.1021/acs.energyfuels.9b03783.

[164] D. Ologunagba, S. Kattel, Machine learning prediction of surface segregation energies on low index bimetallic surfaces, Energies 13 (9) (2020). doi:10.3390/en13092182.
URL https://www.mdpi.com/1996-1073/13/9/2182

[165] K. Rao, Q. Do, K. Pham, D. Maiti, L. C. Grabow, Extendable machine learning model for the stability of single atom alloys, Topics in Catalysis 63 (2020) 728–741.
URL https://doi.org/10.1007/s11244-020-01267-2

[166] M. Salem, M. J. Cowan, G. Mpourmpakis, Predicting segregation energy in single atom alloys using physics and machine learning, ACS Omega 7 (5) (2022) 4471–4481. doi:10.1021/acsomega.1c06337.

[167] B. K. Vainshtein, V. M. Fridkin, V. L. Indenbom, The Structure of Real Crystals, Springer Berlin Heidelberg, Berlin, Heidelberg, 1995, pp. 330–399. doi:10.1007/978-3-642-97512-7_5.
URL https://doi.org/10.1007/978-3-642-97512-7_5

[168] L. Chanussot, A. Das, S. Goyal, T. Lavril, M. Shuaibi, M. Riviere, K. Tran, J. Heras-Domingo, C. Ho, W. Hu, A. Palizhati, A. Sriram, B. Wood, J. Yoon, D. Parikh, C. L. Zitnick, Z. Ulissi, Open catalyst 2020 (oc20) dataset and community challenges, ACS Catalysis 11 (10) (2021) 6059–6072. doi:10.1021/acscatal.0c04525.

[169] Y. C. Kimmel, X. Xu, W. Yu, X. Yang, J. G. Chen, Trends in electrochemical stability of transition metal carbides and their potential use as supports for low-cost electrocatalysts, ACS Catalysis 4 (5) (2014) 1558–1562. doi:10.1021/cs500182h.

[170] P. Tereshchuk, D. Golodnitsky, A. Natan, Trends in the Adsorption of Oxygen and Li2O2 on Transition-Metal Carbide Surfaces: A Theoretical Study, Journal of Physical Chemistry C 124 (14) (2020) 7716–7724. doi:10.1021/acs.jpcc.9b10863.

[171] B. Hammer, J. K. Nørskov, Electronic factors determining the reactivity of metal surfaces, Surface Science 343 (3) (1995) 211–220. doi:10.1016/0039-6028(96)80007-0.

[172] B. Hammer, Y. Morikawa, J. K. Nørskov, CO chemisorption at metal surfaces and overlayers, Physical Review Letters 76 (12) (1996) 2141–2144. doi:10.1103/PhysRevLett.76.2141.

[173] A. Ruban, B. Hammer, P. Stoltze, H. Skriver, J. Nørskov, Surface electronic structure and reactivity of transition and noble metals1communication presented at the first francqui colloquium, brussels, 19–20 february 1996.1, Journal of Molecular Catalysis A: Chemical 115 (3) (1997) 421–429. doi:https://doi.org/10.1016/S1381-1169(96)00348-2.
URL https://www.sciencedirect.com/science/article/pii/S1381116996003482

[174] M. Mavrikakis, B. Hammer, J. K. Nørskov, Effect of strain on the reactivity of metal surfaces, Phys. Rev. Lett. 81 (1998) 2819–2822. doi:10.1103/PhysRevLett.81.2819.
URL https://link.aps.org/doi/10.1103/PhysRevLett.81.2819

[175] J. Greeley, J. K. Nørskov, A general scheme for the estimation of oxygen binding energies on binary transition metal surface alloys, Surface Science 592 (1-3) (2005) 104–111. doi:10.1016/j.susc.2005.07.018.

[176] J. R. Kitchin, J. K. Nørskov, M. A. Barteau, J. G. Chen, Modification of the surface electronic and chemical properties of Pt(111) by subsurface 3d transition metals, Journal of Chemical Physics 120 (21) (2004) 10240–10246. doi:10.1063/1.1737365.

[177] J. R. Kitchin, J. K. Nørskov, M. A. Barteau, J. G. Chen, Role of strain and ligand effects in the modification of the electronic and chemical Properties of bimetallic surfaces, Physical Review Letters 93 (15) (2004) 4–7. doi:10.1103/PhysRevLett.93.156801.

[178] J. R. Kitchin, J. K. Nørskov, M. A. Barteau, J. G. Chen, Trends in the chemical properties of early transition metal carbide surfaces: A density functional study, Catalysis Today 105 (1 SPEC. ISS.) (2005) 66–73. doi:10.1016/j.cattod.2005.04.008.

[179] M. J. Eslamibidgoli, M. H. Eikerling, Atomistic Mechanism of Pt Extraction at Oxidized Surfaces: Insights from DFT, Electrocatalysis 7 (4) (2016) 345–354. doi:10.1007/s12678-016-0313-2.
URL http://dx.doi.org/10.1007/s12678-016-0313-2

[180] D. S. Rivera Rocabado, Y. Nanba, M. Koyama, Density functional theory and machine learning description and prediction of oxygen atom chemisorption on platinum surfaces and nanoparticles, ACS Omega 6 (27) (2021) 17424–17432. doi:10.1021/acsomega.1c01726.

[181] F. Calle-Vallejo, J. I. Martínez, J. M. García-Lastra, P. Sautet, D. Loffreda, Fast prediction of adsorption properties for platinum nanocatalysts with generalized coordination numbers, Angewandte Chemie - International Edition 53 (32) (2014) 8316–8319. doi:10.1002/anie.201402958.

[182] S. Schnur, A. Groß, Strain and coordination effects in the adsorption properties of early transition metals: A density-functional theory study, Physical Review B - Condensed Matter and Materials Physics 81 (3) (2010) 1–4. doi:10.1103/PhysRevB.81.033402.

[183] R. Michalsky, Y. J. Zhang, A. J. Medford, A. A. Peterson, Departures from the adsorption energy scaling relations for metal carbide catalysts, Journal of Physical Chemistry C 118 (24) (2014) 13026–13034. doi:10.1021/jp503756g.

[184] R. J. Fries, C. Kempter, Dimolybdenum Carbide, Crystallographic Data (195) (1962) 1898.

[185] X. R. Shi, S. G. Wang, H. Wang, C. M. Deng, Z. Qin, J. Wang, Structure and stability of β-Mo2C bulk and surfaces: A density functional theory study, Surface Science 603 (6) (2009) 852–859. doi:10.1016/j.susc.2009.01.041.
URL http://dx.doi.org/10.1016/j.susc.2009.01.041

[186] J. Haines, J. M. Léger, C. Chateau, J. E. Lowther, Experimental and theoretical investigation of mosub2/subc at high pressure, Journal of Physics: Condensed Matter 13 (11) (2001) 2447–2454. doi:10.1088/0953-8984/13/11/303.
URL https://doi.org/10.1088/0953-8984/13/11/303

[187] J. W. Han, L. Li, D. S. Sholl, Density Functional Theory Study of H and CO Adsorption on Alkali-Promoted Mo2C Surfaces, The Journal of Physical Chemistry C 115 (14) (2011) 6870–6876. doi:10.1021/jp200950a.
URL https://doi.org/10.1021/jp200950a

[188] T. Wang, X. Liu, S. Wang, C. Huo, Y. W. Li, J. Wang, H. Jiao, Stability of β-Mo2C facets from Ab initio atomistic thermodynamics, Journal of Physical Chemistry C 115 (45) (2011) 22360–22368. doi:10.1021/jp205950x.

[189] M. P. Andersson, T. Bligaard, A. Kustov, K. E. Larsen, J. Greeley, T. Johannessen, C. H. Christensen, J. K. Nørskov, Toward computational screening in heterogeneous catalysis: Pareto-optimal methanation catalysts, Journal of Catalysis 239 (2) (2006) 501–506. doi:https://doi.org/10.1016/j.jcat.2006.02.016.
URL https://www.sciencedirect.com/science/article/pii/S0021951706000674

[190] M. Liu, High-throughput Materials Discovery and its Application to Poly-elemental Nanoparticles, Ph.D. thesis.

[191] S. S. Naghavi, J. He, C. Wolverton, Ceti2o6—a promising oxide for solar thermochemical hydrogen production, ACS Applied Materials & Interfaces 12 (19) (2020) 21521–21527, pMID: 32320199. doi:10.1021/acsami.0c01083.
URL https://doi.org/10.1021/acsami.0c01083

Appendix A: Additional Figures

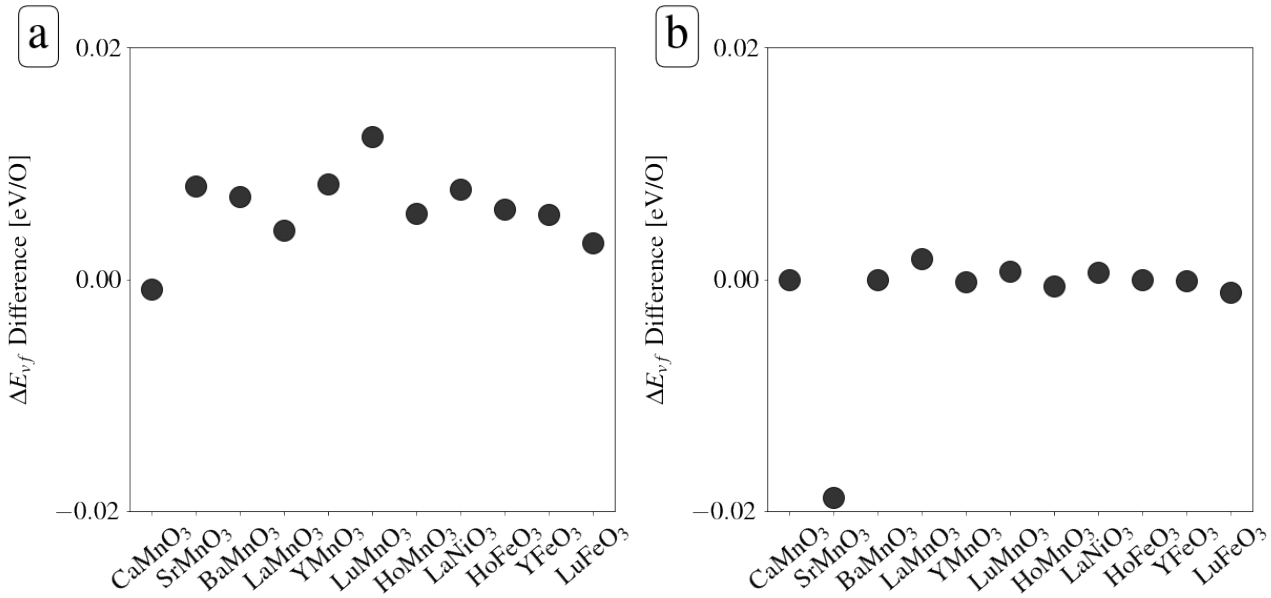

Figure 11.62: Difference in oxygen vacancy formation energy for the compounds in Figure 3.5 (computed for the DSD structure) (a) between using a plane wave cutoff of 800 eV and a 520 eV, and (b) between a threshold of atomic forces of 0.001 eV/Åand of 0.01 eV/Å(note that for $SrMnO_3$ and $BaMnO_3$ a 0.002 eV/Åthreshold was used due to a much slower convergence). In all cases differences in ΔE_{vf} using the two different convergence criteria are less than 0.02 eV/O.

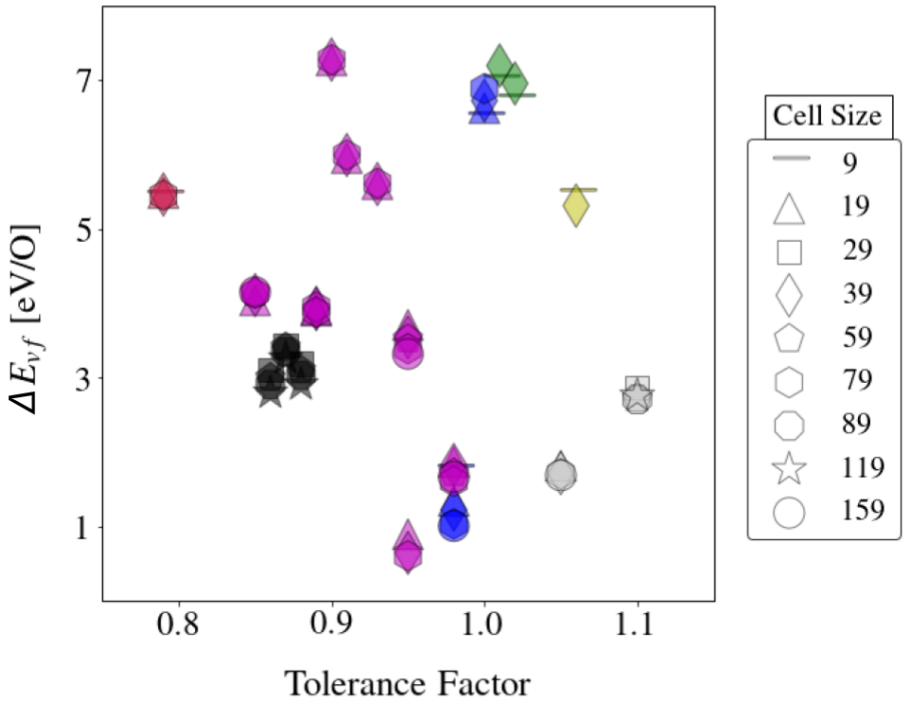

Figure 11.63: Convergence in oxygen vacancy formation energy with cell size as a function of tolerance, with different marker types indicating the cell size. Interestingly, the compounds with the largest difference in E_{vf} between cell sizes are the ones whose tolerance is closest to 1. Colors indicate different structures: pink for ilmenite (R-3), purple for orthorhombic pervoskite (Pnma), blue for rhombohedral perovskite (R-3c), green for cubic perovskite (Pm-3m), yellow for tetragonal perovskite (P4mm), black for hexagonal structure with "$LuMnO_3$" prototype ($P6_3cm$), gray for the DSD structure for $SrMnO_3$, with prototype "$CsCuBr_3$" ($C222_1$), and $BaMnO_3$, with prototype "$KNiCl_3$" ($P6_3cm$). Compounds with orthorhombic structure dominate the high-throughput search, and have thus been thoroughly analysed by choosing A and B site elements from the most common groups identified in the work by Emery et al. Compounds in the figure are, in descending order of ΔE_{vf}: $CaHfO_3$, $BaHfO_3$, $AcAlO_3$, $LaAlO_3$, $DyCrO_3$, $PmGaO_3$, $BaTiO_3$, $FeTiO_3$, $YFeO_3$, $GdRhO_3$, $YbIrO_3$, $LaMnO_3$, $LuMnO_3$, $HoMnO_3$, $YMnO_3$, $BaMnO_3$, $CaMnO_3$, $SrMnO_3$, $LaNiO_3$, $BaPdO_3$

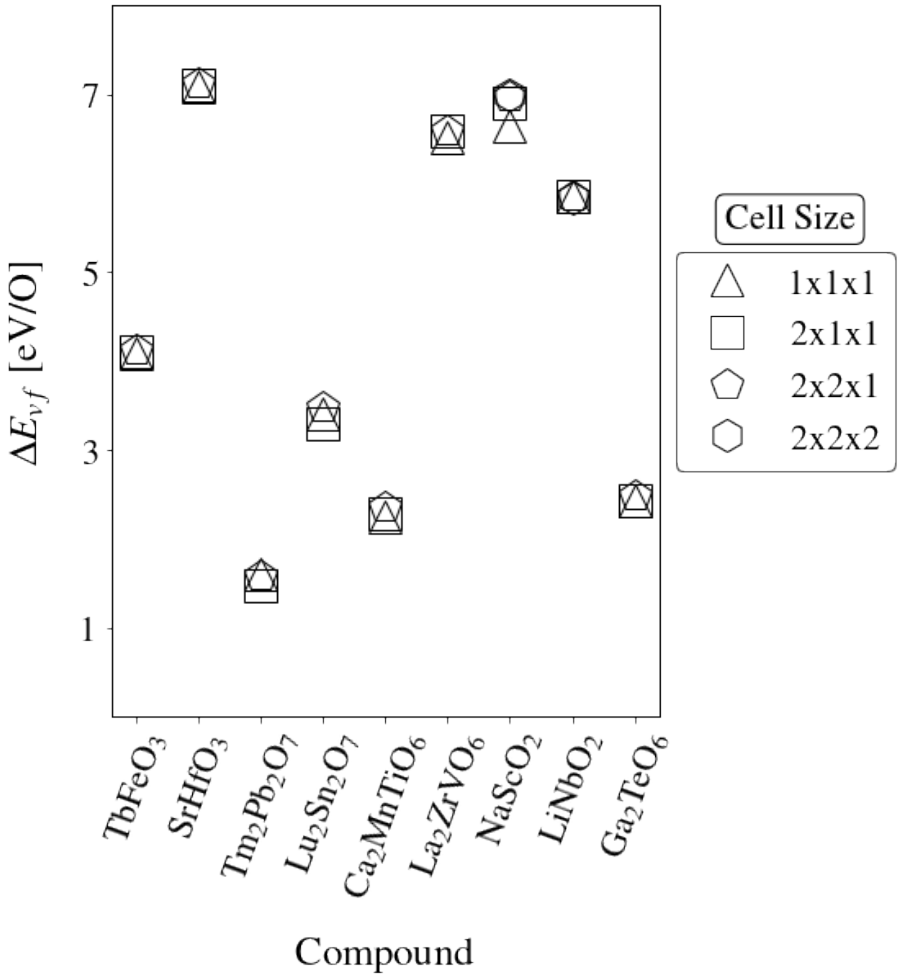

Figure 11.64: Change in oxygen vacancy formation energy of different compounds with size of the vacancy-containing cell. For all cell sizes greater than 16 atoms (which is the case for all compounds presented in the figure other than $LiNbO_2$, which has 8 atoms in its unit cell, and $NaScO_2$, which has 4) ΔE_{vf} is converged to within 0.1eV/O.

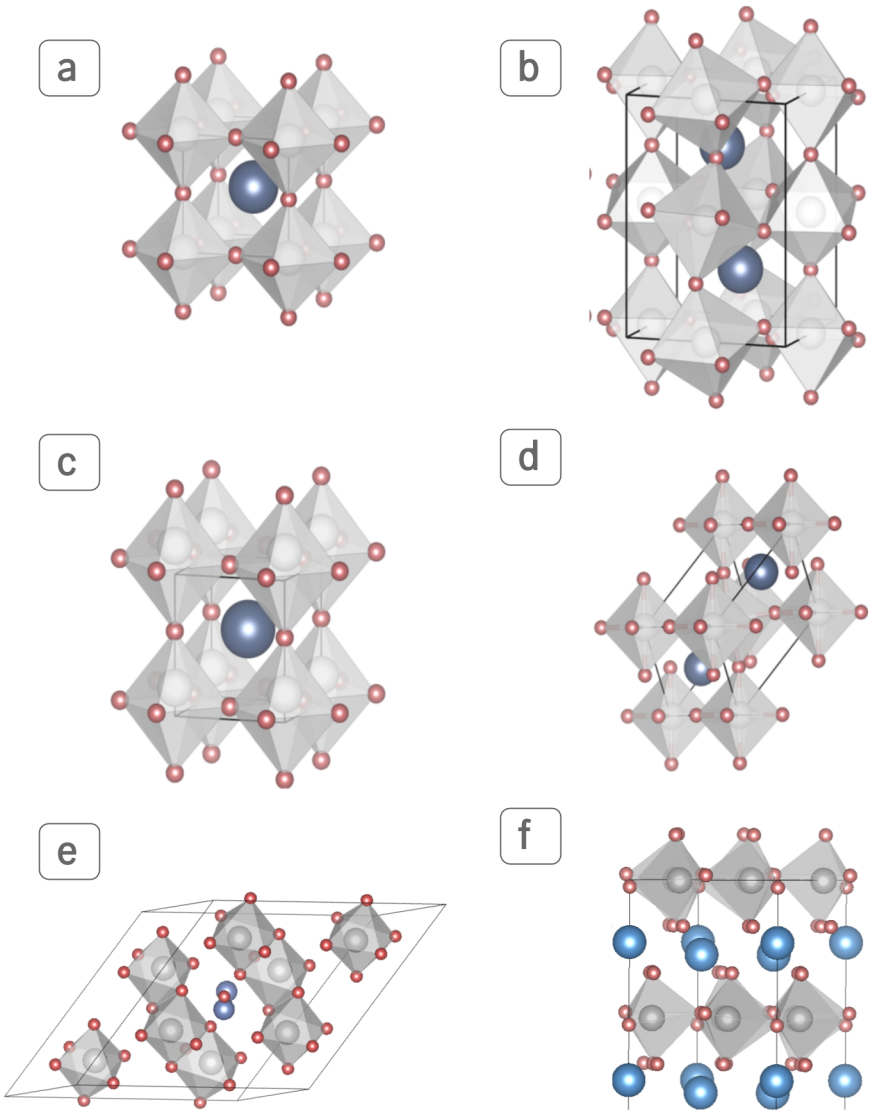

Figure 11.65: Prototype structures used in the high-throughput study of ABO_3 compounds discussed in Section 4.3 The most common perovskite structural distortions (a) cubic (Pm-3m), (b) orthorhombic (Pnma), (c) tetragonal(P4mm), (d) rhombohedral(R-3c) were surveyed for all ABO_3 compositions,. Then, for compositions where at least one of the perovskite structures was found to be within 25 meV/atom from the convex hull, the next 3 most common stable ABO_3 structures on the ICSD were computed: (e) ilmenite (R-3), (f) hexagonal "$LuMnO_3$" prototype ($P6_3cm$), and rhombohedral "$CaCO_3$" prototype (R-3c, here not pictured as it was never found to have lower energy than the stable perovskite structure at the same composition). These are also the structures observed experimentally for multiple compounds discussed in Section 3.3 $CaMnO_3$, $YFeO_3$, $HoFeO_3$, $LuFeO_3$, $PrCoO_3$ and $SmCoO_3$ have both EXP and DSD orthorhombic perovskite structures (b) , $LaCoO_3$ and $LaNiO_3$ have both EXP and DSD rhombohedral perovskite structures (d), $LaMnO_3$ has an EXP rhombohedral perovskite structure (d) and a DSD orthorhombic perovskite structure (b), and $LuMnO_3$, $YMnO_3$ and $HoMnO_3$ have both EXP and DSD structures with "$LuMnO_3$" prototype (f).

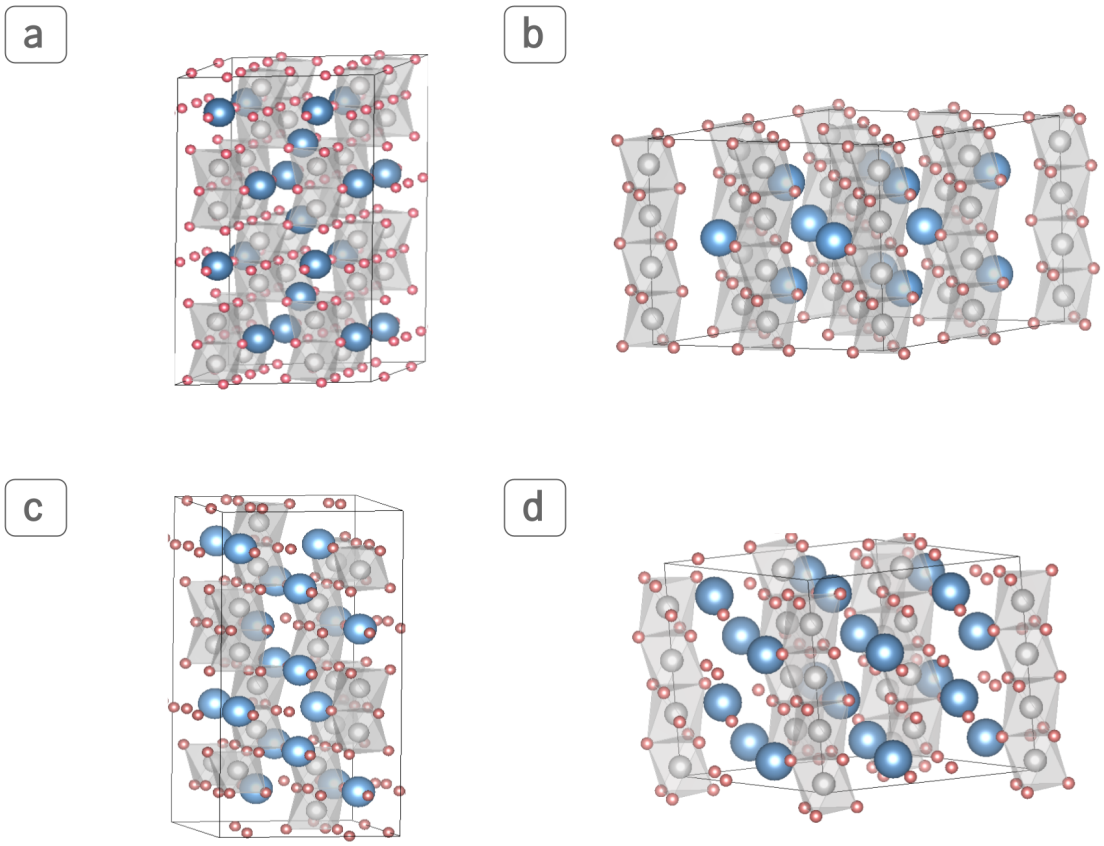

Figure 11.66: Comparison between the dynamically unstable structure observed experimentally (top) and the dynamically stable structure employed in DFT simulations (bottom) for $SrMnO_3$ (left) and $BaMnO_3$ (right), discussed in Section 3.3 . (a) is $SrMnO_3$ with prototype "$BaMnO_3$" ($P6_3/mmc$), (b) is $BaMnO_3$ with prototype "$BaNiO_3$" ($P6_3/mmc$), (c) $SrMnO_3$ with prototype "$CsCuBr_3$" ($C222_1$), (d) $BaMnO_3$ with prototype "$KNiCl_3$" ($P6_3cm$).

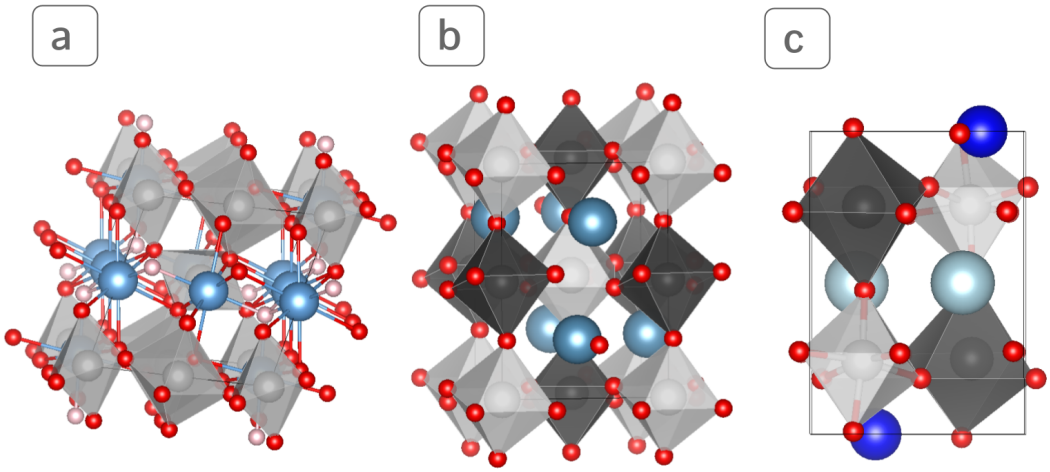

Figure 11.67: Prototype structures used in the high-throughput studies of (a) $A_2B_2O_7$ pyrochlores, and (b) $A_2BB'O_6$ and (c) $AA'BB'O_6$ double perovskites. A cations are in blue (different shades for different species in $AA'BB'O_6$), B cations are in grey (different shades for different species in $AA'BB'O_6$ and $A_2BB'O_6$), and oxygen anions in red (different shades for the two oxygen types, referred to as V1 and V2 in Section 4.3, in $A_2B_2O_7$)

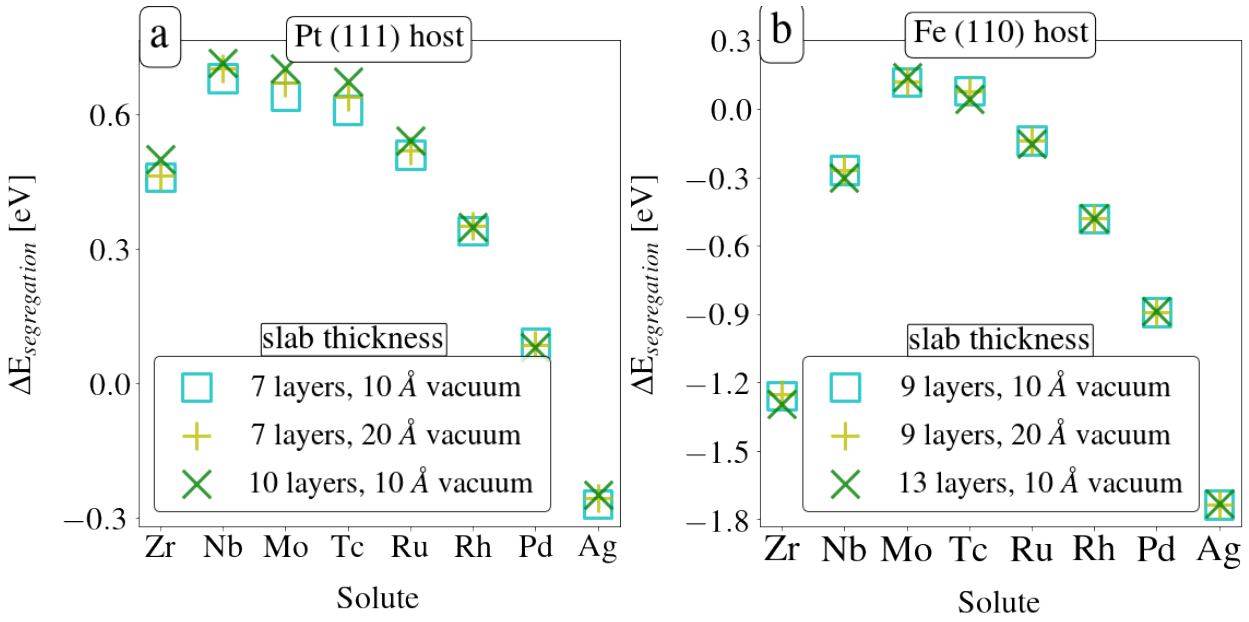

Figure 11.68: Surface segregation energy of transition metal solutes to (a) the 111 surface of FCC Pt and (b) the 110 surface of BCC Fe, with different markers indicating different thickness of the slab and of the vacuum layer.

Appendix B: List of Candidate STCH Compounds

Table 12.4: List of all DFT stable ABO_3 compounds with a vacancy formation energy within the window of interest for STCH applications. Each column indicates (from the left) the compound's formula, stability on the OQMD, DFT-computed oxygen vacancy formation energy of the lowest energy oxygen site, and OQMD entry id. Compounds whose initial structure was not obtained through one of the 4 prototype perovskite distortions in Fig 11.65 are marked with asterisks, two asterisks for structures imported from the ICSD, one for hypothetical prototypes

Composition	ΔE_{stab} [eV/atom]	ΔE_{vf} [eV/O]	OQMD Entry ID
$KRhO_3$*	-0.045	2.0	679672
$SrBiO_3$	0.012	2.0	681684
$BMnO_3$*	0.009	2.0	1390037
$SrPbO_3$	-0.041	2.1	682323
$CsSbO_3$*	-0.009	2.1	692568
$RbAsO_3$*	-0.05	2.1	1367023
$AgAsO_3$*	-0.024	2.1	692657
$LaAuO_3$**	-0.07	2.1	13267
$KAsO_3$*	-0.033	2.1	1349221
$CaPdO_3$*	0.018	2.2	1371367
$BiMnO_3$	0.023	2.2	682095
$NaPtO_3$*	-0.024	2.2	678856
$LiRuO_3$*	-0.015	2.3	1775242
$HgTeO_3$**	0.019	2.3	11518
$BaPdO_3$*	-0.105	2.4	1368197
$YbPdO_3$*	-0.091	2.4	1371628
$CaPbO_3$*	-0.028	2.4	692558
$CuAsO_3$*	0.002	2.5	692845
$NiPdO_3$*	-0.019	2.5	1734039
$CdPtO_3$*	0.004	2.5	1322992
$YbPbO_3$*	-0.019	2.5	692589
$PmCoO_3$	-0.013	2.5	682619
$AgVO_3$**	-0.007	2.5	14776
$PrCoO_3$	-0.0	2.5	1602675
$LaCoO_3$	0.001	2.6	681655
$EuPtO_3$	-0.065	2.7	682040
$AuSbO_3$*	-0.011	2.7	1366270
$LiIrO_3$*	-0.035	2.7	1775246
$TbCoO_3$	0.024	2.7	682958
$TlAsO_3$*	-0.048	2.7	1739267
$KRuO_3$*	0.008	2.7	679312
$MgMnO_3$*	-0.012	2.8	692913
$LiVO_3$*	-0.005	2.8	678942
$NiMnO_3$**	-0.031	2.8	6121
$BaPtO_3$*	-0.116	2.8	1374564

$BaRhO_3$*	-0.053	2.8	1735051
$NaAsO_3$*	-0.03	2.8	678505
KVO_3**	-0.017	2.8	1937
$BaMnO_3$**	-0.034	2.8	15847
$EuPbO_3$	-0.026	2.9	682396
$HgVO_3$**	-0.002	2.9	14798
$SmCoO_3$	0.01	3.0	681405
$TlRhO_3$*	-0.002	3.0	1323315
$RbVO_3$**	-0.02	3.0	1939
$TlRuO_3$*	-0.003	3.0	1323314
$NdCoO_3$	0.004	3.0	682643
$SrPtO_3$*	0.019	3.0	1370500
$CuSbO_3$*	0.007	3.0	692575
$KIrO_3$*	-0.093	3.0	678385
$ErFeO_3$*	-0.025	3.0	1289965
$CaRhO_3$**	-0.007	3.1	20858
$NaIrO_3$*	-0.041	3.1	678620
$YbPtO_3$*	-0.099	3.1	1372997
$LiAsO_3$*	-0.053	3.1	692788
$YMnO_3$**	-0.033	3.1	20815
$TmFeO_3$**	-0.029	3.1	9944
$RbSbO_3$*	-0.094	3.1	678277
$NaRuO_3$*	-0.009	3.2	678662
$NaTcO_3$	-0.053	3.2	351423
$InFeO_3$**	0.006	3.2	12707
$SrRhO_3$*	-0.017	3.2	1366189
$KTcO_3$	-0.025	3.2	354565
$CdGeO_3$**	0.005	3.3	37777
$BaTeO_3$**	-0.042	3.3	2375
$ScMnO_3$**	0.007	3.3	646566
$HoFeO_3$*	-0.02	3.3	1289960
$MnGeO_3$*	-0.029	3.3	1364346
$LiTcO_3$	0.017	3.3	826292
$KSbO_3$*	-0.102	3.3	678860
$BaIrO_3$*	-0.005	3.3	1374687
$FeTeO_3$	-0.006	3.3	1758758
$BTlO_3$*	-0.025	3.3	1377332
$HgIrO_3$*	-0.006	3.4	1323027
$HgSbO_3$*	-0.047	3.4	1365265
$TmMnO_3$**	-0.046	3.4	20526
$FeRhO_3$*	0.02	3.4	1749929
$TbMnO_3$*	-0.032	3.4	1289713
$TlVO_3$*	0.001	3.4	1346120
$NiGeO_3$*	0.012	3.5	1347235
$LaMnO_3$	0.0	3.5	682005
$ZnTeO_3$**	0.001	3.5	37405
$CaIrO_3$**	-0.01	3.5	4775
$SrGeO_3$**	-0.05	3.5	11090
$LuFeO_3$*	-0.028	3.5	1289991
$LiSbO_3$**	-0.056	3.5	4513
$RbOsO_3$*	0.019	3.5	678964
$HgAsO_3$**	-0.039	3.5	25361
$SbAsO_3$**	-0.011	3.6	6869
$SrTeO_3$**	-0.023	3.6	22435
$LaRhO_3$	-0.046	3.6	682003
$GePbO_3$**	-0.05	3.6	21913
$DyMnO_3$**	-0.036	3.6	24010
$CeRhO_3$	-0.048	3.6	681387
$PrRhO_3$	-0.04	3.6	682842
$MgGeO_3$**	-0.024	3.6	6605
$NdRhO_3$	-0.034	3.6	682453
$NaSbO_3$*	-0.137	3.7	678635

$PmRhO_3$	-0.029	3.7	682729
$CeMnO_3$	-0.069	3.7	682131
$HoMnO_3$**	-0.038	3.7	16146
$SrIrO_3$*	-0.005	3.7	1375571
$BFeO_3$**	-0.018	3.7	6449
$TbRhO_3$**	-0.013	3.7	21885
$SmRhO_3$	-0.024	3.7	693355
$CsVO_3$**	-0.049	3.7	32716
$YbIrO_3$*	-0.06	3.7	1367021
$NaOsO_3$	0.005	3.7	682146
$GdMnO_3$*	-0.029	3.7	1289760
$PrMnO_3$	0.002	3.8	681412
$GdRhO_3$	-0.018	3.8	693421
$ErMnO_3$**	-0.039	3.8	20525
$YRhO_3$*	-0.004	3.8	1276731
$SrRuO_3$	-0.013	3.8	681695
$EuIrO_3$*	-0.055	3.8	1363245
$NdMnO_3$	0.001	3.8	682271
$TlSbO_3$**	-0.101	3.8	13943
$PmMnO_3$	-0.056	3.8	681391
$CdSnO_3$*	-0.013	3.8	692621
$YbTeO_3$*	-0.004	3.8	692527
$ErRhO_3$*	-0.008	3.9	1370838
$LuMnO_3$**	-0.04	3.9	20527
$TlOsO_3$*	-0.041	3.9	1323322
$TiCdO_3$*	-0.021	3.9	678398
$PbVO_3$*	0.018	3.9	1752471
$BaGeO_3$*	-0.053	3.9	1364441
$SmMnO_3$*	-0.034	3.9	1708044
$NaReO_3$	0.007	3.9	353271
$RbTcO_3$*	-0.057	3.9	1482539
$TmRhO_3$*	-0.007	3.9	1759375
$LuRhO_3$*	-0.003	3.9	1763609
$LiOsO_3$	0.007	3.9	826281
$BiGaO_3$**	0.005	3.9	21825
$InGeO_3$*	-0.009	3.9	1597020
$CaVO_3$	-0.009	4.0	681780
$CaRuO_3$	-0.017	4.0	681693
$VCdO_3$**	-0.003	4.0	15653
$EuRuO_3$	-0.042	4.0	681894
$NbAgO_3$*	0.021	4.0	678273
$CeFeO_3$	-0.047	4.1	682411
$MnSnO_3$*	-0.023	4.1	692986
$PbSnO_3$*	0.017	4.1	679426
$DyFeO_3$	-0.019	4.2	693143
$TbFeO_3$	-0.021	4.2	693084
$NdFeO_3$	-0.036	4.2	681760
$BaSnO_3$	-0.019	4.2	352504
$GdFeO_3$	0.0	4.2	681830
$CsTcO_3$*	-0.013	4.2	678263
$SmFeO_3$	-0.03	4.2	681794
$YFeO_3$	-0.016	4.2	693115
$CaGeO_3$*	0.014	4.2	1740539
$PrInO_3$*	-0.018	4.2	1289953
$CeInO_3$*	-0.017	4.3	1289928
$PrFeO_3$	-0.04	4.3	682008
$BaOsO_3$*	0.016	4.3	1735058
$NiSnO_3$*	-0.005	4.3	1371889
$MgSnO_3$*	-0.011	4.3	1278185
$SmInO_3$*	-0.015	4.3	1376057
$PmInO_3$*	-0.016	4.3	1289989
$SrSnO_3$	-0.015	4.3	682160

$PmFeO_3$	-0.063	4.3	682227
$BaRuO_3$**	-0.029	4.4	21866
$CrFeO_3$*	0.003	4.4	1743455
$LaInO_3$*	-0.012	4.4	1289942
$NdInO_3$*	-0.02	4.4	1367680
$SnGeO_3$*	-0.021	4.4	678714
$BiCrO_3$	0.018	4.4	682285
$ScGaO_3$*	0.015	4.4	1748177
$YbOsO_3$	0.024	4.4	682034
$GaInO_3$**	0.003	4.5	5814
$EuTcO_3$	-0.067	4.5	681980
$CaSnO_3$*	-0.013	4.5	679059
$FeVO_3$*	-0.013	4.5	1741536
$VBiO_3$	0.007	4.6	682938
$AlSbO_3$*	0.019	4.6	692518
$TiSnO_3$*	0.022	4.6	678608
$ZrCdO_3$*	0.023	4.6	692582
$LuGaO_3$*	0.001	4.6	1748176
$EuSnO_3$	-0.061	4.7	681696
$YbSnO_3$	-0.02	4.7	682934
$VNiO_3$*	0.011	4.7	1745056
$HfCdO_3$*	0.015	4.8	678495
$TiCrO_3$*	0.008	4.8	679714
$ZnVO_3$*	0.002	4.8	1745057
$CaTcO_3$	-0.017	4.9	681718
$BaMoO_3$	0.012	4.9	352904
$PbTiO_3$	-0.021	5.0	679867

Table 12.5: List of all DFT stable double perovskite $A_2B_2O_7$ pyrochlore compounds with vacancy formation energy within the window of interest for STCH applications.

Composition	ΔE_{vf} [eV/O]
$Gd_2Pb_2O_7$	2.0
$Sm_2Mn_2O_7$	2.1
$Ca_2Ir_2O_7$	2.1
$La_2Pd_2O_7$	2.1
$Tm_2Pd_2O_7$	2.1
$Er_2Pd_2O_7$	2.1
$Ho_2Pd_2O_7$	2.2
$Gd_2Mn_2O_7$	2.2
$Tb_2Mn_2O_7$	2.2
$Ce_2Pd_2O_7$	2.2
$Dy_2Mn_2O_7$	2.2
$Sm_2Pb_2O_7$	2.2
$Dy_2Pd_2O_7$	2.2
$Pr_2Pd_2O_7$	2.2
$Tb_2Pd_2O_7$	2.2
$Bi_2Rh_2O_7$	2.2
$Ho_2Mn_2O_7$	2.2
$Tm_2Mn_2O_7$	2.2
$Nd_2Pd_2O_7$	2.2
$Sm_2Pd_2O_7$	2.2
$Nd_2Pb_2O_7$	2.3
$Pr_2Pb_2O_7$	2.4
$La_2Pb_2O_7$	2.4
$Ce_2Pb_2O_7$	2.4
$Tl_2Ge_2O_7$	2.4
$Lu_2Rh_2O_7$	2.6
$Tm_2Rh_2O_7$	2.7
$Er_2Rh_2O_7$	2.8
$Ho_2Rh_2O_7$	2.9
$Dy_2Rh_2O_7$	2.9
$Tb_2Rh_2O_7$	2.9
$Gd_2Rh_2O_7$	3.0
$Sm_2Rh_2O_7$	3.1
$La_2Rh_2O_7$	3.2
$Nd_2Rh_2O_7$	3.2
$Ce_2Rh_2O_7$	3.2
$Pr_2Rh_2O_7$	3.2
$Tm_2Ir_2O_7$	3.4
$Lu_2Sn_2O_7$	3.4
$Tm_2Sn_2O_7$	3.6
$Lu_2V_2O_7$	3.6
$Tb_2Ir_2O_7$	3.7
$Gd_2Ir_2O_7$	3.7
$Tm_2V_2O_7$	3.8
$Ho_2Sn_2O_7$	3.8
$Er_2V_2O_7$	3.8
$Ho_2V_2O_7$	3.8
$Dy_2Sn_2O_7$	3.8
$Nd_2Ir_2O_7$	3.9
$Pr_2Ir_2O_7$	4.0
$Gd_2Sn_2O_7$	4.0
$La_2Ir_2O_7$	4.1
$Sm_2Sn_2O_7$	4.2
$Nd_2Sn_2O_7$	4.3
$Pr_2Sn_2O_7$	4.4
$Gd_2Fe_2O_7$	4.4
$Dy_2V_2O_7$	4.4

$La_2Sn_2O_7$	4.5
$Ce_2Sn_2O_7$	4.5
$Lu_2Ge_2O_7$	4.8

Table 12.6: List of all DFT stable double perovskite $A_2BB'O_6$ compounds with vacancy formation energy within the window of interest for STCH applications.

Composition	ΔE_{vf} [eV/O]
Ca_2ZnRuO_6	2.0
Ba_2TlIrO_6	2.0
Sr_2TiPdO_6	2.0
Ca_2CoSbO_6	2.0
Sr_2PdPbO_6	2.0
Sr_2CoSbO_6	2.1
Ba_2SnPbO_6	2.1
Ba_2HgIrO_6	2.1
Ba_2ZnRuO_6	2.1
Sr_2TiMnO_6	2.1
Ca_2TlSbO_6	2.2
Ca_2InBiO_6	2.2
Sr_2InBiO_6	2.2
Ba_2TlSbO_6	2.2
Sr_2HgIrO_6	2.2
$CdTePb_2O_6$	2.2
Sr_2FeRhO_6	2.2
Sr_2SnPbO_6	2.2
Ba_2HgTeO_6	2.2
Sr_2NbCoO_6	2.3
Ca_2NiRuO_6	2.3
Sr_2NiRuO_6	2.3
Sr_2RuPbO_6	2.3
Sr_2TaTlO_6	2.3
Ba_2ScBiO_6	2.3
Ca_2ScBiO_6	2.3
Ca_2TiMnO_6	2.3
La_2GaCoO_6	2.3
Sr_2TlSbO_6	2.3
Ba_2CoRuO_6	2.3
Ca_2TaCoO_6	2.3
Sr_2ZrCrO_6	2.3
Ca_2TlRuO_6	2.4
Ba_2TaTlO_6	2.4
Sr_2TlRuO_6	2.4
$LiLa_2BiO_6$	2.4
Sr_2MgRuO_6	2.4
Sr_2TaCoO_6	2.4
Sr_2CoRuO_6	2.4
$MnTePb_2O_6$	2.4
La_2CuPdO_6	2.4
$NaLa_2BiO_6$	2.4
Sr_2HfCrO_6	2.4
Ca_2MgRuO_6	2.4
Ca_2PdRuO_6	2.4
Ba_2IrPbO_6	2.4
La_2CdPdO_6	2.5
Ca_2YBiO_6	2.5
Sr_2ScBiO_6	2.5
$NbFePb_2O_6$	2.5
$MnZn_2TeO_6$	2.5
Ba_2ZrPbO_6	2.5
Sr_2SnPdO_6	2.5
Ba_2MnSbO_6	2.6
Sr_2HgTeO_6	2.6
Sr_2ZrPbO_6	2.6
Ba_2MgRuO_6	2.6

Ba_2HfPbO_6	2.6
La_2ZnPdO_6	2.6
Sr_2TlIrO_6	2.6
La_2CrNiO_6	2.7
La_2CoPdO_6	2.7
La_2NiPdO_6	2.7
Ca_2NiIrO_6	2.7
Ba_2YBiO_6	2.7
Ba_2CuWO_6	2.7
Sr_2HfPdO_6	2.7
Ca_2CdIrO_6	2.7
Sr_2MnIrO_6	2.8
Ca_2ZrPdO_6	2.8
La_2MgCrO_6	2.8
Ca_2ZnIrO_6	2.8
Ca_2TaMnO_6	2.8
La_2MnCdO_6	2.8
Sr_2YBiO_6	2.8
Ba_2MnNbO_6	2.8
Sr_2HfPbO_6	2.8
Ca_2ZrMnO_6	2.8
La_2MnZnO_6	2.8
Sr_2ZnIrO_6	2.9
Sr_2ZrMnO_6	2.9
La_2CrCoO_6	2.9
Ca_2MnNbO_6	2.9
Ba_2TePbO_6	2.9
Ca_2CoIrO_6	2.9
La_2MgPdO_6	2.9
Ba_2TaMnO_6	2.9
Ca_2HfMnO_6	2.9
Sr_2HfMnO_6	3.0
Sr_2ZrPdO_6	3.0
La_2CoRhO_6	3.0
Sr_2CdIrO_6	3.0
Ca_2VFeO_6	3.0
Ca_2MgIrO_6	3.1
Sr_2RuRhO_6	3.1
Ba_2MnIrO_6	3.1
Ba_2ZnIrO_6	3.1
Sr_2TiRhO_6	3.1
Ba_2CdTeO_6	3.1
Sr_2FeTeO_6	3.2
Sr_2NiIrO_6	3.2
La_2AgIrO_6	3.2
Ca_2FeTeO_6	3.2
Sr_2BiRuO_6	3.2
Sr_2CoTeO_6	3.2
Ca_2CdTeO_6	3.2
Sr_2CdTeO_6	3.2
Ba_2MnTeO_6	3.2
Sr_2NiTeO_6	3.2
Ca_2MnSbO_6	3.2
Sr_2TePbO_6	3.2
Sr_2CoIrO_6	3.2
Ba_2CdIrO_6	3.3
Ba_2BiIrO_6	3.3
Ca_2NiTeO_6	3.3
La_2NiRhO_6	3.3
Sr_2MnSbO_6	3.3
Ca_2MnTeO_6	3.3
Ca_2IrRhO_6	3.3

Sr_2FeRuO_6	3.4
Ba_2MgTeO_6	3.4
Ca_2MnIrO_6	3.4
La_2CuIrO_6	3.4
Ca_2RuRhO_6	3.4
Ca_2FeIrO_6	3.4
Ba_2MgIrO_6	3.4
$TaInPb_2O_6$	3.5
Sr_2MgTeO_6	3.5
Ca_2FeRuO_6	3.5
Sr_2NbFeO_6	3.5
Sr_2GaSbO_6	3.5
Ba_2BiSbO_6	3.5
Ca_2MgTeO_6	3.5
Sr_2FeIrO_6	3.5
Sr_2CrIrO_6	3.5
La_2MnRhO_6	3.5
$ScZn_2SbO_6$	3.5
La_2CuRuO_6	3.6
Ca_2CuReO_6	3.6
Ba_2FeTeO_6	3.6
$CdRePb_2O_6$	3.6
Ba_2NbFeO_6	3.6
Sr_2ZrRhO_6	3.6
Ba_2InSbO_6	3.7
Ba_2HfRhO_6	3.7
Ca_2NbFeO_6	3.7
Ca_2GaSbO_6	3.7
Ca_2IrRuO_6	3.7
Sr_2CrRuO_6	3.7
Sr_2InIrO_6	3.7
Ba_2TaFeO_6	3.7
La_2MnCrO_6	3.7
Ba_2InRuO_6	3.7
Sr_2AlSbO_6	3.7
Sr_2AlRuO_6	3.7
Ba_2InIrO_6	3.8
Sr_2AlIrO_6	3.8
Sr_2HfRhO_6	3.8
Ca_2InRuO_6	3.8
Ca_2TiIrO_6	3.8
Ba_2TiSnO_6	3.9
Sr_2InRuO_6	3.9
Sr_2TiVO_6	3.9
Sr_2VSbO_6	3.9
Ca_2CrRuO_6	3.9
La_2FeRhO_6	3.9
Ca_2AlSbO_6	3.9
Ba_2ScRuO_6	3.9
Ca_2AlRuO_6	3.9
Sr_2BiSbO_6	3.9
Sr_2InSbO_6	4.0
Ba_2CdMoO_6	4.0
La_2GaRhO_6	4.0
Sr_2ScRuO_6	4.0
Ca_2ScIrO_6	4.0
Sr_2CuReO_6	4.0
Sr_2TiIrO_6	4.0
Ca_2NbRhO_6	4.0
La_2MnFeO_6	4.0
Ba_2NbRhO_6	4.1
Ca_2ScRuO_6	4.1

Sr_2TiSnO_6	4.1
Sr_2CdMoO_6	4.1
Ba_2ScSbO_6	4.1
Sr_2CdReO_6	4.2
La_2CdRuO_6	4.2
Ca_2YRuO_6	4.2
$LiLa_2SbO_6$	4.2
Ca_2TiSnO_6	4.2
$NaLa_2SbO_6$	4.2
$LiLa_2AsO_6$	4.2
Ba_2YRuO_6	4.2
La_2MgIrO_6	4.3
Sr_2NbRhO_6	4.3
Sr_2YRuO_6	4.3
Ca_2CdReO_6	4.3
Ca_2ScSbO_6	4.3
Sr_2ZrIrO_6	4.3
Sr_2ScSbO_6	4.3
Sr_2ZrVO_6	4.4
La_2AlFeO_6	4.4
La_2MnRuO_6	4.4
La_2FeSnO_6	4.4
$NbCrPb_2O_6$	4.4
La_2ScRhO_6	4.4
Ca_2ZrVO_6	4.4
La_2FeRuO_6	4.5
Sr_2TaRhO_6	4.5
La_2NiSnO_6	4.5
Ca_2YSbO_6	4.5
Ba_2NbBiO_6	4.5
Ba_2ZrIrO_6	4.5
La_2MnSnO_6	4.5
Ca_2HfVO_6	4.6
Sr_2NbBiO_6	4.6
Ba_2HfIrO_6	4.6
La_2ScFeO_6	4.6
La_2InGaO_6	4.6
Ba_2ZrSnO_6	4.6
Sr_2HfIrO_6	4.6
La_2InFeO_6	4.6
Sr_2YSbO_6	4.6
La_2MgRuO_6	4.7
Ca_2TaBiO_6	4.7
Ca_2TiGeO_6	4.7
Ca_2ZnReO_6	4.7
La_2VNiO_6	4.7
Ba_2FeMoO_6	4.7
Sr_2TaBiO_6	4.7
Ba_2TaInO_6	4.7
Ca_2ZrSnO_6	4.7
$NbVPb_2O_6$	4.7
La_2CrFeO_6	4.8
Sr_2FeReO_6	4.8
Ca_2TaInO_6	4.8
Ba_2ZrRuO_6	4.8
Ba_2ZnMoO_6	4.8
Ba_2TaBiO_6	4.8
Sr_2ZrSnO_6	4.8
Ba_2CoMoO_6	4.8
Ca_2FeMoO_6	4.8
Ba_2HfRuO_6	4.8
Sr_2ZrRuO_6	4.9

Sr_2FeMoO_6	4.9
La_2VInO_6	4.9
Sr_2HfSnO_6	4.9
La_2CrInO_6	4.9
Ba_2MnMoO_6	4.9
La_2NiGeO_6	4.9
Sr_2MgMoO_6	5.0
Ba_2CrMoO_6	5.0
Sr_2NbRuO_6	5.0
Ca_2ReNiO_6	5.0

Table 12.7: List of all DFT stable AA'BB'O_6 compounds with a vacancy formation energy within the window of interest for STCH applications.

Composition	ΔE_{vf} [eV/O]
$NaYbTaPbO_6$	2.0
$BaEuNbTlO_6$	2.0
$NaEuMnNbO_6$	2.0
$NaEuTaPbO_6$	2.0
$NaTmTiMnO_6$	2.0
$RbNdZrPbO_6$	2.0
$NaHoTiMnO_6$	2.0
$NaErTiMnO_6$	2.0
$KDyHfPbO_6$	2.0
$NaEuTaMnO_6$	2.0
$RbCeTaTlO_6$	2.0
$KDyZrPbO_6$	2.0
$KCeHfMnO_6$	2.0
$NaPrTiMnO_6$	2.0
$NaCeTiPdO_6$	2.0
$NaPrTiPdO_6$	2.0
$KCeMnNbO_6$	2.1
$NaNdTiMnO_6$	2.1
$BaEuTaTlO_6$	2.1
$KGdHfPbO_6$	2.1
$RbCeZrPbO_6$	2.1
$KGdZrPbO_6$	2.1
$KHoHfPbO_6$	2.1
$KYHfPbO_6$	2.1
$NaSmTiPbO_6$	2.1
$RbCeHfPbO_6$	2.2
$NaGdTiPbO_6$	2.2
$NaTbTiPbO_6$	2.2
$NaHoTiPbO_6$	2.2
$NaDyTiPbO_6$	2.2
$KLaMnNbO_6$	2.2
$NaTmTiPbO_6$	2.2
$CaLaTiCoO_6$	2.2
$NaTmZrPbO_6$	2.2
$KNdZrPbO_6$	2.2
$KLaTaMnO_6$	2.3
$SrNdTiCoO_6$	2.3
$NaErZrPbO_6$	2.3
$NaHoZrPbO_6$	2.3
$NaYZrPbO_6$	2.3
$NaTbZrPbO_6$	2.3
$NaDyZrPbO_6$	2.3
$NaGdZrPbO_6$	2.3
$KPrZrPdO_6$	2.3
$KCeTaMnO_6$	2.3
$NaSmZrPbO_6$	2.3
$NaNdZrPbO_6$	2.3
$KLaZrPdO_6$	2.4
$KLaHfPdO_6$	2.4
$KCeHfPbO_6$	2.4
$NaDyHfPbO_6$	2.4
$CaPrTiCoO_6$	2.4
$NaYHfPbO_6$	2.4
$KCeZrPdO_6$	2.4
$NaNdZrMnO_6$	2.4
$NaCeZrMnO_6$	2.4
$KCeHfPdO_6$	2.4

$NaTbHfPbO_6$	2.4
$KLaHfPbO_6$	2.4
$CaNdTiCoO_6$	2.4
$NaSmHfPbO_6$	2.4
$NaNdHfMnO_6$	2.4
$KCeZrPbO_6$	2.5
$CaNdZrTlO_6$	2.5
$KPrHfPbO_6$	2.6
$KHoZrPbO_6$	2.6
$NaPrZrMnO_6$	2.6
$KCeTaTlO_6$	2.6
$NaSmZrMnO_6$	2.6
$KPrTaTlO_6$	2.6
$BaLaTiMnO_6$	2.6
$KTbZrPbO_6$	2.6
$RbPrZrPbO_6$	2.7
$NaPrHfMnO_6$	2.7
$NaYHfMnO_6$	2.7
$NaSmTaMnO_6$	2.7
$NaDyHfMnO_6$	2.7
$NaCeTaMnO_6$	2.7
$NaNdTaMnO_6$	2.7
$NaCeHfMnO_6$	2.7
$NaPrTaMnO_6$	2.7
$NaGdHfMnO_6$	2.7
$NaTbHfMnO_6$	2.7
$KSmZrPbO_6$	2.8
$BaEuTaMnO_6$	2.8
$KPrZrPbO_6$	2.8
$KTbHfPbO_6$	2.8
$CaDyTiCoO_6$	2.8
$RbCeNbFeO_6$	2.8
$NaTmHfPbO_6$	2.8
$KSmHfPbO_6$	2.9
$RbPrTaFeO_6$	2.9
$KNdHfPbO_6$	2.9
$NaNdHfPbO_6$	2.9
$NaHoHfPbO_6$	2.9
$NaErHfPbO_6$	2.9
$NaSmHfMnO_6$	3.0
$SrPrTiMnO_6$	3.1
$NaCeTaTlO_6$	3.1
$SrLaTiMnO_6$	3.1
$CaSmTiMnO_6$	3.1
$NaNdTaTlO_6$	3.1
$KCeNbFeO_6$	3.1
$SrCeTiMnO_6$	3.1
$CaNdTiMnO_6$	3.2
$CaLaTiMnO_6$	3.2
$CaPrTiMnO_6$	3.2
$KGdTaFeO_6$	3.2
$NaHoHfMnO_6$	3.2
$BaPrTiFeO_6$	3.3
$BaLaTiFeO_6$	3.3
$SrCeHfTlO_6$	3.3
$BaYbTaFeO_6$	3.4
$BaCeTiFeO_6$	3.4
$CaTbTiMnO_6$	3.4
$CaCeMnVO_6$	3.4
$CaGdTiMnO_6$	3.4
$CaPrMnVO_6$	3.4
$CaCeTiMnO_6$	3.4

$SrHoTiFeO_6$	3.4
$CaNdMnVO_6$	3.5
$SrDyTiFeO_6$	3.5
$SrTbTiFeO_6$	3.5
$CaNdTaCuO_6$	3.5
$SrGdTiFeO_6$	3.5
$BaLaTiRhO_6$	3.6
$BaPrTiRhO_6$	3.6
$CaGdMnVO_6$	3.6
$CaLuTiFeO_6$	3.6
$BaCeTiRhO_6$	3.6
$CaYMnVO_6$	3.6
$SrSmTiFeO_6$	3.6
$CaDyMnVO_6$	3.7
$BaEuTaFeO_6$	3.7
$CaTmTiFeO_6$	3.7
$CaErTiFeO_6$	3.7
$SrNdTiFeO_6$	3.7
$CaHoTiFeO_6$	3.7
$CaDyTiFeO_6$	3.7
$CaTbTiFeO_6$	3.7
$CaGdTiFeO_6$	3.8
$NaCeTiIrO_6$	3.8
$NaPrTiIrO_6$	3.8
$SrPrTiFeO_6$	3.8
$KLaTiRuO_6$	3.8
$KCeTiRuO_6$	3.8
$BaEuNbRhO_6$	3.8
$CaNdTiFeO_6$	3.8
$SrCeTiFeO_6$	3.8
$CaCeTiFeO_6$	3.8
$CaYVFeO_6$	3.9
$CaYTiFeO_6$	3.9
$KCeZrIrO_6$	3.9
$CaLaTiFeO_6$	3.9
$NaTbVSbO_6$	3.9
$SrNdTiRhO_6$	3.9
$RbEuZrSbO_6$	3.9
$RbTmTiTeO_6$	3.9
$RbHoTiTeO_6$	4.0
$CsSmTiTeO_6$	4.0
$RbLuTiTeO_6$	4.0
$CaErTiRhO_6$	4.0
$CaHoTiRhO_6$	4.0
$RbNdTiTeO_6$	4.0
$CsPrTiTeO_6$	4.0
$NaDyTiRuO_6$	4.0
$CaTbTiRhO_6$	4.0
$NaTbTiRuO_6$	4.0
$CaGdTiRhO_6$	4.0
$KCeTaRhO_6$	4.0
$SrLaTiRhO_6$	4.0
$RbLaTiTeO_6$	4.0
$CaLuTiRhO_6$	4.0
$SrCeTiRhO_6$	4.0
$KEuZrSbO_6$	4.0
$KEuNbRuO_6$	4.0
$NaSmTiRuO_6$	4.0
$CaTmTiRhO_6$	4.0
$CaCeTiRhO_6$	4.0
$RbCeTiTeO_6$	4.0
$CaSmTiRhO_6$	4.0

$NaYbZrSbO_6$	4.0
$CaLaTiRhO_6$	4.1
$NaEuNbIrO_6$	4.1
$RbEuHfSbO_6$	4.1
$NaCeTiRuO_6$	4.1
$SrPrTiRhO_6$	4.1
$CaPrTiRhO_6$	4.1
$RbErTiTeO_6$	4.1
$KCeTiTeO_6$	4.1
$CsHoTiTeO_6$	4.1
$RbYTiTeO_6$	4.1
$CsDyTiTeO_6$	4.1
$SrNdVFeO_6$	4.1
$RbGdTiTeO_6$	4.1
$NaPrTiRuO_6$	4.1
$CsGdTiTeO_6$	4.1
$CaYTiRhO_6$	4.1
$RbTbTiTeO_6$	4.1
$KErTiTeO_6$	4.1
$KTmTiTeO_6$	4.1
$KHoTiTeO_6$	4.1
$CaNdTiRhO_6$	4.1
$KEuHfSbO_6$	4.1
$KPrTiTeO_6$	4.1
$KYTiTeO_6$	4.1
$KSmTiTeO_6$	4.2
$NaLuTiSnO_6$	4.2
$KNdTiTeO_6$	4.2
$RbDyTiTeO_6$	4.2
$KDyTiTeO_6$	4.2
$KTbTiTeO_6$	4.2
$NaCeCdMoO_6$	4.2
$KGdTiTeO_6$	4.2
$SrCeVFeO_6$	4.2
$RbCeCdWO_6$	4.2
$CaLuVFeO_6$	4.2
$NaCeCdWO_6$	4.2
$SrSmTiRhO_6$	4.3
$CaGdVFeO_6$	4.3
$NaTmCdWO_6$	4.3
$NaTbCdWO_6$	4.3
$NaYCdWO_6$	4.3
$CaHoVFeO_6$	4.3
$CaPrVFeO_6$	4.3
$CaSmVFeO_6$	4.3
$KPrCdWO_6$	4.3
$CaDyVFeO_6$	4.3
$NaYbHfSbO_6$	4.3
$KCeZrRuO_6$	4.3
$KLaZrRuO_6$	4.3
$CaDyTiRhO_6$	4.3
$CsEuTaTeO_6$	4.3
$CaErVFeO_6$	4.3
$CaTmVFeO_6$	4.3
$BaEuCdWO_6$	4.3
$NaYTaFeO_6$	4.4
$NaPrCdWO_6$	4.4
$SrCeHfFeO_6$	4.4
$KPrZrRuO_6$	4.4
$NaEuNbRuO_6$	4.4
$KCeCdMoO_6$	4.4
$NaTmTaFeO_6$	4.4

$NaGdTaFeO_6$	4.4
$NaDyTaFeO_6$	4.4
$SrCeZrRhO_6$	4.4
$NaErTaFeO_6$	4.4
$NaYbNbRuO_6$	4.4
$NaNdCdWO_6$	4.4
$NaHoTaFeO_6$	4.4
$KYbHfSbO_6$	4.4
$NaSmCdWO_6$	4.4
$SrGdNbCdO_6$	4.5
$NaLaCdWO_6$	4.5
$CaHoNbCdO_6$	4.5
$BaCeNbCdO_6$	4.5
$CaDyNbCdO_6$	4.5
$NaYbTaRuO_6$	4.5
$BaNdTaCdO_6$	4.5
$KCeCdWO_6$	4.5
$CsYTiTeO_6$	4.5
$RbEuTaTeO_6$	4.5